

Towards Tunneling Electrodes for Nanopore-based DNA Sequencing

THÈSE N° 5700 (2013)

PRÉSENTÉE LE 2 MAI 2013

À LA FACULTÉ DES SCIENCES DE BASE
LABORATOIRE DE PHYSIQUE DE LA MATIÈRE COMPLEXE
PROGRAMME DOCTORAL EN PHYSIQUE

ÉCOLE POLYTECHNIQUE FÉDÉRALE DE LAUSANNE

POUR L'OBTENTION DU GRADE DE DOCTEUR ÈS SCIENCES

PAR

Axel FANGET

acceptée sur proposition du jury:

Prof. O. Schneider, président du jury
Prof. L. Forró, Dr A. Magrez, directeurs de thèse
Prof. C. Hébert, rapporteur
Prof. S. A. Mátéfi-Tempfli, rapporteur
Prof. R. Zikic, rapporteur



ÉCOLE POLYTECHNIQUE
FÉDÉRALE DE LAUSANNE

Suisse
2013

Abstract

The advent of DNA sequencing has revolutionized fundamental research and brought incredible hope for personalized medicine. However, the race still continues for cheaper and faster techniques that can surpass conventional methods and ultimately reach the \$1000 genome goal. This thesis describes the fabrication and first characterizations of nanopores-based devices with embedded tunneling electrodes for single-molecule DNA sensing. This constitutes a unique and very promising approach for label-free detection and structural analysis of individual molecules.

Nanopores are nanometer-sized holes in thin biological or solid-state membranes, which charged molecules or particles, including DNA molecules, can be threaded through under the driving force of an external electric field. When performed in an electrolyte, the translocation of individual molecules results in ionic current blockades that provide useful information about the molecule's properties such as length, conformation and eventually local structure. After more than a decade of extensive investigations, it is widely admitted that pure ionic analysis suffers from limited temporal and structural resolutions for DNA sequencing.

Since it has been demonstrated that single-base resolution can be achieved through transverse tunneling current, coupling nanopores to tunneling junctions might be the solution to nanopore-based sequencing. The fabrication of such devices is extremely challenging, as the electrodes need to be aligned with the nanopore and spaced only few nanometers apart for tunneling to be possible. We have investigated two strategies for such an achievement with solid-state nanopores drilled with an electron beam.

First, we present a method for embedding single-wall carbon nanotubes (SWCNTs) nanoelectrodes across the diameter of a nanopore. A reproducible fabrication process for the synthesis with location control and circuit integration of individual SWCNTs is established and combined to the fabrication of nanopores. By cutting the nanotubes and drilling a pore in a single step using a focused electron beam, we show a proof of principle device but damaging of the SWCNT electrode tips is difficult to avoid.

To overcome the relative low-throughput of the first method, we present a process for nanopores with metallic tunneling junctions using advanced electron beam lithography (EBL) and electrodeposition techniques. It is possible to fabricate electrodes that are separated by 7nm and aligned with the nanopore with an exceptional reproducibility and process yield. By electrodeposition, a large number of nanopore electrodes can be reduced down to few nanometers with spacing control.

Functional nanopores devices are then successfully fabricated by *in situ* drilling of sub-10nm nanopores in between the metallic electrodes.

Finally, we report on the characterization of these new single-molecule sensors in a microfluidic cell. We study the influence of the transverse metallic electrodes on the ionic current and pore conductance as well on the probability of obtaining DNA translocation. Then, we present a proof of principle experiment where the translocation of DNA molecules could be detected in both channels simultaneously.

Keywords: DNA sequencing, solid-state nanopores, transverse tunneling electrodes, nanogap electrodes, single-walled carbon nanotubes, Chemical Vapor Deposition, electron beam lithography, TEM drilling, DNA translocation, ionic current, tunneling current.

Résumé

L'avènement des techniques de séquençage d'ADN a révolutionné la recherche fondamentale et apporté un espoir considérable quant à la médecine personnalisée. Cependant, le besoin croissant pour de nouvelles techniques, toujours plus rapides et peu onéreuses, et qui pourraient atteindre le but ultime de \$1000 par génome est plus que jamais d'actualité. Cette thèse décrit la fabrication et caractérisation de séquenceurs dont le fonctionnement est basé sur l'emploi d'électrodes à effet tunnel intégrées à un nanopore, et qui pourraient constituer une solution unique pour l'analyse de molécules individuelles sans labélisation.

Les nanopores sont des pores de quelques nanomètres de diamètre dans de fines membranes biologiques ou synthétiques et à travers lesquels il est possible de faire passer des molécules chargées à l'aide d'un champ électrique externe. Dans une solution saline, la translocation d'une molécule résulte en un blocage du courant ionique dont l'analyse permet d'obtenir des informations sur ses propriétés, comme sa longueur, conformation ou structure locale. Après une décennie d'intenses études des nanopores, il est admis que le courant ionique ne fournit pas à lui seul la résolution temporelle et spatiale requise pour le séquençage d'ADN.

Comme il a été prouvé que la résolution de base unique est atteinte grâce aux mesures de courant par effet tunnel, la combinaison d'un nanopore à une jonction tunnel permettrait d'achever un séquençage rapide grâce aux nanopores. La fabrication d'un tel dispositif est un vrai défi car il faut que les électrodes soient parfaitement alignées avec le nanopores et qu'elles ne soient séparées que par quelques nanomètres. Nous avons étudié deux stratégies pour qu'une telle réalisation soit faisable et compatible avec la fabrication d'un nanopore avec un faisceau d'électron.

Premièrement, nous présentons une méthode pour incorporer des électrodes en nanotubes de carbone mono-paroi (SWCNTs) à un nanopore. Un procédé reproductible pour la synthèse avec contrôle du positionnement et l'intégration électronique de SWCNTs individuels a été établi et adapté à la fabrication de nanopore. En perçant le nanopore et le tube en même temps, nous démontrons la fabrication d'un tel dispositif et montrons la difficulté d'éviter l'amorphisation des électrodes.

Ensuite, pour surpasser ces difficultés techniques, nous présentons une méthode de fabrication de jonctions tunnel métalliques exploitant la lithographie à faisceau d'électrons haute résolution (EBL) et l'électrodéposition. Par EBL, nous démontrons qu'il est possible de fabriquer des jonctions de 7nm avec une extrême fiabilité et

rapidité. Par electrodeposition, nous montrons qu'il est également possible de réduire celles-ci jusqu'à quelques nanomètres avec très bon contrôle. Des dispositifs fonctionnels sont ensuite fabriqués en perçant *in situ* un nanopore entre les électrodes.

Finalement, nous étudions expérimentalement ces dispositifs dans une chambre microfluidique. Nous caractérisons l'influence des électrodes transverses métalliques sur le courant ionique et sur la conductance du pore, ainsi que la probabilité d'obtenir des translocations d'ADN. Nous présentons ensuite une expérience qui démontre la détection simultanée de translocation d'ADN avec le courant ionique et le courant transverse.

Mots-clés : Séquençage d'ADN, nanopores, électrodes à effet tunnel, nanoelectrodes, nanotubes de carbone mono-paroi, dépôt chimique en phase vapeur, lithographie à faisceau d'électrons, microscope électronique à transmission, translocation d'ADN, courant ionique, courant à effet tunnel.

Table of Contents

Introduction	1
1 Ultrafast DNA sequencing	7
1.1 Introduction	7
1.1.1 Motivation	7
1.1.2 Goals.....	9
1.1.3 Structure of DNA	10
1.2 State of the art.....	11
1.2.1 Sanger’s chain termination classical sequencing	11
1.2.2 Next generation sequencing	12
Roche 454 pyrosequencing	13
Illumina sequencing	14
Other promising Next-Generation Sequencing technologies	15
1.2.3 Challenges and limitations	16
1.3 Nanopore-based sequencing.....	18
1.3.1 Nanopores as single-molecules biosensors	18
Driving DNA single molecules toward a nanopore	18
Biological nanopores.....	20
Solid-state nanopores	21
Hybrid nanopores	22
1.3.2 Ionic current modulation by translocating single DNA molecules	22
Ionic conductance in a nanopore	22
Basics of nanopore measurements: ionic blockades	24
Detection and sequencing.....	28
1.3.3 Challenges of ionic-current based sequencing	30
1.4 Transverse electrodes-embedded nanopores	31
1.4.1 Tunneling-current through polynucleotides	31
1.4.2 A STM microscope in a nanopore.....	32
Carbon nanotube based nanoelectrodes	34
Nanogap metallic electrodes	35
1.4.3 Discussion	36

2	Techniques	37
2.1	Electron beam lithography	37
2.1.1	Principle of lithography.....	37
2.1.2	EBL systems.....	39
	Electron sources	39
	Column	40
	Stage.....	41
2.1.3	Scattering interactions as resolution limitations.....	42
	Forward scattering and backscattering of primary electrons.....	43
	Secondary electrons travel path.....	44
	Proximity effects	44
	Scattering and proximity effect correction.....	45
	Charging effects	46
2.1.4	EBL Resists	46
	Dose, sensitivity and contrast.....	47
	PMMA.....	48
	ZEP.....	48
	HSQ.....	49
2.1.5	Alignment.....	50
	Distortions and coordinates systems	50
	Alignment marks	51
	Alignment process.....	52
	Limitations	53
2.2	Pattern transfer	54
2.2.1	Leybold LAB600H.....	54
2.2.2	Alcatel AMS-200DE	54
2.3	Solid-state nanopores fabrication	54
2.3.1	Substrate	55
2.3.2	Membrane opening.....	55
2.3.3	Nanopore drilling	57
2.4	Microfluidic and nanopore setup.....	59
3	Nanopores embedded with transversal SWCNT tunneling electrodes	61
3.1	Introduction to carbon nanotubes.....	61

3.1.1	History of carbon nanotubes.....	62
3.1.2	Structure and chirality of carbon nanotubes.....	63
3.1.3	Properties of carbon nanotubes	66
	Electronic properties.....	66
	Chemical properties.....	70
3.1.4	Synthesis of Carbon nanotubes	72
	Arc discharge synthesis	72
	Laser ablation synthesis.....	73
	Chemical Vapor Deposition (CVD) synthesis	74
3.1.5	CNTs in nanotechnology - synthesis challenges	76
3.1.6	Focus on Chemical vapor deposition	77
	Growth mechanism.....	77
	Influence of catalyst properties	80
	Catalyst support.....	81
	Carbon feedstock.....	82
	Temperature.....	83
	Catalyst preparation for CVD synthesis of CNTs	83
3.2	Device fabrication strategy.....	84
3.3	Patterned growth of isolated SWCNTs by ethanol CVD	86
	3.3.1 Choice of the CVD conditions	87
	3.3.2 SiO ₂ nanoparticles-supported Mo/Co catalyst	88
3.4	SWCNT transverse electrodes embedded nanopores fabrication	93
	3.4.1 Contacting SWCNTs.....	93
	Strategy.....	93
	Contact resistance.....	95
	3.4.2 The membrane challenge.....	96
	3.4.3 Nanopore drilling	99
3.5	Discussion	101
4	Fabrication of nanopores with metallic transversal tunneling junction	103
4.1	Fabrication of sub-10 nm metallic nanogap electrodes.....	103
	4.1.1 Challenges	103
	4.1.2 Fabrication by direct metallization.....	104
	Strategy.....	104
	Method	106

Results	107
Shape optimization	109
4.1.3 Fabrication by combination of lift-off and etching of HSQ	110
Strategy	110
Method	111
Results	111
4.1.4 Discussion	113
4.2 Nanogap reduction by electrodeposition	114
4.2.1 Experimental details	115
4.2.2 Results and discussion	116
4.3 Nanogap integration into a nanopore device	118
4.3.1 Contacting and insulating nanogaps electrodes	118
Alignment challenges	118
High-resolution alignment	120
Contacting nanogaps electrodes	122
Electrodes passivation	123
4.3.2 Nanopore drilling	124
4.4 Conclusion	126
5 Study of nanopores with embedded metallic tunneling junctions	129
5.1 Introduction	129
5.2 Influence of the nanogap electrodes on the nanopore behavior	133
5.2.1 Nanopore characterization	133
5.2.2 Nanogap characterization	134
5.2.3 Effect on noise and coupling of the two channels	137
5.2.4 Ionic current rectification	138
5.3 DNA translocation detection	139
5.3.1 In a standard nanopore configuration	140
5.3.2 By simultaneous measurements of the ionic and transverse current	141
5.4 Discussion	144
Conclusion and perspectives	147
Bibliography	151
Acknowledgments	165

Curriculum Vitae

167

Introduction

More than 50 years ago, on December 29th, 1959, the American scientist Richard Feynman introduced the basic concepts of nanotechnology during his famous lecture entitled “*There is plenty of room at the bottom*”, symbolized by his idea of fitting the 24 volumes of the *Encyclopedia Britannica* on the head of a pin^[1]. Considered as the father of nanosciences, he first imagined the possibility of observing, manipulating, and engineering materials at the atomic scale as well as the feasibility of creating nanoscale machines, only limited by the size of atoms.

In 2013, nanotechnology is everywhere. It is relevant to all sciences and is a highly interdisciplinary area, including physics, chemistry, biology, semiconductors, and all fields where the use of nano-sized objects has become inevitable. Although the term *nano* is nowadays more than popular, its importance goes beyond a matter of dimensions reduction. For objects of sizes in the range of a nanometer, literally a billionth of meter (10^{-9} m), new properties, new behaviors and new phenomenon are observed, which can't be predicted from their larger scale equivalent. Nanotechnology is not only shrinking objects, it is a totally new world, where radically new physical and chemical changes, and quantum effects occur as the size of the systems is decreased.

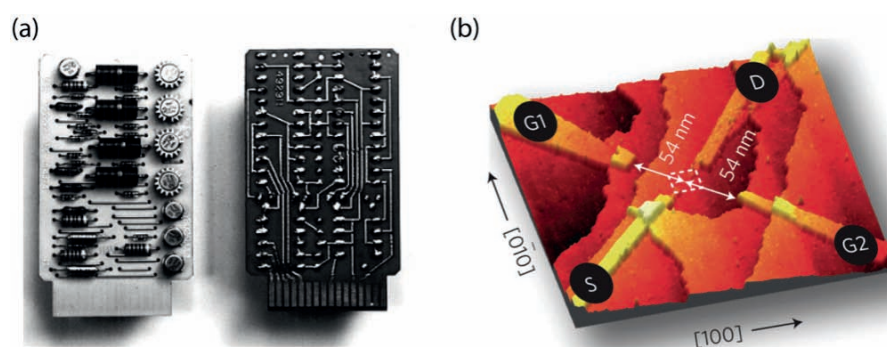


Figure 1. From macro to nano-transistors. (a) Transistor and a printed circuit as released by IBM in 1958. (b) An experimental single-atom transistor studied in 2012^[2].

Miniaturization of information technologies as well as the need for fast calculations has been undoubtedly the main motor of the evolution of science from micro to nano.. Based on empirical data, Gordon Moore^[3] has predicted that the number of transistors on integrated circuits would double every 18 month. Now it is known as with the *Moore's law*. Such an exponential growth is being achieved by patterning hundreds of millions of nanostructures at constantly greater densities and lower scale, yielding always smaller and more powerful devices. From room-filling computers with microprocessors of few thousands of $10\mu\text{m}$ transistors in the seventies, industrial

manufacturing is nowadays performed at the 22nm scale, in a top-down approach where small features are fabricated from larger materials.

Although the trend enunciated by Moore is still believed to remain valid for the next couple of decades, it cannot withstand such an exponential growth indefinitely as the size of atoms constitute a fundamental barrier to downscaling processes. Furthermore, the top-down approach becomes prohibitively expensive and demanding when bulk materials have to be structured with atomic resolution. The alternative strategy to overcome this inherent limitation is the so-called bottom-up approach, where instead of structuring bulk materials, electronic components are built-up atom-by-atom and based on single molecules. In molecular electronics, all electronic components, such as wires and transistors, would be based on molecular building blocks, which are synthesized and engineered in the lab. One of these promising building elements is carbon nanotubes (CNTs) since their advent in 1991. They arrive in two flavors: metallic and semiconducting. Metallic single-walled carbon nanotubes (SWCNTs) have been shown to have extraordinary current density carrying capabilities, with diameters smaller than 2 nanometers and hold the promise to replace conventional metallic wires. CNTs also exhibit semiconducting behaviors and CNTs-based devices have already found applications as actuators, sensors, data storage, *etc.*

Fabricating single-molecule devices will require the combination of top-down and bottom-up technologies in order to integrate numerous functional nanomaterials among bulk components in well-controlled and repeatable assembling processes for large-scale production. In other words, the main challenge of nanotechnology is not only the integration of nanometer-sized structures with micro but also with millimeter-sized features, and hence, the integration of the existing lithographic technologies along with nanoscale engineering.

In parallel, the success of nanotechnology-enabled devices relies as well on the ability to synthesize and to study nanomaterials at the atomic or molecular scales. Fortunately, the advent of nanoprocessing and imaging techniques generated by the spectacular miniaturization of electronic components has benefited to countless numbers of fields. We can now image and visualize structures close to the atomic resolution, which aside providing a better understanding of the nanoworld, help us to control and tune these structures to make new materials with new properties.

The study of single molecules has therefore become a very active field within the last years. For instance, the invention of the atomic force microscopy (AFM) allowed to study the mechanical properties of individual CNTs^[4] and DNA molecules^[5] but also the folding dynamics of single biological proteins^[6]. Similarly, photonic force microscopes (PFM) have been used to investigate the elastic properties of biological

polymers, for instance by stretching individual DNA molecules under various experimental conditions^[7]. Electronic and conductance studies can also be performed at the single-molecule scale. For example, scanning-tunneling spectroscopy (STS) or conductive AFM can probe nanometer-sized materials and provide useful information about their electronic properties. Moreover these tools can also be used as nanomanipulators to move, position or engineer nanostructures. Finally, imaging and 3D studies of single molecules is also possible using numerous techniques, such as scanning and transmission electron microscopes, AFM and STM and more recent technologies such as super resolution microscopy^[8].

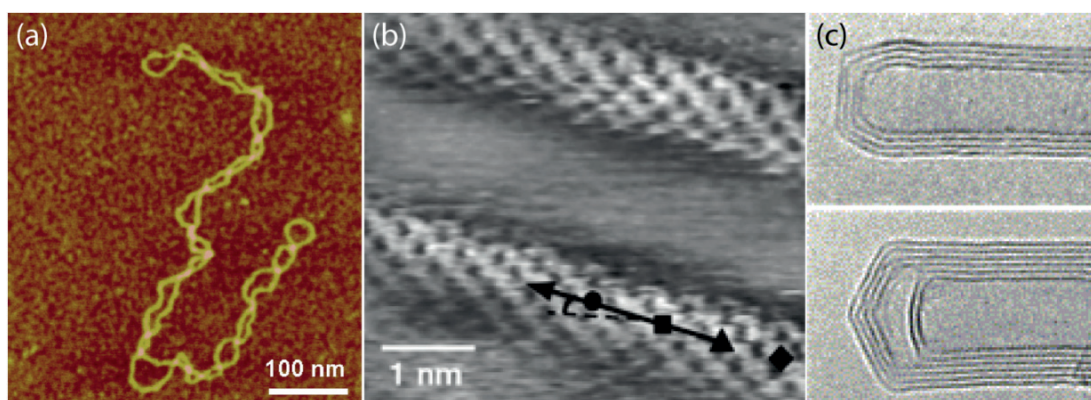


Figure 2. High resolution microscopy techniques. (a) AFM picture of a single supercoiled DNA molecule on a mica substrate^[9] (b) Scanning Tunneling Microscopy image with atomic resolution of isolated single-walled carbon nanotubes on a gold surface^[10] (c) TEM micrographs of multi-walled carbon nanotubes showing concentric carbon monolayers. Diameters are typically in a 10-20nm range^[11].

Single-molecule experiments are becoming inevitable and offer spectacular opportunities, which are going to revolutionize the area of nanotechnology. As stated above, the physics at the nanoscale is different and has to be explored in such a way. But single molecules analysis also allows a drastic cost reduction and processing speed improvement. From micro, biochips are also making the transition to nanofluidics and are capable of single-molecule detection (SMD). Thanks to this miniaturization, detection volumes have been shrunk, reducing reagents and sample consumption, while enhancing the devices' sensitivity.

Nanopore-based DNA sequencing symbolizes by itself all the challenges that have to be overcome on one hand in the fabrication of nanoscale devices and on the other hand in single-molecule detection. Recently, it has been shown that single DNA molecules can be threaded through nanoscale holes formed by biological proteins or in solid-state membranes under the influence of an external electric field. By embedding tiny transverse electrodes across the diameter of the pore, this system has the potential to sequence single DNA molecules with a throughput and cost that will

never be achieved by conventional Sanger-based or sequencing-by-synthesis-based methods.

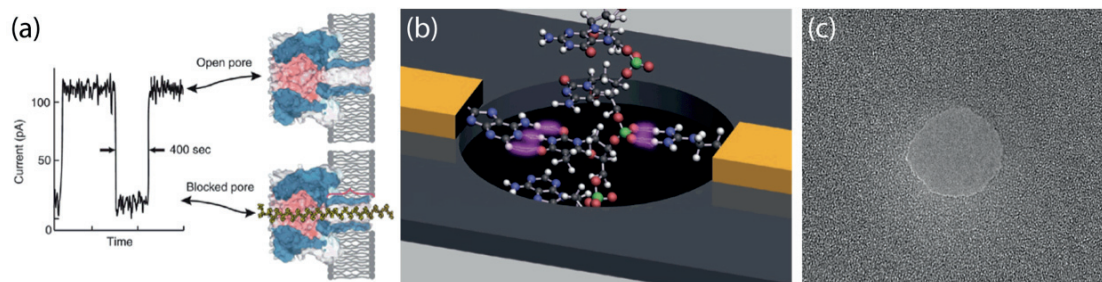
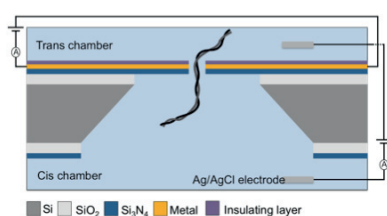


Figure 3. Ultrafast nanopore based DNA sequencing. (a) Classical ionic current modulation by DNA molecules passing through a biological nanochannel. (b) Transverse nanopore electrodes for tunneling current measurements of the DNA backbone with a nanopore. Adapted from Branton *et al.*^[12] (c) TEM image of a 10 nanometers synthetic nanopore sculpted in a silicon nitride membrane at EPFL.

The fabrication of such a nanopore sequencer remains extremely challenging. Nanogap electrodes have to be structured with nanometer resolution on the edge of a nanopore, and the resulting device has to be integrated within a whole microfluidic chamber connected to external measurement systems. The overall process has to be fast and reproducible enough for a large-scale application.

As a proof-of-concept, the possibility of probing single DNA molecules with such a device has also to be demonstrated but would constitute in case of success a major breakthrough for biology and personal medicine.

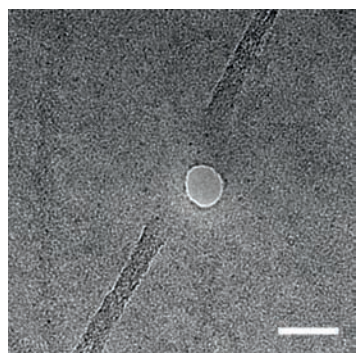
The challenge of my PhD program was to incorporate all the above issues: nanofabrication, carbon nanotubes growth and manipulation, and measurements at nanoscales. By definition it has been highly interdisciplinary, aiming at fabricating and characterizing a novel tool for single molecule probing. The research proposed here combines state-of-the-art technologies for tailoring nanopores with nanogap electrodes made up of carbon nanotubes or by nanolithography and their further integration into molecular devices.



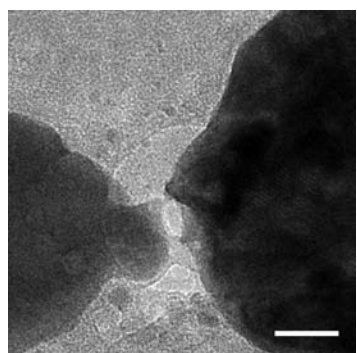
In **chapter 1**, the existing or under development DNA sequencing technologies are briefly introduced and compared to single-molecule nanopore-based technologies. The fundamental concepts of solid-state nanopores, nanopore-based, and nanopore-tunneling-based DNA sequencing are further explained.



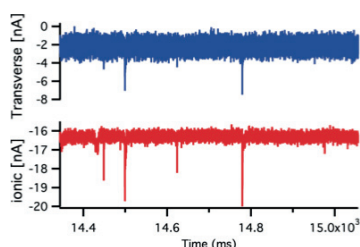
Chapter 2 reviews the main techniques and tools that have been used all along the project for fabrication or characterization purposes. A particular focus is placed on electron beam lithography (EBL), which played a central role in the realization of the devices. The fabrication of solid-state membranes and nanopores fabrication in a TEM microscope is then detailed. The microfluidic and measurements setup is finally described.



After an introduction to carbon nanotubes, **Chapter 3** emphasizes on the synthesis of individual single-walled carbon nanotubes (SWCNTs) with location control and their integration into nanopore devices as nanoscale electrodes. The fabrication challenges and outcomes of such a molecular device are then discussed (Scale bar: 10nm).



In **chapter 4**, the fabrication of metallic nanogap electrodes with exceptional resolution and reproducibility is demonstrated, as well as their full integration into nanopore devices fulfilling all technological requirements for single-molecule analysis as enunciated in chapter 1. (Scale bar: 10nm).



Chapter 5 is dedicated to the experimental characterization and study of nanopore devices with metallic nanogap electrodes for single-molecules detection. A proof-of-principle of simultaneous detection is presented. The main challenges and experimental issues that were encountered are finally discussed.

Chapter 1

Ultrafast DNA sequencing

1.1 Introduction

Cells, which are the fundamental building blocks of all living organisms, contain unique genetic information governing their structure and function. These instructions are carried in molecules that are common for all: DeoxyriboNucleic Acids, widely known as DNA. For all systems, the molecular structure of DNA is identical, a chain arrangement of four building blocks, named nucleotides or more commonly bases, lined-up in a sequence that is proper and unique for every individual. In cells, DNA molecules are physically present as chromosomes, which can be made of up to 250 million base pairs (bp). Some regions of the chromosomes are genes, which encode for the synthesis of proteins, while the rest are non-coding regions. Non-coding regions are responsible for the regulation of the genes expression. A Genome, which is the complete set of chromosomes of an organism, can reach sizes of up to 3.2 billions base pairs for humans.

DNA sequencing is the process of accurately determining the order of the four bases in a DNA molecule. In the case of a full genome, the molecular structure of the whole genetic material is established.

1.1.1 Motivation

Genetics, genomics, there are tens of fields in molecular biology that are rooted to determine how genes work, how they interact with environment, how features are inherited from generation to generation or how to manipulate and use them. Every single time the relationship between a discrete sequence of DNA and a set of proteins or functions is established, the information is added to existing databases, which list the already known sequences (Figure 1.1). The knowledge of DNA sequences is nowadays indispensable and so are the needs for always faster, cheaper and more reliable sequencing methods. The amount of sequences to determine is enormous. The average gene size for humans is about 3000 bp and can be as high as 2 millions. A full human genome is about 3.2 billions (3.2×10^9 bp), among which we can distinguish only 25000 genes, so about 2% of the genome. The 98% left, are non-coding regions

that are as important as the coding ones. Among individuals, 99.9% of the genomes are similar, but not identical, meaning that single nucleotide polymorphisms (SNPs) can confer genes and non-coding regions different properties. Moreover, the need for sequencing is not only focused on the human genome. The fundamental understanding of other biological systems also requires the availability of their genomic information.

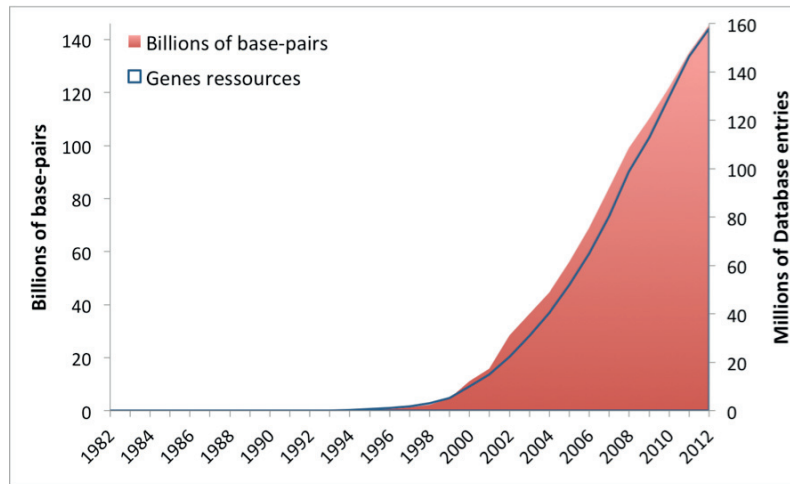


Figure 1.1. The extraordinary growth of data deposited in GenBank from 1982 to 2012^[13]. The right axis shows the number of sequences listed in the database, while the left axis shows the number of base-pairs.

Aside fundamental research, the potential applications and the global market opportunities of sequencing knowledge are tremendously broad. Personalized medicine is with no doubt the most promising application of genomic sequencing. Gene tests offer the opportunity to prevent, diagnose, confirm or predict disease. Customized drugs may correlate individual responses to medical care, so that the most appropriate treatments are used, in term of efficiency and adverse reactions. Finally DNA sequencing has brought a lot of hope to genetic diseases, which could be treated by using genes themselves. Outside of the healthcare domain, recent progress in DNA sequencing had major impacts in many other fields, such as risk assessment, security, agriculture and biotechnology. Few typical application examples are shown in Diagram 1.1.

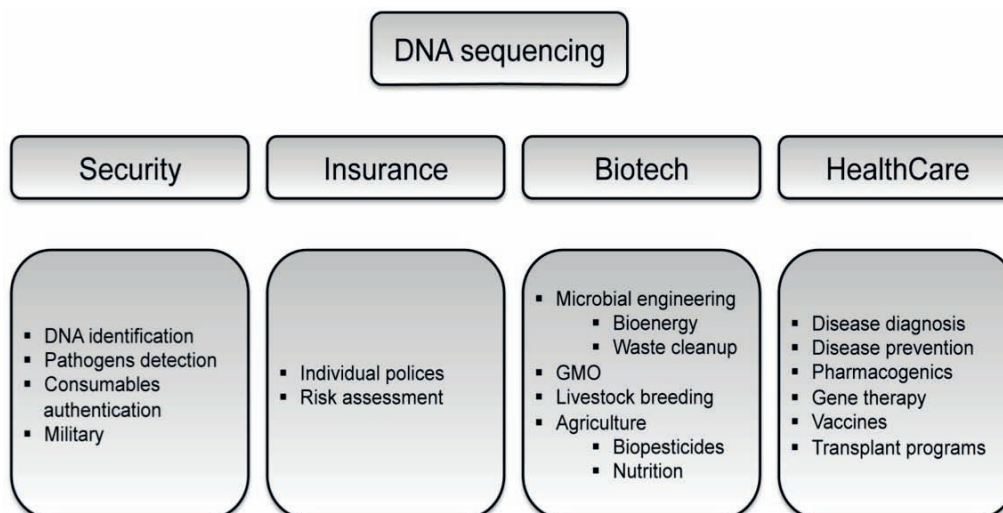


Diagram 1.1. Potential impacts and applications of DNA sequencing.

For more than 30 years now, the race is on. In the early 90s, the Human Genome Project (HGP), a \$3 billion project over 15 years was initiated and aimed to sequence the bases of the 20000 to 25000 genes of the human genome which correspond to about 3 billions bp. The final goal was partially achieved in 2001 when the International Human Genome Sequencing Consortium (IHGSC) reported the first draft of the euchromatic portion of the Human Genome^[14] in spite of 150'000 gaps in the whole sequence. Three years later, the IHGSC published the complete human sequence described as having an error rate of at most one event per 10⁴ bases and a completion of at least 95%^[15]. In 2006, the X PRIZE foundation announced The Archon Genomics X PRIZE, a \$10 million award for sequencing 100 full human genomes in 30 days or less at a maximum cost of \$1000/genomes, and with an error rate of 1 per 10⁶ bases. Nowadays, the arrival of new generation sequencing techniques brings the \$1000 genome within sight.

1.1.2 Goals

The efficiency of a sequencing method may be described through three aspects, accuracy, speed and cost, which are closely related to one another. The accuracy describes the number of sequencing mistakes relative to the total number of bases sequenced. Sequencing the same samples several times can improve the intrinsic method's efficiency, but will lower the process rate and cost. The speed, closely linked to the cost, has to be the highest possible. Present technologies are limited to partial scanning of DNA and the full DNA sequencing procedure costs over \$100,000 and takes months to decode. To be successful in developing a tool that would meet present and future development demands, three major requirements must be fulfilled:

- Long-read length capabilities

- High throughput (less than 24hrs/full scan)
- Low cost – under \$1.000 per full scan

1.1.3 Structure of DNA

Discovered in 1953 by Watson, Crick and Franklin from X-ray diffraction data^[16], the structure of DNA involves a double helix of complementary strands coiled around a central axis.

Each strand is a polymer of four repeating building blocks called nucleotides. A nucleotide is composed of one of the four nucleobases that is attached to a 2-deoxyribose/phosphate group. The four nucleobases include two purines (Adenine [A] and guanine [G]) and two pyrimidines (Cytosine [C] and Thymine [T]). Along a single strand, the nucleotides are linked to one another through phosphodiester bonds between two adjacent sugars. The alternating sugar rings and phosphate groups form the molecular backbone of each strand (Figure 1.2).

The two strands are complementary and held together through a mechanism called base pairing. Each base has a unique complementary base with which it can bind by forming hydrogen bonds. One can therefore distinguish in DNA two sets of base pairs: A-T and G-C. In the double helix of DNA, the sugar-phosphate backbone is on the outside of the molecule, while the bases are on the inside, oriented in a way that the complementary bases on the two opposite chains can form such base-stacking interactions.

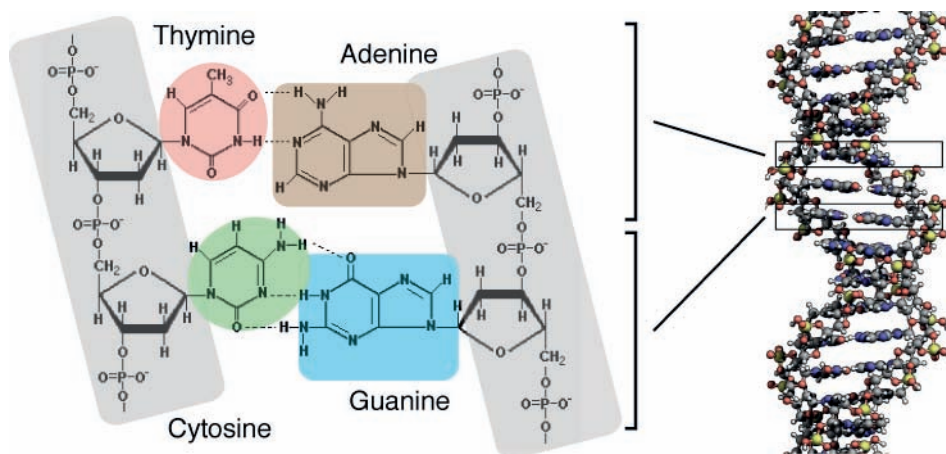


Figure 1.2. Molecular structure of DNA. (left) Bases on opposite strands are paired through hydrogen bonds between Thymine and Adenine, and between Cytosine and Guanine. The bases are lined up along the strands via a phosphodiester bond between two adjacent sugar rings. (right) The two complementary strands assemble into a double helix molecule that can reach lengths of up to millions of base-pairs.

DNA molecules have a width of about 2.5nm and the length of one base pair is about 3.4Å. As the two strands are complementary, DNA sequencing may be limited to the

structure study of only one of the two strands. These two strands can be easily separated in solution at a temperature called the melting temperature T_m . Individual single stranded DNA molecules are not helical structures but are rather described using a worm-like chain model.

An important property of DNA in solution is that at most pH, nucleotides are negatively charged in solution. The pK_a of the phosphate groups is close to 1, meaning that each nucleotide in a single strand carries a single charge. In electrolytic solutions, there is therefore a layer of counterions screening part of the charge.

Two important biological mechanisms are important for DNA sequencing. First, DNA replication is the biological process that produces two new DNA molecules from a parent one. Each single strand from the original double-stranded molecule serves as a template for the synthesis of a complementary strand. In such a process, DNA polymerases read the template sequence and add matching nucleotides via the creation of phosphodiester bonds on the growing strand. Second, DNA molecules can be cut by catalyzing the hydrolysis of the phosphodiester bonds using DNA nucleases. DNA can be cut sequentially from one of its ends, or within its sequence at restriction sites. At the opposite, two strands of DNA can be conjugated by the formation of two phosphodiester bonds by using ligases.

These two mechanisms are widely used in DNA sequencing as they can both be performed *in vitro*. We can therefore distinguish the techniques that are based on biological processes from the single-molecules-based techniques. The advantages and limitations of each of these methods will be further detailed in section 1.2.2.

1.2 State of the art

1.2.1 Sanger's chain termination classical sequencing

Two groups independently developed and published for the first time in history DNA sequencing methods in the late 70s, the Maxam-Gilbert sequencing^[17] and Sanger chain termination methods^[18], considered as the first generation sequencing techniques. The Maxam-Gilbert involving toxic radioactive labeling procedures, the chain termination method quickly became the most used technique because of its experimental ease and reliability.

The Sanger method is based on *in vitro* DNA replication and thus requires DNA templates, a DNA primer, a DNA polymerase, normal deoxynucleotides (dNTPs) and modified dideoxynucleotides (ddNTPs). Four replication reactions are run in parallel, each of them containing the four dNTPs and one of the four ddNTPs. Once the

replication reaction begins, the DNA polymerases start extending the primers by incorporating the matching nucleotides. When a normal dNTPs is added, the reaction goes on, whilst when it's a ddNTPs, the reaction cannot continue and the chain cannot be elongated any more. The result is four collections of fragments whose comparative lengths indicate the positions of the four bases (the sequence) of the DNA under study, with a high accuracy.

In 1986 was released the first automated DNA sequencing machine based on Sanger's method (ABI 370A DNA sequencer). Applied Biosystems managed to combine capillary electrophoresis for size separation to fluorescent ddNTPs (Figure 1.3) for automatic sequencing^[19]. At an original cost of \$10/base, automated Sanger sequencing lowered it 25 years later to \$5/10'000 bp.

In spite of their high accuracy advantage, the main limitation of all Sanger based methods is the read-length that they can provide. Nowadays, only short sequences of 300-1000 bp can be sequenced in a single reaction and only a low parallelization degree can be reached. Up to 384 reactions can be performed in parallel in the latest instruments, bringing the sequencing speed down to 24bp/s^[20].

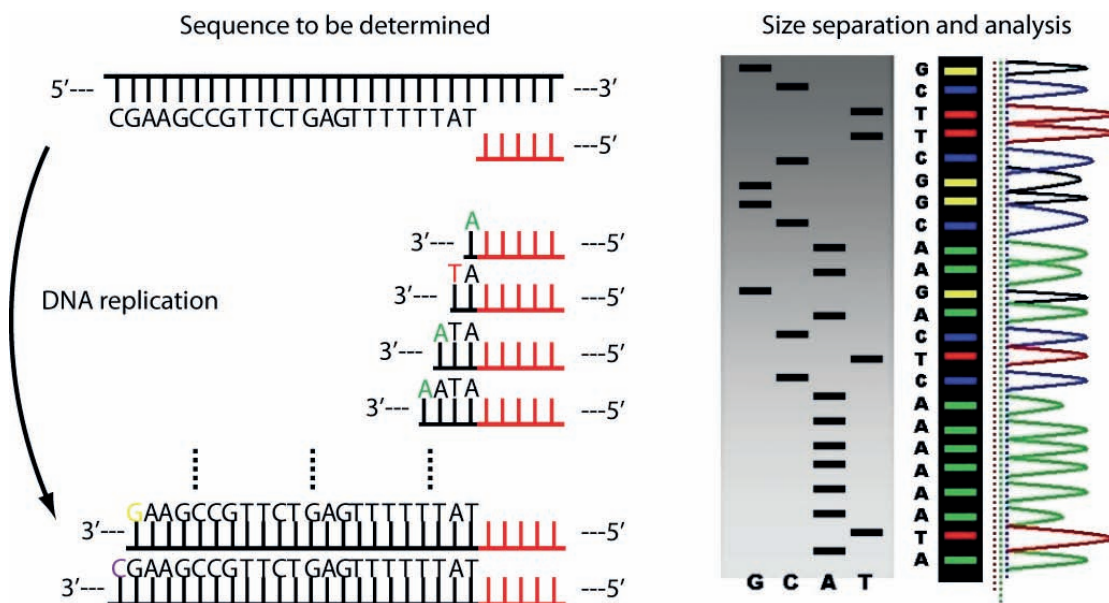


Figure 1.3. Principle of the chain termination method with fluorescently labeled ddNTPs. A complementary DNA strand is synthesized from a single stranded template using DNA polymerase. The synthesis occurs in the presence of labeled ddNTPs that, when incorporated cause DNA replication to stop. The length of the truncated DNA products can be used to infer what bases were present at each position in the original DNA sequence.

1.2.2 Next generation sequencing

Since 2005, novel sequencing technologies are emerging, called next generation sequencing techniques (NGS), and bringing new solutions for high-throughput and high-speed sequencing. The overall strategy of these new methods is similar for all.

The throughput, speed and accuracy are achieved through a vast parallelization of the sequencing reactions and a large reduction of the reaction volumes, but also by sacrificing the length and accuracy of each individual reads. Full genome sequencing can be achieved through the so-called shotgun sequencing approach^[21], in which a long sequence is divided in thousands of smaller fragments individually analyzed. The most popular NGS technologies are described hereafter.

Roche 454 pyrosequencing

The 454 approach is a sequencing-by-synthesis method based on pyrophosphate detection first described in 1985^[22] and first released as a automatic system in 2005 by 454 Life Sciences, now property of Roche. In brief, single-stranded DNA (ssDNA) fragments are first tethered to micrometer beads via specific adapters. An emulsion PCR is then carried out for fragments amplification. After denaturation for removing non-tethered strands, each bead bears at least one DNA fragment. As illustrated in Figure 1.4, the beads are then incubated with DNA polymerases and sequencing primers, and deposited on microarrays of picoliter wells of the size of the beads. Finally, smaller beads bearing immobilized ATP sulfurylase and luciferase are incubated as well. The sequencing is then carried out through several hundred of DNA replication cycles. At each cycle, a single nucleotide specie is introduced into the microreactor and eventually incorporated by the DNA polymerase. In such a case, a pyrophosphate group is released and through a series of enzymatic reactions, light is generated and detected by a CCD camera for each individual well. The microreactor reagents are then flushed away and a new single nucleotide is introduced.

The CCD pattern of detected incorporations reveals the sequence of the individual tethered fragments.

Thanks to picoliter reaction volumes, the 454 FLX instruments can generate up to 400'000 sequencing per run, at average lengths of 300 bp, so about 100Mpb per run. The main limitation is the sequencing of consecutive instances of the same base, which results in a brighter light intensity at a given cycle compared to a single incorporation. The error rate of 454 sequencing is therefore usually higher than other methods. As a lot of reagents volume is consumed, the overall sequencing cost per base is also greater than for other methods.

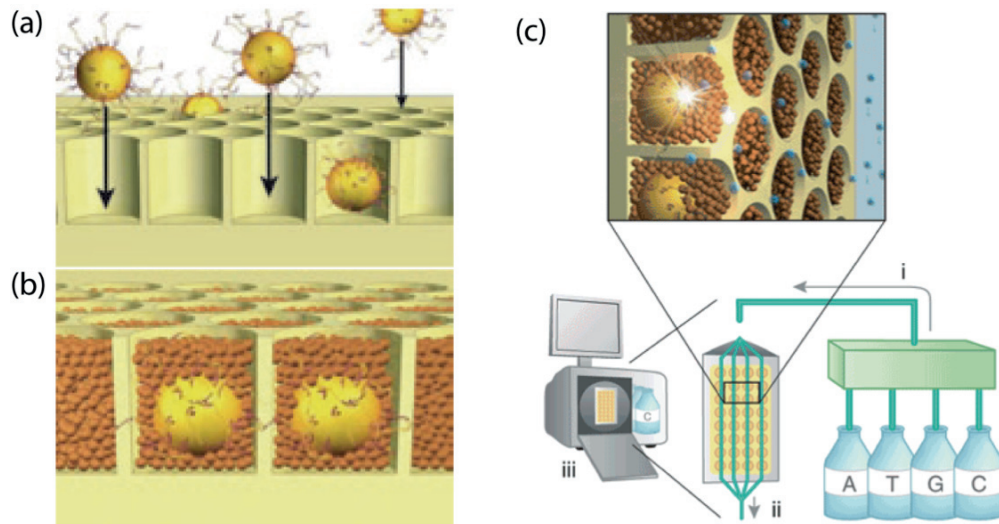


Figure 1.4. Schematic of the 454 pyrosequencing. (a) Beads bearing ssDNA templates are deposited into picoliter wells of a fiber-optic plate coupled to a CCD camera. (b) Smaller beads with immobilized enzymes for pyrosequencing are deposited as well in a second step. (c) The four nucleotides are sequentially flushed at a given cycle. When a matching nucleotide is incorporated, a pyrophosphate group is generated and a burst of light generated. For each individual well, the light signal at a given cycle indicates the corresponding base. Adapted from Rothberg and Leamon^[23].

Illumina sequencing

A year later in 2006 was released the second NGS platform, named Illumina sequencing. The Illumina technology is based as well on the sequencing-by-synthesis principle and takes advantage of fluorescently labeled chain terminating nucleotides. The key difference with Sanger's method is however that the chain termination is a reversible process. Indeed, the fluorescent label on the terminating base, which is the blocking group, can be easily removed to leave an unblocked nucleotide.

First, DNA fragments to be sequenced are ligated to adapters at both ends and tethered at one end to a solid surface, via complementary adapters. Then, a PCR amplification is performed, resulting on the formation of random clusters on the surface of thousands of copies of ssDNA fragments. Finally, the sequencing-by-synthesis is carried out by DNA replication. The reaction mixture, containing the four labeled terminator nucleotides is supplied onto the substrate, resulting at each cycle, in the incorporation of a single nucleotide into the DNA strands. For each cluster of identical DNA fragments, the terminating nucleotide that just has been incorporated by the DNA polymerase can be identified via its fluorescent label. Once identified, the label is removed and a new cycle is started (Figure 1.5).

Despite its short read-length of about 75-100bp, the very high surface density of DNA clusters that can be formed and analyzed in parallel makes the Illumina platform able to sequence in a single run billions of base-pairs, with a run time of few days. Unlike the 454 technology, homopolymers of consecutive identical nucleotides can be

successfully resolved with Illumina. However, a lot of base-substitution errors are usually observed because of the use of engineered nucleotides and DNA polymerase.

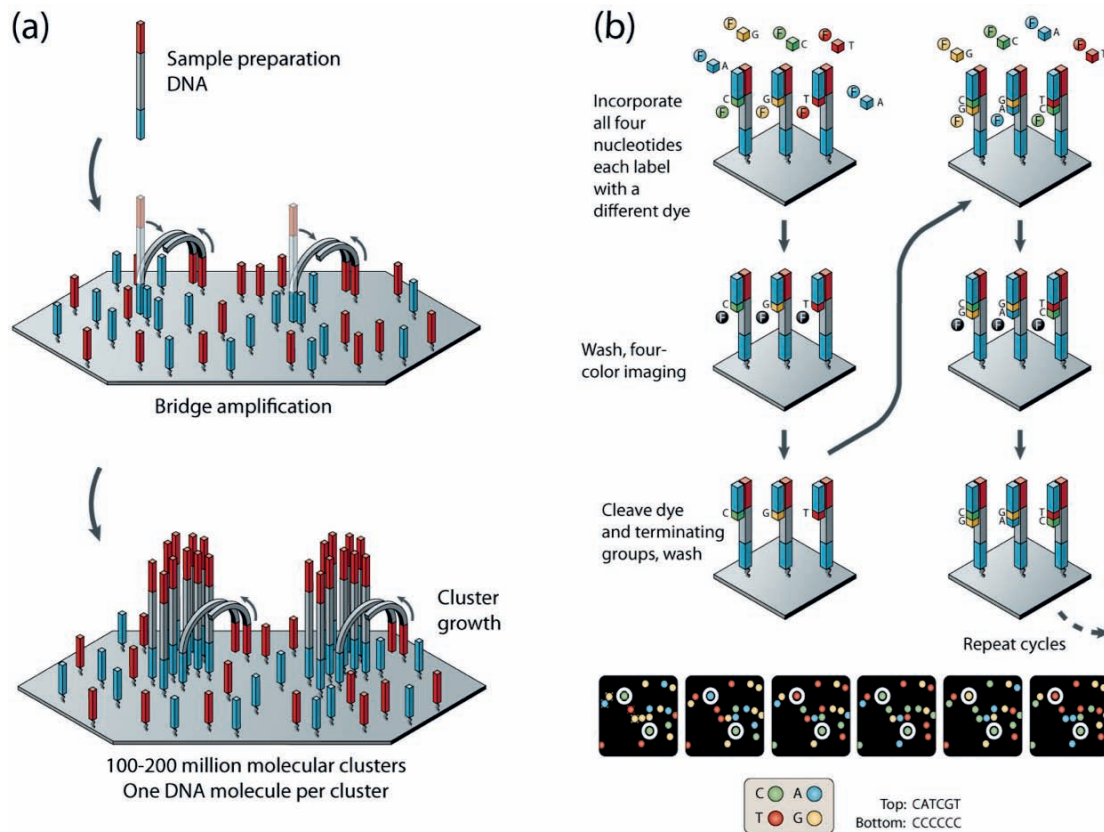


Figure 1.5. Schematic of Illumina sequencing. (a) Immobilized DNA templates are amplified into thousands of copies forming surface clusters. (b) Sequencing is carried out through several cycles of nucleotides incorporation, imaging and cleaving steps, using fluorescently labeled nucleotides. During each cycle, the terminating base is read. Adapted from Metzker *et al.*^[24].

Other promising Next-Generation Sequencing technologies

Applied Biosystems released in 2007 the ABI SOLiD instrument (Sequencing by Oligo Ligation Detection) capable of sequencing tens of Gbp per run with a run time of approximately 4.5 days on the latest version of the system. The read length is limited to about 50 bases. After amplification, bead-immobilized fragments are sequenced by ligation using a DNA ligase instead of a polymerase and specific fluorescent octamer probes^[25].

The Helicos sequencer is a sequencing-by-synthesis method that uses highly sensitive fluorescence imaging system for reading directly single DNA molecules^[26]. Thus, no DNA amplification is required. Single DNA molecules with poly-A tails are anchored to the surface of a flow-cell sequenced in a similar manner as the 454 platform. Single species of fluorescent nucleotides are sequentially flushed and washed away. During each cycle, the last nucleotide is identified by fluorescence at the single-molecule level. With high densities of anchored molecules, several millions of single DNA-fragments can be sequenced in a single run, reaching a sequencing throughput of

several Gbp. Read length are limited to 25bp. As for 454 sequencing, the main issue concerns homopolymers sequencing. In addition, in the case of accidental incorporation of unlabeled or non-emitting bases, the most dominant error is deletion-errors, which can be improved by 2-pass sequencing.

1.2.3 Challenges and limitations

Because of their fundamental differences, both first and next generation sequencing technologies are thoroughly used nowadays, because they can answer to different needs and issues.

Low-coverage sequencing projects requiring a high degree of accuracy still remain an application of choice of Sanger sequencing. Two decades of constant improvements of first generation techniques made them competitive in term of cost and experimental ease for short read-lengths. However, large-scale sequencing, and especially whole genome sequencing fully relies on next generation sequencing technologies, the only methods able to provide billions of reads in a reasonable time and at a decent cost.

	Sanger	454	Illumina	SOLiD	Helicos
First release (Instrument)	1986 (ABI 370A)	2005 (20GS)	2006 (Genome Analyzer)	2007 (SOLiD)	2007 (Helicos System)
Instrument cost	N/A	\$0.5M	\$0.5M	\$0.6M	\$1M
Mb cost	\$500	\$60	\$2	\$2	< \$1
Read-lengths	700-1000	300	100	50	30
Throughput per day	3M	150M	5G	5G	5G
Pros	Accuracy	Read-length Run time	Cost per base Throughput		Single Molecule
Cons	Cost Throughput	Cost Error rate	Error rate Run time		Read length Error rate

Table 1.1. Comparison of current sequencing technologies^[20,24,27,28]

Despite that NGS technologies have in ten years revolutionized the field of genomics by providing huge amount of sequence data, all current high- throughput methods suffer of major drawbacks. First of all, the average error rate is higher than what has been reached by the Sanger method, not only because of their intrinsic sequencing

strategy, but also because they usually imply a pre-amplification that is also a non-negligible source of errors. Then, all methods are based on a similar high parallelization of short read-lengths. This strategy requires a fragmentation of larger genomic sequences, which in addition to tedious preparation procedures, generates the need of a high computational power to put the full sequences back together and makes difficult or impossible mapping applications where small similar sequences have to be placed correctly. Cost wise, although NGS technologies have considerably reduced the prices per Gbp, a \$1000 genome still remains a hypothetical dream. All instruments have high acquisition, running and maintenance costs, and generate prohibitive amount of data requiring huge data and personnel management capabilities.

To make possible a \$1000 genome in 24h, as often stated as the ultimate goal of DNA sequencing, new strategies have still to be explored. Helicos opened a new era in sequencing by introducing single molecule sequencing, which exhibits several advantages over other amplification-based NGS technologies. The preparation of DNA templates requires less material and it avoids PCR, which can be problematic in some cases (GC rich fragments for instance) and introduces replication errors. Single molecule also means less starting materials, less reagents, less wastes and therefore a lower overall cost. However, it is still limited to relatively short sequences. Pacific bioscience followed the same direction with a single molecule real-time sequencing strategy where single molecules of up to 3kb can be sequenced, but still faces accuracy issues.

These are for sure following a promising direction but one can still go further beyond simplification. The ultimate technology that would permit an ultrafast sequencing at low-cost is a technology, which in addition to a single molecule approach, would look directly at the molecular structure and thus, avoid any sequencing-by-synthesis limiting steps.

Atomic Force Microscopy (AFM) has held the promise of distinguishing single nucleotides of DNA molecules, but besides structure differentiation, it is unlikely that AFM will ever be able to scan and resolve micrometer long molecules with random 3D configurations.

A time considered as a valuable option for DNA sequencing, mass spectrometry (MS) can only accurately sequence short fragments of up to 100bp and is therefore limited to very small-scale sequencing projects^[29].

Scanning-tunneling microscopy however, has been shown as a very promising application for sequencing of single DNA molecules functionalized on gold surface. Huang et al^[30] managed to measure nucleotide-specific electron tunneling currents

and to identify bases in a single DNA molecule. Combined with a nanopore-based device, ultrafast sequencing of single molecules with lengths of the order of Mega or Giga base pairs could be sequenced in just a few seconds.

1.3 Nanopore-based sequencing

Nanopores are nanoscale holes in thin membranes that can be used as powerful detectors for single-molecule analysis. With diameters of only few nanometers, nanopores are just small enough to only let one molecule at a time pass through their channel, offering great perspectives in DNA sequencing. Inexpensive to fabricate, easy to engineer, nanopore devices might be the most encouraging solution for identifying and analyzing DNA molecules without any amplification or labeling, making of ultrafast DNA sequencing a close reality.

1.3.1 Nanopores as single-molecules biosensors

Coulter-counters^[31], which are instruments capable of counting, sorting and sizing micrometer-sized particles, can be considered as the ancestor of nanopore-based devices. These apparatus are made up of few microchannels that separate two reservoirs of electrolytic solutions. When a voltage bias is applied across the channels, an ionic current, proportional to the channels resistance, can be measured by standard electrochemistry. While the conductance of a pure electrolyte doesn't change, when a particle enters a microchannel and is driven through it, the corresponding transient occlusion results in resistive pulses, measured as sudden and brief current drops. When the particle exits the channel, the ionic current returns back to its initial value until a new particle translocates. The amplitude of the current drops closely relates to the particles' properties, such as volume and charge, while their duration correspond to the translocation time.

Nanopore devices can be seen as nanometer sized coulter counters, where voltage-driven molecules translocating through a nanoscale pore in a membrane between two electrolyte reservoirs can be analyzed by monitoring the fluctuations of the ionic current. The concept of nanopore-based DNA sequencing is based on the principle that each of the four nucleotides would modulate the ionic current in a way that the full sequence could be extracted from it, allowing sequencing at a rate of thousands of bases per second.

Driving DNA single molecules toward a nanopore

The translocation of DNA molecules through nanoscale pores is a technique widely used in all biology labs when scientists sort out DNA molecules based on size by gel

electrophoresis. In such experiments, negatively charged DNA molecules are voltage-driven through a network of pores, formed by cross-linked polymers, whose porosity is chosen so that molecules of different sizes travel through the gel toward the oppositely charged electrode at different speeds.

The motion of charged molecules under the influence of a uniform electric field is called electrophoresis. When such a molecule is placed in an electric field, it travels at a constant velocity given by the contribution of different forces. First, the external field exerts an electrostatic coulomb force proportional to the surface charge q and to the strength E of the field:

$$\vec{F}_{el} = q \cdot \vec{E} \text{ [N]} \quad (1.1)$$

Then, the frictional force \vec{F}_d , or viscous drag, results in a force opposed to the motion, given by the Stokes equation:

$$\vec{F}_d = -6\pi\eta a \cdot \vec{v} \text{ [N]} \quad (1.2)$$

where η is the dynamic viscosity [$\text{N}\cdot\text{s}\cdot\text{m}^{-2}$] of the medium, a is hydrodynamic radius [m] and \vec{v} is the velocity [$\text{m}\cdot\text{s}^{-1}$].

Finally, the electrophoretic retardation force reduces the overall Coulomb force by transferring through viscous stress part of the electrostatic force exerted on the ions of opposite charge in the electrical double layer to the molecule itself.

In the case of molecules with hydrodynamic radii much greater than the double layer thickness (the Debye length κ^{-1}), the overall electrophoretic mobility μ_e can be expressed according to the Smoluchowski theory:

$$\mu_e = \frac{\varepsilon_r \varepsilon_0 \zeta}{\eta} \text{ [m}^2 \cdot \text{V}^{-1} \cdot \text{s}^{-1}] \quad (1.3)$$

where ε_r is the dielectric constant of the medium, ε_0 the permittivity of vacuum [$\text{C}^2 \cdot \text{N}^{-1} \cdot \text{m}^{-2}$] and ζ the zeta potential [V].

The velocity of a molecule in an electric field is therefore dependent on the following parameters, which are critical for DNA sequencing:

- The strength of the voltage gradient
- The viscosity of the medium and thus of temperature
- The dielectric constant of the electrolyte solution

The translocation of DNA across a single nanopore is just a particular example of DNA electrophoresis. When a voltage bias is applied between two reservoirs of electrolytes separated by a membrane, whose only pathway from one side to the other is through the pore channel, the DNA molecules are drawn through it toward the positively charged electrode.

The translocation velocity inside a nanopore is less obvious than in bulk and additional forces have to be considered. First, potential strong interactions with the walls of the channel may have to be integrated to the previous equations. Second, polymer-unraveling mechanisms during translocation have to be considered as well. More realistic models^[32] and assessments of the dependence of translocation speed with experimental parameters^[33] can be found in the recent literature.

Alternative approaches for guiding DNA through nanopores have involved enzymes functionalized at the entry of the pore, which would mechanically drive molecules inside the channel^[34].

Biological nanopores

The membranes of living cells contain a wide variety of nanopore-forming proteins, whose primary function is to transport ions or small molecules through the cell and nucleus membranes. Whilst RNA is synthesized in the cells nucleus but translated outside of it, it was quickly imagined that nanoporous proteins were responsible for the transport of RNA across the nucleus membrane.

In 1996, Kasianowicz *et al.* opened a whole new field when they reported the first ionic current blockades caused by the translocation of single-stranded RNA and DNA homopolymers through a 1.4 nm wide, 10nm long, channel-forming α -hemolysin (α -HL, Figure 1.6) in an artificial lipid bilayer^[35]. They further suggested that biological pores might be potential sequencing tools when they demonstrated that α -HL could discriminate different polynucleotides or different segments of repetitive nucleotides in a single molecule by analyzing the modulation of the ionic current blockades^[36,37].

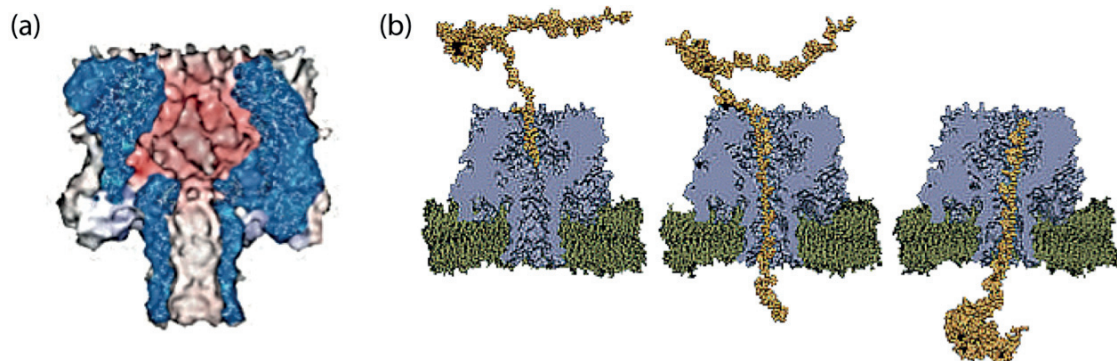


Figure 1.6. Structure of α -hemolysin. (a) Seven subunits self-assemble to form a transmembrane channel, with a limiting aperture of 1.4 nm. (b) Molecular dynamic simulation of a ssDNA molecule translocating from one side of the membrane to the other. Adapted from Dekker's review^[38].

Since then, α HL was demonstrated remarkably stable and functional under extreme conditions and is now widely used as biosensor^[39,40]. Alternatively, other biological nanopores have been studied in the optic of single-base resolution, such as engineered MspA nanopores, which because of a more favorable internal structure, were demonstrated to be more sensitive to nucleotide changes than α -HL^[41-43].

Protein nanopores are well-defined structures that have the advantage to be easily chemically or biologically engineering. From a α -HL template, it is possible to fine-tune the properties of the channel by replacing few amino acids by mutagenesis or to add localized functional groups within the pore, which are going to interact with the translocation species in a customized way, yielding various biosensors with specific properties.

Solid-state nanopores

Although biological nanopores exhibit obvious sensitivity and structural advantages and dominated the nanopore sequencing field for years, the fact that they self-assemble mostly only into lipid bilayers presents a certain disadvantage. The robustness of lipid-bilayers is very sensitive to external and experimental conditions, in particular to pH, salt composition, temperature and mechanical stress, which can make the supporting membrane very unstable. Their integration into devices is therefore unlikely to be possible.

Solid-state nanopores (ss-nanopores) were fast shown to be a viable alternative as single-molecule biosensors. Their high stability and robustness make them perfect candidates for large-scale applications and the possibility of tuning their shape, dimension and surface properties offers a unique manner to mimic biological pores.

Golovchenko *et al.* achieved pioneering works in the fabrication of solid-state nanopores, by using a low-energy ion-beam to mill openings in silicon nitride membranes at the nanometre scale^[44]. Shortly later, higher resolutions were obtained using a focused electron beam of a TEM microscope^[45], which allow a real-time imaging of the drilling process and thus a good size control. Holes of sizes as down as 1 nm can be reproducibly formed in membranes with typical thicknesses in the order of 10 to 20 nm. SiN is traditionally the material of choice because of its low stress and mechanical resistance (Figure 1.7). However stable solid-state nanopores can be fabricated in various other materials such as silicon oxide^[46], metal oxides^[47] or suspended graphene^[48]. An alternative approach used in the early stages of ss-nanopore fabrication involves chemical etching of a membrane with feedback control. As soon as the two electrolytes reservoirs can communicate, an ionic current is detected and the etching process is stopped, allowing the creation of holes as small as 2nm^[49].

The size of the nanopores can be tuned after fabrication. It has been shown that electronic irradiation in a TEM microscope can enlarge or shrink the existing nanopores depending on the experimental conditions^[50]. ALD is another valuable solution for post-modification of nanopores. It allows a progressive and homogenous diameter reduction, which can be controlled with angström accuracy^[51].

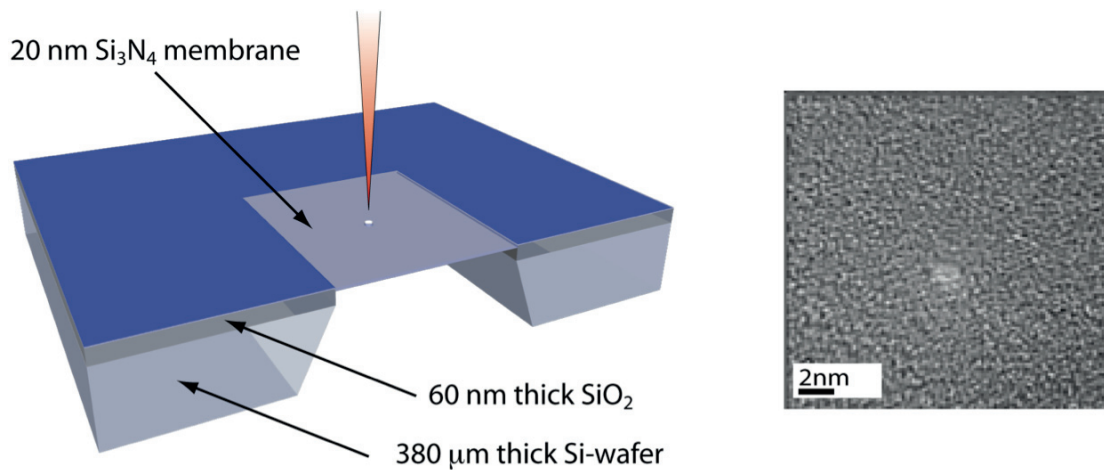


Figure 1.7. Ss-nanopore fabrication process developed at EPFL. (a) 20 nm thick suspended Si_3N_4 membranes are opened in $\text{Si}/\text{SiO}_2/\text{Si}_3\text{N}_4$ wafers. A nanopore is then drilled with a focused electron beam. (b) TEM micrograph of a nanometer sized ss-nanopore.

Hybrid nanopores

Hybrid nanopores are a third type of sensors based on the combination of solid-state nanopores into which biological nanopore-forming proteins are inserted. Hall *et al.* recently reported the first formation of hybrid pores^[52]. They used a genetically engineered α -hemolysin protein functionalized with a DNA tail, which could be used to electrophoretically drive the protein into a SiN nanopore. They proved that such hybrid nanopores were still functional by performing DNA translocation measurements. This result opened up the opportunity to combine the remarkable structural properties of biological nanopores with the durability and robustness of solid-state nanopores.

1.3.2 Ionic current modulation by translocating single DNA molecules

Ionic conductance in a nanopore

When an electric field is applied across a nanopore in an insulating membrane separating two electrolytic solutions (typically monovalent KCl salt), an ionic current can be measured, corresponding to the translocation of the ionic charge carriers themselves. Typically, two non-polarizable Ag/AgCl electrodes are usually used, where two reversible electrochemical reactions take place. At the anode, a Cl^- anion is captured from solution, which results in the oxidative reaction $\text{Ag}(\text{s}) + \text{Cl}^- \rightarrow \text{AgCl} + \text{e}^-$. An electron is given to the circuit and the charge imbalance at the anode results in the migration of a cation toward the cathode (-), where the opposite reaction $\text{Ag}^+ + \text{e}^- \rightarrow \text{Ag}(\text{s})$ occurs. The resulting Cl^- anion migrates toward the anode and an electron is used from the circuit, completing the electrochemical circuit.

At low voltage bias, the current-voltage response of a nanopore is linear (ohmic) and K^+ and Cl^- are the only active species. At larger bias, other species can also be electrochemically active and non-linear responses can be observed. Hence, applying a steady bias results in a stable DC current baseline signal as long as the nanopore is not obstructed.

In a first approximation, surface charges can be neglected and only geometrical considerations can be used to model the nanopore conductance, which governs the ionic current properties in the linear regime. For a cylindrical nanopore of diameter d and length l (the membrane thickness), the conductance G can be approximated as:

$$G = \sigma \cdot \frac{\pi d^2}{4l} \quad (1.4)$$

Here σ is the bulk conductivity [$S \cdot m^{-1}$].

A more realistic representation would take into account the access resistance to the pore, introduced by Hall^[53], which give the following equation for the conductance G of a nanopore, commonly used in the literature^[54]:

$$G = \sigma \left[\frac{4l}{\pi \cdot d^2} + \frac{1}{d} \right]^{-1} \quad (1.5)$$

Several deviations to this idealistic equation may have to be considered to predict more reliably nanopores' conductance. The geometry of TEM drilled nanopores can significantly differ from a classical cylindrical shape and has been shown to be more hyperbole-like^[55]. The pore opening can therefore be much wider than the actual narrowest point, giving rise to a much larger access resistance. Furthermore, in opposition to high salt concentration regimes where the conductance varies linearly with the charge carriers concentration, low salt regimes make the high surface-to-volume ratio have an important effect on conductance. In such a regime, the surface charges density dominates the nanopore conductance^[56]. In practice, the conductance of nanopore exhibits unfortunately a large variability^[57] that can not rely only on geometrical considerations (Figure 1.8a). Particularly, the degree of wettability of the nanopore walls may have the strongest influence among all experimental factors. In case of a strong hydrophobicity, surface pretreatments are necessary to enhance the conductance and signal to noise ratio. The importance of

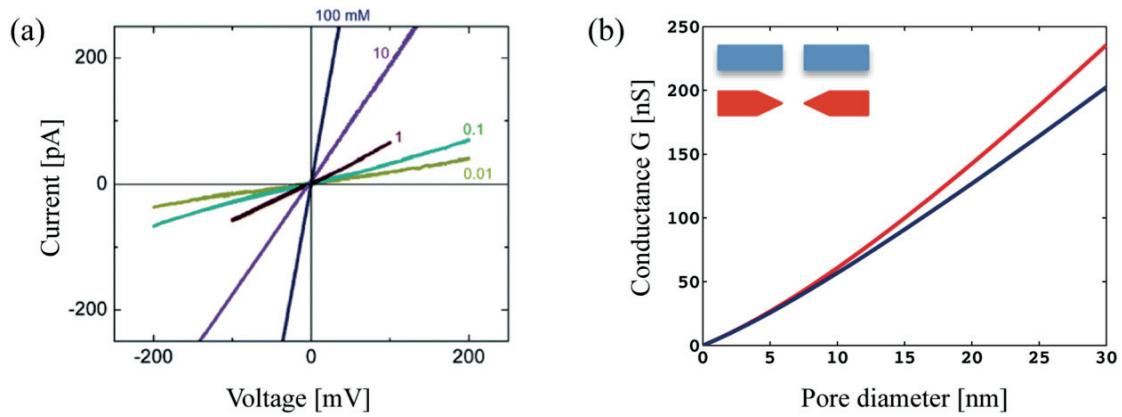


Figure 1.8. (a) Typical I-V responses of a nanopore at different salt concentrations^[56] (b) Conductance of cylindrical and hyperbole-shaped solid-state nanopores for a 20nm thick membrane in 1M KCl calculated from the model of Kowalczyk *et al.*^[54]

Basics of nanopore measurements: ionic blockades

In solution far away from the pore, DNA coils undergo free diffusion, characterized by their diffusion constant D , where the local electric field has a marginal role. Closer to the nanopore, where the potential drop is assumed to occur, the electric potential profile can be estimated as a function of the radial distance r from the pore aperture, as follows:

$$V(r) = \frac{d^2}{8lr} \Delta V \quad (1.6)$$

where d and l are respectively the pore diameter and length, ΔV is the applied potential^[58]. In the pore vicinity, the electric field forms a funneling potential extending out of the opening, which biases the molecules diffusion toward the nanopore entry. The capture radius r_c is the distance at which the electrophoretic force overwhelms the free thermodynamic diffusion and make unlikely a molecule to escape the electric field forced diffusion (Figure 1.9). Once within the capture radius, single molecules are eventually captured and translocate to the other side. From the ionic current analysis, the translocation properties may provide crucial information about the species in solution.

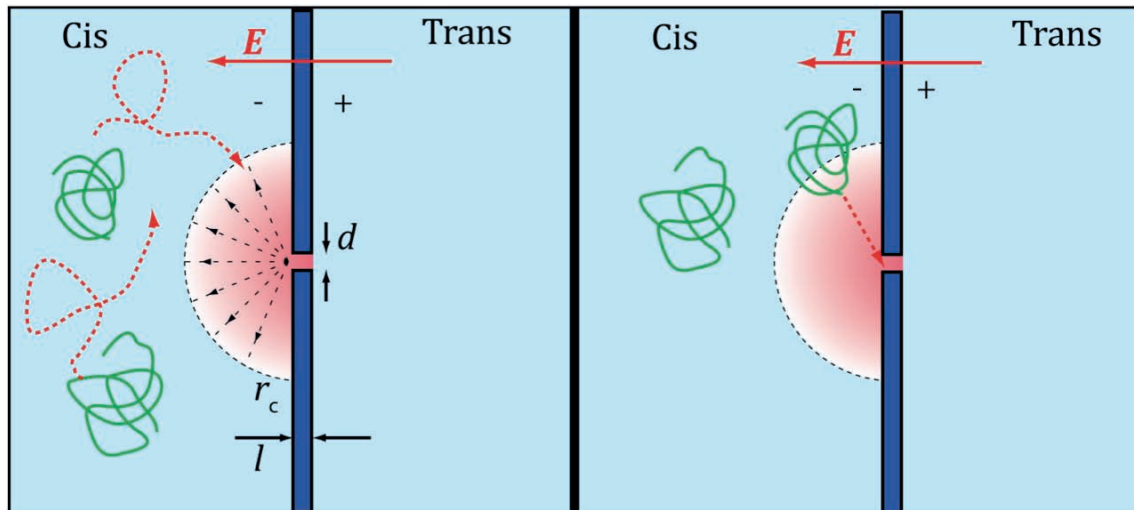


Figure 1.9. Capture of biopolymer in a nanopore. (left) When an electric field is applied across a membrane, the potential drop mainly occurs at the nanopore, forming a funneling field driving the molecule toward the pore aperture. Outside of the capturing radius r_c , the electric field plays a marginal role and the molecules freely diffuse. (right) When a molecule randomly enters the capturing radius, the electrophoretic force is strong enough to bias their motion to the pore.

When a molecule translocates through a nanopore, it occupies a volume, called volume of exclusion, that partially blocks and prevents ions from freely flowing from one side to the other, and thus modifies the ionic transport. Despite that DNA also carries a charge through the pore, its relative speed compared to translocating ions is very slow and this translates into a blockade event, during which the ionic current briefly exhibits a lowered value. These translocation events give rise to spikes, also named pulses, in the ionic current baseline that can be characterized by their frequency, dwell time t_D , and drop amplitude I_D .

The event frequency is directly related to the rate at which single molecules are trapped into the pore. Even though it does depend on the diffusion of molecules from the bulk to the pore, and thus to concentration and voltage bias, it is not always a diffusion-limited process, because the nanopore may reject part of the molecules that are present close to the pore entry. In the case of a diffusion-limited process, it takes more time for a molecule to diffuse toward the pore than to be threaded in, and the capture rate varies linearly with the applied voltage bias. This is the case for high molecular weight (in the range of 104 bp or more). For lighter molecules, the capture rate scales exponentially with the voltage gradient and is limited by the energy barrier at the pore entry that has to be overcome. In such a case, it takes less time for a molecule to reach the pore than to be captured by it. Indeed there is an entropy penalty for bringing one of the free strand ends into such a constrained region, that can be added to an electrostatic energy cost because of unfavorable interactions of highly charged molecules with the pore surface. The capture rate is therefore dependent on the number of translocation attempt, times the probability at each attempt to

translocate. In this barrier-limited regime, the capture rate increases with the DNA size, until it becomes diffusion limited^[58].

Increasing and controlling the capture frequency is crucial for high throughput single-molecule analysis. In such a purpose, different strategies are under investigation. Working at high voltage bias increases the capture radius and hence the number of molecules driven to the pore, as well as favor the crossing of the potential barrier. This has nevertheless to be traded off against higher translocation speeds^[59]. Another approach was followed by Wanunu *et al.* who reported that using a salt gradient across the 2 reservoirs enhances the capture rate by increasing the electric field magnitude close to the pore, compared to symmetrical salt conditions^[58], and has as double advantage to slow down the translocations. A last solution is to fine-tune the surface properties of the membrane and pore to lower the potential barrier in order to increase the translocation probability.

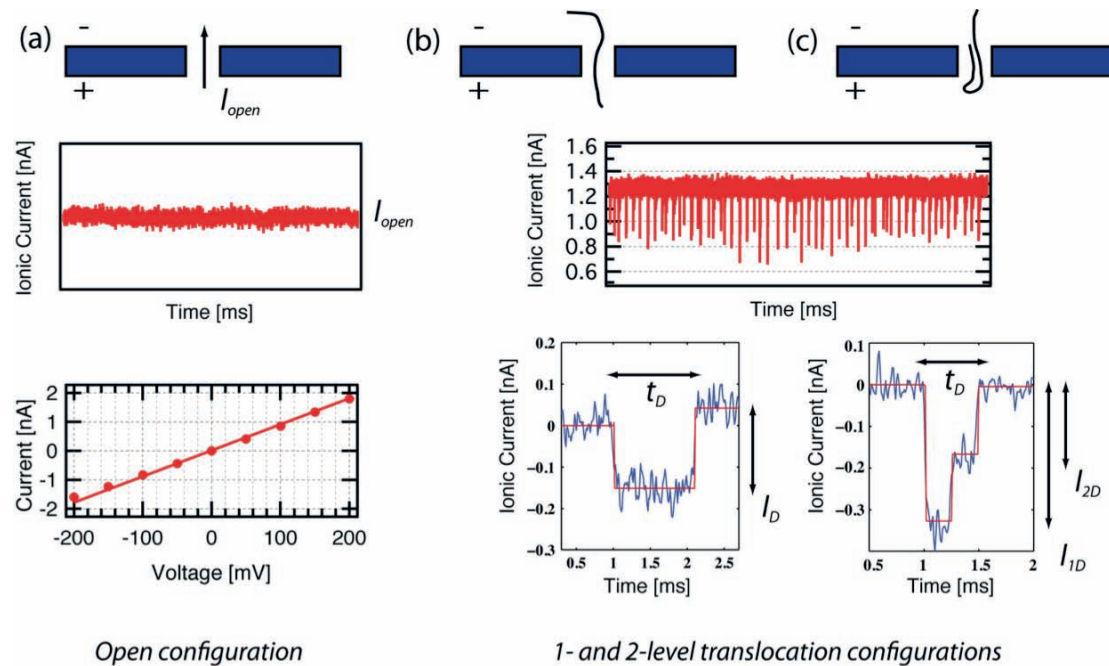


Figure 1.10. Ionic current blockades during translocation through a solid-state nanopore. (a) The pore is open and a steady current is measured while a voltage is applied across the two chambers. (b) Single molecules causes transient current blockades characterized by their duration t_D and drop amplitude I_D . The frequency of the spikes is directly correlated to the molecules capture rate (c) In a single translocation event, more than one current level may be observed, depending on the exclusion volume. The exclusion volume may depend on secondary structures changes and ideally on local molecule structure differences.

The dwell-time t_D is the duration of an ionic current pulse. Intuitively, this is related to the time during which the pore is obstructed and the ionic transport hindered, because of a translocation or because of an interaction with the pore entry, as not all molecules, which present themselves to the pore, translocate. Behind an apparent simplicity, the translocation duration isn't easy information to model, mainly because it is yet not fully understood. The first two obvious factors that influence the

translocation duration are the voltage bias and the molecular length of the polymer strands. The stronger is the electric field, the faster the molecules translocate. On the other hand, a longer molecule needs more time to fully pass through the channel. However, the distribution of t_D usually exhibits a high variability, which does not scale only on those two parameters. For pores with diameter closer to the polymer size, strong nanopore-molecule interactions and slower translocation may be expected, which could in addition be very sensitive to little changes in the secondary structure or electrostatic properties of the molecular species. In larger pores, these interactions may have negligible effects, but larger diameters may give rise to even more duration discrepancy if more than one molecular structure is allowed within the channel (linear strand, one-fold or more, etc.).

For small-diameter pores, the translocation time should scale linearly with the molecules length L if the nanopore resistance dominates over other factors. However, Storm *et al.*^[32] established a power law in which $t_D \propto L^{1.27}$ (Figure 1.11). They attributed such a non-linear behavior to the hydrodynamic drag force arising because of the part of the molecule outside of the pore that is still coiled while the head is translocating. Moreover, the polymer unraveling is another energetic barrier that has to be overcome, and which depends on the DNA structure itself as well as on the ionic strength of the medium.

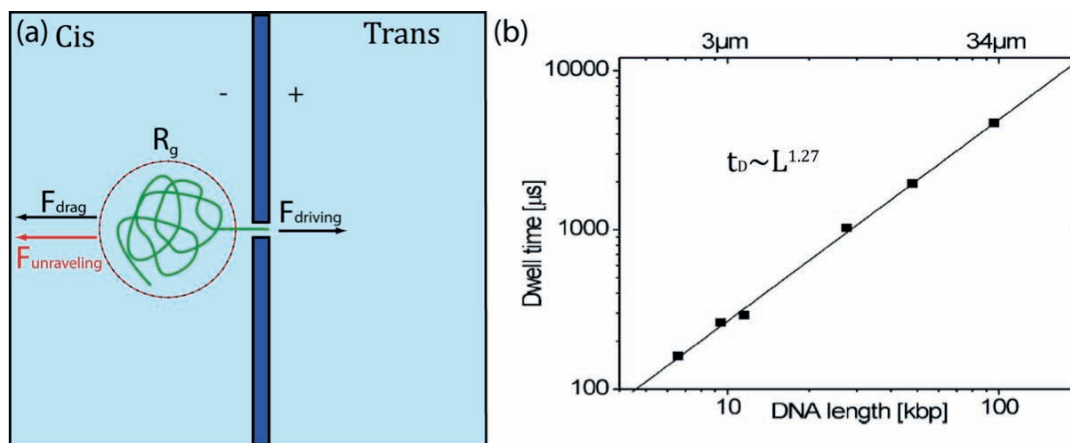


Figure 1.11. Influence of the molecular length over translocation duration. (a) For long molecules, a drag force acting on the coiled-up part (radius of gyration R_G) outside the pore counterbalances the pulling force. In addition, the force for unraveling the molecule also slows down the translocation process. (b) Dwell time versus DNA length as reported by Storm *et al.*^[32] for molecular length higher than 6kb.

Finally, the drop of the ionic current I_D during a translocation event describes how the conductance changes when a molecule disturbs the free motion of the ionic charge carriers. The most important but least straightforward mechanism to understand is therefore how the ionic conductance fluctuations can be related to the molecules in

solution how the exclusion volume depends on the molecular structure and electronic properties.

In a first approximation, the current blockade intensity can be modeled using the volume of exclusion of the molecule, which partially prevents the ionic species from occupying the pore. In such an approach, the carrier density in the pore remains constant at all time but a portion of the pore cannot be occupied. Then for a cylindrical pore, the current drop amplitude I_D reads:

$$I_D = \sigma \cdot A \cdot \frac{V_{bias}}{L_{pore}} \quad (1.7)$$

where σ is the bulk conductivity [$S \cdot m^{-1}$], A the hydrodynamic cross section of the molecule in the pore [m^2], L_{pore} the pore length[m] and V_{bias} the applied bias [V].

The computation of the molecular volume inside a cavity should then be sufficient to predict the change of ionic current. According to this model, the blockade amplitude should be independent of the pore diameter as the excluded volume is constant for a given molecule. However, it appears that this is not the case and that the drops intensity scales with the pore size for a given molecular specie. More complex phenomena that contribute to the conductance changes have to be considered. In particular, electrostatic effects may also play a central role. For small pores, a bigger ionic confinement may put an additional electrostatic barrier, which would repeal part of the ionic transport. Moreover, the role of surface charges, hydration layers electric double layers in the change of ionic current is still poorly understood.

Detection and sequencing

Measuring and analyzing the ionic blockades of translocating molecules has been proven to provide useful information about both the composition and structure of single molecules.

It is clear that the distribution of translocation durations can distinguish between different polymer lengths as shown by Heng *et al.*^[60]. Compared to classical gel-electrophoresis, a size analysis would require infinitesimal amount of material and would be performed at high throughput at the single-base resolution.

As 2D scatter plots, the combined analysis of pulses duration and magnitude can even resolve more complex properties. In wider nanopores, DNA molecules can translocate in a linear way or in a partial folded manner, which give rise to both different translocation time and current blockades because of different interactions with the nanopore walls. The conformation of molecules in different experimental conditions can then be studied in such a way with a nanopore-based sensor, as

reported by Fologea *et al.* who studied conformational changes of ds-DNA molecules upon pH variation with a solid-state nanopore^[61].

In nanopores whose sizes only allow linear head-to-tail translocations, the ionic current modulation only depends on the chemical composition present inside the channel, and eventually of the part close to its aperture. The ultimate goal of nanopore sensing that is sequencing, has been first put in evidence by Akeson *et al.* who, using a α -hemolysin nanopore, first distinguished distinct ionic blockade levels in single translocation events of RNA molecules containing two blocks of 70 C and 30 A bases, suggesting that different bases yield different current blockades^[36]. Similarly, they showed that the translocation of poly(A), poly(U) and poly(C) oligomers could be distinguished. Indeed, poly(U) molecules were found to translocate 3 times slower than poly(A), with nearly identical blockades (Figure 1.12). Poly(C) molecules could be discriminated because they gave rise to larger blockades compared to poly(A) and poly(U), despite that pyrimidine bases are smaller than purines.

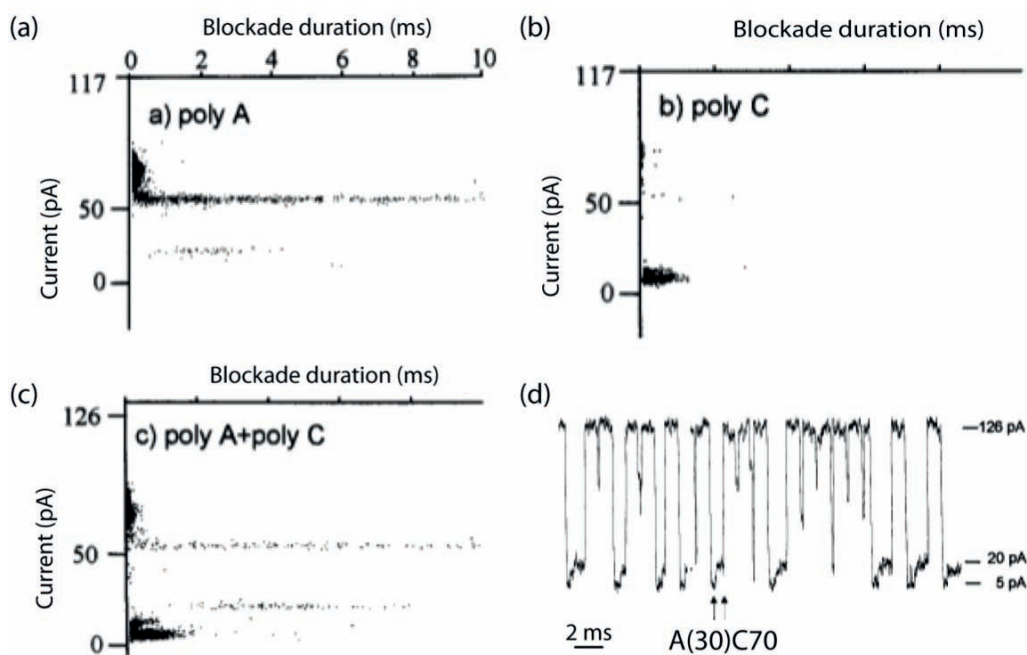


Figure 1.12. Early discrimination of homopolymers using an α -hemolysin pore demonstrated by Akeson *et al.*^[36]. (a-b) 2D scatter plots of poly A and poly C RNA oligomers exhibiting specific current blockade amplitudes. (c) Blockades caused by a mixture of poly A and poly C. Two distinct areas can clearly be observed. All time scales are identical. (d) Typical current blockades caused by the translocation of A₃₀C₇₀ oligomers. Two levels can be extracted from each event, clearly indicating that the ionic current can distinguish between different structures in a single molecule.

Nanopores have then been shown capable of differentiating homopolymers sequences, but it is not clear whether it is the sequence itself or the secondary structure that causes such changes. In order to sequence a DNA strand, single bases resolution has to be achieved, meaning that it is the size difference of single nucleotides that has to be detected, or the interaction of a single base with the nanopore wall. To date, no

nucleotides sequence has been demonstrate from ionic current modulations with a bare nanopore.

1.3.3 Challenges of ionic-current based sequencing

Nanopore-based sensing has intrinsic temporal, current and spatial resolutions, which combined together, set up fundamental limits to what can be measured.

The time resolution of measurements is given by the sampling rate at which data are collected. At 100kHz, the time resolution is then 5 μ s. However, maximum sampling frequencies are not necessarily the best way to go. In spite of the pA resolution of classical patch-clamp amplifiers, high-frequency measurements are accompanied with a noise that limits the accuracy at which the current can be measured. At short time scale, the current is given by such a small amount of ions in the nanopore that the noise caused by the thermal fluctuations of both the charge carriers and the nucleotides inside the nanopore may hide the temporal differences between bases. In standard experimental conditions (1M KCl, 100mV), the translocation rate of dsDNA, which can be roughly estimated to 1 base/ μ s, is therefore a major issue. To reach single-base resolution, the translocation would have to be slowed down by at least a factor of 1000, or even more, so that the bases stay long enough in the channel and that the ionic signature of single bases can be actually measured.

Nevertheless, the major limiting resolution arises from the method principle itself. If one considers a nanopore with a length of 10nm, it means that there is at all time roughly 30 nucleotides present in the nanopore, and each of them contributes to the ionic current blockade. During a translocation, the fluctuation of the ionic current is hence always an average of the change caused by several bases. Even biological pores are at least 5nm long, which at least represent 10 to 15 bases. Reducing the thickness of solid-state membranes to achieve nanopore lengths of few nanometers remains a challenging fabrication process and it is not proved yet that an infinitely short channel, with a length comparable to the length of a single nucleotide would reach such a resolution.

In the recent years, several attempts to reduce the translocation have been successfully reported. The combination of voltage reduction^[35], temperature reduction^[62,63] and viscosity augmentation^[64-66], salt concentration and composition^[58,67] may address the issue that the translocation velocity is for physical measurements.

However, more sophisticated nanopores are needed to differentiate nucleic sequences with the ionic current. The most promising approach was proposed by Bayley *et al.* who introduced a new concept, where they proposed to analyze single nucleotides translocating nanopores instead of single molecules^[68]. By attaching an

aminocyclodextrin adaptor inside an α -hemolysin channel, they showed that the current blockade resulting from the interaction of the adaptor with a single base was specific and different for the four bases (Figure 1.13). By combining an exonuclease enzyme that would successively cleave the last nucleotide of a single-stranded DNA molecule, and a base-per-base nanopore analysis a sequential analysis would be possible. On the other hand, the ultrafast sequencing is compromised because the method is limited by the rate of the enzymatic reaction. Moreover, one has to make sure that all cleaved bases translocate and are analyzed in the correct order.

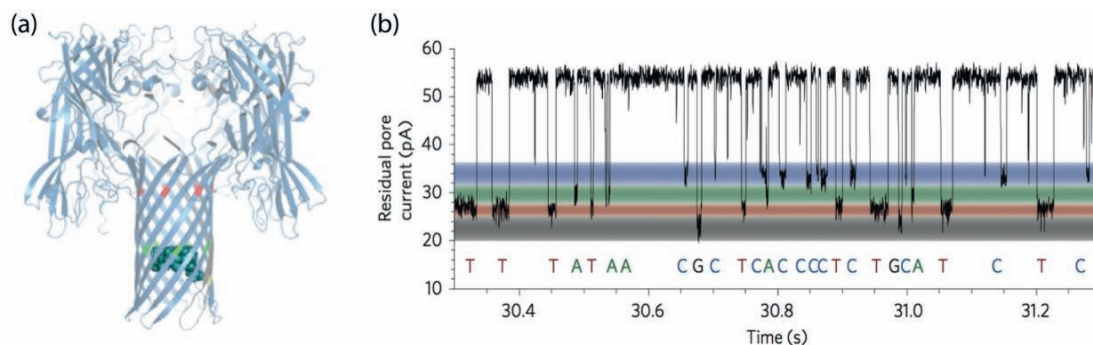


Figure 1.13. Continuous base identification with a covalently bound molecular adaptor in a biological nanopore. (a) Structure of an α -hemolysin nanopore engineered with a cyclodextrin adaptor. (b) Continuous identification of single nucleotides translocating through the channel. Specific interactions between the four bases and the adaptor yield characteristic ionic blockades.

A very limited sample preparation, the opportunity of analyzing ultra short or long single DNA molecules, at very high throughput and very low cost, have put nanopore-based sequencing at the center of the highest expectations. Nevertheless, for more than 15 years of intense research, it is less and less clear if whether or not the analysis of ionic current blockades will ever reach the ultimate goal that has been expected from it.

Nevertheless, even though the ionic current doesn't provide enough information by itself, the properties of nanopores are so unique that other related strategies must be investigated. We believe that the combination of ionic and transverse current measurements may constitute a clever solution to ultrafast sequencing.

1.4 Transverse electrodes-embedded nanopores

1.4.1 Tunneling-current through polynucleotides

Scanning tunneling microscopy (STM) is a powerful technique for imaging surfaces with atomic resolution. STM relies on the measurement of tunneling current between a biased tip and the sample put in a very close proximity. In 2005, M. Zwolak and M. Di Ventra^[69] imagined first that transport measurements carried out in a direction

perpendicular to the DNA backbone may provide useful information about its structure. In their theoretical study, they showed that as the four bases have different chemical and electronic structures, each nucleotide might carry a specific electronic signature that could be measured. Since then, additional simulations have been reported, investigating random orientations and the contribution of the surrounding medium to the tunneling current. The main conclusions of these studies are that if the distance between the molecule and the probe is small enough and if the orientation and translocation speed of DNA is well controlled, the difference of conductance in the transversal direction is sharp enough to be detected^[70-74].

An advantage of transverse electronic current over ionic current measurements is the fact that the current is measured in the range of nano-ampere, meaning that the translocation speed of DNA is less of a problem and that it may be measured at higher frequencies compared to the pico-ampere ionic current of small-diameter nanopores.

The first experimental evidence of nucleotide recognition by tunneling measurement has been performed first in a STM environment by Ohshiro *et al.*^[75]. By functionalizing a probe with nucleotides, they showed that the tunneling current between complementary pairs was greatly enhanced, allowing the identification of isolated bases on a surface. More recently, Huang and colleagues^[30] successfully resolved the sequence of short oligomers with functionalized electrodes in a STM microscope as well. In their study, they used tips that were modified in a way that they specifically bind to nucleotides through hydrogen bonds. Very short DNA oligomers of 5 bases held on a gold surface were scanned using such tips. They observed characteristic current spikes, whose duration, frequency and amplitude distributions could be attributed to specific bases. Despite that oligomers could not be reproducibly scanned in the longitudinal direction, they impressively showed that it was possible to distinguish the contribution of different nucleotides while the probe drifts over a heteropolymer. They then claimed that by pulling the DNA through the tunneling gap in a controlled manner, it would be possible to sequence DNA molecules at speeds of tens of bases per second.

1.4.2 A STM microscope in a nanopore

If one needs to drive single DNA molecules between two sharp STM electrodes, nanopore-based devices may represent a useful tool for such a purpose. By embedding a nanopore with nanoelectrodes, it may be possible of sequentially reading the molecular structure of translocating molecules.

The structure of such a device is depicted in Figure 1.14. Two electrodes are positioned on the edge of a solid-state nanopore with a gap of only a few nanometers

and integrated within an independent external circuit. The device must have the following properties:

- The device is fast and cheap to fabricate. Its geometrical and electronic properties are identical from one device to another. Eventually, it should be possible to make arrays of such nanopore readers in a single membrane. The device is robust and its long lifetime allows long reads of several copies of target molecules.
- As the intensity of tunneling current exponentially decays with the distance between the probes and the molecule, the gap distance should be below 5nm, eventually even smaller, close to the size of the target molecules. Similarly, the nanopore size should be exactly of the size of the nanogap and should only allow the translocation of single molecule in a head-to-tail linear fashion. A high confinement is also favorable to reducing noise arising from thermal fluctuations.
- As tunneling mechanisms are very sensitive to atomic and orbital orientations, the orientation of the molecule within the transverse gap should be reproducible, must it be controlled by the transversal electric field or through the interactions with the nanoelectrodes.
- It is possible to make single molecules translocate slow enough so that each nucleotide spends enough time between the transverse electrodes.

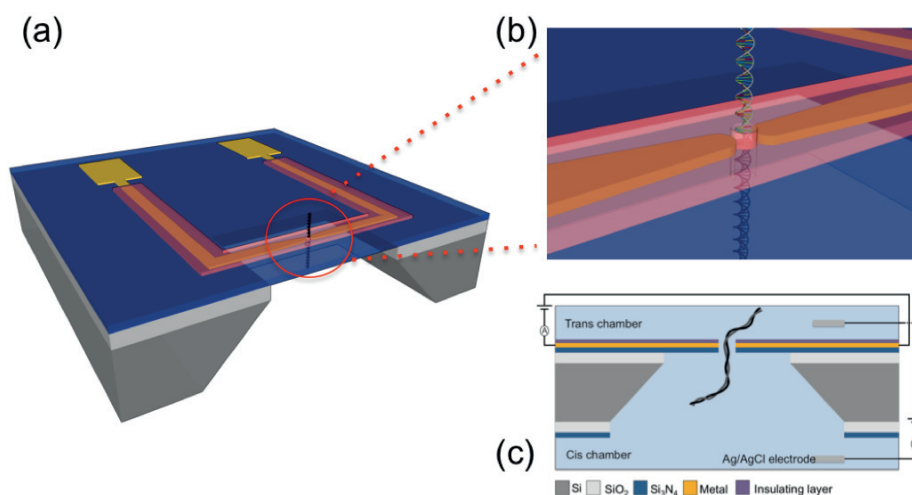


Figure 1.14. Schematic representation of a prototypical device for single-molecule sensing with a transverse-electrodes-embedded nanopore. (a) A nanopore is drilled through a suspended Si_3N_4 membrane. The tunneling junction across its diameter is integrated within the rest of the electronics. An additional insulating layer reduces the electroactive area to the nanopore only. (b) The nanopore and the gap junction should be of the size of a single-stranded DNA molecule. (c) Cross sectional view of the total apparatus.

The fabrication of a device respecting all these requirements is a challenge by itself, but is necessary to experimentally investigate the feasibility of tunneling measurements inside of a nanopore. The recent progresses in the fabrication,

modification and functionalization of solid-state nanopores constitute a unique opportunity to pursue this challenging goal.

Carbon nanotube based nanoelectrodes

The idea of using carbon nanotubes as tunneling tips (Figure 1.15) has emerged from their unusual but outstanding electronic and structural properties. In particular, single-walled carbon nanotubes may fulfill part of the requirements stated above.

First, they usually exhibit very narrow diameters that can be below 2nm with metallic or small bandgap semiconducting behaviors, which make them well suited for electrically probing individual nucleotides of similar sizes. Such nanotips would provide higher spatial resolution than conventional metallic nanoelectrodes that have much bigger radius of curvature.

Second, CNTs are known to non-covalently interact with DNA through π -stacking and Van-der-Waals interactions in a specific manner^[76]. These interactions may constitute a double advantage as they might reduce the translocation speed on one hand and help orient in a reproducible way the nucleotides inside the nanochannel on the other hand.

Third, several theoretical studies have reported that carbon nanotubes could successfully replace metallic electrodes as tunneling probes. Moreover, the potential of surface functionalizations of CNTs may represent an additional advantage for optimizing the transverse conductance^[77-79]

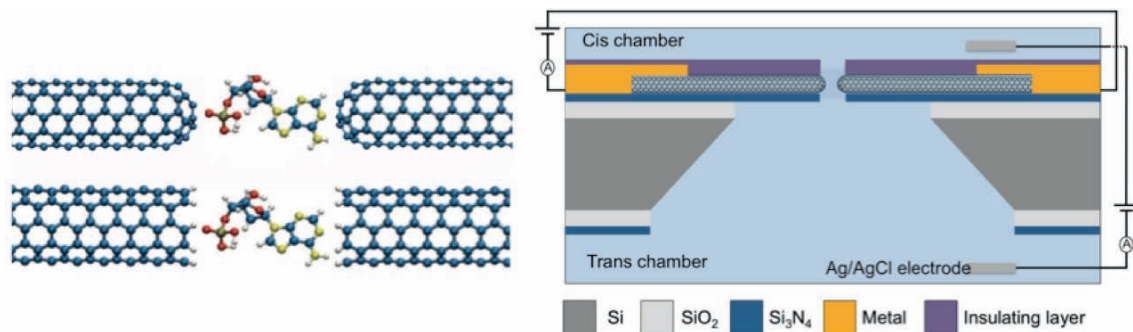


Figure 1.15. Carbon nanotubes as transverse tunneling electrodes. (left) Two configurations are shown, depending if whether the tips are capped or open (carbon and hydrogen atoms respectively). Shown in blue and white). In addition to ideal aspect ratios and unique electronic properties, CNTs may help orient nucleotides in the nanopore through specific π -stacking interactions. (right) Conceptual illustration of device containing CNT electrodes with electrical contacts connecting them to the outside world. An insulating layer ensures that only the CNT tips are electroactive.

The challenge that represents producing a device containing a nanopore with an embedded single walled carbon nanotube across its diameter is as exciting as the possibility it offers. Indeed, the use of carbon nanotubes in every day's applications suffers from the difficulty of controlling their location in a nanoscale device, especially with such nanometer needs. We propose here a fabrication method

demonstrating that the realization of a tunneling detector combining a nanopore and gapped SWCNTs electrodes is feasible with a reasonable rate.

In addition to the project's requirement described above, working with CNTs implies the following needs:

The tunneling electrodes must exclusively been made of small diameter SWCNTs, ideally below 2-3nm. The spatial resolution of larger CNTs such as MWCNTs may indeed not allow probing individual nucleotides. For reasons that will be detailed in chapter 3.2, chemical vapor deposition is the best-suited method for synthesizing CNTs on a substrate with optimized properties. To date, there is however no way to control electronic properties of CNTs.

The embedded CNT must be integrated into a larger circuit and therefore be contacted. The contact resistance should exhibit ohmic behaviors with low resistance. Different approaches might be considered for contacting CNTs, such as dielectrophoresis, directed growth or lithography procedures. Dielectrophoresis has major drawbacks, such as poor control over CNT properties, large contacts resistance and tedious procedures. Directed growth of CNTs by CVD between metallic electrodes is an elegant process^[80], but in addition to be challenging, it requires a consolidation of the contacts with a post-lithographic step. Therefore, the combination of CVD synthesis and lithography represents the most straightforward method. In such a process, an individual SWCNT is synthesized with location control and further contacted in a post ebeam lithographic-metallization procedure.

The combination of solid-state nanopores with gapped carbon nanotubes is the most challenging part of the process, as sub-10nm nanopores must be functionalized with gapped carbon nanotubes electrodes. The nanomanipulation of CNTs is feasible but at ultralow throughput. Bridging nanopores with individually grown CNTs is a promising approach but requires a well-directed growth method with nanometer precision and a further cleavage of a single CNT into two separated electrodes. A last method would consist in cleaving the CNT when drilling the nanopore, with the potential of higher process rate. In this technique, a CNT is first grown and contacted, while after membrane opening, a focused electron beam of a TEM microscope is used to drill the pore and cleave the CNT in a single step, yielding two CNT tips laying exactly on the nanopore edges and along its diameter.

Nanogap metallic electrodes

Using metallic electrodes as nanotips for tunneling current measurements in a nanopore is a more conservative approach that combines nanofabrication of nanogap electrodes to standard solid-state nanopore fabrication. Despite that both processes were independently demonstrated in recent literatures, a reliable procedure for the

realization of our device is still missing. We propose here a complete process allowing the fabrication of a STM nanopore with sub 10nm resolution and a very high and reliable production rate, involving state-of-the-art nanotechnology processes and electrochemistry.

The geometrical properties of metallic electrodes that are required are challenging to achieve and at the cutting edge of electron beam lithography. However, even if the unique shape of carbon nanotubes cannot be reproduced with metallic nanowires, their surface functionalization with molecular adapters as described above may fulfill the requirements.

1.4.3 Discussion

Besides the experimental characterization of transverse-electrodes-embedded nanopores, the fabrication itself of such devices remains a tremendous task because of very demanding geometrical requirements for STM sensing. The structural fluctuations of DNA during translocation or a too large tunneling junction may cause a serious deterioration of the signal to noise ratio and a dramatic diminution of the sensitivity for the electrical sequencing of DNA. In the ideal case, the gap junction should be just small enough to let a single-stranded DNA molecule translocate, and so should be the nanopore constriction. In such a configuration, the orientation and speed of the translocating molecule may be controlled through the transverse electric field and through the tips and molecule interactions, offering optimal experimental conditions. More importantly than the gap size, the radius of curvature of the electrode tips is critical and should be smaller than the size of a single nucleotide. Additionally, these small nanowires should be able to withstand high current densities, which is a well-known issue in nanoscale electronic. CNTs offer the possibility of high aspect ratios combined to outstanding electronic transport properties. On the other hand, nanometer scale metallic gap junctions are also a valuable alternative that needs to be investigated.

Chapter 2

Techniques

2.1 Electron beam lithography

Electron beam lithography (EBL), which is the method of choice for the fabrication of structures at the nanoscale onto planar substrates, played a key role in the results achieved during the project. It allowed both the realization of nanojunctions with an extremely high resolution and the alignment of different features with very good accuracy. The principle of EBL is similar to photolithography. A focused electron beam is used to expose a resist that is sensitive to electrons. Upon irradiation, depending on the material tone, a developer is used to remove either the exposed or non-exposed areas. Patterns can then be transferred to the substrate via material deposition or etching.

The current section is dedicated to explaining the key concepts allowing the fabrication of sub-10 nm structures and their integration into more complex devices with high precision.

2.1.1 Principle of lithography

Lithography is a general term grouping patterning methods used to structure a material at the micro or nanometer scale. Photolithography and electron beam lithography are the mainly used techniques in the fabrication of MEMS devices but other processes such as stencil, nanoimprint or soft lithography may be of potential interest.

The principle of lithography is depicted in Figure 2.1. A flat substrate, such as a Si or glass wafer for instance, is first cleaned and coated homogeneously with a special material, called resist, that is sensitive to UV or electrons, depending on the technique. Several coating options are available, like spin, dip, or spray coating. In the spin coating method, a liquid resist solution is dispensed at the center of the substrate, which is then spun at constant speed to yield a film of uniform thickness. The solvent is evaporated by moderate temperature baking. Specific areas of the substrate are then exposed to UV or electrons, causing a local change in the molecular structure of the

resist and a modification of its solubility properties in a solvent called developer. For positive tone resists, the exposed regions become soluble in developer, while it is the opposite for negative tone resists. Thereafter, the substrate is finally soaked into a developer solution, yielding areas where the substrate is protected by the resist, and other areas material free. The patterns structured in the resist are finally transferred to the substrate either by etching of the non-protected areas or through material deposition. At the end of the process, the resist is removed in a solution of resist stripper.

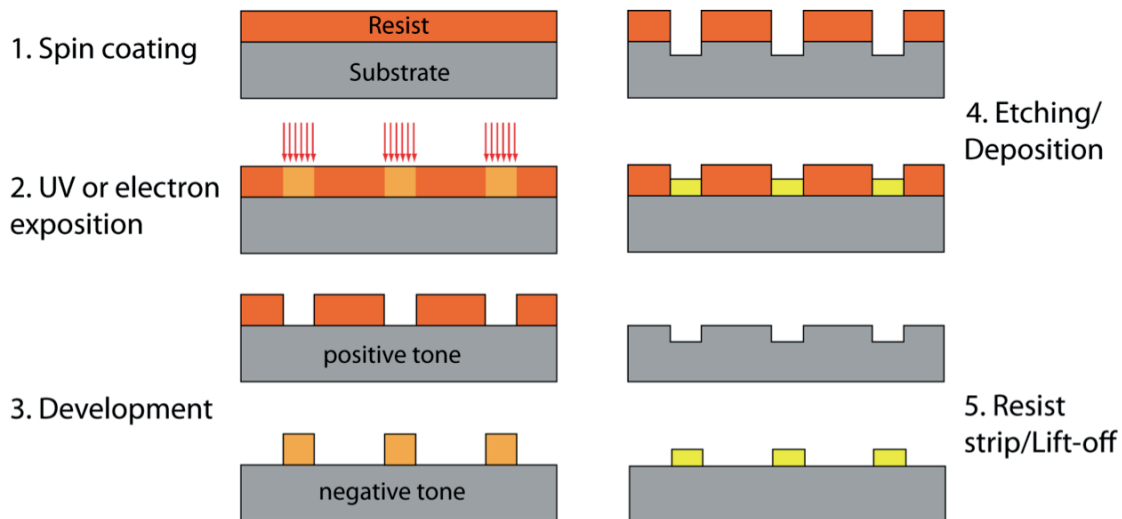


Figure 2.1. Illustration of the principle of lithography. (left) A substrate is first coated with a resist, which is first patterned by UV or electron irradiation and subsequent development. (right) The patterns are transferred onto the substrate by further etching or deposition and resist removal (example with positive resist)

In photolithography, the substrate is usually illuminated using a UV lamp combined to a mask, which contains the pattern to reproduce. A mask is a plate that allows light to shine through only at desired area. Typically, a patterned chrome layer at the surface of a quartz plate is used to absorb UV radiations where it is present. On the opposite, there are other systems similar to electron beam lithography, which involve a focused beam and write the surface as a pencil to reproduce a design that has been designed using software.

The main and most important difference between UV and EB lithography is the size of the structures than can be achieved. As for microscopy, the diffraction limit puts a fundamental barrier to the resolution that can be reached. Therefore the small wavelength of high-energy electrons compared to UV photons is a considerable advantage. Photolithography is thus used to pattern sub-microns features while EBL can achieve structures at the sub-10nm scale.

2.1.2 EBL systems

The first EBL systems have emerged from the transformation of scanning electron microscopes in the early 60s and evolved to dedicated instruments optimized for nanolithography. EBL machines therefore closely resemble scanning electron microscopes as they mainly consist of an electron gun, a column and a mechanical stage. The main components are further detailed hereafter and linked to the Vistec EPBG-5000 EBL system in service at the Center of MicroNanoTechnology (CMI).

Electron sources

There are three types of electron sources used in electron microscopes and EBL setups: thermionic, field emission (FEG) and Schottky gun. Thermionic emitters are usually W or LaB₆ filaments heated up to temperatures at which electrons have enough thermal energy to overcome the work function energy barrier for escaping the gun surface in vacuum. The electrons are then extracted by an electric field toward the column. The current density of thermionic gun depends on the temperature and cathode work function. Their advantages are mainly a high current stability and a modest required vacuum, but are usually of lower brightness and lifetime compared to the other two types of guns. Field emission sources are sharp tips of W operating at room temperature, from which electrons are extracted by tunneling using a strong electrostatic field ($>10^8$ V/cm) in the tip area. As electrons can only tunnel out from the tip apex, the resulting beam is brighter and the spot size smaller than for thermionic sources. In addition, cold FEGs generate low energy spread and highly coherent beams. The downside of FEGs is that an ultra high vacuum is required to ensure that the tip remains clean at all time. However, the tip usually still gets a monolayer of gas atoms adsorbed on its surface and needs to be thermally flashed regularly. Therefore, if best for high-resolution electronic imaging, pure FE sources are not suitable for EBL as the current is too unstable over long period. Finally Schottky emitters are field assisted thermionic sources made up of tungsten tips coated with a layer of zirconium oxide that combine the advantages of thermionic and FE guns. As they are operated at hot temperature, they are less prone to contamination than cold FEG but still provide coherent, bright and small spot size beams as electrons are extracted from the tip apex. Schottky emitters also generate higher currents and more stable beams. They are therefore the most common guns for high-resolution lithography.

The quality of an electron source may be estimated by its brightness, energy spread and source size. The brightness is a measure of the current intensity per unit area per steradian. It depends on the electrons acceleration voltage and should be the highest possible. The energy spread is the difference of energy between the electrons leaving

the gun. Because of chromatic aberration, this should be as small as possible. For FEG and Schottky emitters, the energy spread is typically below 1eV, while above 1.5eV for pure thermionic sources. The source size finally is the size of the spot from which the electrons appear to be produced. The source size is important but does not guarantee a small spot size, as column aberrations are the limiting factors for the final resolution.

The EBPG-5000's electron source is a Schottky ZrO coated tungsten gun, which can be operated at acceleration voltages of 20, 50 and 100 kV.

Column

The column contains all the elements required to accelerate the electrons, and to create, focus, deflect and blank the beam. The trajectory of electrons in the column is controlled using electrostatic and magnetic lenses. As for optical lenses, the quality of the optics is of first importance for the final resolution. A typical column configuration is illustrated in Figure 2.2. At the top of the column, the electron source is coupled to an anode, which extracts and accelerates the electrons to their final energy, where a first lens initially focuses the electrons as well. SEM based systems usually operate at 30kV whilst dedicated EBL machines do at up to 100kV. Further down, a second condenser lenses refocus the beam and an adjustable aperture prevents the electrons with too wide angle from entering the objective lens, which finally focuses the beam onto the substrate surface. Between the condenser lenses and aperture, an electrostatic deflector plays the role of beam blanker, which can switch the beam on and off at high frequency by deviating it onto the aperture surface. The surface scan by the beam is ensured by the deflector lenses, which deviate the beam off-axis. The maximum deviation sets the scan size (writing field) of the machine, above which the stage has to move. Deflectors usually consist of eight poles arranged around the optical axis, which can perform additional functions such as stigmatism. The astigmatism correction may be ensured by a dedicated lens or by the objective lens. Finally, backscattered and secondary electrons detectors are detected above the stage for calibration and alignment procedures.

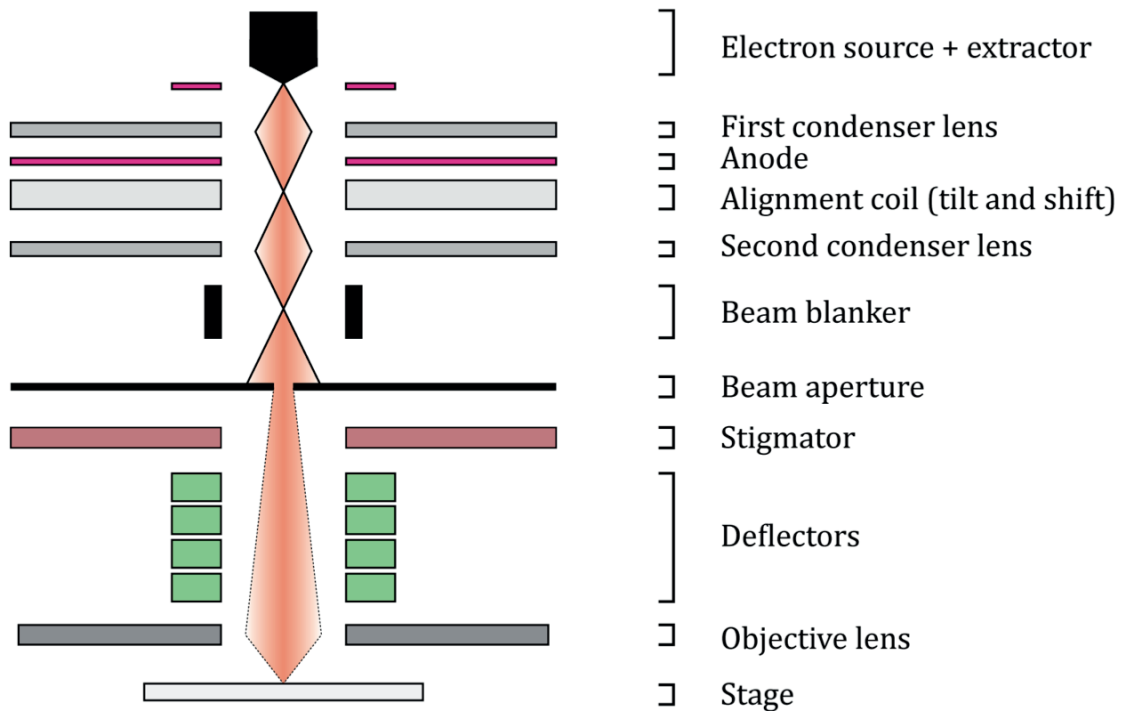


Figure 2.2. Illustration of typical electron beam lithography column.

In the ideal case, the spot size, e.g. the diameter of the circular beam spot is as small as needed for a given beam current. However, lenses induce geometrical (spherical, astigmatism, distortion, coma and field curvature) and non-geometrical aberrations (chromatic, diffraction) that tend to expand the beam diameter on the surface. High-acceleration voltages provide a useful mean for reducing most of the aberrations and energy spread and thus a smaller spot size and higher resolution. On the opposite, EBL requires higher beam currents in comparison to electron microscopes, making tight focusing more difficult. In EBL, the smallest beam currents that can reasonably be operated are 100 to 200pA, which at 100kV hardly provide spots smaller than 10 nm^[81].

EBL systems can be separated in Gaussian and shaped beam categories. In round Gaussian beams, the beam is focused to a circular spot while shaped beams are usually rectangular spot. The Gaussian beam tools are the most prominent for R&D as they offer higher resolutions.

Stage

The deflector lenses deviate the beam off-axis for scanning the substrate surface without a physical displacement of the stage. Vector scan is a method where within a writing field, the beam scans in x- and y- directions and write patterns pixel-by-pixel, by extensively using beam blanking. However, because of spherical aberration, the maximum possible deviation is limited to few hundreds of microns. At EPFL, the

maximum writing field size is 256 microns. For larger patterns, when a field is completed, the stage has to be moved so that the adjacent field can be exposed. While mechanical stages of SEM have very poor accuracy, in the range of $5\mu\text{m}$, the stages of EBL systems can be positioned by laser interferometry, so that the writing fields can be aligned almost perfectly. The stitching resolution is the accuracy at which the writing fields are stitched together. The stitching specification of our machine is 18nm mean + 3σ . In addition, a height sensor measures continuously the surface height in order to compensate the fields' position and beam defocus.

Another scan strategy is named raster scan, where the beam is only scanned in one direction. Herein, the substrate is written line-by-line with beam blanking along a single line. The stage is then translated in the perpendicular direction, resulting in series of parallel exposures.

Vector scan is best suited for nanolithography as exposure doses can be adapted between every single pattern and as unwritten areas are skipped, making writing of isolated patterns fast contrary to raster scans.

Gaussian beams are used for high-resolution writings, where a single pixel is usually of the size of the beam spot. At the opposite, low-resolution works take advantage of shaped rectangular beams where a single pixel is a square of up to 100nm , of the size of the spot.

The stage usually carries calibration and alignment markers. The calibration markers are used with the BSE and SE detectors for setting the gun and column alignment, adjusting the focus and spot size, correcting the astigmatism, and measuring the beam current. Alignment markers are used to calibrate the beam position in the stage coordinates system. From there, a finer alignment is further performed using markers on the substrate itself. The quality of the alignment therefore depends on the design and quality of the substrate markers.

2.1.3 Scattering interactions as resolution limitations

In electron microscopy, the quality of the focus and the size of the beam spot are of first importance for imaging because it is the primary electrons that provide the resolution. However, for EBL, the resist material is mainly exposed by the secondary electrons generated by the primary electrons of the incident beam. Indeed, the energy required for disrupting bonds or initiate a chain reaction is typically below 50eV , whilst primary electrons are of much higher energy. Even though small spot sizes are required and needed, the final patterns resolution is therefore limited by the scattering interactions between the primary electrons and the substrate, which lead to exposures

over much wider areas than a typical spot size. The main sources of limitation for achieving sub-10nm nanolithography are detailed in the current section.

Forward scattering and backscattering of primary electrons

The interaction between electrons and matters is well known since the advent of electron microscopy. Inelastic scatterings are interactions between high-energy electrons and the electrons surrounding atoms in the resist or material, during which there is a transfer of energy and eventually ejection of secondary electrons of lower energy. In such an interaction, the trajectory of the incident electron is slightly modified. These are called small angles interactions. At the opposite, there are backscattering interactions, which are of larger angles and where the initial trajectory of incident electrons is modified to a much larger extent. These are mainly elastic interactions caused by interactions with nucleus. The backscattered electrons have therefore similar energies compared to the primary electrons and a large travel path length. When the incident electrons hit the substrate, they penetrate into the resist and further down into the substrate and experience a succession of elastic and inelastic scattering events with the materials atoms and electrons, until their initial energy is fully dissipated.

Once the beam hit the surface, incident electrons first mainly undergo a forward scattering of small angle inelastic interactions, which tends to broaden the beam in the resist. These forward scattering events generate SE that expose the resist. When these electrons reach the material, they also experience backscattering events, which may make them travel laterally or even back to the resist with random trajectories. Figure 2.3 shows Monte-Carlo simulations of the trajectory of 1000 electrons from the point of incidence and gives an idea of how far the electrons can laterally travel from an ideal path. BSE also generate SE, which participate to the resist exposure.

High-energy electrons are preferred because they undergo much smaller angle interactions compared to lower energy electrons and therefore go deeper in the material. Similarly low Z and low-density materials are also preferred because lateral diffusions are diluted over larger areas.

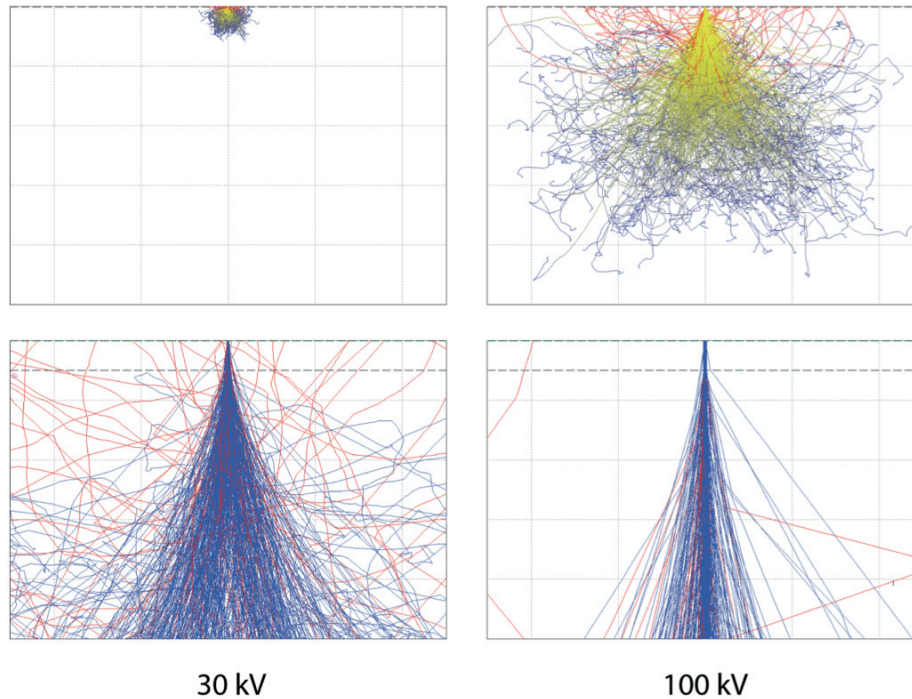


Figure 2.3. Monte-Carlo simulations of 1000 electron trajectories in Si substrates coated with 150nm PMMA (dashed line) at 30kV and 100kV (8nm spot size). Top. Comparison of the importance of electron scattering at 30kV (left) and 100kV (right). Red trajectories are backscattered electrons. Color gradient indicates progressive energy loss. Frames are $100 \times 75 \mu\text{m}$. Bottom. Zoom in near the point of incidence and the extent of forward and backscattering near the resist layer ($20 \times 15 \mu\text{m}$). The beam broadening is more important at lower acceleration, while at 100kV, most of the lateral spreading occurs in the substrate. The amount of BSE is also less important close to the surface at high energy. Scattering simulations were performed with Casino^[82].

Secondary electrons travel path

The discussion above concerned scattering mechanisms for primary electrons. However, inelastic scatterings result in the creation of secondary electrons that are mobile and thus also subject to the same interactions. Secondary electrons are ejected from atoms and can have energy of up to 1keV. Their trajectory is perpendicular to the incident primary electrons, meaning that the secondary electrons created in the resist may travel lateral distances that are over 10nm, a path along which they will progressively lose their energy by scattering. This means that it doesn't matter how small the spot size is, there will always be an energy broadening around the point of incidence^[83].

Proximity effects

In EBL, the resist exposure outside of the scanned area is named proximity effect and is a direct consequence of the random scattering events discussed previously. Proximity effects have different results on the actual features shape and size.

For isolated shapes, meaning that the distance between patterns is much larger than the patterns size, the proximity effect is negligible. The only observable facts are that patterns are slightly bigger than expected and sharp angles may appear rounded. Even

though it may be an issue for ultrahigh resolution lithography, proximity effect can be useful for large areas exposure. Indeed, the size of a pixel can be set as much larger than the beam spot size. For fine and dense structures, proximity effect may be a crucial issue to solve as features may merge all together because dense features are overexposed compared to the same sparse features (Figure 2.4).

The resist profile and features robustness are also affected by the proximity effect and forward scattering. Because of forward scattering, positive and negative respectively exhibit undercut and tapered profile. In the case of very dense and fine features, proximity effect induces instability of the structures.

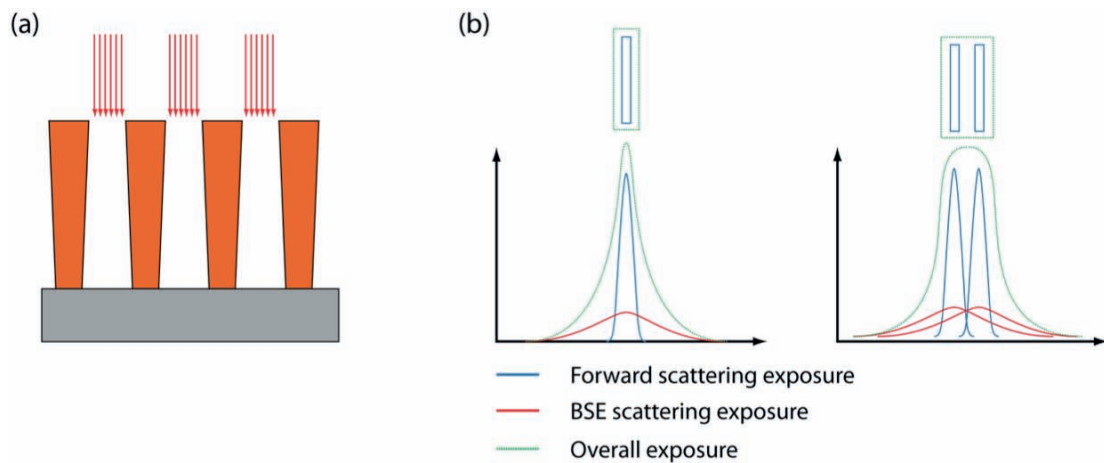


Figure 2.4. Electron scattering and proximity effects on patterns. (a) Typical undercut profiles of positive resist are due to forward scattering of the incident electrons (tapered for negative resist). Fine structures are often weakened by such profiles. (b) Because of proximity effect, isolated features appear bigger than the scanned area. However, dense patterns may merge without correction.

Scattering and proximity effect correction

The correction of scattering and proximity effect is necessary for high resolution patterning of irregular or dense structures.

Because of forward scattering, a thin resist layer is usually preferred to a thicker layer. From the point of incidence, the scattering gets wider with the penetration depth. With thin resist layers, most of the lateral scattering occurs in the substrate and not in the resist. Similarly, a high acceleration voltage is more suited, because the trajectory deviations at the surface are of small angles

A low Z and low-density material help reduce electron backscattering. When a metal layer is deposited on top of the substrate for charge reduction purposes, the backscattering is significantly increased and the resolution lowered. At the opposite, it is possible to reduce the electron backscattering and to significantly enhance the resolution by patterning directly on thin-films substrates^[84].

These are general advices that provide a good starting point for achieving good lithography. However, most of the optimization works is performed by dose

correction for minimizing as much as possible proximity effects. Dose correction is the process that takes into account proximity effects and make sure that the dose is uniformly distributed. Typically, dense or bigger features are less exposed and isolated or smaller ones are more exposed, so that all get the same amount of energy. Such a kind of dose correction is performed by computation of the energy distributions in all the patterns but may be complicated for complex structures.

For simple features such as lines and squares, the dose optimization may be performed empirically, by performing dose tests until the correct structure is obtained. In parallel, the dose correction can be accompanied by resizing of the patterns. Overexposed zones are therefore down sized and under-exposed areas are resized wider.

Charging effects

Charging effects, the accumulation of charges in a region, can be a potential issue in EBL. For high acceleration voltage, the penetration depth of the incident electrons is big enough for the charges to be evacuated by the substrate. In the case where EBL has to be performed on insulating substrates, charges accumulation may lead to undesired artifacts. Indeed, because of electrostatic repulsion forces between the incident electrons and the underlying charges, the beam may be deflected to a non-negligible extent. The first consequence is a potential distortion or improper location of the patterns. Second when the beam reads the alignment markers (see section 2.1.5), the established coordinate system may be as well distorted, resulting in poor features alignment.

2.1.4 EBL Resists

Electron beam resists are materials that are chemically sensitive to energetic electrons and that can be selectively removed after exposure using a developer. One can distinguish two types of ebeam resists depending on the type of reaction occurring upon exposition (Figure 2.6). Positive tone resists are high molecular weight polymeric chains that are fragmented into lower weight oligomers. For positive resists, the secondary electrons generated by the incident primary electrons beam break down chemical bonds between oligomers. For negative tone resists, the secondary electrons induce a cross-linking of small polymeric chains into longer ones. While the developer removes exposed area for positive resists, unexposed areas are washed away in the case of negative resists. The resist properties and process optimization are fundamental for high-resolution EBL.

Dose, sensitivity and contrast

The resolution of a resist, which is the smallest feature that can be reproducibly structured in a resist, is directly correlated to its sensitivity and contrast. It is sometimes preferred to refer resolution as the minimum pitch at which small features can be structured, because dense patterns are the most difficult to achieve.

The sensitivity of a resist describe how large should be the exposure dose for fully clear irradiated areas during development. The higher the sensitivity is, the fewer electrons are needed. Several experimental conditions have effect on the sensitivity:

- Acceleration voltage: The higher is the acceleration voltage is, the lower is the sensitivity because a higher dose is needed as high-energy electrons generate less secondary electrons in the resist layer.
- Substrate: A resist coated on substrates favoring backscattering has a higher sensitivity because BSE also contribute to exposure.
- Developer. The developer and development conditions influence the resist sensitivity, in particular concentration, temperature and duration.
- Resist thickness. Thin resist are less sensitive because less secondary electrons are generated in the resist layer.

Low sensitivity resists need longer exposure time because higher doses are needed. However, they are very suitable for high resolution EBL because they are obviously less sensitive to scattered electrons. There are no resist that are both highly sensitive and of high resolution. In addition to be more affected by scattered electrons, very sensitive resists are also affected by noise to a much bigger extent. When writing very small patterns at high frequencies, shot and statistical noises induce a higher line-edge-roughness that further decrease the final resolution.

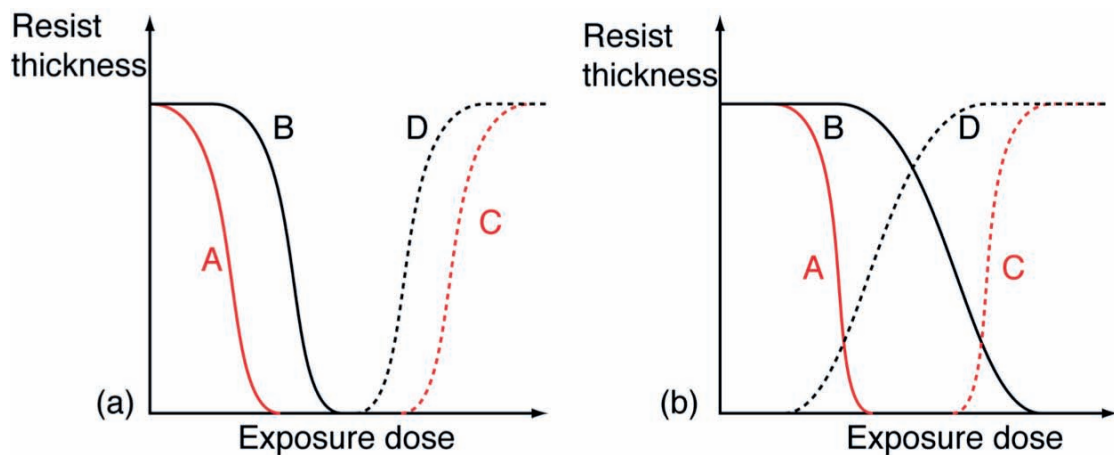


Figure 2.5. Development curves of positive (plain) and negative (dashed) resists with different sensitivity and contrast. (a) A, D of higher sensitivity than B, C. (b) A, C of higher contrast than B, D.

Resist contrast is a second important property for resolution. It can be described as how steep the sidewalls are or by the slope of the development curve. An ultra high contrast would yield vertical sidewalls. Resist contrast is critical for the transfer to the substrate of high aspect ratio or dense patterns by etching for instance (Figure 2.5)

PMMA

PMMA (poly-methylmethacrylate) is the most common positive resist in EBL. Two main molecular weights are available, 495 and 950 kg.mol⁻¹, dissolved in anisole or chlorobenzene. PMMA is a low-sensitivity and high resolution and contrast resist, capable of achieving sub-10nm lithography. Lower molecular weights are also available for an enhanced sensitivity, sacrificing over resolution. Typical clearing doses for large structures are around 600 μ C/cm² at 100kV. PMMA is available in several dilutions, allowing a wide range of thickness.

The most used developer for PMMA is MiBK (methyl-isobutyl-ketone), whose concentration in IPA (isopropanol) can be adjusted to favor either sensitivity or resolution. A standard concentration for high-resolution lithography is 1:3 MiBK:IPA. PMMA can be stripped with a wide range of solvent including acetone or by oxygen plasma.

PMMA has a poor resistance to reactive ion etching (RIE) and is more likely used for lift-off. In such a case, it is often used in bilayers of PMMA/MMA for producing undercut profiles after development. MMA is in fact a copolymer (MMA-MMA) of higher sensitivity than PMMA and of low resolution.

If not mentioned otherwise, the following procedure was followed for EBL with PMMA or MMA/PMMA: After substrate dehydration for 5' at 180°C, resists are spin-coated using a manual ATM_{sse} OPTIspin SB20 spinning module. For lift-off processes, bilayers of MMA/PMMA are used, with an inner layer at least 3x thicker than the expected thickness of deposited material. After each spin-coating, substrates are baked at 180°C for 5'. EBL is performed in a Vistec EBPG-5000. Samples are developed for 1' in 1:3 MiBK:IPA, rinsed in IPA for 10'' and blown dried with nitrogen. For low-resolution EBL, O₂ descum is performed in an Oxford PRS900 for 9'' (estimated etch rate of PMMA: 35nm/min).

ZEP

ZEP series resists (styrene methylacrylate) are positive tone resists that have been chemically amplified for an enhanced sensitivity while keeping a good resolution. ZEP resists have been developed in the purpose of a higher dry-etch resistance but their resolution is limited to about 20nm. The most common ZEP resist is the ZEP520 that has a molecular weight of 57kg/mol, available in various dilution in anisole or

dichlorobenzene. Typical clearing doses for large structures are around $200\mu\text{C}/\text{cm}^2$ at 100kV. The most popular developer for ZEP is pure n-amylacetate. ZEP can be stripped in anisole, remover 1165 or by oxygen plasma.

ZEP is usually used in a single layer for further etching and when a good contrast, e.g. vertical walls, is necessary. Its resistance to RIE is as good as conventional photoresists, allowing the fabrication of high-aspect ratio structures.

If not mentioned otherwise, the following procedure was followed for EBL with ZEP: After substrate dehydration for 5' at 180°C , ZEP-520A is spin-coated using a manual ATM_{sse} OPTIspin SB20 spinning module. For membranes opening (see section 2.3.2), a typical thickness of 500nm was used. Substrates are then baked at 180°C for 5'. EBL is performed in a Vistec EBPG-5000 with typical clearing dose of $225\mu\text{C}/\text{cm}^2$ at a resolution of $0.1\mu\text{m}$. Samples are developed for 1' in n-amyl-acetate, rinsed in MiBK:IPA 9:1 for 10'' and blown dried with nitrogen.

HSQ

HSQ (hydrogen silsesquioxane) is a negative resist considered to be the highest resolution EBL resist, with which sub-10nm features can be reliably realized. HSQ is an unusually resist because it is not a polymer based resist but an inorganic material. During exposure, HSQ is transformed to amorphous SiO_2 , which has very interesting properties for dry etching of Si substrates. Working with HSQ requires a lot of experience, as it is very sensitive to surface conditions and is very unstable. Very variable results can be obtained when the processing time is not well controlled. HSQ is of low sensitivity and requires high doses for small features. HSQ is usually released as 2 or 6% solutions for a thickness between 20 and 200nm

The development of HSQ is unusual as well because unexposed areas are removed by chemical reaction rather than by simple dissolution using aqueous NH_4OH or TMAH-based developers.

The complete removal of HSQ can be difficult because it is an inorganic material. Standard SiO_2 chemistry is usually required such as BHF wet etching.

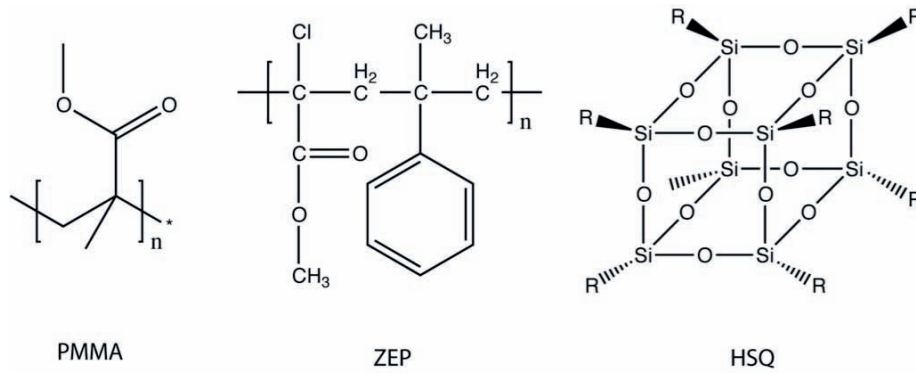


Figure 2.6. Molecular structures of PMMA, ZEP and HSQ.

If not mentioned otherwise, the following procedure was followed for EBL with HSQ: Samples are first cleaned by O_2 plasma (500W, 1') and soaked in TMAH-based developer (MF-CD26, 1') prior to spin-coating in order to improve HSQ adhesion. Samples are then rinsed with DI water, dried with N_2 . 2% HSQ (Dow Corning® XR-1541-002) is spin-coated at speeds ranging from 4000 to 6000 rpm, yielding thicknesses from 50nm to 20nm. EBL is performed in a Vistec EBPG-5000. Samples are developed in MF-CD26 for 30 seconds, rinsed in DI water and finally blown dried with N_2 .

2.1.5 Alignment

As for photolithography, the fabrication of nanoscale devices often requires multiple independent lithographic steps that each includes exposure and pattern transfer. An accurate alignment is therefore needed to ensure that features are perfectly positioned with respect to each other. Furthermore, patterns distortions may have to be corrected as well. In EBL, alignment and corrections are carried out automatically using dedicated markers, fabricated by photo- or EB lithography in a preliminary step.

Distortions and coordinates systems

In parallel to an accurate positioning, there are four types of distortions that can be corrected by a precise alignment: translational offset, rotation, scale, and keystone. Translational and rotational distortions are shear distortions that can easily occur as they are introduced during manual positioning of the substrate onto the holder, which is never identical between two successive steps. Scale distortions occur because of slight height variations over the substrate surface or because of height variations between two subsequent exposures, which modify the working distance (the distance between the surface and the objective lens). Although most of the changes are corrected by the height meter, fine changes can't be measured accurately enough. Finally, keystone distortions arise when the substrate surface is slightly tilted.

Distortions can be homogeneous, in which case a single alignment is necessary, or local. In the later case, multiple alignments may be necessary. Thermal expansion is a significant source of distortion in high resolution EBL.

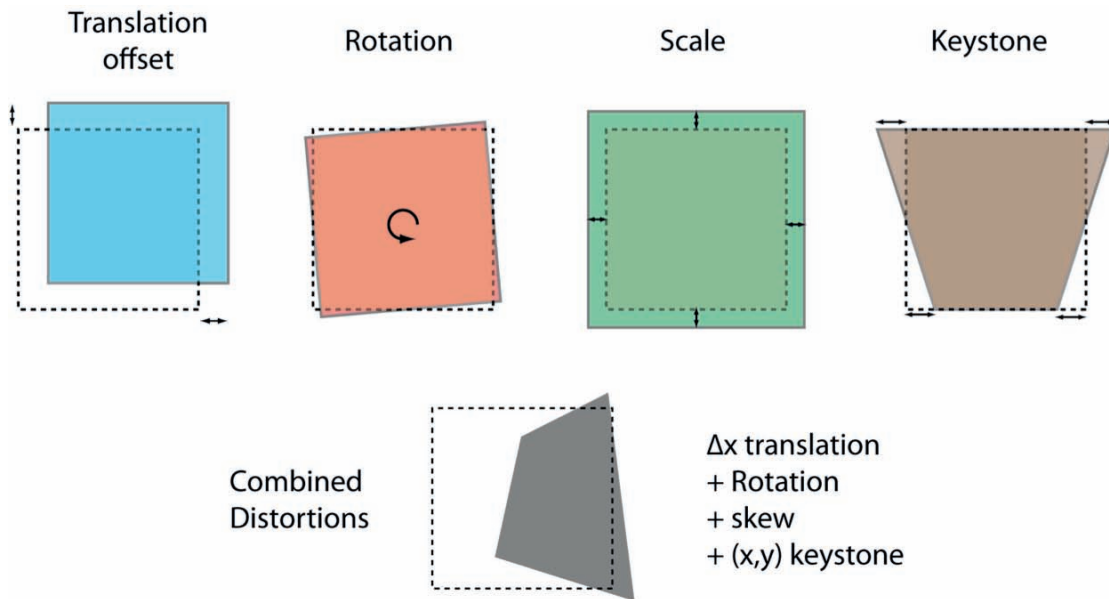


Figure 2.7. Distortions in electron beam lithography. Translation, rotation, scale and keystone distortions may occur independently in x or y or both directions. Dashed squares represent patterns as designed.

In an ideal case, in which there are no distortions, no thermal expansion, no drift and where the mounting procedure is perfectly reproducible, the substrate holder coordinates system would be sufficient to expose patterns with high position accuracy. In the real case, the ideal patterns' coordinates are transformed into distorted ones by using alignment marks at the substrate surface. The machine is therefore capable of establishing additional coordinate frames with respect to alignment marks designed by the lithographer.

Alignment marks

The alignment is performed by accurately measuring the position of markers prepatterned on the sample. Four alignment marks are enough to correct the four types of distortion. With 3 marks, only the shears and scale errors are corrected. Ultimately, a single mark only allows the translational offset to be corrected.

There are two types of alignment marks: topographical or Z-contrast markers, which are usually in the form of simple geometrical shapes such as squares, even though more complex structures may be used^[85,86]. During alignment, the instrument is converted into a classical SEM microscope, performing surface imaging using the integrated four-quadrant BSE detector. The contrast profile provided by the backscattered electrons when the beam scans a marker is correlated to the beam and stage position, allowing an accurate determination of its position.

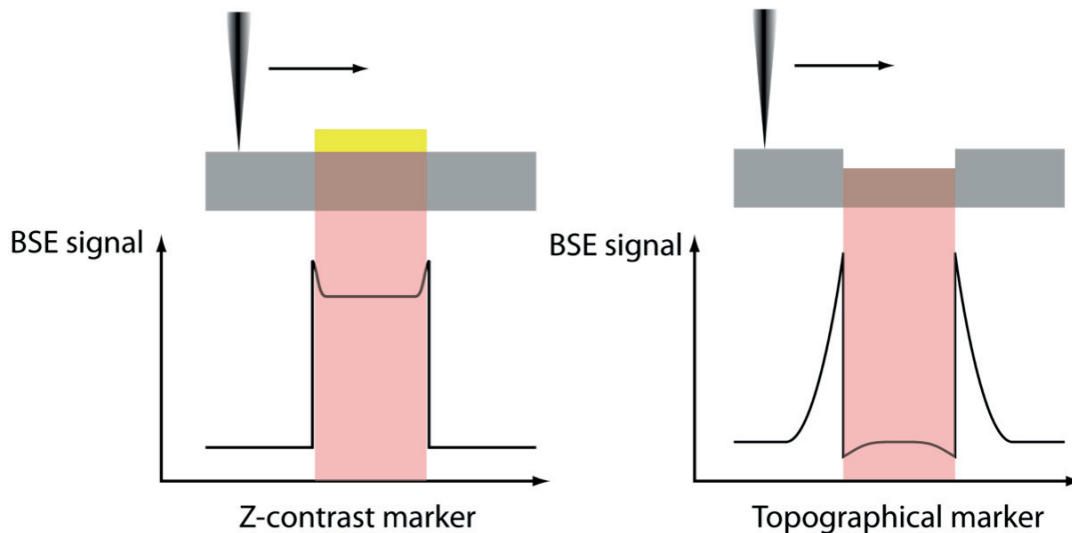


Figure 2.8. Simplified contrast mechanisms for automatic alignment. Z-contrast markers are high atomic number structures fabricated by lift-off (left) while topographical markers are usually etched cavities (right). The markers' edges are precisely determined by BSE imaging with a four-quadrant detector.

Topographical markers are etched pits (negative) or raised area (positive) while Z-contrast markers are made of high Z material deposited on the surface to provide a high BSE contrast. Figure 2.8 shows the BSE signal of typical markers when the beam is scanned across the each edge. Alignment is performed by scanning multiple times each edge of the marker in both directions.

If not mentioned otherwise, all alignment markers used for devices fabrication were $2.5\mu\text{m}$ deep squares fabricated by EBL and RIE, using ZEP resist. PAMs are arrays of 15×15 squares of $10\times 10\mu\text{m}$ positioned at the top center of the devices. Local alignment markers are 4-level $20\times 20\mu\text{m}$ squares (Figure 2.9) positioned at the device's corners.

Alignment process

When an exposure job is started, the beam position is first calibrated with respect to the stage using a faraday cup integrated to the sample holder.

A first coarse alignment with respect to the substrate is performed using a pre-alignment marker (PAM). A PAM typically consists of an array of identical marks spaced at intervals that increase regularly in both directions away from the array center. The coordinates of the array are roughly provided to the machine that starts looking for it first. Once five distinct marks are located, the center of the array can be established and a first global alignment is set for the overall substrate.

A finer alignment is then realized for high-resolution exposure. Local alignment marks are accurately measured, which provide the final corrected alignment. In case

of large exposure area, multiple local alignments may be performed using the PAM as starting point, which is in any case located only once.

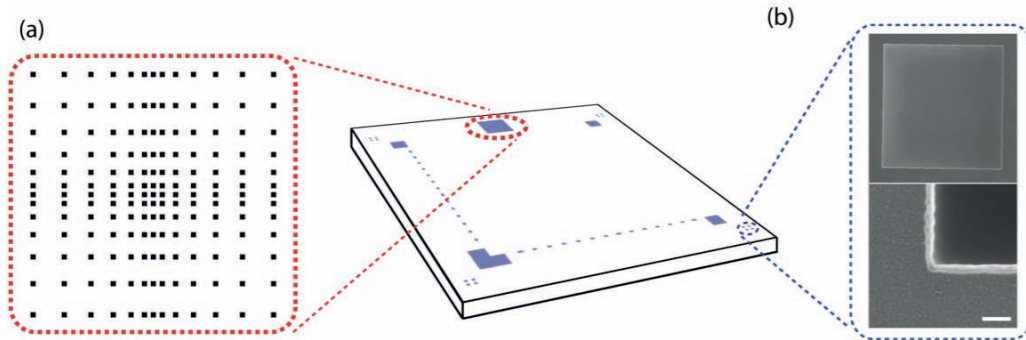


Figure 2.9. Illustration of the alignment process. (a) A 1x1 mm pre-alignment mark is first located for a coarse substrate alignment. (b) Secondary markers, usually positioned at the substrate corners or close to the exposure area, are then finely measured. SEM pictures show a 20×20µm topographical alignment marker (2.5µm deep in Si) and a zoom in the bottom left corner, indicating a very good line-edge-roughness. Scale bar: 200nm.

Limitations

As the alignment is performed by reading the edges of dedicated marks, the accuracy at which they are located is directly given by the line-edge-roughness and contrast of these structures. Additionally, for a good contrast, thick enough or deep enough marks are necessary. For these reasons, thick metallic markers fabricated by lift-off yield lower accuracy compared to well-defined markers made by RIE. Similarly, markers fabricated by EBL are of better quality than those fabricated by photolithography.

The need for a good contrast limits as well the range of beam current that can be used for alignment. If low-current beams can't perform alignment because of a poor signal to noise ratio, it has to be realized with another higher-current beam, which is a non-negligible source of error. Indeed, any time between alignment and exposure is a time where there are drifts phenomena, which can lead to tens of nanometers of overlay misplacements. Exposure must therefore be performed fast after alignment, and multiple beam calibrations lengthen this duration. For EBL, thermal and electronic drift is a major issue for high resolution positioning of patterns, as it can reach speeds of several nm per minutes. For the same reasons, short writing time should always be preferred. Long exposures should therefore be fragmented into shorter ones, between which an alignment is regularly performed.

Furthermore, where a mark is scanned, the resist is exposed, meaning that it becomes damaged or even destroyed during the pattern transfer. If the mark is still functional for a second lithography step, the alignment accuracy will be degraded. If it is destroyed, different marks have to be used, which introduces another source of error.

Finally, the position of the marks is usually carefully chosen to the most adequate areas. One has to keep in mind that the further they are from the exposure area, the

lower is the accuracy. A close proximity to the exposure area is most of the time suited for high-resolution alignment. Experimental issues and the best methods to limit them will be further discussed in section 4.3.1.

2.2 Pattern transfer

2.2.1 Leybold LAB600H

If not mentioned otherwise, all physical vapor depositions (PVD) were realized by electron beam evaporation using a Leybold-Optics LAB-600H available at CMI. The LAB-600H is specifically designed for lift-off processes (Figure 2.1) with its high source-substrate distance (1.01m) and an incident flux normal to the substrate surface, yielding quasi-vertical walls after lift-off. The machine was typically operated at room temperature and at a pressure below $2 \cdot 10^{-6}$ mbar at deposition rate of 4.0 \AA/s , allowing the deposition of metal and dielectric layers with high purity.

2.2.2 Alcatel AMS-200DE

After electron beam or photolithography, dry reactive ion etching (RIE) for the fabrication of alignment markers and Si_3N_4 membranes was performed using an Alcatel AMS-200DE available at CMI. The AMS etcher is an optimized deep RIE system for silicon and dielectrics, involving a temperature-controlled chamber and wafer chuck combined to an inductive couple plasma.

Si_3N_4 and SiO_2 layers were etched by standard C_4F_8 chemistry (17sccm C_4F_8 , 150sccm H_2 , 13sccm CH_4 , $8 \cdot 10^{-3}$ mbar, P_{coil} : 1500W, P_{chuck} : 120W, 30'') at 20°C using ZEP or AZ1512 resist as dry etch mask with a typical thicknesses ratio of 10:1 relative to the total dielectric thickness.

For alignment markers, etching of Si_3N_4 and SiO_2 was followed by a vertical etch of bulk Si using $\text{SF}_6/\text{C}_4\text{F}_8$ chemistry (40sccm SF_6 , 55sccm C_4F_8 , $3 \cdot 10^{-2}$ mbar, P_{coil} : 1500W, P_{chuck} : 30W, 2'30'') at 20°C , yielding about $2.5\mu\text{m}$ deep pits in $\text{Si}_3\text{N}_4/\text{SiO}_2/\text{Si}$.

2.3 Solid-state nanopores fabrication

For years now, researchers have fabricated solid-state nanopores using state-of-the art silicon technology combined with advanced microscopy techniques. Typically, an insulating membrane, usually SiO_2 or Si_3N_4 , is opened by a combination of RIE and anisotropic etching of silicon wafers, followed by the actual drilling process by ion or

electron beam sculpting. The method of using a microscope for milling tiny hole in a membrane provides many advantages over other techniques, and in particular the possibility of having a real-time feedback from the imaging detectors. There are other techniques that have been shown to yield nanopores with good size control^[49] but the highest throughput method is by far by conventional drilling.

The following section reports on state-of-the art fabrication of Si_3N_4 membranes with location control, followed by drilling in a TEM microscope.

2.3.1 Substrate

Si_3N_4 is a material of choice for our application because of its high mechanical stability and robustness, and the ability of accurately control its position in a substrate. Moreover, its use for the fabrication of ss-nanopores has been widely studied. All experimental devices were fabricated using custom Si wafers with epilayers of SiO_2 (60nm) and Si_3N_4 (20nm). Double-side polished 100mm diameter 380 μm thick boron doped Si <100> wafers (1-10 $\Omega\cdot\text{cm}$) were first cleaned in a three steps procedure involving sequential rinsing in base piranha, diluted HF, and acid piranha. Shortly after cleaning, 60 nm of SiO_2 were grown on both sides by dry oxidation. 20 nm layers of Si_3N_4 are finally deposited on both sides by low-stress low-pressure CVD (LPCVD). The presence of SiO_2 is to ensure a correct insulation and a reduced membrane capacitance.

Single wafers are patterned on both sides by EBL and photolithography with 6x6 sets of alignment marks, constituting 36 independent devices. Topside alignment markers are first patterned by EBL in ZEP resist and subsequent deep RIE. Identical and aligned backside markers are then patterned by photolithography (AZ1512, 1.3 μm) using an EVG150 automatic coater/developer and a Süss MA6/BA6 double side mask aligner and subsequent deep RIE. The resulting wafers exhibit top and backside EBL alignment marks, which allow a precise membrane positioning with respect to the topside patterns (Figure 2.10.1-5). The alignment resolution of features on the backside with respect to the topside was observed to be better than 2 μm .

2.3.2 Membrane opening

The process flow for the fabrication of suspended membranes is depicted in Figure 2.10.6-8. Square windows are patterned on the backside of the wafer by EBL using ZEP resist. Using the resist as RIE mask, the Si_3N_4 and SiO_2 layers are etched in a single step of C_4H_8 chemistry, releasing the Si surface. After stripping of the resist, using the Si_3N_4 backside as a mask, Si is anisotropically etched in 25-wt % KOH at 80°C during 6h. The top SiO_2 layer is etched as well during the process but at a much

slower rate. We approximate the etching rate of Si in such condition to about $70\mu\text{m}\cdot\text{h}^{-1}$, while 20 minutes are roughly needed to etch 60nm of dry oxide. The etch rate of Si in KOH is proportional to temperature and depends on concentration. The maximum rate is obtained at around 25%. The etch rate of low stress Si_3N_4 is negligible but any damage or pinhole in the layer may lead to disastrous results such as large openings or to the loss of the sample. As described in section 3.4.2, high temperatures have terrible effects on the quality of Si_3N_4 as a mask for KOH etching.

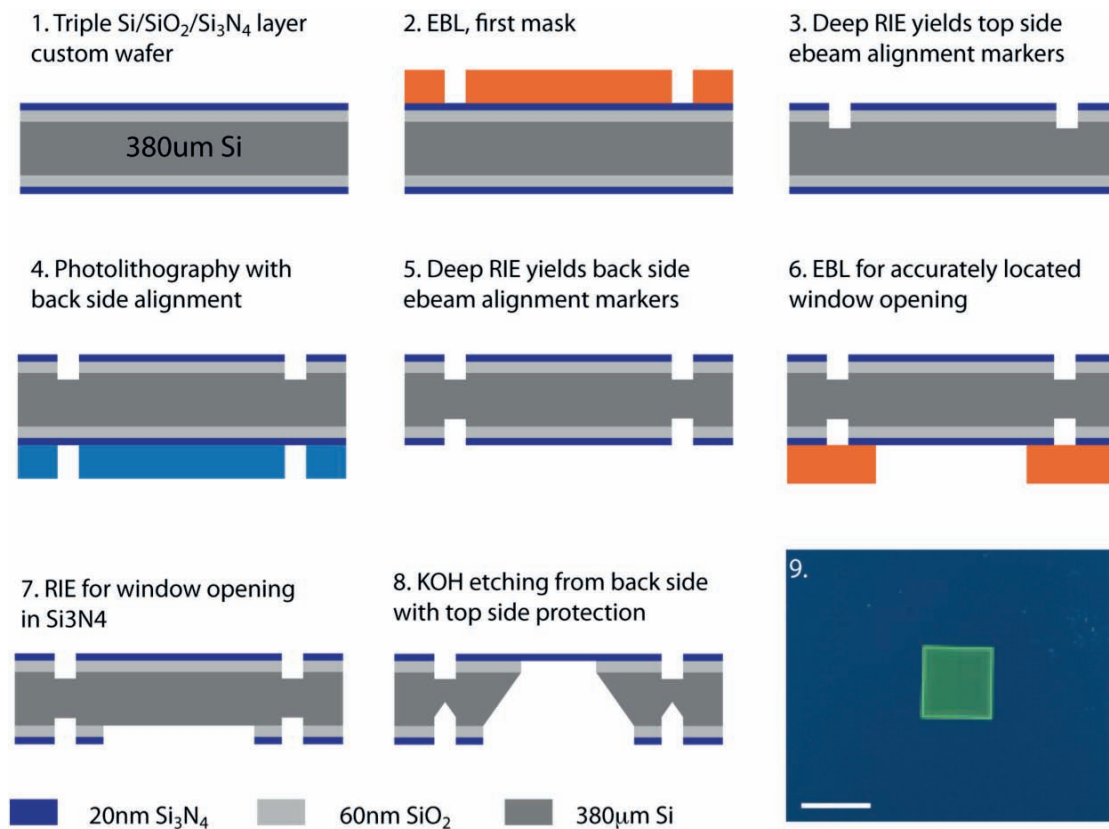


Figure 2.10. Typical process flow for the fabrication of suspended Si_3N_4 membrane with position control. 1-5. Fabrication of top and backside EBL alignment marks for precise membrane positioning. 6-8. 2-steps membrane opening. 9. Optical top view picture of a typical $20\times 20\ \mu\text{m}$ Si_3N_4 membrane. Scale bar is $20\ \mu\text{m}$.

KOH etching of silicon is an anisotropic process as there is selectivity between the $\langle 111 \rangle$ and $\langle 100 \rangle$ directions, which is attacked about 400 times faster. When opening a square window into Si_3N_4 , the Si surface is attacked, resulting in a pit having (111) oriented sidewalls, which form an angle of 54.7° with respect to horizontal. By changing the size or shape of the initial backside window, the resulting membrane can be finely tuned (Figure 2.11).

KOH etching can be performed independently at the wafer scale or single dye scale. In both cases, the protection of the topside from KOH is crucial for the survival of the devices and requires the use of dedicated TEFLON chucks. Up to 180 functional

devices with $20 \times 20 \mu\text{m}$ membranes were opened in a single wafer, using a single wafer holder (AMMT^[87]). For chip-scale etching, home-built chucks were used, fitting $11.2 \times 11.2 \times 0.38$ mm samples with topside protection.

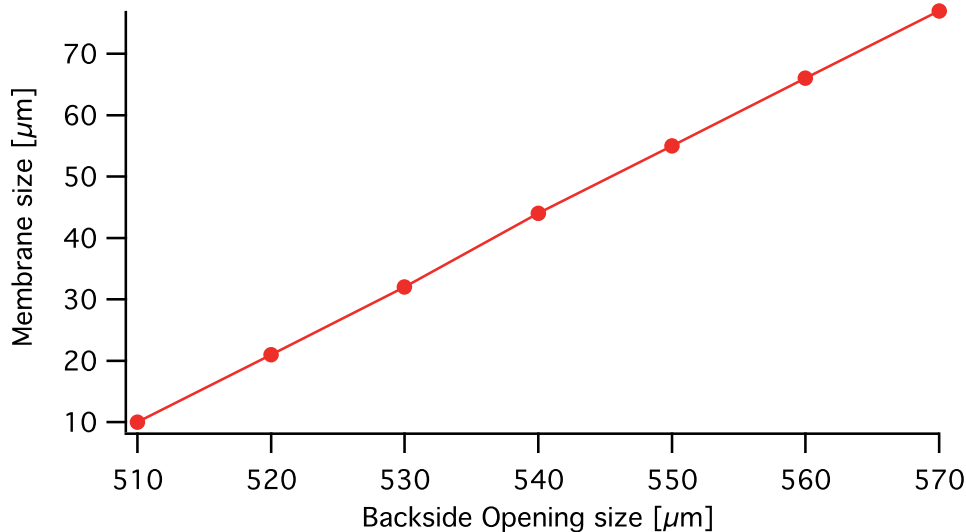


Figure 2.11. Membrane size in function of the size of the backside square opening, measured in an optical microscope.

2.3.3 Nanopore drilling

Milling of nanopores in TEM microscope quickly became the method of choice because of its experimental ease and real-time feedback capability. Milling using focused ion beam (FIB) is a similar technique that uses heavy ions such as Ga^+ for the drilling process. However drilling in a TEM microscope allows the fabrication of nanopores of much smaller diameters, down to a single nanometer.

Conventional TEM holders are designed for holding small carbon grids of about 3mm in diameter. A custom sample holder was specifically designed and fabricated at EPFL for our application, which fits $8 \times 4 \times 0.38$ mm samples for use in a Phillips CM300 TEM. Therefore, the final dimensions of all our devices were set to 8×4 mm. Devices of bigger initial sizes were either diced or cleaved. In case of cleaving, tranches were opened during KOH etching to facilitate the process.

Before drilling, samples are cleaned for 2h at 200°C under a 10 sccm H_2 and 100 sccm Ar flux, in order to remove any residual of organic material left on the surface by the microfabrication processing. If needed, ALD deposition of Al_2O_3 is performed by cyclic pumping of trimethylaluminum (TMA) and water vapor (H_2O) at a temperature of 200°C . Precursors are diluted in a constant N_2 flux at a base pressure of 60 mbar. Al_2O_3 is typically deposited up to a thickness of 6 nm before pore drilling.

Electron beam drilling is performed in a Philips field emission CM300 in TEM mode operated at 200 kV at CIME-EFPL (Interdisciplinary Center for Electron Microscopy). A mechanical stabilization period of at least 30 min is mandatory in order to avoid drifting of the sample during drilling and to drill round pores.

After careful gun and column alignment, typically spot size 5 (10 nm nominal diameter) or spot size 4 (15 nm nominal diameter) are chosen for drilling. The magnification is set to 200000x and the membrane is focused. The beam is then condensed down to a tight spot, during which the focus and the spot position are constantly adjusted. A typical drilling time for a 20 nm, low-stress Si_3N_4 membrane with 6 nm of Al_2O_3 deposited is one minute. In order to avoid contamination of the membrane or pore walls with hydrocarbons, the vacuum quality is of first importance.

The opening of the pore is monitored in real-time and the drilling is stopped as soon as a pore of desired dimensions has formed. The smallest pores naturally open with more or less the dimensions of the well-condensed beam, i.e. 10-15 nm for the used spot sizes. According to tomography studies, TEM drilled nanopores in Si_3N_4 are believed to adopt hourglass-like or cylindrical shapes depending on the drilling conditions^[55,88].

Shrinkage of the drilled nanopore can be achieved by electron exposure with a slightly defocused beam or at lower beam intensity. The shrinking mechanism is hypothesized to be caused by a local joule heating, which induces a fluidization of the membrane and a material diffusion toward the pore^[45,55,89]. In such cases, atoms sputtering is restrained while the nanopore contraction is caused by the surface tensions of the fluidized membrane near the pore. By varying the exposure time, nanopores may be shrunk to single-nanometre size. An alternative approach consists in using electron beam induced deposition (EBID) in order to progressively shrink the pores with hydrocarbon deposit under electron irradiation in a SEM^[90].

The size reduction of nanopores can be performed in a post procedure using atomic layer deposition. After drilling, the layer-by-layer deposition allowed by ALD allows a uniform and fine control with atomic resolution of the pore diameter.

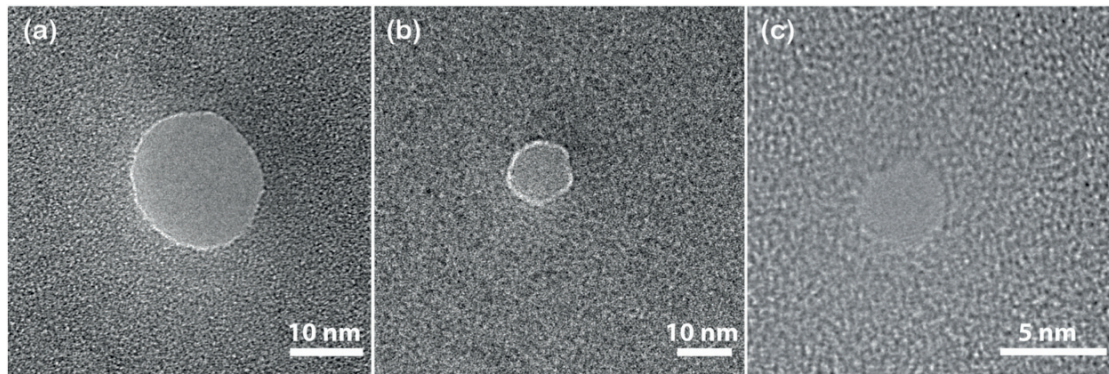


Figure 2.12. Nanopores drilled in a CM300 TEM microscope operated at 200kV in 20nm thick Si₃N₄ membranes. Sizes range from (a) 19×17nm, (b) 10×11nm to (c) 3×3nm.

2.4 Microfluidic and nanopore setup

All nanopore experiments have been performed in collaboration with the Laboratory of Nanoscale Biology (LBEN-EPFL) led by Prof. A. Radenovic. After successful fabrication of nanopores with embedded tunneling electrodes (see Chapter 4), functional devices are mounted in a microfluidic cell. The microfluidic cell consists of two PMMA reservoirs with silicon O-rings that seal the two sides of the 8×4mm devices. The two reservoirs can be independently filled with buffers through Omnifit connectors and a tubing/syringes system, and therefore constitute the *cis* and *trans* side of the nanopore devices. In addition, the two reservoirs can accommodate Ag/AgCl electrodes for translocation experiments. Transverse tunneling electrodes are contacted with 800×400μm contact pads present at the surface at the devices. The pads are connected to the external measurement setup via metallic connectors structured in one of the PMMA chambers. The electrical contact is ensured by using silver paste (DuPont).

PMMA chambers are cleaned in 2% RBS with bath sonication and thoroughly rinsed with DIwater. Once the chip is sealed and the pads connected, the two chambers are filled first with filtered and degassed mixture of 1:1 diH₂O:EtOH. The presence of air bubbles in the microchannels is carefully verified, in which case they are removed. The nanopore devices are ideally left to incubate overnight before experiments to improve their wettability and obtain ohmic behaviors. The use of O₂ plasma to improve the hydrophobicity of the pores was avoided as it most often resulted in abnormally high conductances. The appropriate buffers for experiments and translocation are then flushed into the two reservoirs. Buffers are filtered and degassed 10mM-2M KCl with 1mM EDTA buffered at pH 7.4 with 10mM Tris. For DNA translocation experiments, HindIII digested λ-DNA (New England BioLabs) is flushed through the *cis* compartment at a concentration of 50 μg/ml.

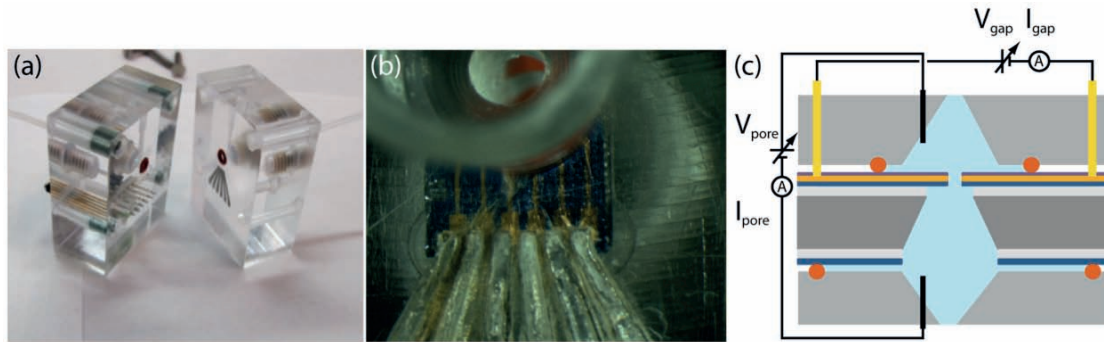


Figure 2.13. Illustrations of the experimental cell. (a) Picture of the PMMA chambers for nanopore experiments. (b) The cell allows to electrically connect contact pads and hence to the embedded transverse electrodes. (c) Measurement principle. The ionic and transverse currents are the two channels that can be monitored simultaneously for single-DNA sensing.

The ionic current is amplified using an Axopatch 200B patch clamp amplifier (Molecular Devices) with a built-in 10kHz Bessel filter coupled, to two Ag/AgCl electrodes. The transverse current is amplified using a 400kHz current amplifier (FEMTO). Both channel data are acquired with a PXI-4461 acquisition card (National Instruments) at a 100 kHz sampling frequency and filtered at 50 kHz. The microfluidic cell is placed in a double-Faraday cage, where the two Ag electrodes, previously chlorinated in bleach, are immersed in the chambers. The pins connecting the tunneling electrodes are plugged to a connection board with switches in open circuit positions. Ionic current can therefore be monitored independently or simultaneously with the transverse current.

A custom Labview GUI is used to control the whole setup. Voltage biases can be independently applied to the nanopore or to the nanogap electrodes. In both cases, I-V sweeps can be performed as well. Voltage sweeps are performed on the pores from 0 to maximum 300mV, with steps of 1/10 of the voltage window, a dwell time of 10s and alternatively positive and negative voltages. Voltage sweeps on the nanogap are done from maximum -30mV to maximum 30mV, with 5mV increments and 10'' dwell time. I-V traces are sampled at 6250Hz. The software provides in real time the PSD, I_{RMS} , peak-to-peak, and average values of both channels.

In addition, it contains a built-in filter for DNA translocation events for both channels. The user chooses threshold parameters that indicate translocations and during which the ionic and transverse current are recorded. These parameters are the height of the current blockades or peaks (in multiple of I_{RMS}) and the duration of such current variations. The translocation events could be analyzed using the OpenNanopore tool recently released by C. Raillon *et al.*^[91].

Chapter 3

Nanopores embedded with transversal SWCNT tunneling electrodes

3.1 Introduction to carbon nanotubes

Carbon is one of the most common and studied elements on earth and has also the most fascinating chemical properties in the way it can form structures with entirely different properties (Figure 3.1). When hybridized sp^3 , carbon atoms can organize as diamond, a face-centered cubic crystal with the highest hardness and thermal conductivity properties. However, when hybridized sp^2 , where a free valence electron can be delocalized among neighbor atoms over long distances, graphitic structures can be created. Graphite is hence a layered material, with strong in-plane bonds and weak van-der-Waals out-of-plane interactions between so-called graphite sheets, which can slide along one another. The ultimate mono-layer, one-atom thick, configuration is named graphene and is a planar assembly of sp^2 bonded carbon atoms organized in a honeycomb crystal lattice, which is behind the formation of closed shell structures such as fullerenes and carbon nanotubes. These new compounds have been in the last 20 years at the center of the scientific community because of their outstanding properties.

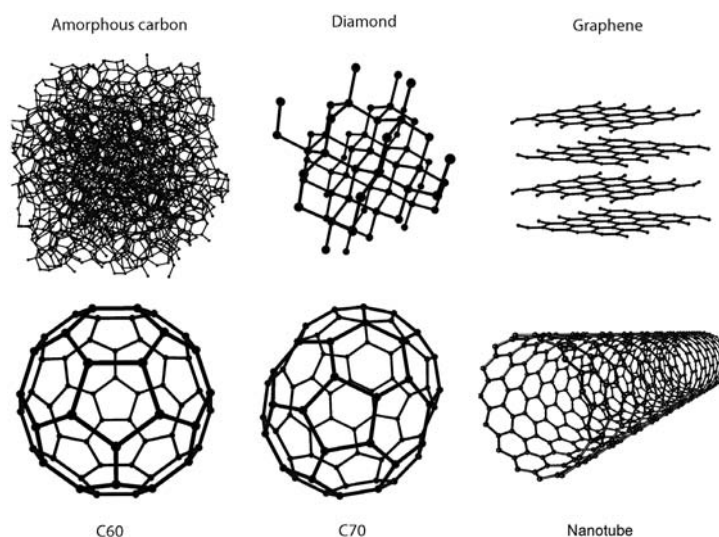


Figure 3.1. Different allotropes of carbon structures.

3.1.1 History of carbon nanotubes.

Fullerene is a wide family composed of spherical, ellipsoidal or tubular closed structure made only of carbon, in which each atom, sp^2 bonded, is linked to 3 other atoms in hexagonal or pentagonal rings.

As early as in 1970, E. Osawa was the first researcher to hypothesize the possible existence of a full ball shape made only of carbon atoms and a theoretical model was built and published in 1973 by a Russian group. Whilst these studies remained poorly accepted and attracted not much attention for years, H. Kroto, R. Curl and R. Smalley reported in *Nature* in 1985 for the first time the existence of C_{60} , that they name buckminsterfullerene, in homage to Buckminster Fuller and his famous geodesic domes^[92]. From laser vaporized graphite samples, they observed by MS-ToF, the presence of C_n clusters, of which a structure with exactly 60 carbon atoms was the most common. This discovery launched a completely new field in chemistry: the chemistry of fullerenes, molecules with unusual geometries and unique chemical properties. C_{60} was shortly after characterized as truncated icosahedron with 60 carbon atom vertices, 20 hexagons and 12 pentagons and a nucleus-to-nucleus diameter of about 0.7nm. The ability of its hollow structure to entrap small molecules, its fascinating surface chemistry combined with its remarkable geometrical stability quickly brought a lot of hope about the potential applications behind fullerenes.

The carbon allotropes revolution took a new dimension when carbon nanotubes were added to the list of the fullerene family compounds. The discovery of CNTs is often attributed to S.Iijima in 1991^[93] who published first clear TEM images revealing carbon needles comprising “coaxial tubes of graphitic sheets, ranging in number from 2 up to about 50” (Figure 3.2). The credit for the CNTs discovery remains however a hot topic in the field when one considers the publication of Radushkevich in a Russian journal as early as in 1952^[94]. In this document, the micrograph introduced the scientific community already to nano-scaled graphitic carbon fibers but the current experimental limitations in transmission electron microscopy didn't reveal the detailed structure and the importance of the discovery. All would nevertheless agree on the impact of this new compound on the chemical, physical and material sciences: CNTs are unique and can only be described with superlatives. They have a high aspect ratio with lengths up to several millimeters and diameters down to 1nm, they are among the stiffest and strongest materials, have an extraordinary high thermal conductivity and outstanding electronic properties.

The potential applications are therefore as various as their amazing properties can be: from energy storage or conversion, nanoscale semiconductors, chemical sensors, sharp AFM probes, NEM switches to new types of composites, they are expected to

take place in many fields and are promised to a great future when the current experimental limitations will be overcome. The processing and assembly challenges in CNTs based devices will be developed and discussed later.

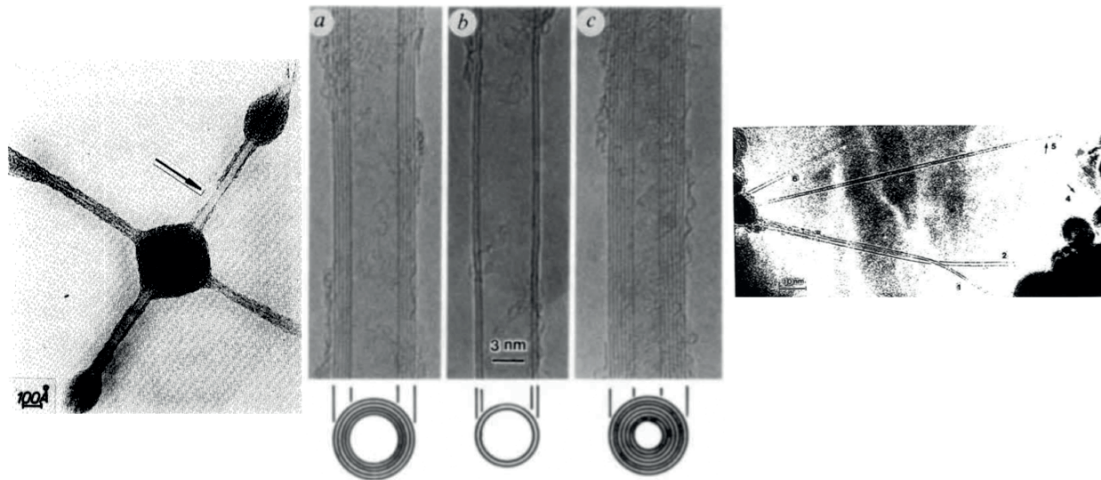


Figure 3.2. Early imaging reports of carbon nanotubes (left) Filamentous growth of carbon through benzene decomposition^[95]. (middle) Helical microtubule of graphitic carbon^[93]. (right) Single shell carbon nanotube of 1nm diameter^[96].

3.1.2 Structure and chirality of carbon nanotubes

Graphene, introduced before as a mono-atomic layer of carbon atoms arranged in hexagonal rings, is the basic constituent of CNTs. Indeed, from a structural point of view, CNTs can be considered as single graphene sheets wrapped concentrically into a cylindrical shape. Two groups of CNTs can be distinguished according to the number of sheets, or walls, present in the structure.

The first are called single walled carbon nanotubes (SWCNTs) and are made of a single sheet of graphene rolled up into a tubule that looks like an elongated fullerene. In such a configuration, the diameter of SWCNTs is usually around 1nm and very few defects are present. Ideal SWCNTs are defect-free and are only constituted of millions of hexagons along the cylinder axis and of $\frac{1}{2}$ fullerenes closing the tube at the ends. However, when defective, they contain topological and structural defects such as pentagons or heptagons or chemical defects, such as surface modifications. The actual SWCNT diameter ranges thus from 0.4nm to 3-4nm. The narrow diameters distribution often leads to the formation of SWCNTs bundles (Figure 3.3), in which individual tubes are held together by electrostatic interactions in carbon ropes^[97], phenomenon making tricky the dispersion of high purity samples.

The second are called multi-walled carbon nanotubes (MWCNTs) and were the first to be discovered as they are also more easily synthesized. MWCNTs are basically made of an array of SWCNTs concentrically nested around a central hollow with a

diameter ranging from few to up to tens of nanometers (Figure 3.3). When higher than 100nm, they are more likely considered as carbon fibrils. Double-walled carbon nanotubes (DWCNTs), which are in the MWCNTs family, are often considered as a special class of CNTs because they have properties closer to the SWCNTs family but are more interesting for functionalization purposes. The number of walls in MWCNTs can vary from two to several tens with wall-to-wall distances slightly larger than the interplanar spacing in graphite that is 0.335nm, and the individual shells are rotationally disordered with respect to each other. Because of the geometrical constraints imposed by the structure, the Van-der-Waals interactions between the walls are weaker than the ones in graphite.

Finally, there are also other very interesting structures and shapes, such as CNT junctions, in which there are no dangling bonds and where all carbon atoms are bonded to the three nearest neighbors. However lattice defects are necessary to allow unusual curvatures. Examples of such structure are Y-junctions, toroidal CNTs as well as 2-CNTs junctions.

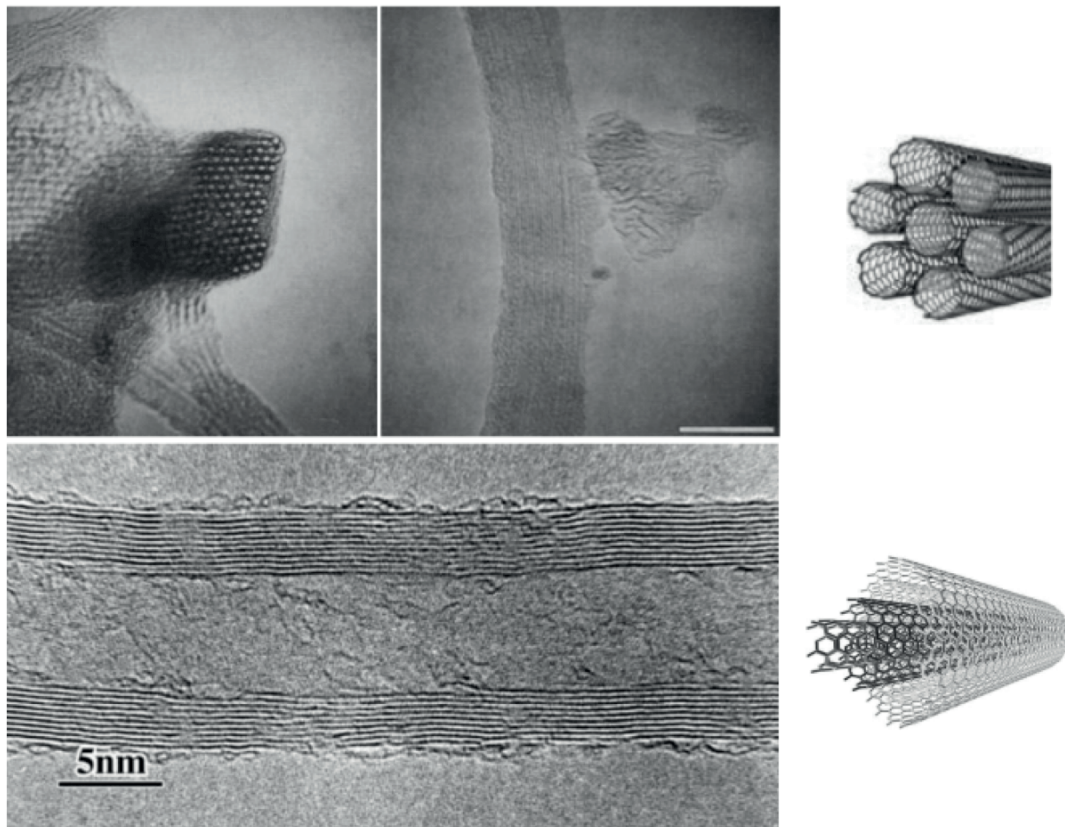


Figure 3.3. (top) Coaxial and side TEM views of a SWCNTs bundles^[97]. (bottom) High-resolution TEM image of a 9-wall carbon nanotube.

There is an infinite way to roll up a graphene sheet into a cylinder, giving rise to an infinite number of lattice orientations with respect to the tube axis. The *chirality* or axial symmetry of a SWCNT is one of the most important properties to take into

account and can be described by the so-called *chiral vector* \vec{C}_h or *chiral angle* θ . \vec{C}_h , representing the direction along which the graphene sheet is rolled up (Figure 3.4), and in case of a defect-free CNT, can be expressed as follow:

$$\vec{C}_h = n\vec{a}_1 + m\vec{a}_2 \quad (3.1)$$

where the integers n and m are named chiral indices and \vec{a}_1 , \vec{a}_2 are the unit vectors of the hexagonal honeycomb lattice of graphene.

The nanotube diameter d can be derived from the module of \vec{C}_h , that is the circumferential length and the (n, m) indices :

$$d = |\vec{C}_h| / \pi = \frac{a}{\pi} \sqrt{n^2 + nm + m^2} \quad (3.2)$$

where a is the lattice constant of graphene ($a = 0.246 \text{ nm}$).

Finally the chiral angle θ between \vec{C}_h and \vec{a}_1 is given by:

$$\theta = \arccos \frac{n + m/2}{\sqrt{n^2 + nm + m^2}} \quad (3.3)$$

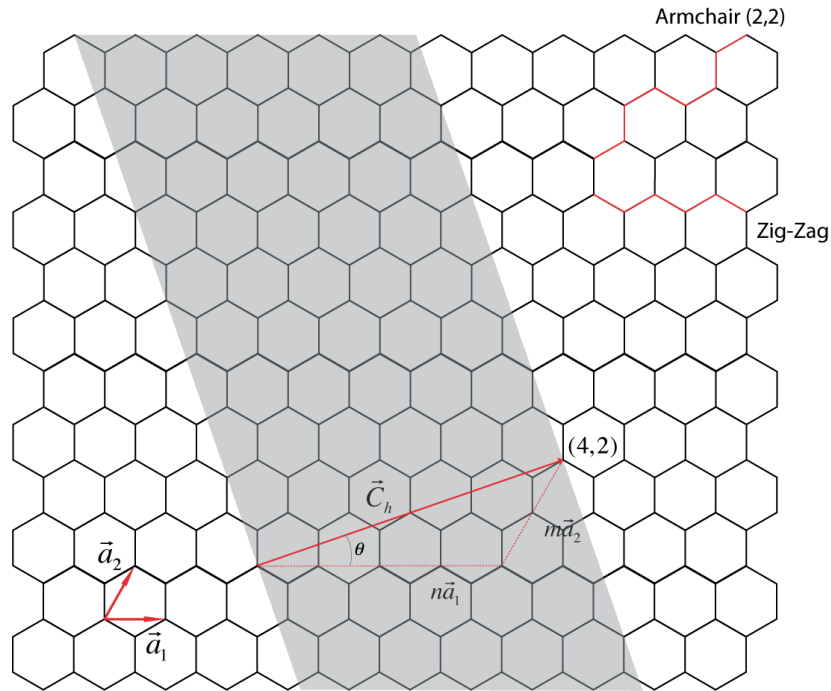


Figure 3.4. The chiral vector \vec{C}_h is the vector along which a graphene sheet would be rolled up to form a (n, m) CNT. n and m are the so-called chiral indices. Two specific patterns are put in evidence: the armchair and zig-zag nanotubes.

The chirality of a nanotube is therefore formally represented with the pair of indices (n, m) , out of which 3 categories are derived (Figure 3.5). First, the armchair nanotubes are all the tubes with same n and m indices, denoted (n, n) with $\theta = 30^\circ$.

Second, the zig-zag nanotubes with (n, m) as $(n, 0)$ with $\theta=0^\circ$, named as of the zig-zag sequence along the circumference. Third, the chiral nanotubes (n, m) are the ones with θ between 0° and 30° . The chirality of a nanotube is a prominent parameter that dictates its metallic or semiconducting behavior.

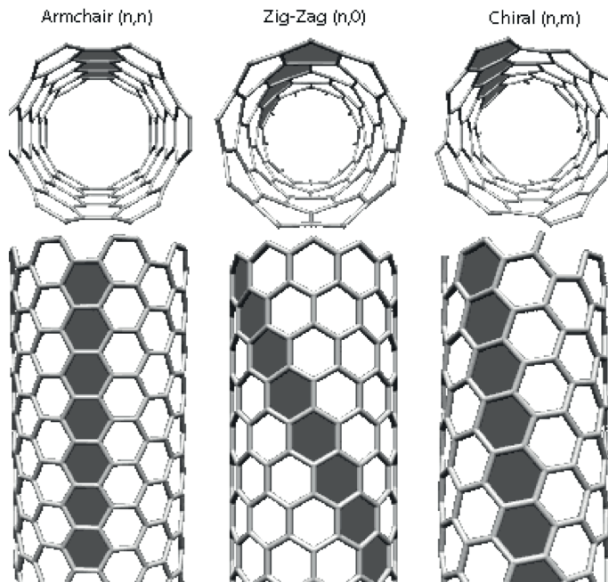


Figure 3.5. Illustrations of the chiral structure of an armchair (left), zig-zag (middle) and chiral carbon nanotube.

As SWCNT have three possible chiral structures, MWCNTs are rarely monochiral (i.e. made of only nanotubes with the same chirality) but contain most likely walls with the 3 different chiral configurations. Determining the chirality of a nanotube is not an easy experimental task and only imaging techniques with atomic resolution like STM or electronic diffraction in TEM can differentiate the structure of CNTs.

The chiral classification assumes that the nanotubes are defect free. However, one has to keep in mind that each defect, such as an atomic vacancy or a lattice irregularity, will have an influence on the chirality along a single nanotube, and hence, on the related properties. Furthermore, even the narrowest diameter distribution in the production or purification of CNTs will lead to a chiral disparity, which give a first insight into the limiting barriers in CNTs applications.

3.1.3 Properties of carbon nanotubes

Electronic properties

Carbon nanotubes have been at the center of an immense interest in the past years because their one-dimensional nature confers them unique electronic properties and promising applications in the nanoelectronic fields. CNTs may be either metallic or semi-conducting depending on their chirality and with a band gap closely linked to their diameter. Moreover, metallic nanotubes are capable of carrying tremendous

amount of currents with limited heating. This paragraph will focus on explaining the fundamental physics governing the unusual electronic behavior of carbon nanotubes and will provide the basic understandings necessary in the field of CNT-based devices.

Armchair (n,n) SWCNTs always exhibit a metallic behavior whilst SWCNTs satisfying the condition $|n - m| = 3I$ (I is a non-zero integer) are small band gap semiconductors with semi-metallic behavior. SWCNTs with chiral indices not fulfilling previous conditions are large band gap semiconductors. Because of their specific symmetry, the metallic behavior of armchair nanotubes is independent of the diameter whereas the band gap of semi-metallic nanotubes varies inversely with it.

The electronic properties of CNTs are usually discussed on the bases of the band structure of graphene. In the graphene lattice, carbon has 6 electrons, two 1s core electrons, three $2sp^2$ electrons, which form three strong planar bonds in σ orbitals, and one 2p electron in an unsaturated π orbital perpendicular to the surface. In graphene or in CNTs, the π orbitals are responsible for the electronic properties along the structure by forming a delocalized π network. The band structure of graphene can be calculated using a tight-binding representation of the interactions between the π orbitals of two nearest C atoms. This method leads to the following 2D energy dispersion, plotted in Figure 3.6:

$$E(k_x, k_y) = \pm\gamma \sqrt{1 + 4 \cos\left(\frac{3}{2}k_y a\right) \cos\left(\frac{\sqrt{3}}{2}k_x a\right) + 4 \cos^2\left(\frac{\sqrt{3}}{2}k_x a\right)} \quad (3.4)$$

where $E(k_x, k_y)$ is the 2D graphene wave vector and γ is the hopping matrix element ($\approx 3\text{eV}$). Graphene exhibits a semi metal behavior as the conduction and valance bands touch at 6 points, defining the Brillouin zone and the Fermi surface. Carbon nanotubes being rolled graphene sheets, the periodic boundary conditions require to quantize the wave vector in the circumferential direction, which can take only a set of values satisfying:

$$\vec{k} \cdot \vec{C}_h = k_x C_{hx} + k_y C_{hy} = 2\pi v \quad (3.5)$$

where v is a non-zero integer. The linear relation between k_x and k_y imposed by this equation defines vectors in the 2D projection of the band structure of graphene (Figure 3.6). These lines form the one-dimensional energy bands of carbon nanotubes, and the fact that whether or not these lines intersect the Fermi points of graphene will dictate the metallic or semiconducting properties of CNTs. Formally, by combining 3.4 and 3.5 and expressing C_x and C_y as a function of (n, m) , the boundary condition expressed above leads to the metallicity condition:

$$|n - m| = 3l \quad 3.6$$

In case of semi-conducting nanotubes, the two lines coming the closest to a Fermi point define the band gap, given by:

$$E_g = 2d_{C-C}\gamma / d_{CNT} \quad 3.7$$

where d_{C-C} is the C-C bond length (0.142nm) and d_{CNT} is the nanotube diameter. According to this equation, semiconducting CNTs of diameters close to 1nm would for instance have a band gap around 0.8eV.

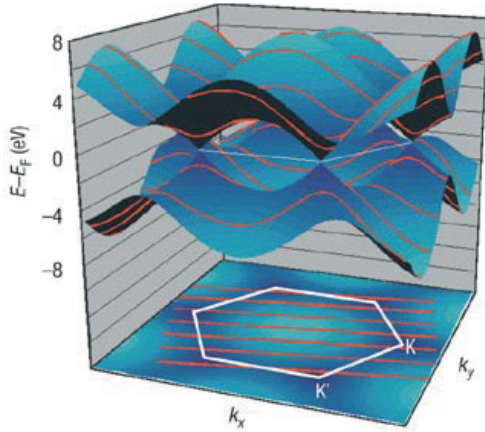


Figure 3.6. The electronic structure of graphene, calculated with a tight-binding model of π electrons, with the projected Brillouin zone. The valance and conduction bands meet in 6 Fermi points. The interactions between the quantized wave vectors and the Fermi points define the metallic or semiconducting properties of CNTs. Adapted from Avouris *et al.*^[98].

This model is based on the simple π -orbital approximation of graphene where the σ and π orbitals do not interact. However, curvature induces a small band gap even for CNTs satisfying eq. 3.6, which is the reason why they are often called semi-metallic. Indeed unlike in graphene, the circular curvature causes a hybridization of the σ and π orbitals, which has a non-negligible effect on the electronic properties of small diameter CNTs. In such tiny cylinders, the σ orbitals along and perpendicular to the axis are not identical and can be slightly out of plane with the π orbital even more delocalized, resulting in a broken planar symmetry and in a partial mixing of the σ and π states^[99]. The band gap of quasi-metallic nanotubes scales inversely with the square of the diameter: $E_g \propto 1/d^2$. Compared to the previous example where a semi-conducting 1nm CNT has a calculated band gap close to 1eV, a similar semi-metallic CNT would have a band gap of only 40meV.

One third of SWCNTs are purely metallic, a second third are semiconducting with quasi-metallic behavior and a last third are large band gap semiconductors. However, one now has to consider the whole CNT family and to describe the properties of MWCNTs or SWCNTs bundles. How does an armchair nanotube behave inside a MWCNT or in a SWCNTs bundle? Is it still truly metallic and how in general do

CNT-CNT interactions affect their properties compared to the isolated equivalent nanotubes?

It has been shown by STM that for armchair CNTs in a bundle, the wall-wall interactions induce a small band gap of about $0.1\text{eV}^{[100]}$ by lowering the symmetry. At the opposite, bundles preserving the original CNTs symmetry don't exhibit such a pseudogap opening^[101]. Inside a MWCNT, the π -orbitals odd to the surface also induce weak interactions between the walls of the concentric nanotubes that may also induce a loss of symmetry. Nevertheless, in case of semiconducting CNTs, intershell coupling tends to reduce the observed band gap by charge transfer from one tube to another.

The whole MWCNT family is considered as a zero band gap metal. Indeed, with one third of the SWCNTs being metallic, the statistical probability of having at least one in a MWCNT quickly rises with the number of walls. In addition, all semiconducting individual CNTs inside a multiwall system tend to be semi-metallic because of reduced band gaps with larger diameters and π -electron transfers between the shells.

All the previous discussion relies on structurally perfect and infinitely long CNTs, when realistic nanotubes are only rarely defect-free. The presence of heptagons or pentagons and of atomic vacancies or doping is susceptible of modifying the pseudo-hexagonal lattice or chirality, and hence the related metallic or semiconducting behavior. Similarly, the structure of the ending tips can also contribute to electronic properties differing from the theory.

CNTs hold promise as nanoscale contacts and interconnects mainly because of their current carrying capabilities and low resistance properties, due to ballistic transport, which could possibly overcome a major issue in classical nanoelectronics, the electrical breakdown of nanoscale wires. Indeed, metallic SWCNTs have been measured to be able to carry up to $10^9\text{A}\cdot\text{cm}^{-2}$, 4 orders of magnitude higher than for metallic nanowires^[102]. In a defect free metallic CNT where there is no carrier scattering or any kind of energy dissipation, the transport is ballistic and the only current resistance is the quantum resistance, governed by the number of conduction channels. The uppermost theoretical conductance limit G between two ohmic contacts is independent of the CNT length and is twice the conductance quantum G_0 because armchair metallic CNTs present two quantum channels at the Fermi energy:

$$G = 2 \cdot G_0 = 4e^2 / h = 1 / 6.5k\Omega \quad 3.8$$

The quantum resistance R_Q ($R_Q = 1/G_0$) arises from the fact that there is only a small number of discrete states that can conduct current in the CNT that are at the Fermi

levels of the continuous states of the metallic contacts, hence limiting the current transport.

In practice, ballistic motion in metallic CNTs can be achieved over lengths of several hundreds of nanometers, from which the carriers will reach the diffusive limit of transport because of topological defects or electronic coupling that induce backscattering and reduce the probability of conduction of the transmission channels. The real resistance will therefore become proportional to the length considered between the metallic contacts and to the occurrence of transport perturbations. In addition to the necessity to use defect-free CNTs, one of the key parameters in the integration of CNTs into devices is the contact resistance of metal-CNT junctions, which is very specific to these systems because of the low dimensionality of CNTs and the unusual contacts geometries. The contact resistance represents the ability of a carrier to travel between a metallic electrode and a carbon nanotubes and dictates by far the overall performance of a CNT-based device. In case of a metal-metal ohmic contact, the resistance is directly linked to geometrical considerations such as contacting surface, atomic bonding or orbital hybridizations at the junction. In case of a metal-semiconductor ohmic junction, the barrier height for a carrier to tunnel through is mostly given by the difference between the metal workfunction and the CNT electrochemical potential. It has been indeed shown that metals like Au or Pd often exhibit ohmic properties by contacting the CNTs in their conduction band. The choice of the contacting metal thus plays a crucial role for the resistance value. However, the worst but common case in a semiconducting CNT/metal junction is when the contact has no ohmic behavior but acts instead as a Schottky barrier with a large resistance.

Chemical properties

Because of their outstanding properties described above, CNTs are of wide interests for semiconductors, material science and even medicine. However, integrating them in composites or biological systems for instance often requires functionalization or chemical modification. CNTs can be modified through several ways such as covalent binding to the conjugated π -electrons, non-covalent binding by Van der Waals interactions or adsorption, doping, intercalation, filling of the inner cavity, etc. In all cases, the reactivity control, the purification and the products characterization remains an important challenge in the chemistry of CNTs and new methods are still needed.

The major issue in the chemistry of as-grown CNTs is their insolubility in either aqueous or organic solvents and in general their lack of wettability. CNTs are rather dispersed in solution by strong sonication, which despite causing damages to CNTs, help separate individual tubes from bundles but precipitation and aggregation occur

ineluctably with time. Nevertheless, wetting of CNTs can be partially improved by the mean of functional groups attached to the sidewalls or ends of nanotubes. Those external groups can also be useful as separation tools. For example, a typical well-controlled reaction is the addition of diazonium groups, which can be performed selectively only on metallic CNTs, allowing there further purification^[103].

Chemical groups can be covalently attached in wet or dry conditions through thermal, photo or electrochemical routes. Hydrophilic or hydrophobic groups, alkyl chains, radicals, polymers have already been functionalized on the skeleton. The main source of reactivity arises from the curvature-induced strain of the non-planar geometry of sp^2 carbon atoms as well as the misalignments of the π orbitals on the walls, but defects in the hexagonal structure can also be used as reactive sites. For instance sidewall holes or heptagons at the ends of CNTs can be decorated with oxygenated species like carboxylic groups, which are starting points for many other derivatization reactions^[104]. Covalent modifications of the skeleton induce a localization of the electrons in the bond vicinity, while the electronic behaviors of CNTs are based on the delocalized π -network of graphene. They therefore have a significant effect on the semiconducting or metallic properties.

Non-covalent functionalizations are based on Van der Waals interactions, charge-transfer interactions and π - π stacking, meaning that mostly all polyaromatic molecules, polymers, biomolecules or surfactants are prone to interact and wrap CNTs in a reversible manner. These molecule-nanotube interactions are found to change sensitively the electrical conductance of the bound CNTs, providing promising biosensing applications^[105].

The filling of the inner cavity of CNTs can be useful for many applications such as molecular carriers, nanofluidics, storage, It has been shown that low surface tension liquid could wet the inside of CNTs through an open end and that various other atoms or molecules can fill CNTs as well. Transition metals, inorganic salts, C_{60} and other carbon cages, biomolecules of suitable size have been indeed driven to the internal cavity of CNTs through different mechanisms such as Van der Waals interactions, hydrophobic forces, electrophoresis or capillary forces.

The doping of CNTs can be performed through different mechanisms and doping reactions with electron donors or acceptors are both possible. For both SWCNTs and MWCNTs, it is feasible to insert in the central canal a wide range of molecular species. However it is also possible to intercalate small molecules or atoms in the intershell space of MWCNTs or in the intertubular region of SWCNTs bundles. Finally, another kind of doping is the substitution of carbon atoms with Boron or

Nitrogen atoms through substitution reactions, yielding p or n-doped carbon nanotubes.

3.1.4 Synthesis of Carbon nanotubes

Since their discovery, the synthesis of CNTs has drastically improved and evolved to techniques that allow large-scale production of material along with good quality and diameter control. These methods, which mainly include laser ablation, arc-discharge and chemical vapor deposition, will be detailed individually. The production of CNTs, even in large quantity is nowadays a rather common and easy procedure. However, the potential applications often require specific CNTs properties, which can be physical requirements, in term of size or diameter but also electronic, thermal or mechanical needs. These properties, as stated earlier are highly dependent on their intrinsic structure, which is directly impacted by the synthesis method and conditions. Diameter as well as length distributions, structure, quality, purity, and yield are all determined by the growth conditions, making the synthesis strategy a crucial choice. While laser ablation and arc-discharge usually yield high quality CNTs, mainly due to the high synthesis temperature, CVD offers a good opportunity for tuning their properties and integrating them into electronic devices.

Arc discharge synthesis

The arc discharge method is considered as the first method employed initially for the synthesis of C_{60} fullerenes and later for carbon nanotubes by S. Iijima^[106]. This technique is an excellent method for the production of both low-defect SWCNTs and MWCNTs, possibly at the gram scale, with a very high cristallinity and narrow size distribution. The major drawbacks are the tendency of bundle formations and the need for further purification due to the parallel formation of graphitic particles, fullerenes and amorphous carbon and the eventual presence of metallic catalyst particles.

For the synthesis of CNTs by arc discharge, two pure graphite vertical electrodes in a low-pressure atmosphere of inert gas are used to generate a dc arc discharge. Such a high current, typically around 100A, ignites a plasma that evaporates the anodic carbon (Figure 3.7). The distance between the two electrode tips is kept at a constant value, typically around 1mm while the anode is consumed and its size reduces. The evaporated carbon then condensates in the form of CNTs, fullerenes, multilayered particles or amorphous carbon and deposit as soot on the top of the cathode tip and on the cold chamber walls. The temperature involved in such a process is close to the sublimation temperature of graphite, around 3000 to 4000°C. The synthesis of SWCNTs by arc-discharge requires doping of the anode graphite rod with catalytic metals and was discovered by two independent groups that used Fe and Co as

catalyst^[96,107]. Whilst MWCNTs are rather confined on the cathode deposit, SWCNTs are mostly found on the chamber soot. In both cases, large-scale production is possible by optimizing the growth conditions^[108,109]. The critical parameters in arc discharge are the distance between the rod tips, the arcing current intensity, the gas pressure and mixture as well as the catalyst nature and doping quality. They affect the CNTs properties and growth yield. The separation and purification of CNTs from the by-products is usually carried out in post synthesis treatments such as thermal or acidic oxidation^[108,110].

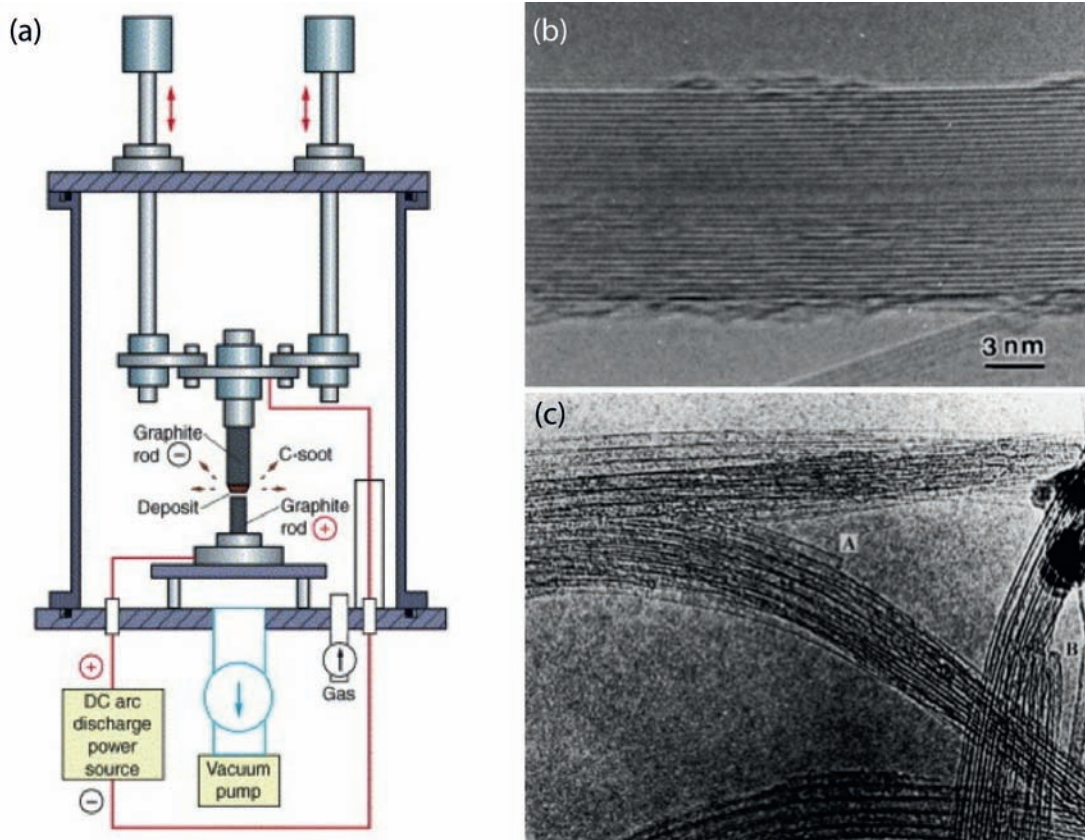


Figure 3.7. (a) Schematic picture of an arc-discharge setup^[111]. TEM micrographs (b) of a 15-wall CNT with an inner diameter of 1 nm^[112] and (c) of SWCNTs bundles^[113] produced by arc-discharge.

Laser ablation synthesis

The production of CNTs by laser ablation is similar to the arc-discharge technique as it involves the condensation of carbon materials originating from a solid carbon source. In the laser ablation method, an intense pulsed laser is used to vaporize and to ablate a carbon target in an inert atmosphere and at high temperature (Figure 3.8). It usually takes place in a tubular furnace, through which an inert gas flows and carries the evaporated material. A cold copper collector is placed down the target, where carbon nanotubes get deposited. In such a process, graphitic and fullerenes co-products are also formed. Whilst a pure graphitic source yields MWCNTs^[114], graphite targets doped with metallic catalyst such as nickel and cobalt yield very high

quality SWCNTs^[97]. However, the contamination by metal nanoparticles is a major drawback. Just as for arc-discharge, the narrow diameters distribution of the produced SWCNTs induces the formation of ropes of closely packed individual SWCNTs in hexagonal crystal, usually in the range of 5 to 20 nm with micrometer length.

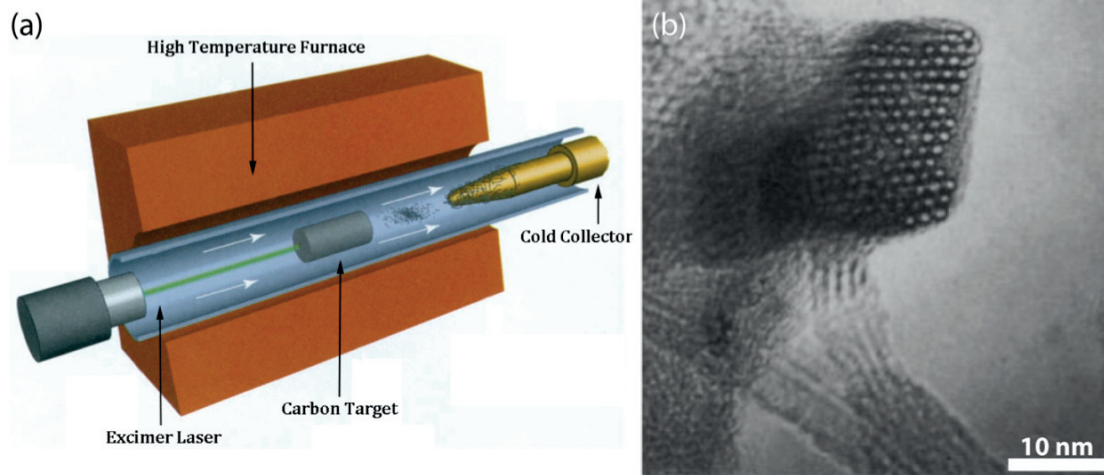


Figure 3.8. (a) Schematic representation of a laser ablation system for CNTs synthesis, adapted from Yakobson^[115]. (b) TEM micrograph of a single rope of SWCNTs made by laser ablation of a carbon-cobalt-nickel target at 1200°C^[97].

The quality and yield of the CNTs depend on the furnace temperature that can vary in range of 800 to 1200°C. At 1200°C, the CNTs are almost defects free and the number of defects increases with lower temperatures while the yield increases with increasing temperature. The laser operation mode and wavelength, the nature and pressure of the gas flow are other critical parameters that require a fine-tuning.

Chemical Vapor Deposition (CVD) synthesis

A full chapter is dedicated to this subject as CVD synthesis of carbon nanotubes is at the heart of this dissertation. CVD is a very powerful method for the growth of all kind of carbon fibers and filaments, which can be fibrils, MW or SWCNTs in bundles, ropes or individual configurations. It is the technique the most compatible with nanoelectronics as it allows a broad range of customization and tuning of both properties and structure of CNTs. Whereas arc-discharge or laser ablation where the CNTs are collected in cotton-like deposits and often require post-synthesis purification, CVD makes possible the growth of CNTs on almost any substrates, a substantial advantage for many applications where they can be used “as-grown”.

In a CVD process (Figure 3.9), catalyst materials, usually transition metals in the form of nanoparticles, are heated up to high temperatures in the range of 400 to 1000°C in a tube reactor. At some point, a gaseous hydrocarbon source is flowed and decomposes over active catalyst particles to yield CNTs through mechanisms that will be

explained later in paragraph 3.1.6. The reaction may last from seconds to hours and the products are either collected on the reactor wall or on substrate surfaces after cooling. The chemistry behind the nanotubes formation is not yet fully understood and still subject to debates but is fundamental to improve the growth conditions. In spite of the relative experimental ease of CVD, several parameters have nevertheless to be carefully optimized. The yield and quality of the products are affected by the choice of the carbon feedstock, growth temperature, flow conditions, substrate and by the catalyst nature and properties.

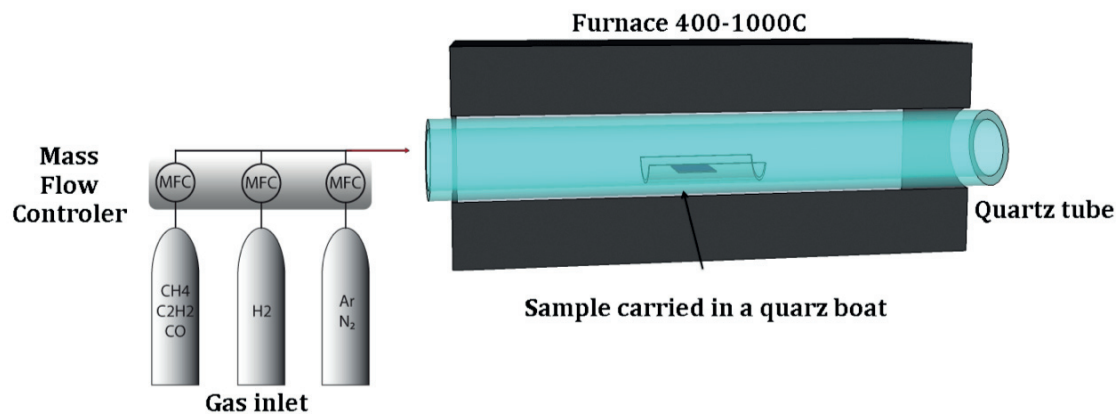


Figure 3.9. Schematic of a typical CVD apparatus. A hydrocarbon source, eventually carried by an inert gas along with reducing agents decomposes over catalyst particles heated at high temperature to produce CNTs

Despite the difficulty of synthesizing low-defect MWCNTs, the CVD method can be effectively used for individual to large-scale of MW or SWCNTs production, high perfection and custom diameter SWCNTs synthesis, nano to centimeters long CNTs synthesis, vertical, horizontal, aligned, suspended, *etc*, CNTs synthesis and is therefore the most versatile technique among all (Figure 3.10).

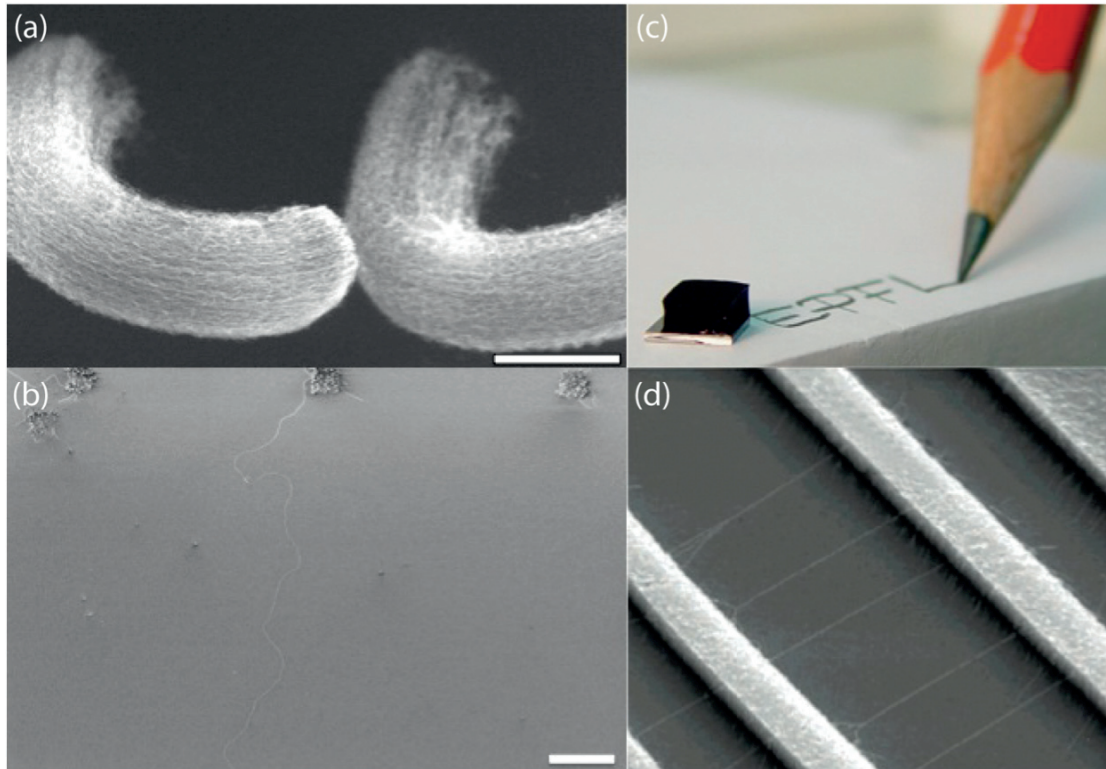


Figure 3.10. Different CVD products. (a) MWCNTs synthesized by oxidative dehydrogenation of C_2H_2 with CO_2 ^[116,117]. Scale bar: 5 μ m. (b) An individual CNT synthesized from a patterned $SiO_2/Mo/Co$ catalyst island by ethanol CVD. Scale bar 10 μ m. (c) Carpet of vertically aligned MWCNTs by basic treatment of the Al_2O_3 substrate and water-assisted ethylene CVD. (d) SWCNTs suspended between silicon structures. (a-c) Products synthesized at EPFL-LPMC. (d) Adapted from Dai *et al.*^[118].

3.1.5 CNTs in nanotechnology - synthesis challenges

The extraordinary properties of CNTs make them promising in many applications as bulk materials or as individuals. Incorporation and dispersion of CNTs into polymers and plastics can provide these new composites with enhanced electromechanical properties at low CNT loading percentages^[119,120]. Bulk quantities have also been proved as powerful hydrogen storage media^[121,122], supercapacitors and actuators based on CNT electrodes^[123], and for field-emission electron sources^[124,125]. On the other hand, individual SWCNTs have been long heralded as outstanding central elements for downsizing nanoelectronic devices and for field-effect transistors^[126,127]. Finally, their unusual dimension and high aspect ratio combined to unique mechanical properties welled up a lot of interest for sharp sensors and probes based on CNTs^[128-130].

Despite that working prototypes have been successfully built for most of these applications, many challenges have to be overcome to exploit the new possibility offered by CNTs outside of the research area. For applications requiring CNTs in bulk quantities, an efficient growth method for high purity and quality synthesis at larger-scale is still missing. Current techniques often yield CNTs with a fair amount of

impurities, which further require a post-purification, source of defects and structural modifications, and increase the final cost. Large-scale synthesis of low-defect multi-walled nanotubes is still lacking and SWCNTs can only be produced in small quantities, which make them very expensive.

For electronic devices based on carbon nanotubes, major issues have to be faced as well. First of all, none of the current synthesis techniques give a control over the products chirality, and all applications requiring specific electronic properties, i.e. metallic versus semiconducting, can not be scaled up to mass production. Second, despite the high theoretical current density carrying capability of CNTs, the usual high contacts resistance annihilates this advantage. Finally, aiming to manipulate individual CNTs to build nanometer-sized electronic devices require conjugating synthesis to nanofabrication methods in order to assemble and organize such circuits, which again go against processes scale-up and cost effectiveness.

A lot of efforts have been focused on the catalytic chemical vapor deposition of CNTs, which is now the most encouraging method for both macro and nano-applications of CNTs. As of today, large quantities of MWCNTs with tuned properties can be produced at a reasonable cost. A lot of progresses are being made to improve the products quality and major breakthroughs are expected in the near future. Then, CVD is the most suited method for controlling both the location and orientation of nanotubes on a surface. Indeed, by patterning catalytic nanoparticles, CNTs can be grown from specific locations, which conjugated to self-assembly forces (Van der Waals, electric fields) make feasible the construction of arrays of nanotubes at the wafer-scale.

3.1.6 Focus on Chemical vapor deposition

Using carbon nanotubes as applied materials requires homogeneous properties and hence a perfect synthesis reliability. How the CVD growth conditions are chosen sets the product properties. For instance, inhomogeneous catalyst sizes yield broader diameter distributions compared to well-defined nanoparticles, while the structural quality is more affected by the synthesis temperature or gas reactivity. On the other hand, the synthesis yield and CNTs length can be altered by the catalyst poisoning or flow conditions. The following subchapters summarize the growth of carbon material by CVD and detail the individual aspect of importance involved in such a process.

Growth mechanism

In a catalytic CVD process (CCVD), a hydrocarbon vapor precursor decomposes over metal catalyst. Hence, the growth of carbon nanotubes by CVD is usually carried out in two steps where the preparation and eventual patterning of such catalysts usually

constitute a whole procedure prior to the CVD growth itself. In some techniques, the formation of the catalyst particles takes place within the reactor, such as for volatile organometallic species that undergo self-pyrolysis in the gas phase^[131], a method named *floating catalyst CVD*.

Typically, the most popular catalysts are first row transition metals like iron, cobalt, and their alloys in the form of nanometer sized particles. However, second row metals as well as noble metals have also been found to catalyze the CNTs growth under particular conditions^[132,133]. The CCVD method can be seen as a reaction where a catalyst lowers the energy and thus the required temperature for the cracking of a hydrocarbon source into carbon and hydrogen. In the past 20 years, the growth mechanism and role of the catalyst have been extensively studied but is, to date, still subject to controversy and the published models are often contradictory.

Proposed first by Baker et al^[134], the most widely accepted mechanism involves a decomposition-diffusion-precipitation reaction (Figure 3.11): (i) the decomposition of the hydrocarbon feedstock is initiated at the surface of active catalyst particles. This decomposition is in competition with its corresponding self-pyrolysis reaction in the gas phase. (ii) The carbon atoms subsequently dissolve and diffuse into the catalyst material until saturation, while hydrogen flies away. This is supported by the uniformly high solubility and diffusion rate of carbon in catalytic materials at high temperature, and especially in transition metals. (iii) when the supersaturation point is reached, carbon starts to precipitate and crystalize as solid tubular structures at the surface of the catalyst. The size of the nanoparticles therefore dictates the diameter of the CNTs, a correlation that will be developed later in the paragraph on the Influence of catalyst properties.

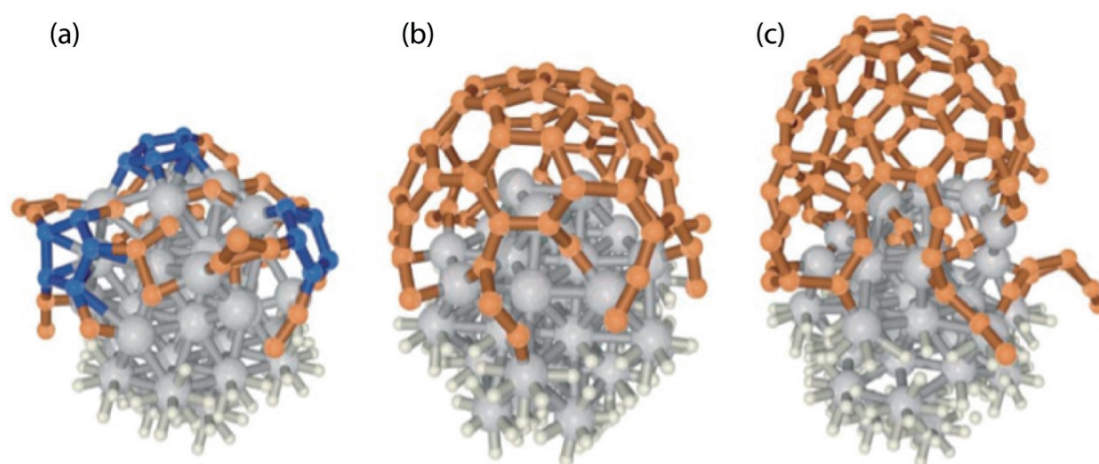


Figure 3.11. *ab initio* molecular dynamics simulation of the early stages of the formation of a SWCNT on a 1nm Fe nanoparticles proposed by J.Y. Raty *et al.*^[135]. (a) After diffusion and precipitation of C atoms on the metal surface, the first hexagons and pentagons (in blue) are formed. (b) and (c) Snapshots of the growth simulation.

From there, two growth modes have been observed and can be differentiated: the *tip-growth* and *base-growth* mode, also known as *tip and root growth*, depending on the surface-catalyst interactions and if whether or not the nanoparticles remain on the surface while the CNTs elongate or not (Figure 3.12).

For strongly interacting substrate and catalyst, it is assumed that the synthesis mode is a *root growth*^[136,137] in which the catalyst stays the whole time anchored to the surface and the CNTs grow from the particles apex with a close-end. In such a mode, the carbon dissolves and diffuses into a particle until a closed dome forms farthest from the surface. The carbon then keeps dissolving on the side of the particle and diffuses upward where the initial dome extends into a cylindrical structure. The CNTs therefore grow from the root. In contrast, for weakly interacting substrate-catalyst pairs, which is often the case with nickel as catalyst, *tip-growth* mechanisms take place where the CNTs grow from the tip^[138-140]. During the elongation process, the catalyst particles are lifted-off by the growing nanotubes and carried along at the tube ends. The hydrocarbon source decomposes on top of the catalyst particles and diffuses downward to the bottom where it crystallizes and pushes the particles off the substrate. One end of the CNTs is therefore anchored to the surface with the other end bound to the catalytic particle that moves with it. The reaction continues with the CNTs growing from the tip.

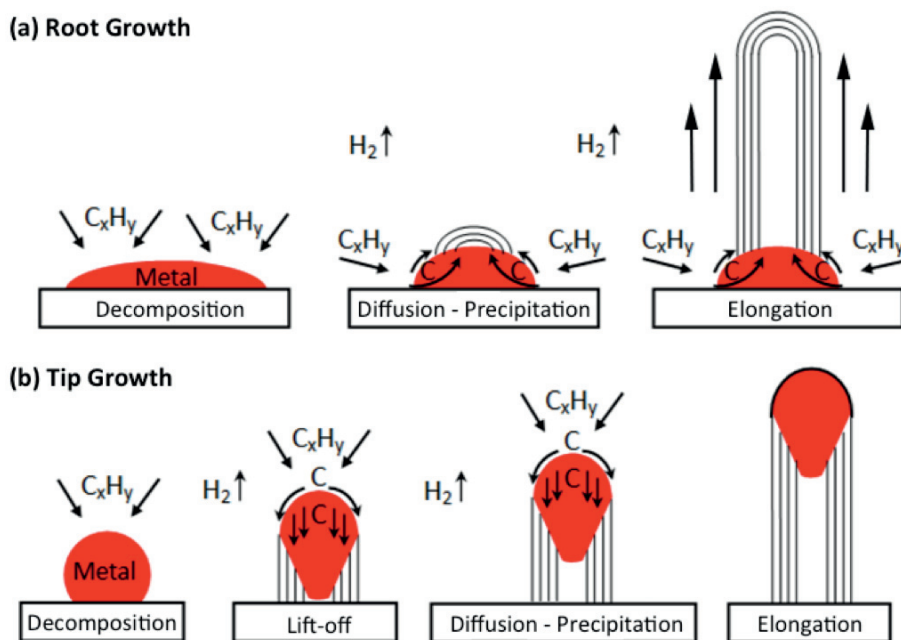


Figure 3.12. Schematic of (a) tip growth and (b) root growth mechanism in catalytic chemical vapor deposition for CNTs synthesis.

There are many open questions behind this hypothetical mechanism. The first would be about the physical state of the catalyst nanoparticles. For most transition metals,

the melting point is around 1500°C but below 10nm, it decreases abruptly. In these mechanisms, the melting temperature of the catalyst is crucial, but the fact that catalysts are nanosized implies that their melting temperature is unknown and cannot be obtained from phase diagram. The catalyst can therefore be either in a liquid or solid state depending on their relative size, without even considering shape modifications at high temperature. Moreover, as the tip-root growth mechanism closely links the tubes diameter to the nanoparticles size, it would appear that MW and SWCNTs are grown from different mechanisms with catalyst in different physical states as bigger particles have higher melting temperature. About the growth mechanism itself, it is not obvious that a temperature gradient can occur in 1-2nm particles but one may also have to consider a carbon concentration gradient. It is also not known whether the carbon diffuses on the surface or inside the nanoparticles. It has been suggested that the nanoparticles could take a modeling shape, such as cylindrical or pear-like shapes, that could, through a surface diffusion mechanism, act as a template^[141]. Finally, it is still commonly questioned what chemical state the actual catalyst specie is in. Is it the metallic form or do natural oxides or transitory carbides also act as catalyst? Because the full mechanism is still unclear, many crucial aspects remain not understood: How does the yield depend on the catalyst? How does the catalyst material get poisoned and how to avoid it for getting infinite CNTs length? Only empirical observations, often contradictory have been proposed so far and more research is still needed.

Influence of catalyst properties

The choice of the catalyst is with no doubt the most important parameter in CVD synthesis of CNTs as it directly determines the quality and nature of the products as well as the growth rate and yield.

The first and main crucial parameter is the size of the catalyst nanoparticles. It is believed that there is an existing correlation between the nanoparticles size and products average diameter and wall number, and that there is an optimum particles size window within which CNTs can be obtained. Several groups reported studies in which the predetermined size of the catalyst was closely related to the products diameter distribution^[142-144]. These observations are the main motivation for, on one hand, the preparation of catalysts with extremely narrow size distribution to reduce in the same way the diameter range of the products, and on the other hand, the preparation of the smallest active catalyst for the synthesis of SWCNTs.

It is once more unclear how the size of the catalyst material relates with the product properties. From the *tip-root* model, it is believed that 1-5nm nanoparticles yield primarily SWCNTs and DWCNTs with a progressive increase of the number of walls as the particles size increases. However, this can not explain that SWCNTs bundles

have been synthesized from bigger particles^[145], where the individual tubes have smaller diameter than the catalyst, and how in general such bundles are produced. In the same way, not always does the diameter of the products relate accordingly to the nanoparticles size. Therefore, this suggests that the real catalyst species may be different than the predetermined ones and that different phenomena may occur while heating nanoparticles to high temperatures. The catalyst material may diffuse on the surface, merge with others to yield bigger particles, split into smaller entities because of the surface roughness, or even partially evaporate. In particular, it has also been suggested that several sharp edges in a single nanometer-sized particle could act as nucleation centers^[146], possibly resulting in bundles formation with individual SWCNTs having smaller size than the actual catalyst. More than the catalyst nanoparticle sizes, it is therefore the size of these nucleation sites that one should try to control. For nanoparticles, the size of the nucleation center and hence the diameter of the products may vary from the size of the smallest SWCNTs ever synthesized (i.e. 0.4nm^[147]) to the particle diameter.

Aside the size parameter, which roughly dictates the diameter and number of walls of the product, the catalyst nature is also of extreme importance for the reaction rate and yield. For a given carbon feedstock, different catalysts can have different activities, in term of lifetime, growth rate and products quality. No general rule can be well established as published results often exhibit contradictory trends. However, several experimental observations showed that iron is usually the most active mono-metallic catalyst with the highest CNTs density compared to cobalt and nickel but that cobalt yields improved CNTs quality with better graphitization and less amorphous carbon deposit^[148-153].

Pure metals can also be conjugated with other elements, for instance other 3d metals or molybdenum. Bimetallic catalyst alloys are indeed more successful in decomposing the carbon source from lower temperatures because they have lower melting point and higher carbon solubility, and give higher quality CNTs and yield^[154-158]. Moreover, the addition in small quantities of molybdenum to cobalt and iron catalysts has been reported to enhance their respective activity and products selectivity, while Mo doesn't exhibit any catalyst activity itself^[155,159,160]. Experimental details will be discussed in section 3.3.2 as Mo/Co has been widely used for the synthesis of individual SWCNTs.

Catalyst support

When using a non-supported catalyst, a powder is placed in a quartz holder and loaded into the CVD reactor. In all other cases, a substrate is usually used. The influence of the catalyst support has been widely studied by comparing the CVD

products of reactions carried out with the same catalyst but different supporting materials. It has therefore been observed that the support plays an essential role in the products and reaction properties. Popular supports are for instance Al_2O_3 and SiO_2 , which are known to give good catalyst activities. At the opposite, a poor substrate choice, like silicon, can lead to reduced growth rate or yield.

First of all, as stated above, the catalyst-support interaction strength is believed to dictate the growth mechanism of CNTs, tip growth for poorly interacting pairs, and root growth for strongly interacting ones. Strong physical interactions, through electrostatic forces or high roughness, have another favorable effect as they prevent the catalyst from diffusing on the surface and sintering into bigger particles. Thus, they stabilize the nanoparticles size and shape and yield more consistent CVD products. High surface roughness substrates are also known to create more nucleation sites and an enhanced catalyst activity.

Chemical interactions between the support and catalyst nanoparticles, through acid/base and oxidoreduction reactions, change the catalytic activity as well by modifying the catalyst electronic properties. For instance, substrates increasing the catalyst electronic density strengthen the electronic donation to the carbon precursors, which enhances its decomposition activity^[161].

The direct interaction between the carbon precursors and support has also been shown to have a strong influence on the growth rate. Magrez *et al.*^[162] showed that tuning the acid-base character of the alumina support yield CNTs with lengths 3 order of magnitude higher than for conventional Al_2O_3 . With a basic pretreatment, they assess that the carbon source molecules are transformed by the substrate into polyaromatic fragments, which diffuse then to the catalyst nanoparticles and incorporated in the nanotube structure.

Carbon feedstock

Numerous carbon sources can be used for CVD synthesis of carbon nanotubes, including methane, acetylene, ethylene, carbon monoxide, methanol, ethanol and benzene. Gaseous hydrocarbons can be flushed as pure gas or diluted with an inert gas. Liquid carbon precursors may be used as well, in which case a noble gas carries the carbon vapors. Mixtures of carbon sources may exhibit interesting properties as well.

A major drawback in CVD reactions is the self-pyrolysis of the carbon source and the associated amorphous carbon deposition and catalyst poisoning. High-temperature processes require more stable gas, while more reactive gas can be used at lower temperatures. Methane is the most stable hydrocarbon with a high resistance to self-pyrolysis up to 900C, which make it suitable for SWCNTs synthesis. Self-pyrolysis

can be also lowered with a less concentrated precursor or higher flow rates, which however may go against growth yield and rate.

The choice of the carbon feedstock has therefore to be carefully optimized along with the flow conditions, temperature and pressure, but also with the catalyst and targeted products and the optimum results will always be a compromise between yield and quality.

Temperature

CVD syntheses are performed at moderate to high temperatures compared to the arc-discharge and laser ablation methods, in a range of 450 to 1100°C. MWCNTs can be produced from rather low to moderate temperatures while SWCNTs required higher temperatures, most likely above 750°C, because of their high enthalpy of formation.

Temperature is an important parameter in CVD processes. It may alter the product quality and growth yield. High temperatures may favor higher catalyst mobility and diffusion, leading to greater CNT diameters, or lead to self-pyrolysis of the carbon source. At the opposite, low temperatures may reduce the growth yield because of a low carbon source decomposition rate. There are no clear trends between temperature and catalyst activity, nor between temperature and products diameter as reported studies are often contradictory. As other CVD parameters, temperature requires a long optimization.

Catalyst preparation for CVD synthesis of CNTs

The preparation method of the catalyst in CVD synthesis of CNTs is as important as the CVD parameters as it will define the catalyst properties, and hence, the properties of the products and the yield of the reaction. Even though there are an infinite numbers of preparation methods, this section summarizes the main techniques for nanoparticles definition.

Metal evaporation and sputtering. Evaporation and sputtering are deposition methods widely used in microelectronics in order to obtain homogeneous thin films of amorphous metallic or dielectric materials on a flat substrate. During annealing at high temperature in inert atmosphere, the atoms diffuse over the surface and form nanoparticles islands with the lowest surface energy possible. The size and shape of the nanoparticles directly depends on the initial film thickness and roughness, and on the surface energy.

Metal precipitation. An organometallic catalyst precursor is dissolved in a suitable solvent and mixed with or deposited on a substrate. After solvent evaporation, the substrate usually undergoes thermal oxidation to get rid of the carbon material, yielding supported metal-oxides nanoparticles. The properties of the material depend

on the precursor, aggregation state or dispersion in solution and concentration. Sonication or surfactants are often used for preventing aggregation in solution. This method offers a broad range of possibilities but a low control over the nanoparticles properties and requires a good experience.

Inorganic synthesis of nanoparticles. Nanoparticles are produced by inorganic chemistry and dispersed in solution. A substrate is then coated as for metal precipitation. The properties of the nanoparticles directly depend on the synthesis method, the aggregation prevention, concentration, and deposition technique. A common method is the thermal decomposition of carbonyl complex under reflux for nanoclusters formation^[144].

Pores entrapping. Sol-gel methods are used to fabricate porous materials homogeneously doped with catalyst. The size of the catalyst material is therefore defined by the size of the pores and the CNT density by the pores density and surface area. Closely related methods involve the use of zeolite substrate or silica nanoparticles, which also entrap catalyst particles within their pores and prevent them from sintering. Porous substrates often exhibit aligned CNTs growing with a direction normal to the substrate plane.

Ferropoteins. Ferropoteins are proteins enclosing an iron core of a definite number of iron cations. For example, ferritin, an intracellular iron-storage protein storing about 4500 Fe³⁺, has been several times reported as starting material for CNTs synthesis. Enclosing an iron core of 3-5nm, they can easily be adsorbed on a substrate. After thermal oxidation, they release iron clusters with a very narrow size distribution, which catalyze the formation of small-diameter SWCNTs^[163,164].

All the preparation methods attempt to define as well as possible the desired catalytic particles. These products can roughly be in three different states. (i) they contain a carbon shell, which is usually remove by a thermal oxidation step before CVD. (ii) they are in the oxide form, and are therefore reduced at high temperature with a hydrogen flow. In some cases, the by-products of the CVD reaction also contribute to reduce the oxides to the active state. (iii) the catalyst is already in its active state. However, a native oxide is often to be considered.

3.2 Device fabrication strategy

At large-scales, the integration of CNTs into nanometer-sized electronic circuit remains nowadays an unsolved challenge. Assembling such tiny building blocks together with metallic electrodes requires fabrication approaches that must provide

straightforward controls on the positioning and orientation of CNTs onto a surface. Two general and opposite strategies are usually used.

First, CNTs from dispersed solutions are deposited and assembled in a directed approach on a surface. A typical example would be the dielectrophoretic deposition of individual CNTs between lithographically defined electrodes^[165,166]. However, all methods involving dispersed CNTs exhibit the same experimental issues as those associated to CNTs in solution. In addition to contamination with catalyst material and other carbon species, SWCNTs in solution are usually found as entangled tubes and tend to form bundles, which need to be separated and cut into suitable sizes for device fabrication. This is usually performed by ultrasonication and by using surfactants, which both have several disadvantages. Ultrasonication results in broad length distributions and induces structural defects that affect the overall electronic properties of the final devices. The use of surfactants also induces higher electrical contact resistances and non-ohmic behaviors that should also be avoided. Wet processes therefore exhibit a rather low degree of control and are in need of new techniques for sorting out and purifying CNTs.

Second, CNTs are grown directly on silicon wafers from well-defined catalyst islands and contacted in a next step by lithographic methods or electron beam induced deposition (EBID). These methods offer the advantages (i) to control the location of the islands (ii) to engineer the catalyst and related CNTs properties (iii) to optimize the CVD conditions for the most suited products (iv) to contact as-grown CNTs through lithographic methods.

The CVD synthesis of SWCNTs from pre-patterned catalyst islands is the most suited approach that satisfies the project requirements. As described in chapter 1.4.2, one of the two strategies for ultrafast DNA sequencing is based on CNT-embedded solid-state nanopores. In such a device, an individual small-diameter SWCNT lies on a Si_3N_4 membrane and is contacted with metallic electrodes. It is finally cut into two nanoelectrodes while the nanopore is being drilled. The key approach for a mass production of such a device relies on the CVD synthesis of isolated SWCNTs with location control. The associated CVD process must (i) yield in a reproducible way several micrometers long individual SWCNTs, of small diameter and metallic (ii) generate a negligible amorphous carbon deposition to preserve a clean surface and high purity products (iii) be carried out at moderate temperatures to preserve the Si_3N_4 layer (iv) be compatible with up-scaling. The location control, preferably combined with an orientation control is necessary so that CNTs can be reliably contacted with metal electrodes by lithography and metallization

3.3 Patterned growth of isolated SWCNTs by ethanol CVD

Patterned growth of CNTs stands for a site-selective growth from patterned catalyst islands. The related fabrication process relies on two distinct steps. First, catalyst nanoparticles are deposited on specific location of the substrate. Then, the CVD growth is carried out and CNTs only extend from the pre-defined sites.

The most popular techniques for patterning substrates are lithography-based processes, which allow to selectively depositing a wide range of materials, through thin films deposition, spin or dip coating of liquid precursors and resist removal^[167,168]. Using lithography makes possible the definition of islands at a sub-micrometer scale, only limited by the technique employed.

Aside structured resists, other patterning techniques have been investigated for controlled growth of CNTs. In micro-contact printing, a PDMS stamp is first wetted with a catalyst solution, which is then transferred to the substrate by physical contact^[169]. AFM, and in general all scanning probe microscopes, can be also used as tools for patterning substrates with catalyst material, in which case, a liquid precursor solution is used as an ink^[170].

To facilitate the contacting procedure of individual SWCNTs, all patterned growths were realized by EBL, using dedicated alignment marks and standard MMA/PMMA resists.

Figure 3.13 shows the growth of MWCNTs by $C_2H_2-CO_2$ equimolar CVD reaction^[116] from patterned catalyst islands at 550°C, realized according to the following procedure:

Substrate preparation and CVD conditions. The catalyst material is deposited on 12×12mm double-sided polished p-doped Si (100) chips with 60 nm SiO_2 and 20 nm Si_3N_4 epilayers. Circular catalytic sites (2µm diameter) were patterned in MMA/PMMA (120/150nm) by EBL. After development and plasma descum, a 2nm thick Fe film was deposited by thermal-evaporation, followed by lift-off. Substrates were first calcinated in air at 500°C for 30' to remove any resist or organic residuals. Then, a 10' annealing in argon (45l/h) at 550°C is performed, immediately followed by the introduction of $C_2H_2-CO_2$ in an equimolar ratio (0.5l/h both in 45l/h Ar) for 10min, after which pure argon is flushed for 5'. Samples are finally cooled down to room temperature in inert atmosphere.

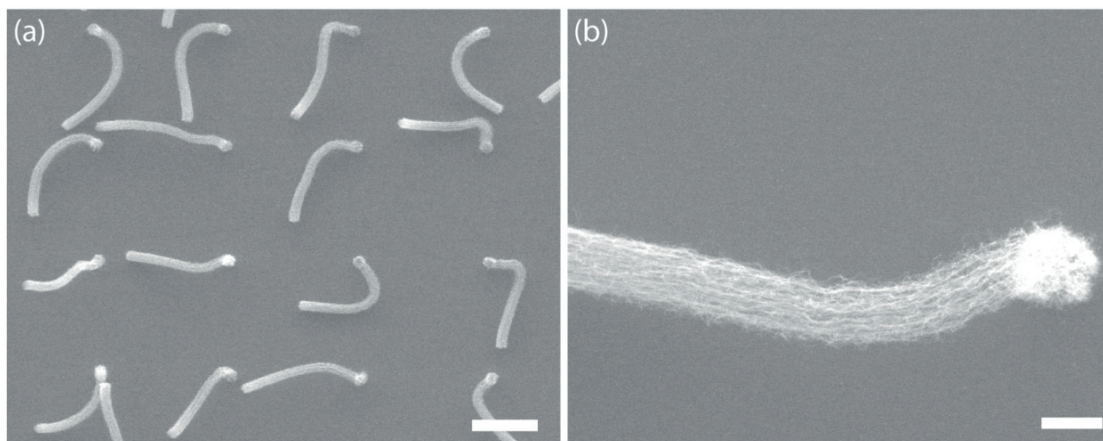


Figure 3.13. Patterned growth of CNTs using lithographic techniques. (a) Catalytic sites are defined by EBL in MMA/PMMA, followed by thermal evaporation of a 2nm Fe film and lift-off. Well-localized CNTs are grown by equimolar $C_2H_2-CO_2$ CVD reaction at 550°C. Scale bar: 20 μ m. (b) SEM image of MWCNTs bundle extending from a single island. Scale bar: 2 μ m.

In preliminary experiments, the exceptional yield of the equimolar reaction was used to demonstrate the possibility of localizing the growth of CNTs by EBL and CVD at moderate temperatures. The high reactivity of acetylene makes it unsuitable for higher temperature CVD growth of SWCNTs because it easily undergoes self-pyrolysis. However, the CVD conditions and catalyst properties have been optimized and integrated within a process compatible with microfabrication.

3.3.1 Choice of the CVD conditions

The CVD conditions have been optimized considering the project requirements. In particular, the constituent of the carbon feedstock and the associated temperature must induce a clean surface state after the growth process, especially in term of amorphous carbon deposition to preserve the ability of electrically address individual CNTs. The amount of amorphous carbon deposition is also crucial for the yield of the reaction and length of the CNTs by affecting the catalyst activity.

Additionally, low to moderate temperature growths have been rather studied to preserve the properties of the Si_3N_4 epilayers (see chapter 3.4.2). Different catalysts have been studied, such as thin films of 3d transition metals, in particular Fe, Co and Fe_2Co films respectively deposited by thermal, electron beam evaporation and sputtering, and liquid catalyst precursors, more specifically, nanoparticles-supported Mo/Co and Mo/Fe catalyst.

The growth of CNTs at moderate temperatures (<700°C) requires highly reactive carbon feedstocks, which in counterpart are unlikely to produce SWCNTs. In addition, very reactive carbon sources tend to produce a non-negligible amount of amorphous carbon. On the other hand, methane is a common source for CVD

synthesis of SWCNTs but requires elevated temperature ($>900^{\circ}\text{C}$) because of its high chemical stability, which may be deleterious to our substrate.

As amorphous carbon-free CVD reactions are crucial for nanoelectronic application, the use of diluted carbon sources, such as ethanol CVD, is a very interesting alternative for the synthesis of high-purity SWCNTs. Compared to methane that is used at high partial pressure (100% CH_4 , $900\text{-}1000^{\circ}\text{C}$), ethanol vapors are diluted to low-concentration in a carrier gas, usually argon. Moreover, ethanol CVD has also been shown to be an excellent carbon precursor for the synthesis of long SWCNTs at moderate to high temperatures ($550\text{-}800^{\circ}\text{C}$)^[132,171-174]. Self-contained water in ethanol is indeed believed to be a useful additive, which preserves the catalyst lifetime by etching the amorphous carbon shell eventually forming around the catalyst nanoparticles. Moreover, ethanol is also known decomposes into highly reactive radicals based on oxygen, which prevent as well catalyst from poisoning^[175].

Ethanol-CVD has constituted the starting point for the optimization of the catalyst nature and properties and the synthesis of individual SWCNTs with location control.

3.3.2 SiO_2 nanoparticles-supported Mo/Co catalyst

For the synthesis of SWCNTs by catalytic CVD, the definition of catalyst nanoparticles with narrow size and activity distributions is crucial. Despite that ultrathin catalyst films deposited by evaporation or sputtering presents the advantage of being fully compatible with nanofabrication processes, the main drawback of such films is the non-homogeneity of the nanoparticles size distribution after thermal annealing, which induces a disparity in the resulting CNTs diameters. Moreover, preliminary tests showed a very low catalyst activity with 0.5-2nm films of Co, Fe or Fe_2Co , which failed in growing horizontal SWCNTs from catalyst islands by ethanol CVD at temperature ranging from 700 to 900°C .

However, the use of binary Mo/Co catalyst has been reported to effectively grow SWCNTs from different carbon sources such as CO and ethanol^[155,171,176,177] and can be adapted for patterned growth of CNTs. Such catalysts have been widely studied, as it appears that in the presence of molybdenum, the selectivity of Co for the growth of SWCNTs is greatly enhanced. Whilst cobalt alone tends to sinter into large nanoparticle aggregates after reduction, which induces the formation of defective MWCNTs, the geometry of bimetallic Mo/Co is stabilized through interactions between Mo oxides and Co^[178,179]. The Mo/Co composition ratio also affects the CNT growth. A high Mo content has been reported to lower the overall catalyst activity whereas a higher Co content lowers its selectivity.

As the supporting substrate also plays an important role in both the purity and yield of the reaction and as Si_3N_4 is not the best material for such purposes, the process described here suggests the use of Mo/Co catalyst nanoparticles supported on silica nanoparticles. SiO_2 is a substrate that is known to improve the CVD yields by participating in the decomposition of the carbon source. Furthermore, the particles size of the catalyst is in such a way well controlled in the mesoporous network formed by the SiO_2 nanoparticles, which prevent the metallic species to aggregate^[171,180-183].

Catalyst preparation. 0.02mmol $\text{Co}(\text{acac})_2$, 0.005mmol $\text{MoO}_2(\text{acac})_2$ and 0.1mmol of SiO_2 (Aerosil 90, fumed silica, specific surface area $90\text{m}^2/\text{g}$, average particles diameter 20nm) is added to 10ml methanol, to obtain silica nanoparticles embedded with Mo/Co nanoparticles in a 0.2:0.05:1 Co:Mo: SiO_2 molar ratio. The solution is stirred overnight and tip sonicated for 10' in ice before use. As the solution can't be stored, it is always prepared fresh the day before CVD.

Substrate preparation. Catalyst material is deposited on $12\times 12\text{mm}$ double-sided polished p-doped Si (100) chips with 60nm SiO_2 and 20nm Si_3N_4 epilayers. In the case of patterned growth, catalyst islands are patterned in 150nm 495K PMMA. A $4\mu\text{l}$ drop of the catalyst suspension is deposited onto patterned or bare substrates at room temperature. After methanol evaporation, substrates are baked at 140°C for 10'. Lift-off of PMMA is performed in acetone at room temperature, after which samples are rinsed with IPA and dried with N_2 . Samples are finally calcinated at 550°C in air to decompose acetates and other organic residues to form an oxide of bimetallic Mo/Co catalyst supported on SiO_2 nanoparticles.

Ethanol CVD. In a "fast heating" approach, the substrates are placed in a quartz boat in the middle of a 1.5cm-diameter quartz tube furnace kept at 800°C and under argon atmosphere (400sccm). Before CVD, the catalyst is reduced in Ar/H_2 (400/50sccm) for 10 min. Then, ethanol vapor is delivered by bubbling argon at 400sccm through a glass vacuum trap containing absolute ethanol (<0.01% H_2O) kept at 0°C (estimated vapor pressure: $11.6\text{mm Hg}^{[184]}$) through a 4-way valve. CVD reaction takes place for 10 to 30', after which the valve is switched to deliver pure argon for 10'. The quartz boat is finally pushed to a cold area, where it cools down in argon atmosphere.

Characterization. CVD reaction products were imaged in a ZEISS-Merlin SEM microscope operated at 1kV and in a PHILLIPS-FE-CM300 TEM microscope operated at 200kV. AFM measurements are carried out in a Bruker Dimension FastScan system in standard ScanAsyst tapping mode. Raman scattering measurements were performed in a LabRam HR confocal Raman spectrometer (incident laser: 532nm, 2.33eV, 0.1mW, spot size < $1\mu\text{m}$).

Figure 3.14 and Figure 3.15 show SEM images of carbon nanotubes grown from Mo/Co-SiO₂ catalyst by ethanol CVD on unpatterned and patterned Si₃N₄ substrates. At the edge of the patterns, individual CNTs grow in random orientations with respect to the flow direction, with an average length of 10 to 30µm, which does not seem to depend on reaction duration as growths from 10 to 40min yield similar products. This suggests a relatively fast growth at the first stage of the reaction followed by the inactivation of the catalyst materials by poisoning. However, millimeter long CNTs can also be observed with a lower occurrence. A possible strategy to lengthen the CNT products is to carry out water-assisted ethanol-CVD, as it has been showed that water molecules may significantly extend the catalyst lifetime and reaction yield^[185].

Studies have reported that a strong gas flow could induce a directed growth. However on our substrates, increasing the argon flow results in a progressive decrease of the reaction yield without evidence of such a behavior.

The presence of SiO₂ was found to greatly enhance the catalyst activity compared to unsupported Mo/Co catalyst nanoparticles. SEM imaging revealed that CNTs mainly nucleate from silica aggregates, which demonstrate that most of the metallic material gets adsorbed on SiO₂. The Co:Mo molar ratio has been long optimized between catalyst activity and selectivity. In agreement with the literature, the presence of Mo in little amount has been found to be determinant for the growth of SWCNTs, while the activity dramatically decreases with higher Mo content, with a good compromise at the ratio described above. By comparison, Fe:Mo bimetallic catalyst yields totally different products. The overall catalyst activity is much lower with ethanol as reactive carbon source and the products are rather onionated or defective MWCNTs. Finally, the reduction in Ar/H₂ before delivering ethanol vapors was found to be not so important for the reaction yield. Although the catalyst material is in an oxidized inactive state after calcination and has to be reduced before CVD, reactions carried out without preliminary reduction put in evidence that the decomposition of EtOH at high temperature clearly produce also reducing H₂ species, which participate in the process, as the catalyst activity remains good.

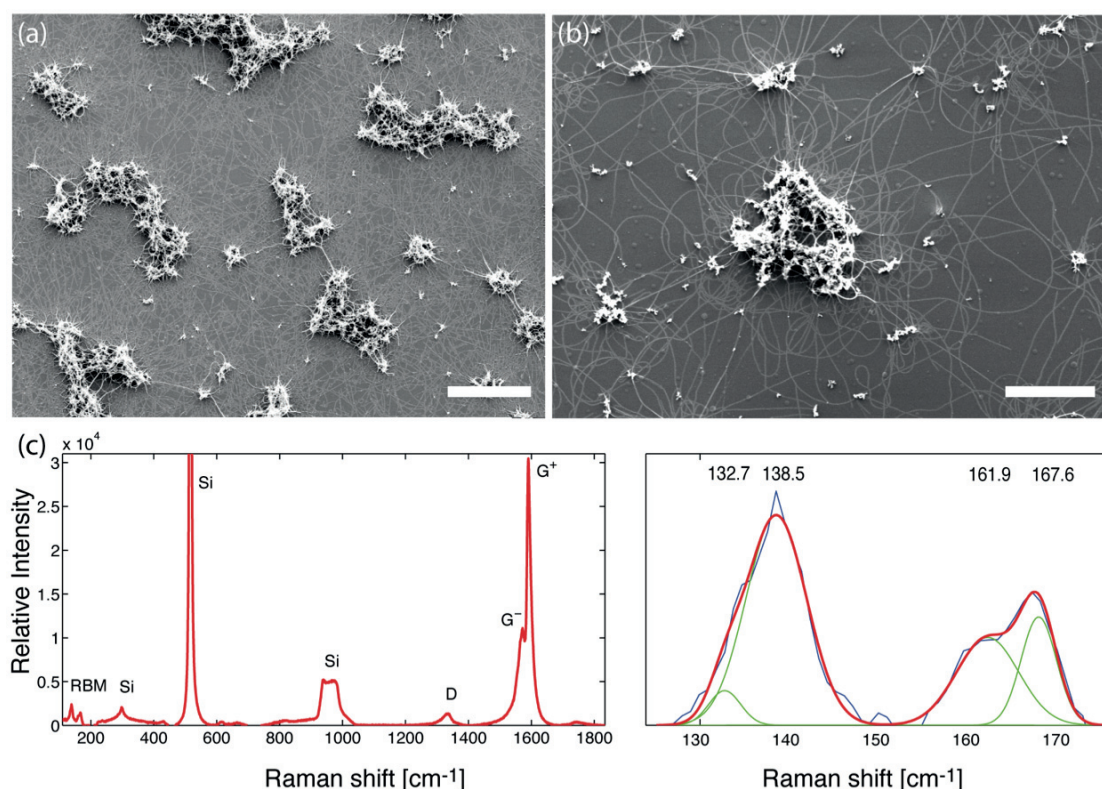


Figure 3.14. Horizontal SWCNTs grown from SiO₂-supported Mo/Co catalyst by ethanol CVD at 800°C. (a-b) SEM micrographs of a non-patterned Si₃N₄ substrates. The catalyst material exhibits a very high activity combined to an excellent selectivity for the synthesis of SWCNTs. Scale bar: 5 μm and 1 μm. (c) Typical Raman scattering spectrum of as-grown CNTs (left) and the corresponding deconvoluted radial breathing mode band (right, 4-peaks Gaussian fit). SWCNTs with diameters in a 1.2-1.8 nm range are usually measured.

The characterization of the CNTs diameter and quality was mainly performed by Raman scattering spectroscopy and confirmed by TEM imaging. Tubes in the close proximity of SiO₂ aggregates are mainly very short and curly MWCNTs that don't horizontally extend on the substrate surfaces. However, longer tubes elongating over large distances are SWCNTs, whose diameters were probed by Raman scattering. A typical Raman spectrum is shown in Figure 3.14, realized on non-patterned substrates. Depending on the initial solution dilution, numerous CNTs are probed with a laser spot size of about 1 μm. Diameters were assessed from the shift of the Radial Breathing Mode (RBM) band, which correlate to one another according to the relationship $d_t = 248/v_{\text{RBM}}$ for SWCNTs^[186]. In all the cases where the G peaks could be observed, the RBM band was also present. The average diameter for SWCNT grown from SiO₂ supported Co:Mo catalyst was measured to be $1.54 \pm 0.06 \text{ nm}$ and $1.67 \pm 0.04 \text{ nm}$ for non-supported Co:Mo, out of respectively 7 and 8 Raman spectra. The G/D ratio, usually in a 20-30 range, confirmed the excellent structural quality of the CVD products (G/D of 24 in Figure 3.14) and a negligible deposition of amorphous carbon.

The experimental ease to pattern substrates with $\text{SiO}_2\text{-Mo/Co}$ catalyst was a considerable asset for the integration of the process within the device fabrication. Catalyst islands were usually patterned as rows of $5\mu\text{m}$ squares at a pitch of $50\mu\text{m}$ (Figure 3.15). The presence of SiO_2 nanoparticles greatly helped in the islands localization that could be imaged by SEM. The position of the catalyst sites is defined with respect to EBL alignment markers with sub-micrometer resolution. Careful lift-off of PMMA yields a perfectly clean surface, which provides an efficient mean for controlling the location of growth. We observed that the initial concentration of $\text{SiO}_2\text{-Mo/Co}$ in methanol plays an important role for patterning the substrate. The islands take up the shape of PMMA patterns for low concentration and well-sonicated solutions, whilst lift-off is more problematic in the opposite case.

The usually curvy shape of the CNTs extending from the islands tends to indicate that the interaction with the Si_3N_4 layer is rather strong, but no kinks are observed, confirming the structural quality of the products. For each catalyst islands, long individual SWCNTs synthesized off the edges are found with an excellent probability, opening the way for the fabrication of electrical circuits based on SWCNTs by direct CVD synthesis on Si_3N_4 , and especially for the fabrication of solid-state nanopores with embedded transverse SWCNT electrodes. Whilst the Raman studies of the CVD products indicate a good selectivity of the catalyst for SWCNTs, it is clear that SEM imaging doesn't provide a sufficient resolution for investigating the number of walls of each individual CNT. It is therefore by TEM imaging before the pore drilling that this is confirmed (see section 3.4.3). In addition, the method presented here can be scaled-up on 4-inch wafers to improve the fabrication rate.

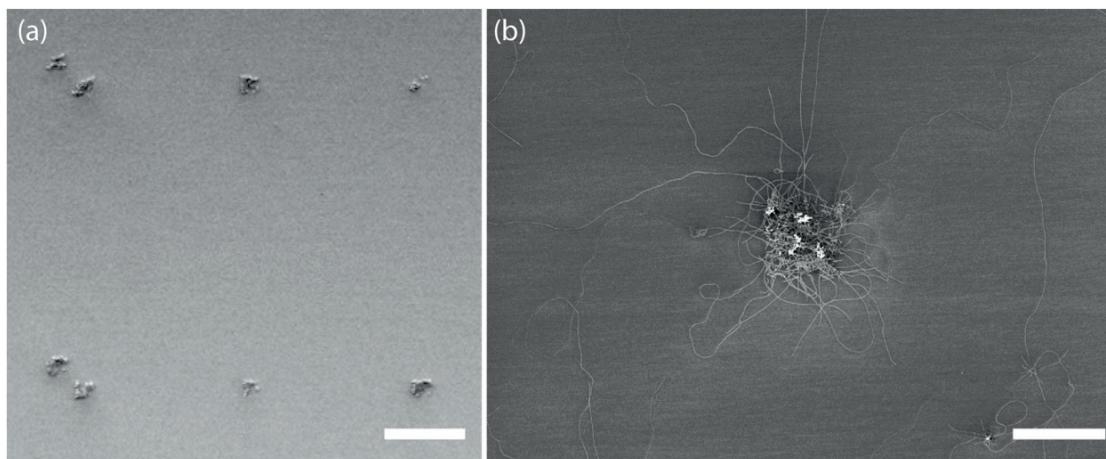


Figure 3.15. Isolated SWCNTs grown from patterned catalyst islands (a) SEM micrograph of a Si_3N_4 substrate patterned with $\text{SiO}_2\text{-Mo/Co}$ catalytic sites. $5\mu\text{m}$ squares at a pitch of $50\mu\text{m}$ are patterned by EBL in PMMA. A drop of catalyst solution is then deposited onto the surface, which yields after lift-off a clean surface with well-localized islands. Scale bar: $25\mu\text{m}$. (b) SEM image of a single $5\mu\text{m}$ catalyst site after CVD. $10\text{-}30\mu\text{m}$ long SWCNTs extend from the edge of the pattern in random orientations from controlled locations. Scale bar: $5\mu\text{m}$.

3.4 SWCNT transverse electrodes embedded nanopores fabrication

We demonstrated in the previous paragraph that isolated single-walled carbon nanotubes could be efficiently grown on Si_3N_4 substrates with location control by patterning catalyst islands by lithographic methods. SWCNTs are valuable options for nanoscale electronics because of their unusual high aspect ratio combined to outstanding electronic properties. In particular, their potential use as transverse electrodes for nanopore-based sequencing brought a lot of attention. When it comes to integrate CNTs into nanoscale electronic devices, the control of the position of target CNTs is of first importance. Herein, we take advantage of electron beam lithography to contact them and build a nanopore-based sequencer with embedded nanotube tunneling electrodes.

3.4.1 Contacting SWCNTs

Strategy

One of the main reasons why CNTs are still mainly limited to research purposes more than 20 years after their discovery is the extreme difficulty to work out a reliable and fast method for integrating them with electrodes and gates onto a silicon wafer. For the project, the growth of individual SWCNTs was designed in such a way that an easy and relatively fast contacting procedure could be established. All growths were carried out on chips compatible with fine EBL alignment, so that catalyst islands and electrical contacts can be patterned with respect to each other with sub-micrometer accuracy.

The full process flow is illustrated in Figure 3.16. First, catalyst islands are patterned by EBL at the surface of Si_3N_4 chips as described in 3.3, whose locations are controlled by using alignment marks, yielding catalytic sites with well defined surface coordinates. After CVD growth, the resulting CNTs are imaged in a SEM microscope and the best candidates are selected for contacts.

Second, two-terminal source/drain contacts are designed with respect to the catalyst island positions. The accuracy of the contact positioning directly depends on the precision at which the SEM pictures are imported into CAD software. With experience, sub-micrometer precision can be achieved. The CVD growth was specifically designed for facilitating this procedure, by yielding long and straight individual SWCNTs, allowing a higher degree of freedom. The contacts are patterned with standard MMA/PMMA EBL and subsequent ebeam evaporation and lift-off, yielding contacts with typical size of $0.6 \times 7 \times 0.05 \mu\text{m}$ with vertical sidewalls. In

addition to local contacts, micrometer-scale electrodes and contact pads were patterned as well for the full device integration with external measurement setups.

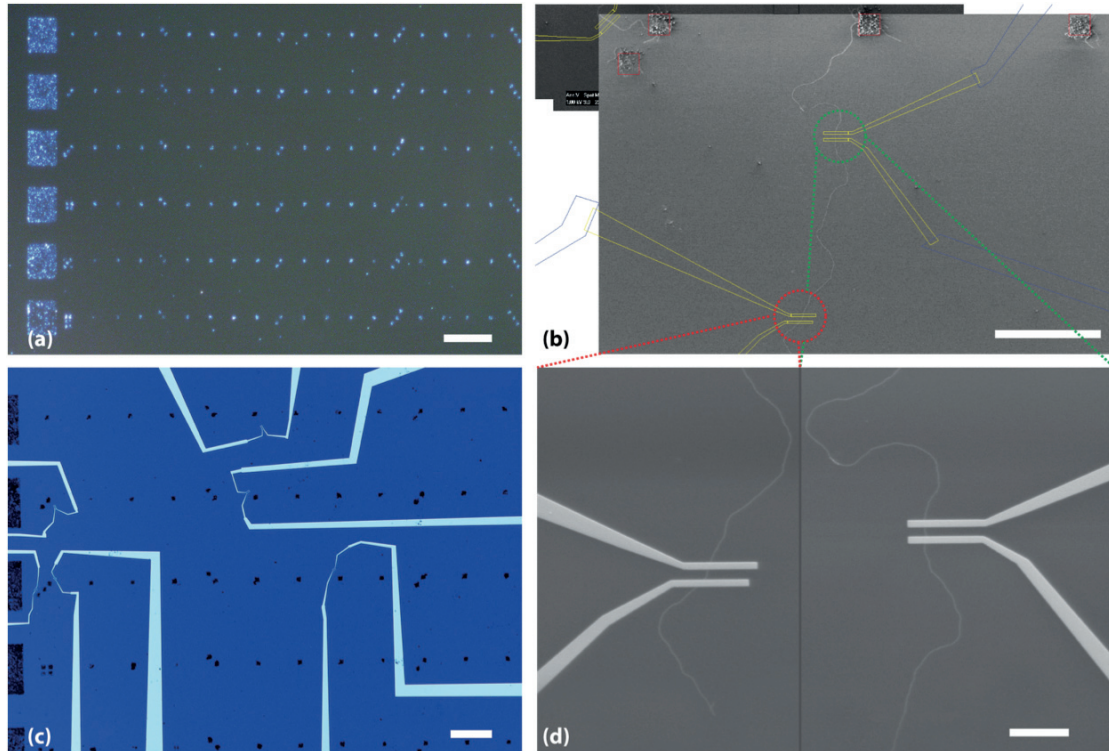


Figure 3.16. Process flow for contacting individual CNTs. (a) Dark-field optical image of catalyst islands patterned by EBL on at controlled locations. Scale bar: $100\mu\text{m}$. (b) After CVD growth, individual SWCNTs are imaged by SEM and their positions are recorded with respect to the catalyst islands. SEM micrographs are imported into a CAD software and integrated within the catalyst islands patterns (red squares). Scale bar: $25\mu\text{m}$. (c) Optical micrograph of a typical chip after EBL and Pd evaporation, showing several pairs of contacts. Scale bar: $50\mu\text{m}$. (d) SEM micrographs of the contacts designed in (b). Alignment accuracy is usually better than the micrometer. Scale bar: $5\mu\text{m}$.

All lithographic procedures require precisely locating CNTs after growth. Historical methods involve atomic force or electron microscopy to locate nanotubes with respect to local fiducial markers patterned on the surface. AFM based approaches are very low throughput and time consuming methods but present the advantage to avoid electrons irradiation that may damage CNTs or induce hydrocarbon contamination. We estimated that using the catalyst islands as fiducial markers provided an easy way to design electrical contact. In addition, by imaging at very low acceleration voltage, the electron irradiation's effects are considered as negligible.

The surface cleanness is fundamental for contacting CNTs. The CVD growth was optimized in order to give rise to the lowest amorphous carbon deposition possible. In the opposite case, few nanometers are enough to shortcut the source and drain electrodes. Moreover, hydrocarbon contamination during SEM imaging can drastically affect contacts' properties.

The number of tubes that can be contacted on a single sample is limited by the chip dimensions. For typical 8x4mm devices, 6 pairs of contacts and pads were usually designed, although only a single SWCNT is actually needed for the final device construction. Indeed, the two-terminal resistances of individual metallic SWCNTs is known to range from few k Ω to several M Ω because of the high variability of contact resistances. SWCNTs are also found as metallic or semiconducting entities, which even further reduce the probability of getting low-resistance ohmic contacts on a metallic SWCNT.

Contact resistance

Although CNTs seem ideal candidate for nanotechnology applications as quantum wires and interconnects with a quantum conductance predicted to be $h/4e^2$ (6.5k Ω resistance), the ballistic current carrying capability usually vanishes because of dramatically high contact resistances at the nanotube/metal interface (see section 3.1.3).

In the case of a semiconducting nanotube, there is a Schottky barrier at the interface if the Fermi level of the metal is between the valence or conduction bands of the CNTs. If the Fermi level is respectively either above the conduction band or below the valence band, the contact is ohmic. The Schottky barrier ϕ_b can be estimated from the difference between the metal workfunction Φ and the electron affinity χ of the semiconductor. In the case of a metallic nanotube, the resistance value depends if the conduction requires tunneling or scattering at the junction. In both cases, the contact resistance has also been shown to be predictable based on the CNTs diameter^[187], for which it becomes difficult to obtain ohmic behaviors when the diameter gets below 1.6nm.

The most common method for making metal-CNT contacts is by simple deposition of a CNT over metallic electrodes, which however usually leads to prohibitively high contact resistance. In our process, we chose to embed laying CNTs on a surface in metal by ebeam evaporation. This has several advantages. First, to maximize the chance of getting a pair of ohmic source/drain (S/D) contacts, a single tube can be patterned by EBL with several electrodes, depending on its length. Second, the dimensions, shape and thickness of the electrodes can be tuned to maximize the interaction surface at the interface. Third, several metal can be tested for optimizing the contacts behavior on the same nanotube.

In typical experiments, S/D metals were put in direct contact with the nanotubes by evaporation of a 50nm thick metallic layer. The CNTs and contacts were electrically characterized by 2-probes dc measurements using a Süss PM8 probe station. Different metals were tested, such as Pt, Au or Pd. At the early stages of the project where

SWCNTs were synthesized by methane CVD at 1000°C, S/D contacts were most of the time shortened, indicating that a non-negligible layer of conducting amorphous carbon was deposited beside CNTs. The CVD strategy has then been adapted to ethanol CVD, resulting in an ultra clean surface state.

Au and Pt contacts gave rise to the lowest probability of getting ohmic behaviors. In most of the cases, no linear I-V dependence or no current could be measured with such contacts. When ohmic behaviors were obtained, 2-points resistances ranged from hundreds of k Ω to several tens of M Ω . In agreement with the literature^[188,189], Pd contacts exhibited ohmic behaviors with the best reproducibility, although we found as expected large resistance variations (Figure 3.17).

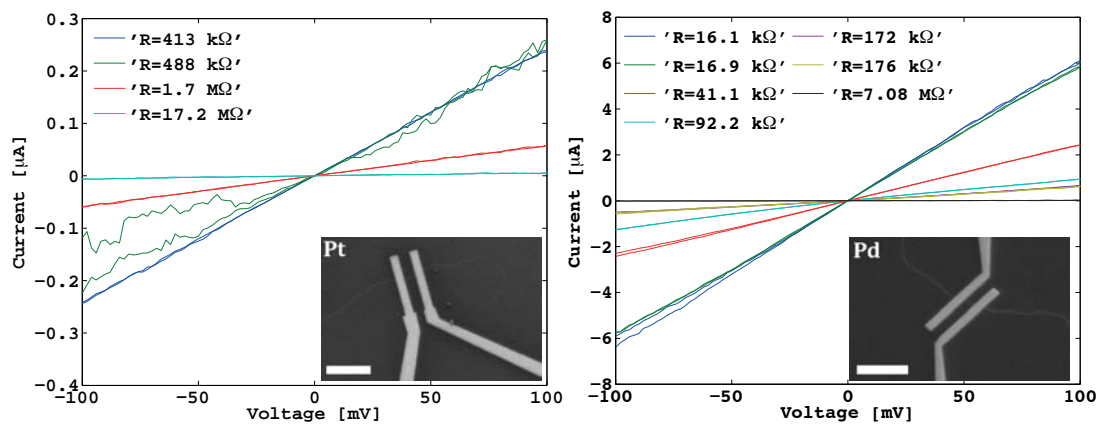


Figure 3.17. Typical I-V properties resulting from Pt and Pd contacts. Eight CNTs grown in identical conditions were contacted with Pt and Pd contacts. (left). When ohmic, Pt contacts usually exhibit very high resistances of few hundred of k Ω or few M Ω . For 4 pairs of contacts, no current could be measured within 100mV. (right) Although large variations are also observed with Pd contacts, only 1 pair exhibited a non-ohmic behavior. For two pairs, the resistance measured was close to the maximum quantum resistance (6.5k Ω). Scale bars: 5 μ m.

Ti adhesion layers were avoided because it has a Fermi level in the nanotubes bandgap and such contacts are more prone to form a Schottky barrier. In addition, Ti based contacts had a moderate lifetime, likely indicating a progressive oxidation after few days, which was not observed using Pd. Different methods have been reported for improving the contact resistance. For instance, thermal annealing in inert atmosphere or electron irradiation have been proved to reduce the effective contact resistance by few orders of magnitude^[190,191].

3.4.2 The membrane challenge

Constructing a nanopore with embedded carbon nanotubes electrodes require integrating a contacted SWCNT within a suspended insulating membrane. The membrane fabrication for such a device fabrication turned out to be the most challenging step of the process.

Si_3N_4 is a very robust material in term of mechanical stability even at elevated temperature, combined to inert chemical properties and was therefore chosen as the most suitable material to overcome extreme physical conditions, such as in CVD growth of CNTs. Two opposite strategies have been considered for the fabrication process. On one hand, the membranes can be opened at the early stages of the device fabrication, typically before CVD, which then would have to survive the whole procedure. Otherwise, the membrane is opened at the very end of the process just before nanopore drilling.

Opening membranes at first present various disadvantages. Most importantly, it is likely that multiple nanofabrication steps would cause membrane failures along the process flow and cause a drastic reduction of the production yield. Moreover, it would require growing and contacting individual SWCNTs on relatively small surfaces, corresponding to the membrane sizes and imaging CNTs on thin insulating membranes for contacting, which is very difficult

We therefore considered first producing large amounts of contacted individual CNTs on chips compatible with KOH etching. However, it quickly appeared that despite LPCVD Si_3N_4 is robust to high temperatures, its chemical integrity is affected to a much larger extent than expected after CNTs synthesis. After calcination in O_2 at 500°C and CVD at 800°C under Ar/EtOH atmosphere, the inherent chemical resistance of silicon nitride to KOH is compromised and it becomes unsuitable for use as an etch mask. We have noticed that most of the time, wet etching results in catastrophic openings in the chips structure, which in most of the cases, led to their disintegration in solution. During less terrible attempts, hundreds of membranes get opened at the surface, and it was systematic that at least few of them leaked, as the top Si_3N_4 layer is damaged as well. In such a scenario, the chip becomes unusable for nanopore sensing on one hand, and KOH etches anyway electrodes away.

It remains unclear how the structure of Si_3N_4 is modified. We successfully opened membranes on chips that underwent thermal oxidation at 500°C , indicating that the CVD process in Ar/EtOH at 800°C is more likely to be responsible. The long range ordering of the initial crystalline Si_3N_4 is certainly lost and local defects and cracks are very likely introduced.

Different materials have been investigated as substitution mask, such as amorphous Si_3N_4 deposited by plasma-enhanced CVD (PECVD) or by sputtering. Typically, thin films of 200nm of thickness were deposited on the backside after CVD reaction, the main limitation being the temperatures that the contacts/CNTs can withstand with no damage. Experimental conditions are detailed in Figure 3.18. To date, no material successfully fulfilled the role of mask for wet KOH etching, as no improvements have

been noticed compared to unprotected chips. Amorphous Si_3N_4 exhibits several differences with respect to crystalline Si_3N_4 . In particular, its stoichiometry significantly differs from a pure 3:4 ratio and a substantial amount of hydrogen can be incorporated. The chemical structure of amorphous silicon nitrides deposited by PECVD or sputtering methods is therefore better described as $\text{Si}_x\text{N}_y\text{H}_z$ ^[192]. Aside a different structure, it also has a lower density and a lower resistance to chemical etch than silicon nitrides grown at high temperatures. All attempts involving alternative silicon nitride thin film as protective mask resulted in device failures.

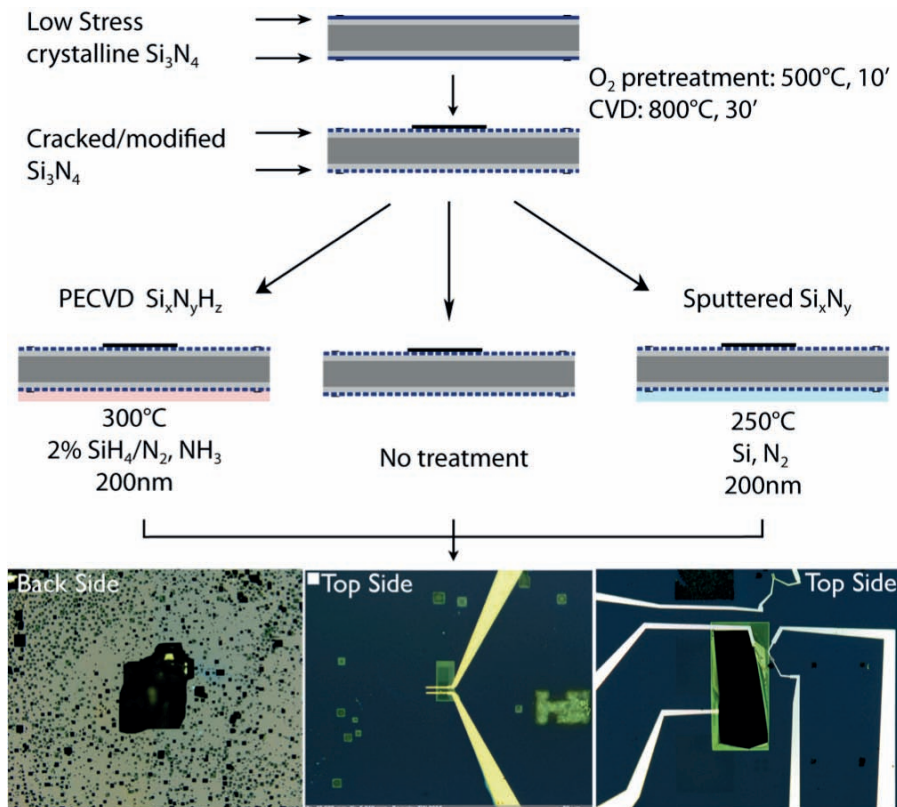


Figure 3.18. KOH etching after high temperature ethanol CVD. Usually used as mask for KOH etching, the Si_3N_4 backside is attacked all over the surface even when protected with additional layers of PECVD or sputtered silicon nitrides. It results multiples membranes opened on the topside, which also don't resist to KOH.

Fabricating nanopores with embedded nanotubes electrodes is a complex process that therefore required working directly on suspended membranes. Low-stress LPCVD grown silicon nitride is a hard ceramic with low thermal expansion coefficient and high strength over a broad range of temperature. Preliminary experiments put in evidence that small membranes are capable of withstanding typical CVD temperatures (up to 900°C has been successfully tested, including thermal shock arising during fast loading into the reactor). They are also capable of supporting heavy materials even at high temperatures. Membranes after CVD are however usually no longer flat but exhibit distorted wavy surfaces. In the case of failures, local cracks often appear at the corners. Figure 3.19 shows that it's experimentally possible to build a functional

device for nanopore sensing. Typically, $5 \times 5 \mu\text{m}$ catalyst squares were patterned by EBL on membranes that were $40 \times 40 \mu\text{m}$. After CVD, grown CNTs were imaged by SEM. In the case of successful growth where individual long CNTs could be found on the membranes, they were subsequently contacted in an additional EBL procedure as described in 3.4.1. Due to the small membrane sizes, no more than 3 pairs of contacts were designed at a time, resulting in a much lower probability of getting low-resistance ohmic contacts on a single sample.

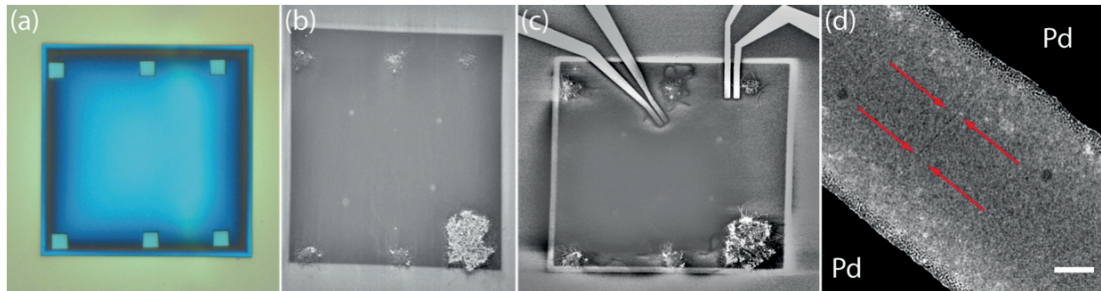


Figure 3.19. Contacting CNTs on $40 \times 40 \mu\text{m}$ Si_3N_4 membranes. (a-b) Catalyst islands are patterned by EBL on $40 \times 40 \mu\text{m}$ membranes, from which CNTs are grown by ethanol CVD at 800°C . (c) SEM pictures of 2 pairs of contacts patterned by EBL on the catalyst islands. (d) TEM micrograph of a SWCNT contacted by 2 Pd electrodes (in black). Scale bar: 100nm.

3.4.3 Nanopore drilling

The next step of the fabrication process is to use the electron beam of a transmission electron microscope to drill nanopores through the membrane and carbon nanotube in a single shot, in order to obtain a nanopore decorated with carbon nanoelectrodes. As explained in paragraph 2.3.3, nanopores are drilled in a field-emission PHILLIPS-CM300 TEM microscope operated at 200kV. All drilling experiments were performed on $4 \times 8 \text{mm}$ chips loaded using a dedicated TEM-holder. If not mentioned, CNTs are drilled from the topside (CNT side).

For practical reasons, most of the drilling attempts were performed on non-contacted carbon nanotubes until a reliable production method has been established. Standard column alignment and stigmatism correction are first performed on non-important areas of the Si_3N_4 membrane. The CNT of interest is then found by regular BF imaging and centered on the imaging screen. After fine focusing of the membrane, the beam is converged using the condenser lens to an intense halo positioned onto the CNT. The pore apparition is monitored in real-time and drilling is stopped as soon as a hole appears.

A drilling attempt is considered as successful when:

- A pore of suitable dimension is formed, typically below 10nm of diameter.
- The CNT is cut into two nanometer-spaced electrodes around the pore.

Achieving such results has been a very demanding task. The main problem arises from the very little contrast produced by small diameter single-walled carbon nanotubes when the membrane is in focus. It becomes therefore extremely difficult to locate the nanotube and to position the condensed spot for drilling. During the first tests, it mostly resulted nanopores drilled at the wrong location with still intact or partially drilled nanotubes. To go beyond this issue, the only solution was to target larger diameter nanotubes, which produce enough contrast to precisely position the beam spot. Although this goes against the project guidelines, drilling such tubes succeeded in getting a nanopore with embedded carbon nanoelectrodes. Another important issue for drilling through carbon nanotubes is the fact that we clearly noticed that when not properly clamped, carbon nanotubes were oscillating on the silicon nitride surface upon imaging. When imaging contacted CNTs, such a behavior was not observed.

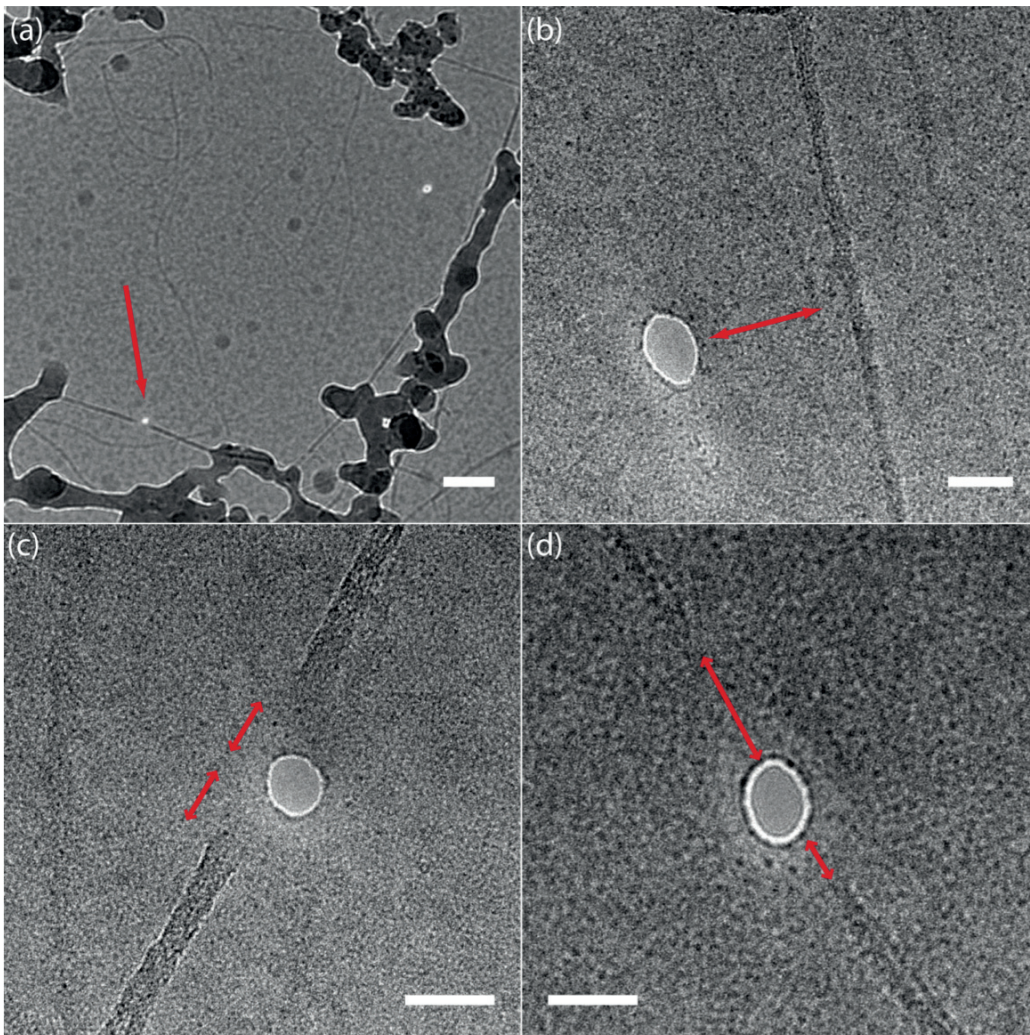


Figure 3.20. Nanopores embedded with carbon nanotubes nanoelectrodes. (a) Because of contrast issue, only large diameter CNTs can be reliably drilled. Scale bar: 100nm (b) When the membrane is in focus, small diameter CNTs are hardly distinguishable, often resulting in misplaced nanopores. Scale bars: 20nm (c-d) CNTs after drilling. Red arrows indicate the gap between the CNT tips and nanopores edge, arising from carbon amorphization. Scale bars: 20nm.

Figure 3.20 shows TEM micrographs CNTs after drilling. The CNTs have been effectively cut into two distinct strands, but the gap between the pore edges and the nanotube tips is substantially larger than expected. In most of the cases, gaps of 10 to 20nm are observed, either symmetrical or not. The systematic amorphization of the sp^2 carbon in the close proximity of the beam spot indicates that electron irradiation causes severe damages to the CNT structure over large distances. It is known that primary electrons with sufficiently high energy (typically above 86keV) induce damages in SWCNT by ballistic ejection of carbon atoms^[193]. The Gaussian profile of the electron beam may therefore affect the CNT to a larger extent than the spot size and the focused spot is probably not a Gaussian, which is even worse. However, it is more likely that other irradiation induced defects mechanisms occur, as it has also been shown that SEM imaging of CNTs can also induce severe defects upon irradiation^[194], showing that even low energy electrons may have deleterious consequences. We believe that local joule heating in the insulating Si_3N_4 membranes, combined to the generation of secondary electrons are responsible for burning the CNTs over few tens of nanometers.

To date, we didn't manage to obtain nanotubes electrodes perfectly laying on the nanopore edge. An alternative approach has been considered by drilling from the backside. Despite that in such configuration the contrast resulting from the CNTs is even lower, drilling attempts were performed but showed not improvement compared to regular drilling from the topside. Sometimes shown as an example in the literature^[195], embedding CNTs in a material before drilling, such as by ALD or CVD, was not considered. In such a case, the generation of secondary electrons is believed to cause even more damages than for a CNT on a surface.

3.5 Discussion

Using metallic carbon nanotubes as tunneling electrodes on the side of a solid-state nanopore is a promising route, which is fundamental to investigate for single-molecule sensing with nanopores. The ability of CNTs to carry high current densities with a low resistance, associated to diameters smaller than 2nm for SWCNTs are very unlikely to be reproduced by any other material.

We have demonstrated a full process for decorating solid-state nanopores with electrically connected carbon nanotubes electrodes. A direct CVD method was established to grow high-quality individual SWCNTs on Si_3N_4 with location control, which could be contacted by electron-beam lithography, using catalyst islands as fiducial markers. The procedure could be combined to the fabrication of solid-state Si_3N_4 membranes through which nanopores have been drilled.

We faced and tried to overcome the common difficulty that is proper to CNTs in large-scale applications: the challenge for processing them into electrically addressable features. Although we proposed an optimized process flow that can generate relatively good quantities of functional devices for research purposes, more elaborate fabrication methods will be required if capacitive measurement of translocating DNA is demonstrated. In particular, contacting should not rely on the selection of individual CNTs by imaging. So far, a controlled method to position and contact CNTs with no intermediate characterization has not been described. Similarly, CNTs present intrinsic drawbacks for their integration into electronic circuitry. For instance, it is not yet possible to control by synthesis their chirality, and hence their metallic or semiconducting properties, which leads to the need for new synthesis or new sorting technologies before a technology platform can be developed.

The fabrication of a device for DNA sequencing that entirely fulfills the geometrical requirements enounced in chapter 1.4.2 is a challenge that could not be overcome. In particular, drilling nanopores and nanotubes in a single step using a transmission electron microscope turned out not to be a viable method as it results in the contraction of the CNT tips away from the pore. In addition, TEM imaging of CNTs is not without consequences as it results in an alteration of their electrical properties by inducing structural defects.

TEM milling was preferred for its relatively good fabrication throughput, but alternative approaches may have to be considered. Nanomanipulation of individual CNTs by AFM or nanomanipulator robot^[196] is a route under investigation. Typically a nanotube is positioned “by hand” across the diameter of a nanopore. Such results have been achieved by Sadki *et al.*^[197] with a poorly controlled method involving CVD grown CNTs randomly bridging pre-drilled nanopores. Such CNTs can be used as FET sensors but it may be possible as well to cut them in a post procedure, for instance by heat-induced electrical breakdown at the exact nanopore location.

Chapter 4

Fabrication of nanopores with metallic transversal tunneling junction

4.1 Fabrication of sub-10 nm metallic nanogap electrodes

Within the past decade, nanogap electrodes have attracted a lot of attention because of their potential applications in the progressive miniaturization of electronics and as nanoscale tool for analysis of molecular properties. Nanogap electrodes can be simply defined as a pair of electrodes with a gap that can be measured in nanometers. Therefore, an intense effort has been put for reducing as much as possible the nanogap size, with the ultimate goal of a single nanometre. The investigation of molecular properties is a typical application involving nanogap electrodes, such as in our case. The required sizes must typically be close to the targeted molecules, most often below 5nm and need to be well controlled, ideally with a resolution of a single nanometer. Several fabrication methods have been reported lately, such as mechanical^[198] or electromigration-induced^[199] break junctions, electrodeposition^[200], electron beam lithography or electron beam induced deposition^[201]. Promising results have been achieved but not all methods allow their integration into more complicated devices, especially into solid-state nanopores based devices. The methods presented here allow a high throughput fabrication of sub-10nm planar nanogap electrodes by high-resolution electron beam lithography and their full integration within a solid-state nanopore. Moreover, a straightforward electrodeposition strategy has been developed for a further gap reduction in a well-controlled manner. The main advantages of our fabrication process are a high reproducibility and reliability combined to a relatively fast processing time.

4.1.1 Challenges

Electron beam lithography is a very efficient technique for patterning substrates with metallic structures at the nanoscale but pushing the limits of EBL in term of resolution is a challenge in itself. We should first discuss how to define the concept of ultimate resolution in EBL depending on the process. First of all, we have to differentiate the resolution limits for isolated features and for dense arrays of nanostructures. For the

latest, the limit is reached because of proximity issues discussed earlier in chapter 2.1.3. Hence, the pitch of pattern arrays is currently limited to about 15 nm. For isolated features, it has been demonstrated that much smaller patterns could be written, depending on the resist resolution but not on proximity effects. However, an EBL process is based on two main steps: the electron exposure combined to the resist development and the pattern transfer, which is the second main source of resolution loss. In particular, the definition of metallic structures is usually performed through standard metal evaporation and lift-off, which even if the EBL process is mastered, can ruin the final resolution if poorly optimized.

The fabrication of nanometre sized nanogap electrodes have to overcome these two critical steps. The resist development must exhibit sub-10nm patterns, which have to be conserved during the transfer by PVD. We present here two distinct methods allowing the fabrication of sub-10nm metallic nanogaps with different properties. The first method involves standard EBL using PMMA and subsequent metal evaporation and liftoff. The nanogaps produced according to this process flow are sub-10nm gaps with narrow electrode tips. The second method is a multiple-step procedure involving the use of different EBL resists combined to metallization and etching. The nanogaps obtained from this method are also below 10nm but can be much wider, which is not possible by standard lift-off. A more complete description follows in the next sections.

4.1.2 Fabrication by direct metallization

Strategy

PMMA is the highest resolution positive resist for EBL and is therefore suitable for the definition of planar nanogap electrodes onto a substrate. The fabrication of such features with a good yield and reproducibility require a lot of experience and a well designed and optimized process.

If one has to pattern the narrowest line on a substrate, the best strategy is to do it by single pass, which means that the width of the line is exactly of one pixel and that there is no parallel exposure along it. Similarly, if the smallest dots were to be patterned, the best results would be obtained with an exposure of a single pixel. Hence the limiting resolution should be the smallest pixel size, that is 1.25nm for the EPBG-5000 available at CMI.

However, at 100kV, the smallest spot size is way above 1.25nm. Figure 4.1 shows the spot size specifications as a function of beam current of our machine. For small beam currents that are needed for high-resolution procedures, e.g. less than 5nA, the spot sizes reach a plateau, around 5 nm, which theoretically constitutes the narrowest line

that can be written. If one uses low current beams, associated issues must be considered. Indeed lower currents mean lower writing frequencies and longer settling time between each pixel. Noise and drift therefore play a significant role when one needs high-resolution exposure and can lead to high line-edge-roughness or to distorted patterns. The relative low sensitivity of PMMA fortunately counterbalances noise effects as small dose variations only have little influence.

Furthermore, the final linewidth is increased by the electrons interaction volume. When the incident electrons hit the resist, secondary electrons are instantaneously generated, which are also traveling laterally over distances that can be larger than the spot size. Low resist sensitivity is therefore again preferred to avoid a too large broadening.

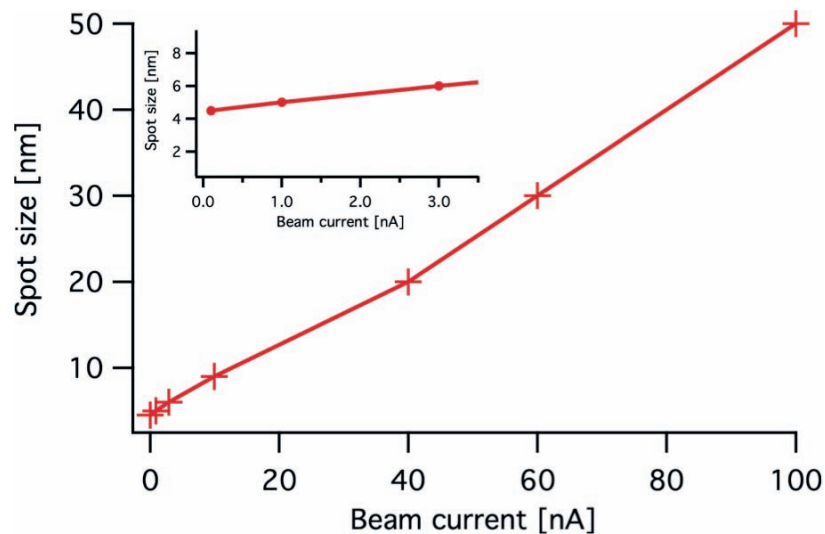


Figure 4.1. Electron beam spot sizes versus beam current. Inset: zoom in low-current beams.

For the fabrication of nanogap electrodes by standard EBL using PMMA, we optimized the exposure to the maximum extent, in order to avoid proximity effect and lift-off issues. Such electrodes were therefore designed as a single pixel line with a gap in the middle, corresponding to an unexposed zone. The number of unexposed pixels along the line defines the gap distance in combination with the exposition dose. The minimum gap for given resist and metal thicknesses is found according to the systematic approach illustrated in Figure 4.2. 2D arrays of electrodes pairs are exposed. In the x direction, the gap size is incremented from 2.5nm to 25nm. In the y direction, the dose is progressively increased by 10% increments. The value of the initial dose is set according to an initial dose test, corresponding to the first dose yielding a complete single-pixel line. The increase in dose has two major effects. First, the lines width progressively increases by over-exposition. Second, at high doses, the resulting gaps are smaller than in the design. For instance, at a nominal size

of 10nm, the gap size can be reduced to 0 nm by using a dose that is high enough to merge the two lines.

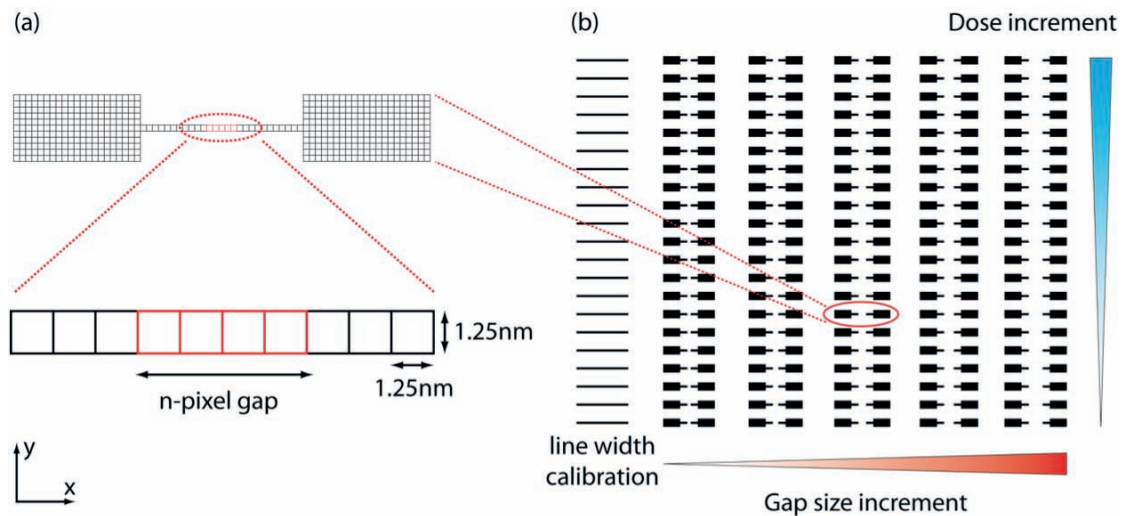


Figure 4.2. Systematic approach for sub-10nm nanogap electrodes fabrication by standard EBL and lift-off. (a) Nanogaps are defined as 1 pixel large lines. The optimized number of non-exposed pixels for a given dose is found according to (b). 2D arrays of nanogaps are patterned with gap size and dose incrementation. The optimized dose for a nominal gap size is determined by SEM imaging.

The strategy described in Figure 4.2 allows a methodical investigation of the best combinations in term of resist and metal thicknesses for achieving the highest resolution EBL and pattern transfer. In order to minimize beam broadening by forward scattering and maximize the exposure resolution, an ultrathin resist layer was preferred typically a monolayer of PMMA below 50nm. On the other hand, the metal thickness is chosen as a compromise between the feasibility of the process and the resolution after pattern transfer. With a too thick metal layer, the lift-off in the nanogap region is not possible, in which case a metallic bridge forms between the two electrodes. Ultra-thin metal layers may give the best final resolution but are unfortunately unsuitable for nanoscale electronics. At low-thicknesses, thin films may be inhomogeneous and consist of small grains where coalescence has not taken place, yielding high resistance electrodes. Similarly, the quality of the PVD process is important, because the size of the gaps may be limited by the size of the thin film grains. A process yielding very small grains size is again preferred for an easy lift-off and high pattern transfer resolution.

Method

EBL was performed using a Vistec EPPG-5000 operated at 100kV on 11.2×11.2mm chips as described in Fig 4.10.1. Exposures were carried out with a 200pA beam with a spot size in the range of 8nm. A layer of PMMA 495K was spin-coated onto the Si₃N₄ layer at various speeds to achieve thicknesses ranging from 50 to 150nm. In order to minimize thermal expansion and drift, the samples were left at room

temperature for two hours before loading, and for another hour once loaded for temperature stabilization. The patterns were written from 6000 to 90000 $\mu\text{C}/\text{cm}^2$. After development, a 3nm thick Ti layer was first deposited as an adhesion layer between the platinum and substrate, followed by the deposition of Pt ranging from 8 to 20nm. Platinum was chosen for its high electronic mobility and preferred against gold to minimize surface diffusion at moderate temperatures, typically during successive baking. Lift-off is performed in acetone at room temperature for 1h. The samples were at last rinsed in IPA and dried under N_2 . Gaps were finally imaged and characterized in a ZEISS MERLIN SEM or in a PHILLIPS CM300 TEM microscope.

Results

The method described here allows the fabrication of sub-10nm nanogap electrodes with a very high reproducibility and a fast fabrication process. By patterning 2D arrays of nanogap with gap size and dose variation, the desired dimensions can be chosen during SEM imaging for further integration into a larger device. Depending on the metal layer thickness, nanogaps as small as 7nm can easily be found (Figure 4.3). Nanogaps smaller than 5nm were also observed but with very little occurrence.

The key parameter was found to be the resist thickness that was critical for achieving high resolution EBL and pattern transfer. A PMMA thickness of about 50nm became the standard process for nanogaps fabrication. With thicker layers, the overall nanogap dimensions quickly increase. Similarly, a double layer system consisting of MMA-PMMA was avoided as well to minimize forward scattering and because MMA is too sensitive for high-resolution lithography.

As ultrathin resist layers were required, it also limits the thickness of metal that can be deposited. In the limit of non-uniform thin film of high resistance, it was shown that 8nm Pt film yields the smallest nanogaps with the best reproducibility. For thicker films, it is likely that despite sub-10nm gaps are successfully patterned in the resist, the pattern transfer is not achieved because metallic Pt bridges remain after lift-off. In such case, gentle sonication has been shown to help breaking these structures apart. With a 30nm Pt layer on top of 3nm Ti, the smallest nanogaps appeared to be in the range of 10nm to 13nm.

The comparison of the smallest linewidth that can be structured after lift-off with PMMA and the size of the nanogap that can be patterned put in clear evidence that the main limiting factor is not the resolution of PMMA but the beam spot size. With a negligible influence of the beam current, Figure 4.3 shows the width of lines that were patterned in a single-pass in function of the exposure dose. At a dose around 12000 $\mu\text{C}/\text{cm}^2$, a resolution of about 13 to 15nm can be achieved. This is indeed much more than what we could achieve with the fabrication of nanogaps. The purpose of the

gap incrementation is to go beyond the size of the spot and to take advantage of scattering effects to control the exposition. With a nominal gap size between 2.5nm (2-pixel) 7.5nm (6-pixel), no nanogap could be fabricated. Between 10nm (8-pixel) and 15nm (12-pixel), the dose window yielding opened nanogaps is first extremely narrow, and second, mostly results in randomly sized nanogaps. However, nominal gap sizes of 20nm (16-pixel) and more yield extremely good results. At 20nm, doses between 33000 and 49000 $\mu\text{C}/\text{cm}^2$ results in gaps whose sizes are homogeneously distributed between 7 and 10nm (50nm PMMA, 3/8-20nm Ti/Pt). At 200pA, if the beam spot size is estimated to 8nm, the real nanogap distance is already of 12nm (spot edges distance). By slightly over-exposing, we take advantage of scattering effects to approach the ultimate resolution of PMMA and reproducibly pattern sub-10nm gaps at high throughput.

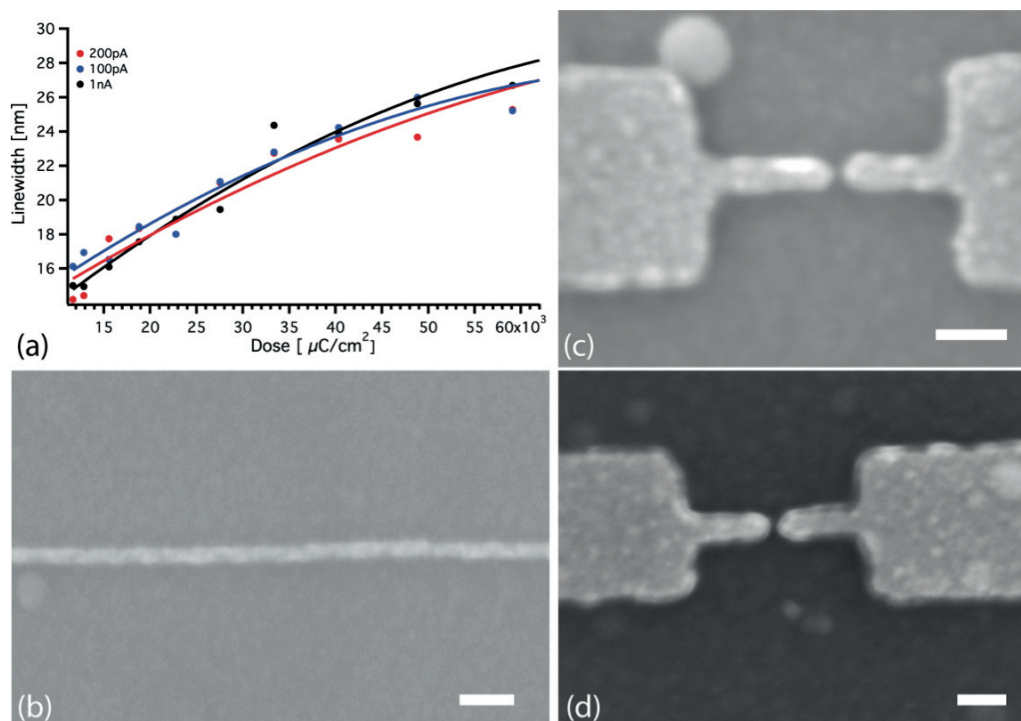


Figure 4.3. Nanogap electrodes from single-pixel lines. (a) Linewidth of Ti/Pt lines (12nm) patterned in 50nm PMMA in a single pass (pixel size: 1.25nm). At low current, the choice of the beam has very little influence, indicating similar spot sizes. (b) 3/8nm Ti/Pt line after lift-off of 50nm PMMA. Typical linewidth at 12000 $\mu\text{C}/\text{cm}^2$ is 15nm. (c-d) SEM images of nanogap electrodes made from 1-pixel large lines. The nominal gap size is 20nm, reduced to less than 10nm through scattering effects. Scale bars: 20nm.

The feasibility of this process rests on the use of very thin resist and metal layers, which intrinsically induce resistive electrodes. However, it is anyway necessary for single-molecule DNA sequencing with transverse electrodes to limit the size of the electrodes tips to reach single-base resolution. In addition, the expected resistance at the electrode-DNA junction is expected larger. The process presented here is therefore in line with the project requirements.

Shape optimization

Triangle-shaped nanogaps were further designed by optimization of the initial design. The nanogap region was kept as a single pixel large line that is scanned only once by the beam. The line is however progressively broadened while going further away from the gap region (blue surface, see Figure 4.4). A dose incrementation (red line) allows to finely correct any proximity effect compared to an isolated single pixel line. In such a way, the exposition dose in the gap proximity is kept constant and triangle-like nanogap electrodes can be fabricated. The main advantages over narrow metallic lines are a lowered junction resistance as well as a higher electrical and mechanical robustness. Triangular electrodes of about 80nm in length are connected to microelectrodes (green surface) spaced by about 200nm written at lower resolution. In order to avoid proximity effects in the gap region, these electrodes are designed far away from the gap but are over-exposed, resulting in patterns bigger than the initial design and closer to the nanogap electrodes.

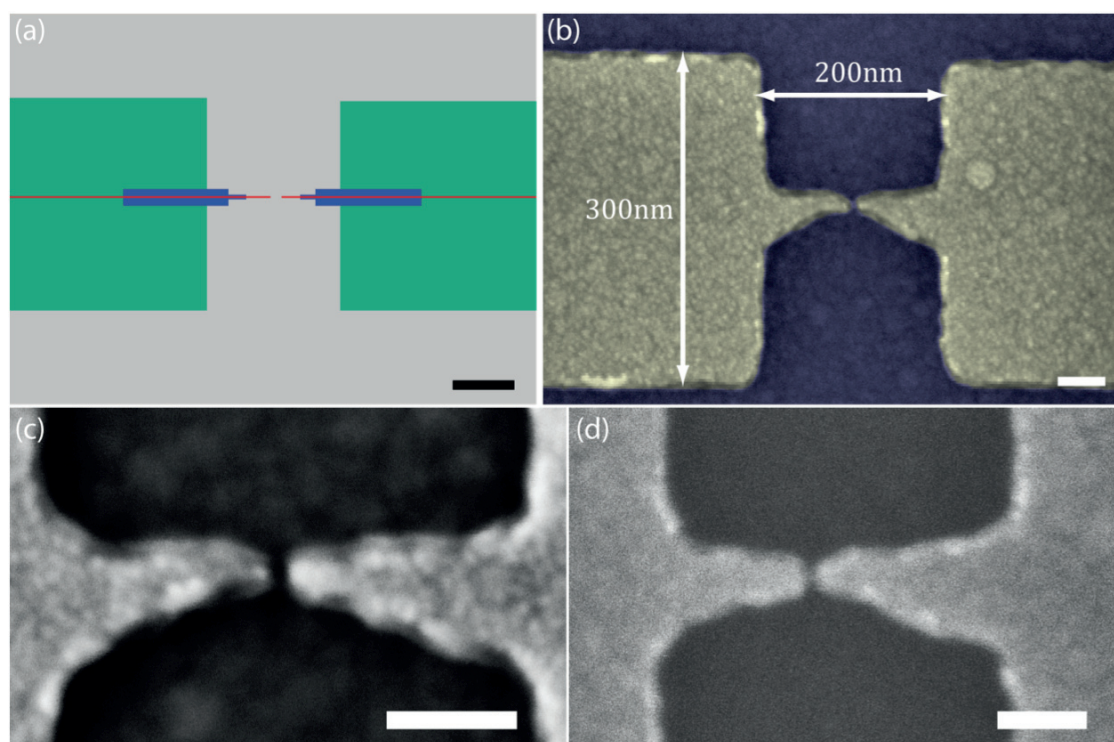


Figure 4.4. Nanogaps after design optimization. (a) Triangular electrodes are designed by taking advantage of proximity effects. The green and blue patterns are written at constant dose with a slight over-exposition. The nanogap electrodes (red) are patterned by varying the dose and gap size in 2D arrays as shown in Figure 4.2. Scale bar: 100nm. (b) Colored SEM micrograph of typical nanogap electrodes used for experiments. According to (a), the sub-10nm gap electrodes are connected to microelectrodes spaced by 200nm. The nominal unexposed pixel length was 20nm (gap in the red line), exposed at a resolution and beam step size of 1.25nm at a dose of $41000\mu\text{C}/\text{cm}^2$. Scale bar: 50nm. (c-d) SEM images of sub-10nm triangular gaps (respectively 3/8 and 3/20nm Ti/Pt). Scale bar: 50nm.

4.1.3 Fabrication by combination of lift-off and etching of HSQ

Strategy

A single EBL step combined to metal evaporation allowed the fabrication of hundreds of nanogap electrodes with sub-10nm resolution. In spite of the high resolution of PMMA, the highest resolution electron beam resist has been proven to be HSQ^[202]. We therefore designed a process flow, as shown in Figure 4.5, taking advantage of HSQ for the fabrication of nanogaps. Similarly to PMMA, the sharpest isolated feature that can be patterned with HSQ was imagined to be a single-pixel large line, exposed in a single-pass. However, as HSQ is a negative resist, a different strategy had to be established combining HSQ with another positive resist in an additional EBL step. The first step consists in patterning the narrowest HSQ line possible. After development, isolated lines are lying on the substrate with a width corresponding to the resolution achieved and of height corresponding to the initial resist thickness. In a second step, rectangular electrodes are structured into PMMA, so that after metal evaporation and liftoff, the rectangles cover HSQ lines in a perpendicular direction. Therefore, the second EBL requires an accurate alignment with respect to the prepatterned HSQ lines. After etching of HSQ, the metallic rectangles yield two nanogap electrodes, whose gap size corresponds to the initial HSQ lines width.

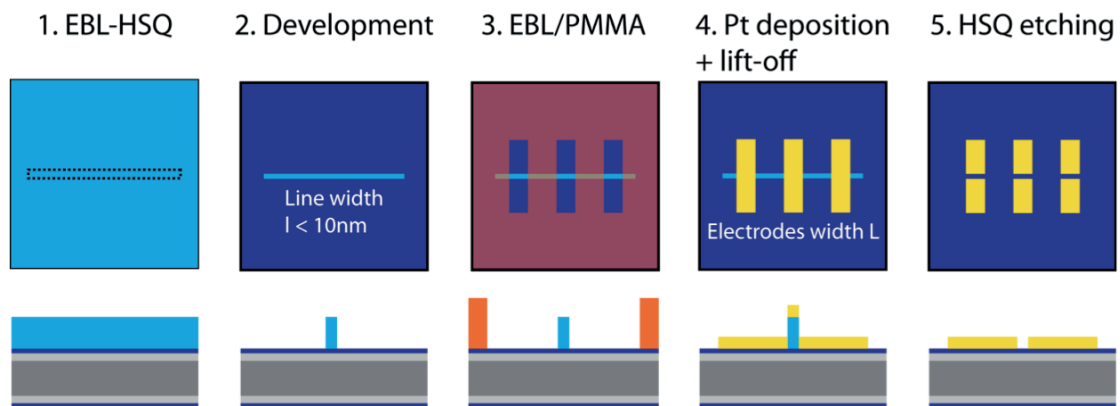


Figure 4.5. Illustration of the fabrication of nanogaps electrodes by combining high resolution HSQ resist to standard PMMA EBL. (1-2) Narrow HSQ lines are first defined by EBL. (3-4) Metallic electrodes are deposited over the HSQ lines by standard EBL using PMMA resist. (5) HSQ lines are etched away in buffered HF (BHF), yielding nanogaps electrodes with a gap distance corresponding to initial lines' width.

The width at which HSQ lines can be patterned is then critical because it defines the gap size itself. HSQ is very high-resolution resist, but the width that can be achieved directly depends on the resist thickness. Indeed, because of forward scattering and beam broadening, ultra thin layers yield narrower lines comparatively to thicker resist. However, the feasibility of the process relies on the fact that the metal layer is of smaller thickness than the resist, so that the metal lid can be removed during etching.

A compromise between metal thickness, thin-film resistance and gap distance is therefore again needed.

Method

The nanogaps are created on a process based on three lithographic layers and an etching procedure. The starting samples are standard 11.2×11.2mm with Si₃N₄ epilayers. The advantage of the top Si₃N₄ layer is its resistance to buffered hydrofluoric acid (BHF) but it has no other significant role in the process. In a preliminary procedure not shown in Figure 4.5, alignment markers are patterned by EBL and RIE at each corner of the chip, which are used for the 2 following EBL layers illustrated above.

In agreement with the procedure described in chapter 2.1.4, samples are spin-coated with 2% HSQ at speeds ranging from 4000 to 6000 rpm, yielding thicknesses from 50nm to 20nm. Exposure of single-pixel lines is performed using a 200pA beam at doses ranging from 25000 to 85000 $\mu\text{C}/\text{cm}^2$ with 5% increment. Alignment is performed in automatic mode using the 5nA beam. Samples are developed in MF-CD26 for 30 seconds, rinsed in DI water and finally blown dried with N₂.

For the second EBL layer, a double layer of MMA/PMMA (100/60nm) is used for patterning metallic electrodes of widths ranging from 20 to 100nm. The exposure is carried out with a 200pA beam and 1.25nm resolution at 1600 $\mu\text{C}/\text{cm}^2$. Alignment is performed in automatic mode using the same alignment marks as used in the previous step and the 5nA beam. After development, A resist descum is performed by O₂ plasma using an Oxford PRS900 (9'', estimated resist etch rate 35nm/min) in order to remove any resist residual before metal deposition. Using the LAB600 ebeam evaporator, a Ti layer of 3nm is eventually first deposited as adhesion layer, followed by the deposition of a Au or Pt layer with thicknesses ranging from 8 to 20nm, depending on the initial HSQ thickness. Lift-off is performed in acetone at room temperature, eventually helped with gentle sonication. Samples are rinsed in IPA and dried under N₂.

HSQ removal is performed by wet etching in a buffered HF bath (49% HF:40% NH₄F 7:1) for 10 seconds at 22°C. Samples are then thoroughly rinsed in DI water and blown dried under N₂. Samples are finally imaged in a ZEISS-Merlin SEM microscope.

Results

HSQ is indubitably capable of very high resolution and we successfully managed to push the limit of EBL in term of resolution. Figure 4.6a shows a 6-7nm wide line patterned in 20 nm thick HSQ. Consolidating patterns were also structured to avoid

the whole line to collapse due to a high aspect ratio. Indeed, when reaching aspect ratio higher than 5, the lines were likely to fall down on their side because of capillary forces during development.

The optimum dose was shown to be slightly below $30000\mu\text{C}/\text{cm}^2$ at a resolution of 1.25nm, but also very dependent on the resist state. The use of 100 or 200pA beams is not critical in term of linewidth, but the relatively high clearing dose required for the process implies that high beam currents should rather be preferred. At low current, small writing frequency induces noise along the structure, which translates into wavy lines.

More importantly, the thickness of the resist has been shown to be critical as the linewidth quickly increases with it. For a thickness of 40nm, the smallest linewidth that got achieved was already slightly above 10nm. Also, the best results are achieved by using a resolution and beam step size of 1.25nm, where the lines are written in a single-pass. The difference with a 4-pass strategy is also shown in Figure 4.6b. The smallest linewidth obtained for a given strategy is very dose-sensitive, which is why a dose incrementation from $25000\mu\text{C}/\text{cm}^2$ is always necessary.

MF-CD26 is a TMAH based developer, which showed optimum resolution for development time of 30 seconds at room temperature. For longer duration, structures were usually washed away. Sonication-assisted development was avoided because of the fragility of the structures.

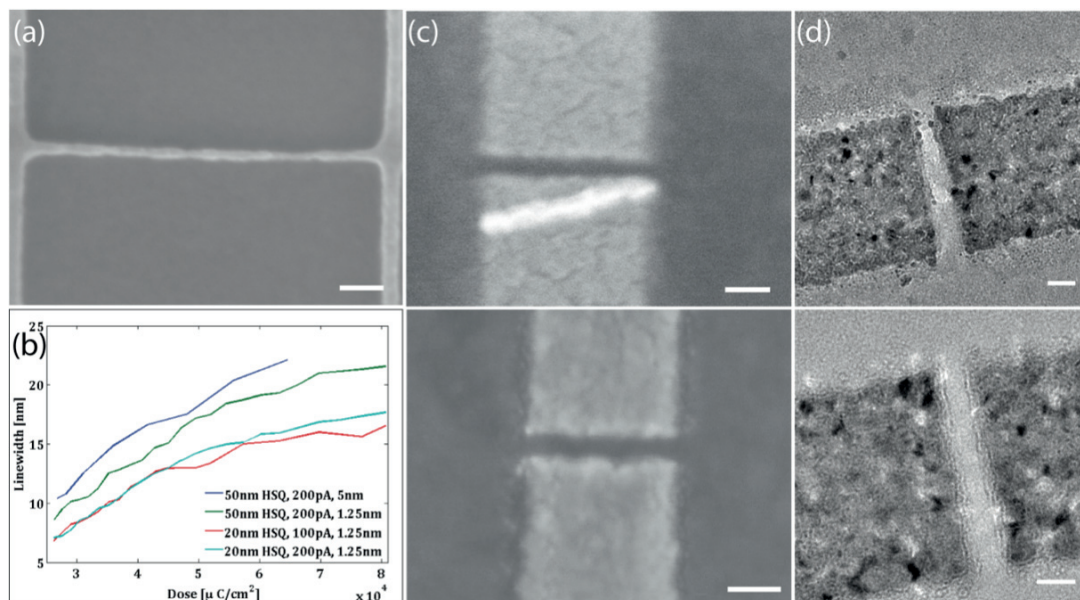


Figure 4.6. Sub-10nm nanogap fabrication by combination of lift-off and etching. (a) SEM picture of a 6-7nm wide HSQ line patterned in 20nm HSQ. (b) HSQ linewidth in function of the initial resist thickness, beam current, and designed width at a resolution of 1.25nm. The linewidth is highly dependent on the initial thickness. (c) SEM pictures of nanogap electrodes after evaporation of 8nm Au, lift-off and HSQ etching. On the top picture, the metallic lid remained on one of the electrodes. Scale bars: 20nm. (d) TEM pictures before pore drilling. Scale bars: 10nm.

The high resolution achieved with HSQ successfully got transferred to the fabrication of nanogap electrodes. We indeed observed the formation of sub-10nm gap after etching. AFM measurements put in evidence that the final HSQ thickness after development is slightly reduced, requiring to work with very thin metallic layers, thinner than HSQ. With metallic layer of thickness below 12nm (for 20nm HSQ), the reproducibility of the process was found to be fairly good. In the case of thicker layer, the metallic lid is however very likely to remain and bridge the two electrodes, in which case, gentle sonication was shown to help (Figure 4.6c). To reduce the total thickness, the adhesion layer may be skipped, yielding even better results. Additionally, the nature of the metallic layer was also proved to be critical. The probability of getting opened nanogaps was also improved by evaporating gold instead of platinum.

One of the crucial advantages provided by the method described here is the electrodes width that can be obtained. Whilst the process involving direct metallization using PMMA and lift-off is limited to narrow electrode tips, it is possible with such an approach to fabricate sub-10nm electrodes with any arbitrary width. The occurrence of gap opening is even higher as the electrodes width increases.

4.1.4 Discussion

We have shown that sub-10nm metallic nanogap electrodes could be fabricated in well-controlled and reproducible processes using optimized electron beam lithography. In the two strategies presented, all steps have been optimized. The main factor that seems to limit the final resolution is the beam size, resist and metal thicknesses.

On one hand, we showed that such electrodes could be obtained by standard lift-off with PMMA as positive tone resist. The writing strategy has been shown to be critical for the final resolution. By combining single-pass exposures to ultra-thin resist and metal layers, the ultimate resolution after pattern transfer has been achieved in a simple and fast procedure. Large amount of devices can be fabricated with a perfect reproducibility, whose time-limiting step is SEM imaging. Sub-10nm nanogap electrodes were obtained with total metal thicknesses ranging from 8 to 20nm.

On the other hand, we have shown that using ultra thin layers of HSQ, straight lines could be patterned with a spectacular linewidth. Less than 7nm has been obtained by exposing in a single pass with a pixel size of 1.25nm. The linewidth is highly dose sensitive, suggesting that a dose incrementation is valuable for reaching the ultimate resolution. The high resolution of HSQ has then been transferred to the final patterns in a second lithographic step by lift-off and etching. Nanogap electrodes with sizes

comparable to the initial HSQ line widths were indeed successfully fabricated. An interesting fact is that the nanogap size is not dependent on the electrodes width. However, the reproducibility is limited to very thin layers of metal, ideally without adhesion layer, which make the final device more fragile and resistive than those fabricated with the first method.

As the needs for the project in term of devices quantity is tremendous, we mainly used the first method, based on a single EBL step, whose reproducibility and simplicity after optimization have been a considerable advantage for large-scale fabrication.

4.2 Nanogap reduction by electrodeposition

The potential of nanogap electrodes to investigate electronic transport through single-molecule, such as of DNA in a nanopore, or to build molecular devices that could replace conventional silicon-based semiconductors is exceptional. Although two different methods have been proposed for the fabrication of sub-10nm electrodes by electron beam lithography, it is necessary to propose a complementary method that can overcome the resolution of EBL to reach the size of single molecules, which is only of few nanometers.

The current paragraph provides a robust and easy electrodeposition method to gradually reduce the nanogap size down to a nanometer in a controllable fashion. In a first step, Ti/Pt nanogap electrodes and pads are fabricated by EBL and lift-off on insulating Si_3N_4 substrates. The gap size is chosen arbitrary large, typically above 15nm and is not critical. In a second step, electrodeposition of Pt is realized by successively using the two patterned electrodes as counter and working electrodes. It results a progressive deposition of Pt on both electrodes, leading to a gradual increase of dimension and also to the reduction of the gap separation. The reliability of the process is ensured on one side by controlling the electroactive Pt surface area (fixed to exactly $100\mu\text{m}^2$) and on the other side by operating in voltage pulses mode. The nanogap separation is controlled by monitoring the dc current flowing between the working and counter electrodes during each voltage pulse, which provides a clear indication of the moment where the two electrodes get into close contact. By stopping the electrodeposition when a sudden increase of current is observed, nanometer-sized nanogap electrodes can be successfully and reproducibly fabricated.

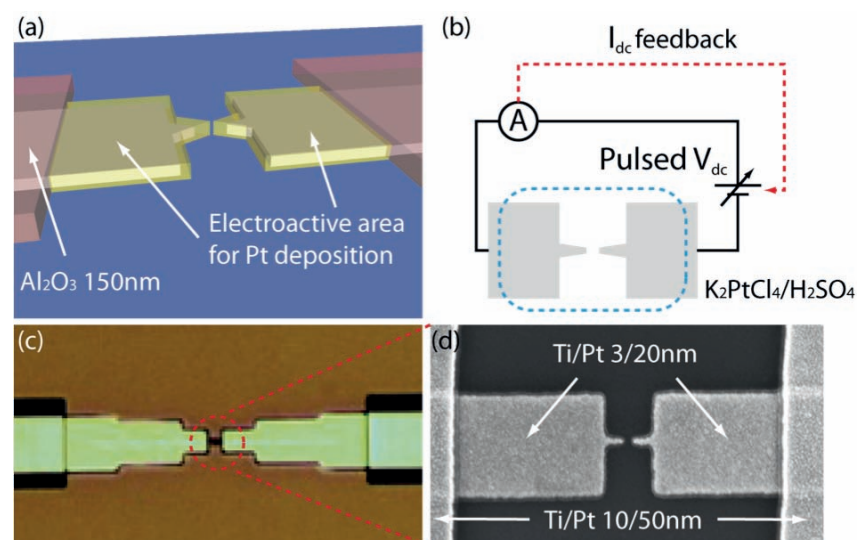


Figure 4.7. Controlled nanogap reduction by platinum electrodeposition. (a) large nanogap electrodes are first patterned by EBL and lift-off (light grey), on which a $100\mu\text{m}^2$ electroactive area is also defined by masking the rest of the electrodes with Al_2O_3 . Pt deposition occurs on the electrodes, gradually reducing the initial gap size (transparent yellow). (b) Bipolar voltage pulses control the electrodeposition alternatingly on the two electrodes. I_{dc} between the two electrodes is continuously monitored and the deposition continues until a sudden current increase is detected. (c) Optical picture of the electroactive Pt surface and Al_2O_3 mask (black). (d) SEM image of typical initial nanogap electrodes before deposition with 15-30nm separation.

4.2.1 Experimental details

Nanogap electrodes fabrication. Ti/Pt (3/20nm) electrodes with separation of 15 to 30nm were fabricated by EBL and lift-off according to the procedure shown in chapter 4.1.2 on Si_3N_4 substrates. In a second EBL step, Ti/Pt (10/50nm) microelectrodes and contacting pads are patterned on top of the initial electrodes (see section 4.3.1). In a third EBL step, electrodes are passivated with 150nm of Al_2O_3 , except in the nanogap proximity where a total surface of $100\mu\text{m}^2$ ($2 \times 50\mu\text{m}^2$) is left unprotected, constituting the electrochemically active Pt surface. Before electrodeposition, substrates are cleaned for 30' in Ar plasma at 30W.

Electrodeposition setup. Two contact pads are electrically connected with tungsten probes and linked to a source-meter-unit (SMU, Keithley 2400). A home-made Labview software is used to control the unit as a voltage source and current meter. Typically, voltage pulses (0.6-1.2V amplitude), alternatively positive and negative (V_{on} : 20ms, V_0 : 1s) are applied to the 2-electrodes system while the dc current is continuously monitored. The two electrodes therefore alternatively play the role of counter and working electrodes. A current compliance, usually set up at $1\mu\text{A}$, is used to preserve the electrodes.

Pt electrodeposition. The electrolytic bath consists of an aqueous solution of 10mM K_2PtCl_4 (ABCR, 99.9%) in 0.5M H_2SO_4 . A 2mm diameter PDMS O-ring placed at

the surface of the substrate is used to locally immerse the nanogap electrodes, leaving the rest of the circuit dry. The electrodes are first electrochemically cleaned in 0.5M H₂SO₄ by applying a series of 15 bipolar pulses at the same voltage amplitude used for electrodeposition, after which a droplet of Pt solution of identical volume is added. Similarly to cleaning, Pt deposition is performed with a series of bipolar voltage pulses and is stopped when a sudden increase of current is detected. Samples are finally rinsed with diH₂O and dried with a nitrogen stream.

4.2.2 Results and discussion

The electrodeposition of Pt was shown to be extremely dependent on the state of the electrodes surface. While cleaning by O₂ plasma mostly resulted in passivated electrodes or random grain growth, Ar plasma combined to electrochemical cleaning before electroplating yield a homogeneous surface deposition and grain sizes. Numerous voltage biases, from 0.6 to 1.2V in amplitude, have been shown to result in Pt deposition. However, for device fabrication, rather high voltages (1.2V) have been preferred in order to maximize the number of nucleation sites, obtain a smooth surface and limit self-organization of monocrystals. With such high voltages, the Pt grains are small enough to provide an excellent reduction resolution. For higher values, the nanogap electrodes couldn't withstand the deposition conditions and were very often blown away. The duration of the pulses has been chosen as the shortest possible value allowed by the SMU (20ms with I_{dc} sensing) to provide the greatest sensitivity relative to the short-circuiting events.

During electrocleaning with $\pm 1.2V$ bias in 0.5M H₂SO₄ when the electrodes are far apart, an ionic current ranging from $\pm 80nA$ to $\pm 120nA$ is usually measured, which gradually increases and reach a plateau with the number of pulses, indicating the progressive surface state enhancement.

During electrodeposition, two main phases are expected and indeed observed (Figure 4.8). In a first step, a gradual increase of the deposition current is measured, starting from 150-200nA with $\pm 1.2V$ pulses. This current increase corresponds to the augmentation of the electroactive surface, and to a lesser extent to the reduction of the electrolyte resistance because of the progressive decrease of the nanogap distance. In a second step, as electrodeposition goes on and the distance between the two electrodes decreases, a sudden current increase is observed, which corresponds to two phenomena. When the gap distance gets below a certain threshold, likely less than 10nm, in addition to an ionic current, a direct tunneling current between the electrodes tips establishes (34'' in Figure 4.8). Then if the reduction is further continued, the two electrodes finally merge, shorting the electrical circuit.

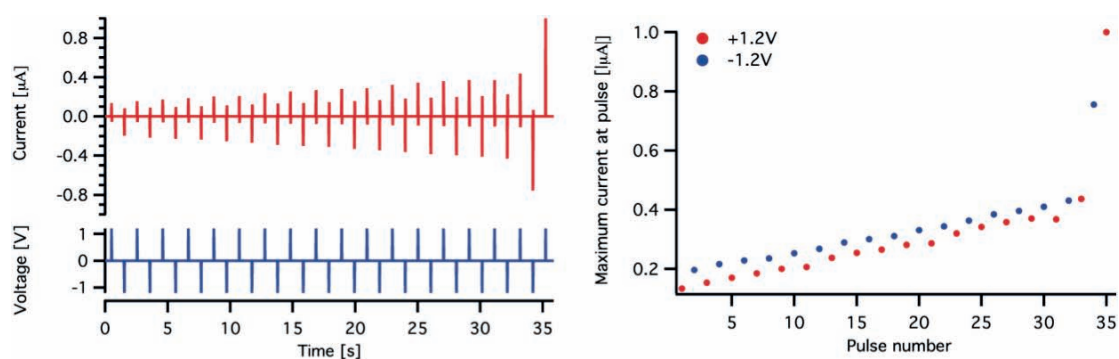


Figure 4.8. Pulsed Pt electrodeposition and short-circuit detection. (a) Bipolar voltage pulses ($\pm 1.2\text{V}$) are applied to the two-electrodes system. When the nanogap electrodes come into close contact, a sudden current increase is detected. (b) Two electrodeposition regimes are observed. First, due to the Pt surface augmentation, the deposition current gradually increases (0-34''). Second, a direct current establishes between the electrode tips, eventually followed by short-circuit ($> 34''$).

The moment at which the process is stopped is therefore crucial. Stopping the process as soon as the current increase is detected (ideally in the direct tunneling regime) results in non-shortened electrodes that are spaced by only few nanometers. A current threshold of $1\mu\text{A}$ was shown to reproducibly yield nanogaps of about 3nm (Figure 4.9). The nanogaps were considered as shorted only if the sourced voltage was measured close to 0V at the current compliance. In such a case, it is possible that part of the deposited Pt dissolves back in the electrolyte and that the gap reopens. In addition, by masking the electrodes and limiting the electroactive area to a fixed value from device to device, the process was proved to be remarkably reproducible. For 25nm-gapped electrodes, no more than 50 pulses were most of the time enough to reach saturation.

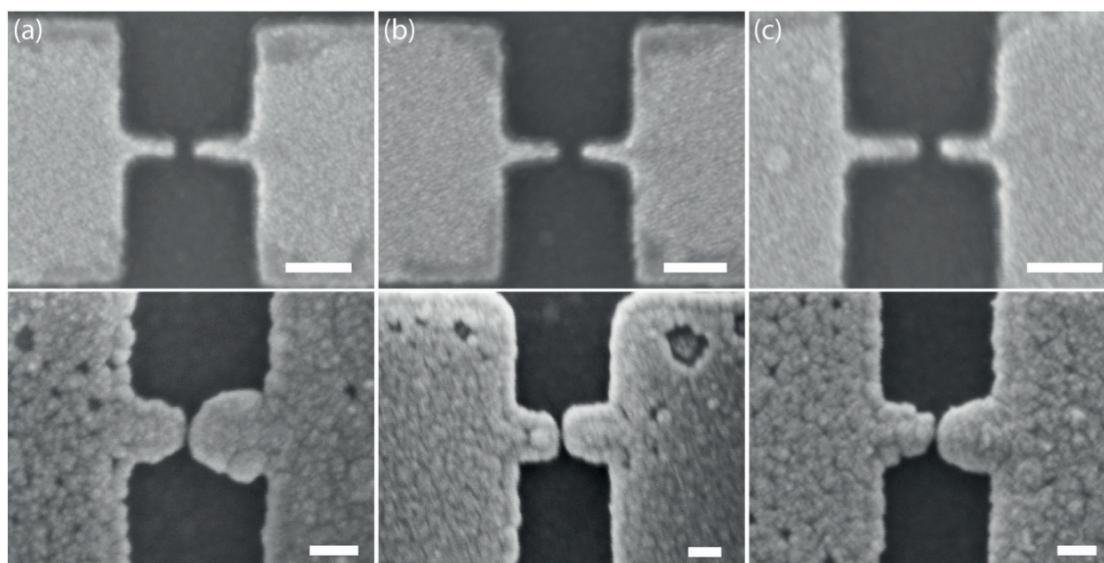


Figure 4.9. Three same devices with nanogaps before and after reduction by electrodeposition. Estimated gap sizes are below 3nm and were obtained after 34 (a) 41 (b) and 45 (c) bipolar pulses of 1.2V. Scale bars are 100nm (top) and 50nm (bottom).

The main advantage of the method presented here is its extreme simplicity combined to an excellent reproducibility. The process is realized in a two-electrodes configuration where no third electrode is needed and with a very basic instrumentation. This is important with respect to the project, because it allows a relatively high throughput fabrication. By taking advantage of the advanced EBL techniques developed earlier for the fabrication of the initial nanogap electrodes, the reduction of the nanogap can be performed in only few tens of seconds. Moreover, in the scope of DNA sequencing, the fabrication of ultrathin nanogap electrodes is needed. Using a pulse-based method, we could successfully reduce electrodes that cannot normally withstand high current densities.

4.3 Nanogap integration into a nanopore device.

4.3.1 Contacting and insulating nanogaps electrodes

Alignment challenges

The methods described above report on the fabrication of isolated sub-10nm nanogaps electrodes onto Si_3N_4 with high reproducibility and reliability, along with a very good fabrication rate. The achievement of the full device rests on the possibility to connect them to contact pads for their further integration within the outside electronics. Contacting procedures can be seen at first sight as a conventional technique in nanotechnology. However, in our case, a major challenge had to be overcome: the positioning of contacting electrodes. As very-thin films are required for the successful fabrication of sub-10nm nanogap electrodes, the resulting electrodes resistivity can be high and the distance between the gap and the contacting electrodes needs to be reduced to the maximum extent. In addition, as discussed in section 1.4.2, the contacting electrodes have to be passivated, so that thick metallic electrodes are electrochemically inactive, whilst the thin nanogap area can still be drilled. Another EBL layer is therefore needed to selectively insulate part of the device (Figure 4.10).

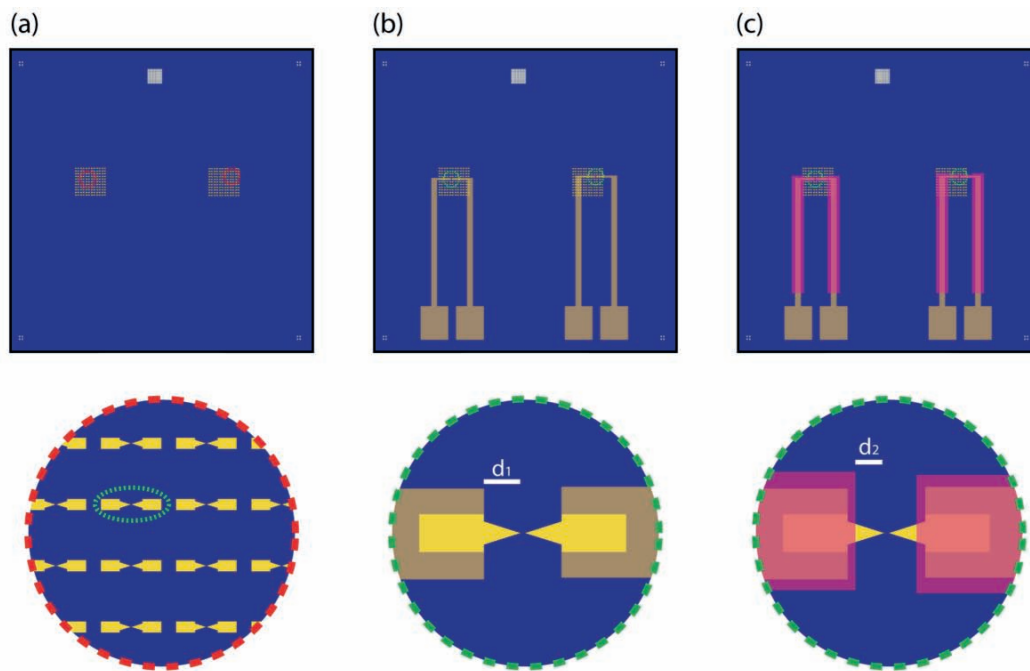


Figure 4.10. Illustration of the integration of nanogaps into functional devices and the associated alignment requirements. (a) Sub-10nm gap are first patterned with fine position control. The smallest gap is selected by SEM imaging. (b) Thicker electrodes and pads are patterned in a second EBL step. The distance d_1 between the gap and the new electrodes has to be the smallest possible. (c) The electrodes are finally protected with an insulating layer, located at distance d_2 from the gap, in a third EBL step.

After pushing the limits of EBL in term of patterns resolution, the alignment accuracy had to be mastered for performing 3 EBL layers, whose overlays are perfectly aligned. The exposure and alignment strategies will be shown to play a crucial role for limiting thermal expansion and drift.

During the first attempts for contacting nanogaps, a lot of technical issues have been encountered while trying to finely pattern macro electrodes with respect to the gap position. Despite that state-of-the-art alignment marks were used, overlay misplacements could reach several hundred of nanometers, making impossible the proper fabrication of nanogap devices (Figure 4.11a).

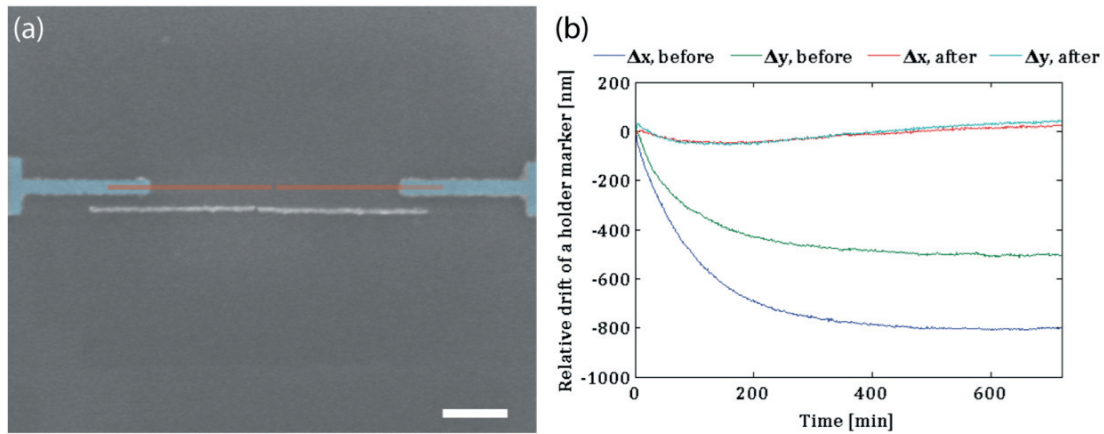


Figure 4.11. Importance of thermal drift in EBL. (a) SEM micrograph comparing the initial design (in color) to the actual patterns. The red line was written about 6 minutes after the blue pattern. A misplacement of about 100nm in x and y directions is caused by thermal drift. Scale bar: 200nm (b) Thermal drift measurements before and after optimization of the EBL experimental conditions.

Troubleshooting alignment and especially measuring the displacement of markers over time put in evidence the importance of thermal drift during exposure (Figure 4.11.b). The initial high value of marker drift during exposure was finally attributed to a mismatch between the stage temperature and the temperature at which holders are stored between successive loadings. At the beginning of our investigations, more than 10 hours were required for the thermal drift to become negligible after loading the holder onto the stage, with drift speeds of up to 8nm/min. With such high values, high-resolution overlay alignment was impossible between lithographic steps. A major improvement was achieved by adjusting the stage temperature in parallel to controlling storage temperature of holders. Indeed, the drift speed could be reduced down to 8nm/h by lowering the stage temperature of 1.5°C compared to its factory settings, while a water-cooled bench was installed to regulate holders temperature to 21.5°C prior to loading.

High-resolution alignment

For automatic alignment with high-resolution, alignment markers are patterned by EBL and RIE, yielding 2.5 μ m deep 20 \times 20 μ m squares with low line-edge roughness. By using such marks, automatic alignment is performed at high-resolution and high-contrast edges are accurately measured. In prevision of multiple lithographic layers required for the full process, 4 levels of alignment marks are structured.

Solving drift issues has been the breakthrough step for the project progress. However, small drifts can only be achieved if extreme experimental precautions are taken, and are necessary for successfully aligning lithographic layers at the nanometer scale. To minimize thermal drift during exposure, samples were loaded according to the following procedure:

- After spin-coating and baking, samples are loaded and aligned onto a substrate holder and stored for 1h at 21.5°C.
- After thermal stabilization, holders are loaded onto the stage and another thermalization step is performed by waiting 1h before starting exposure.

To minimize any undesired drift consequence on patterns placement, the writing procedure was optimized in the following way:

- When long exposures are required, jobs are fragmented into multiple short exposures whose maximum duration was fixed to 5 minutes. A new alignment is carried out between each sub-exposure.
- The features that require extreme location accuracy are always exposed first after alignment. If the required beam can't perform alignment (case of low-current beams), a higher current beam is used for this purpose, immediately followed by calibration and exposure with the low-current beam.
- All lithographic layers are aligned using the same beam and same parameters (resolution, beam step size). The same holder is preferably used for all.
- Alignment marks are positioned in a close proximity to the important exposure area. Not respecting this procedure, e.g. by placing marks at the samples' corners results in a dramatic alignment resolution.

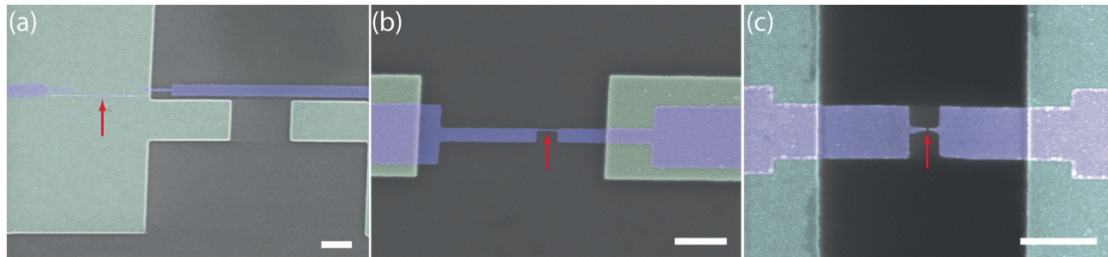


Figure 4.12. Typical overlay alignment resolution at different stages of the project. The nanogap electrodes (purple) are the first EBL layer. Micro-contacts and pads are patterned in a second EBL step on top of the nanogap and should be centered around the gap position (red arrows) The SEM micrographs are artificially colored (a). Before drift correction. (b). After drift correction. (c). After alignment markers placement optimization. Scale bars: 500nm.

The placement of the alignment markers with respect to the patterns was the second major achievement that allowed a sub-50nm overlay alignment resolution. The standard design for 1×1cm piece part provided by CMI includes 4-levels markers positioned at ($\pm 5000\mu\text{m}$; $\pm 5000\mu\text{m}$) coordinates with respect to the chip center (0, 0). Such markers lead to typical results shown in Figure 4.12b with typical misplacement of few hundreds of nanometers. The markers were therefore positioned at maximum ($\pm 700\mu\text{m}$; $\pm 700\mu\text{m}$) coordinates with respect to the nanogap position (0, 0), which furthermore led to sub-50nm resolution as shown in Figure 4.12c.

Contacting nanogaps electrodes

Most of the functional nanogaps were fabricated according to procedure described in chapter 4.1.2, by direct EBL and metallization. The initial alignment is therefore performed using a 5nA beam for coarse electrodes patterning (5nm bss and resolution, $1400\mu\text{C}/\text{cm}^2$), followed by the exposure of the nanogap electrodes with a 200pA beam (1.25nm bss and resolution, $21000\text{-}37000\mu\text{C}/\text{cm}^2$). The alignment markers are located in the center forming a surface of $1.4\times 1.4\text{mm}$, within which the patterns are exposed.

The contacting electrodes are patterned using a 5nA beam (5nm bss and resolution, $1400\mu\text{C}/\text{cm}^2$) for the region overlapping the nanogaps electrodes and a 200nA beam ($0.1\mu\text{m}$ bss and resolution, $800\mu\text{C}/\text{cm}^2$) for the rest of the electrodes and pads. Alignment is performed before the first exposure using a second set of alignment markers. Metallization is realized by evaporating 10/50nm Ti/Pt and standard lift-off in acetone at room temperature.

The contacting electrodes are patterned at a distance d_1 of 500nm from the gap center. The resulting electrodes are usually positioned with accuracy below 100nm (Figure 4.13c-d) by respecting the procedure described above.

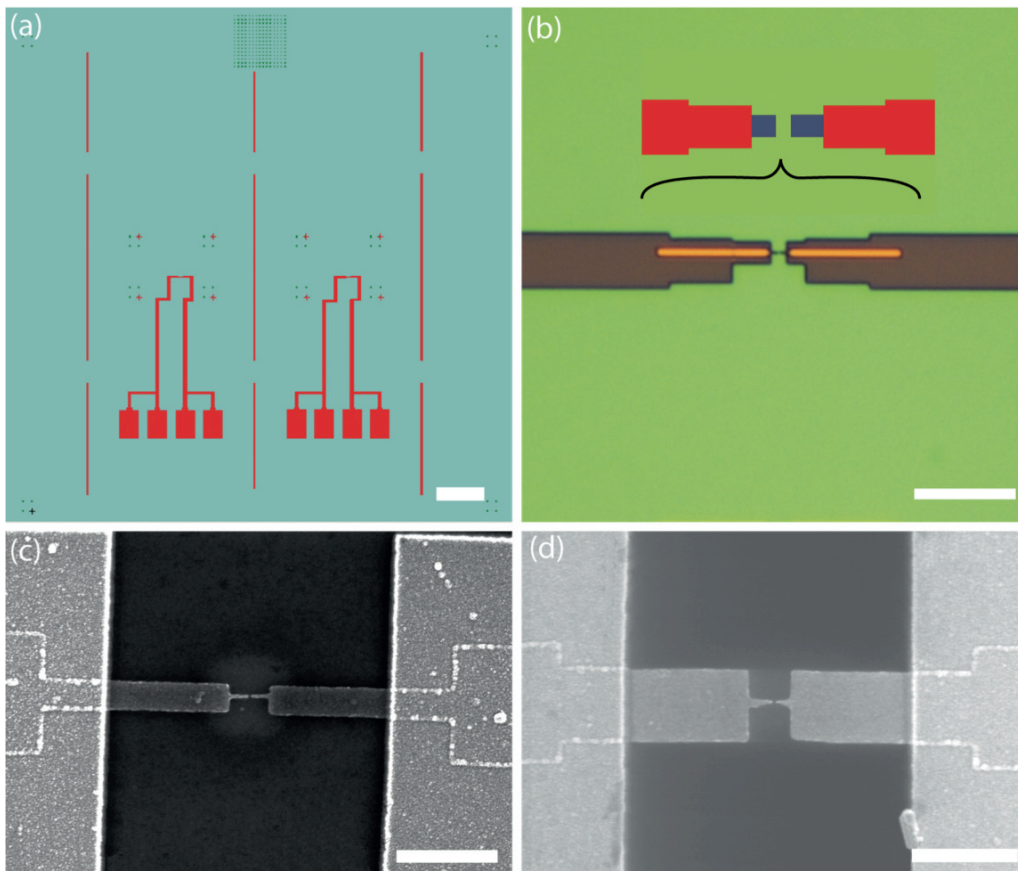


Figure 4.13. Nanogap integration into functional devices. (a) Pads and microelectrodes are designed for contacting nanoscale electrodes. Alignment is performed using nearby markers. Scale bar: 1mm (b) Optical picture after development. The blue patterns exposed first after alignment are well aligned. Red

parts written after few minutes are shifted of few tens of nanometers because of thermal drift, with no consequence on the device. Scale bar: $10\mu\text{m}$ (c, d) SEM pictures of microelectrodes contacting gaps respectively made with HSQ technique and standard EBL. Scale bars: 500nm

Electrodes passivation

Insulating the device is crucial to limit the current to flow only between the nanogap electrodes tips and avoid any current leakage that could arise from a flow between electrode areas further away from the pore. Outside of the nanogap area, the insulating layer should be thick enough to fully protect the electrodes. It is therefore performed through a 3rd EBL step (Figure 4.14).

Patterns overlapping the nanogap electrodes are first written using a 5nA beam (5nm bss and resolution, $1400\mu\text{C}/\text{cm}^2$) using a third set of alignment marks. The rest of the patterns covering the whole electrodes are then exposed using a 200nA beam ($0.1\mu\text{m}$ bss and resolution, $800\mu\text{C}/\text{cm}^2$). The patterns are transferred by evaporating 150nm of Al_2O_3 and subsequent lift-off.

The insulating layer is patterned at a distance of 300nm from the gap center, positioned with accuracy below 100nm .

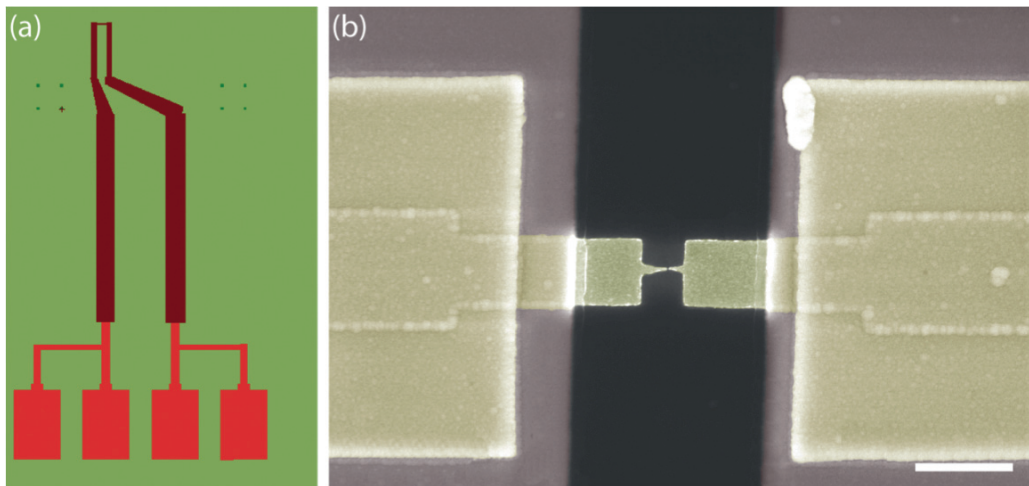


Figure 4.14. Device insulation. (a) Except the pads and nanogap area, the whole electrodes are covered with a 150nm thick layer of Al_2O_3 patterned by EBL and deposited by ebeam evaporation (brown). (b) Colored SEM micrograph of nanogap electrodes, which are left unprotected over a 600nm length, and on which a 6nm thick layer of Al_2O_3 is deposited by ALD before drilling. Scale bar: 500nm .

The electrodes in the nanogap area need to be insulated in a different way. Indeed, drilling of nanopores is only possible through membranes of thicknesses of only few tens of nm. The nanogap electrodes are therefore insulated by depositing a 6nm layer of Al_2O_3 by ALD as described in paragraph 2.3.3. Such a thin layer should be sufficient for correctly insulating small electrodes surfaces. Insulation with ALD is typically performed after KOH etching and cleaning, to ensure a perfect surface state.

4.3.2 Nanopore drilling

The silicon nitride chips with nanogap electrodes and insulation undergo a final procedure as described in paragraph 2.3.2 for membrane opening. Square membranes with sizes usually ranging from 20×20 to $30 \times 30 \mu\text{m}$ are fabricated by EBL and subsequent dry and wet etching. The initial backside opening is accurately positioned using backside EBL alignment marks, yielding membranes perfectly centered around the nanogap electrodes. In parallel to membrane opening, 1.6mm large tranches are also opened to further cleave samples into 8×4 mm devices.

After cleaning and eventually ALD as described in 2.3.3, devices are then inserted into a PHILLIPS-CM300 field emission TEM microscope operated at 200kV, using a home-built TEM holder specifically designed for accommodating $8 \times 4 \times 0.38$ mm silicon chips. Before drilling, the membrane surface is first carefully inspected to detect any membrane crack, in which case the sample is discarded.

Nanopores are drilled in between nanogap electrodes with real-time feedback imaging. Depending on the desired results, nanopores smaller than the nanogap or merging with the electrodes are obtained (Figure 4.15). In the ideal case, the electrodes tips should be in contact with the nanopore edges. For tunneling measurement, the distance between the electrodes and the target molecule is of crucial importance. Another advantage of drilling pores merging with electrodes is to eventually etch the aluminum oxide present on the tip surface, so that the metallic electrodes are in direct contact with the electrolyte. On the opposite, if a reduction of the nanopore size is needed, ALD can be performed to gradually shrink it with atomic resolution to the desired diameter.

Nanosculpting metallic electrodes on membrane using an electron beam in a high-resolution TEM microscope was previously reported by M. Fischbein and M. Drndić^[203]. It was demonstrated that complicated structures could be structured in metal with a near-atomic precision by ablation. We tried to drill nanopores directly through narrow metallic Ti/Pt nanowires in a similar fashion. However it appeared that the rate at which the metal is ablated is much lower than the rate at which the Si_3N_4 membrane itself is etched, resulting in most of the cases in 2 nanopores on the sides of the nanowire.

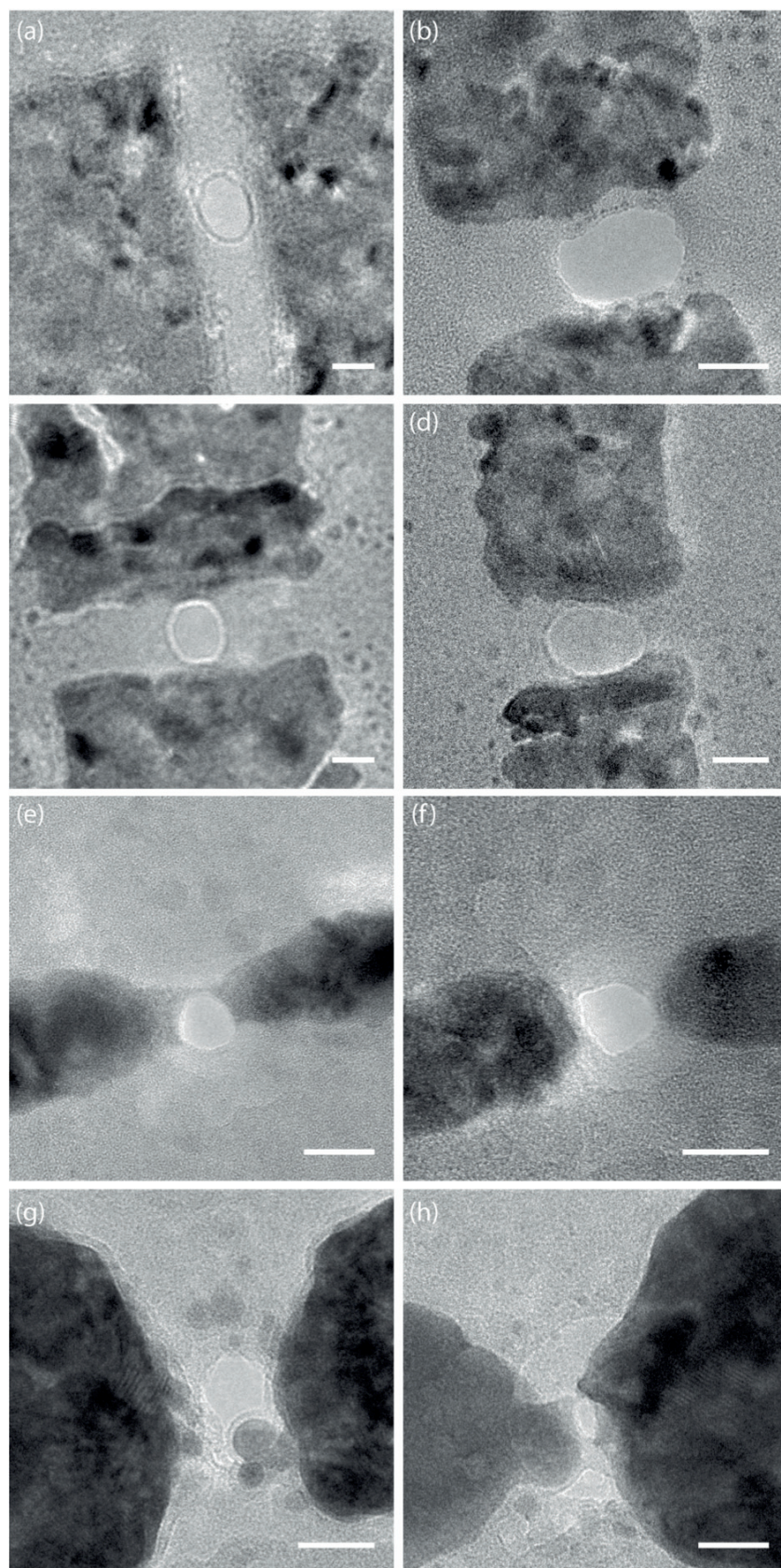


Figure 4.15. TEM pictures of nanopores embedded with metallic nanogap electrodes. (a-d). Fabricated from HSQ etching. (e-f) Fabricated by EBL and lift-off. (g-h) Nanogap reduced by platinum electrodeposition. Scale bars: 10nm.

4.4 Conclusion

We demonstrated the fabrication of devices that fulfill the entire requirements for nanopore-based DNA sequencing with metallic transverse electrodes.

By pushing the limits of electron beam lithography and lift-off, we managed to fabricate sub-10 nm nanogap electrodes with narrow tips and with an extraordinary reproducibility and process rate. In a different process, involving the combination of negative and positive EBL resist, sub-10nm nanogap electrodes of larger dimensions could also be fabricated, even though the process reproducibility is lower. It is clear that the intrinsic nature of EBL and lift-off processes always yield a size distribution, especially when patterning at the sub-10nm scale. Indeed, because of little beam current or spot size variations during EBL, or because of a distribution in the grain size of the deposited thin-film, single-nanometre resolution cannot be achieved with such an approach.

In order to compensate the difficulty to reliably pattern nanostructures of sizes below 7-8nm by EBL, an electrodeposition procedure has been worked out. Nanogaps electrodes of sizes below 30nm could be gradually reduced by pulsed DC electroplating of platinum alternatively using the two electrodes as working and counter-electrodes. By monitoring the current between the two electrodes, the moment at which they get into close proximity could be successfully detected and numerous sub-5nm nanogap electrodes could be reliably fabricated.

In parallel, the processes have been adapted to be compatible for a full integration within nanopore-based devices for DNA sequencing. In particular, the nanogap electrodes were contacted for connecting them to the whole measurement setup, while making sure that they fulfill all requirements in term of resistance and insulation in a wet electrolytic environment. The silicon wafers were customized for the fabrication of suspended insulating membrane at specific location. In such a way, solid-state nanopores can efficiently be drilled in between nanogap electrodes with a well-controlled position, shape and diameter.

In 2 years, more than 300 nanogap devices were made. Initially produced at the single chip scale, the process flow has then been scaled up to the wafer scale, allowing the fabrication of 72 functional devices per wafer. The rate-limiting step is SEM imaging of each device to ensure that the smallest nanogap electrodes are selected or for characterizing devices before electrodeposition or drilling. For less demanding project, in which the nanogap sizes can have broader size distributions, the whole process flow could be carried out with no intermediate characterization.

A home-built TEM-holder was used to fit 4×8mm silicon chips and to drill nanopores in between nanogap electrodes. Compared to SWCNTs, nanogap electrodes offer a very good contrast while drilling, which allowed to reliably mill round pores in the center of the nanogap.

After the final drilling, the devices contain nanopores with embedded sub-10nm transversal metallic electrodes and are fully functional.

Chapter 5

Study of nanopores with embedded metallic tunneling junctions

5.1 Introduction

Single-molecule sensing with transverse electrodes in a nanopore has been the object of intense studies from several groups in the past years. To overcome the limitations of the methods based on ionic current blockades, researchers have imagined different detection mechanisms based on additional transverse electrodes. Aside classical quantum tunneling, sensing may be achieved through measurements of capacitive coupling, field effect transistors (FET) or transverse current modulations. The problematic has been approached from both theoretical and experimental perspectives and various results have been reported.

Gracheva *et al.* simulated the electric response of semiconductor nanopore-capacitor sensors^[204] and suggested that DNA translocations cause the voltage between two semiconducting transverse electrodes to significantly change. However, no experimental evidence of such a device has been reported up to date, either for DNA translocation, or for single base detection by capacitive coupling measurements.

The modulation of current flowing through a nanowire by DNA molecules has also been proposed as high throughput sequencing techniques. Xie *et al.* successfully detected the translocation of DNA molecules through a nanopore drilled at the edge of a Si nanowire connected with S/D electrodes^[205]. Using such a nanowire-nanopore FET sensor, they demonstrated that localized changes in the electrical potential during DNA translocations were responsible for FET conductance decreases that correlated with the ionic current blockades (Figure 5.1a-b). Despite that this device is not yet capable of single-base resolution, this result constitutes a real motivation for high-throughput sequencing. Indeed, the fabrication of nanopores in atomically thick suspended graphene membranes is a promising route also relying on the transverse current modulation by DNA molecules. Recent experimental results have reported the ionic detection of translocations through graphene nanopores^[206,207]. Because of the monoatomic thinness of graphene compared to classical solid-state membranes, it was first imagined that single-base resolution could be achieved based on ionic current

fluctuations but further investigations are still needed. However, as for Si nanowires FET sensors, it is also possible to build a two-terminal device consisting of a graphene nanoribbon combined with a conventional solid-state nanopore. As for the mechanism proposed by Xie *et al.*, local electric potential changes induced by the translocation of individual molecules around the graphene nanopore may cause transient variations in the graphene conductance, which could reflect single-nucleotides' signature^[208,209] (Figure 5.1). Experimental efforts to achieve such a goal have been carried out by several research groups and it is very probable that publications will be released soon.

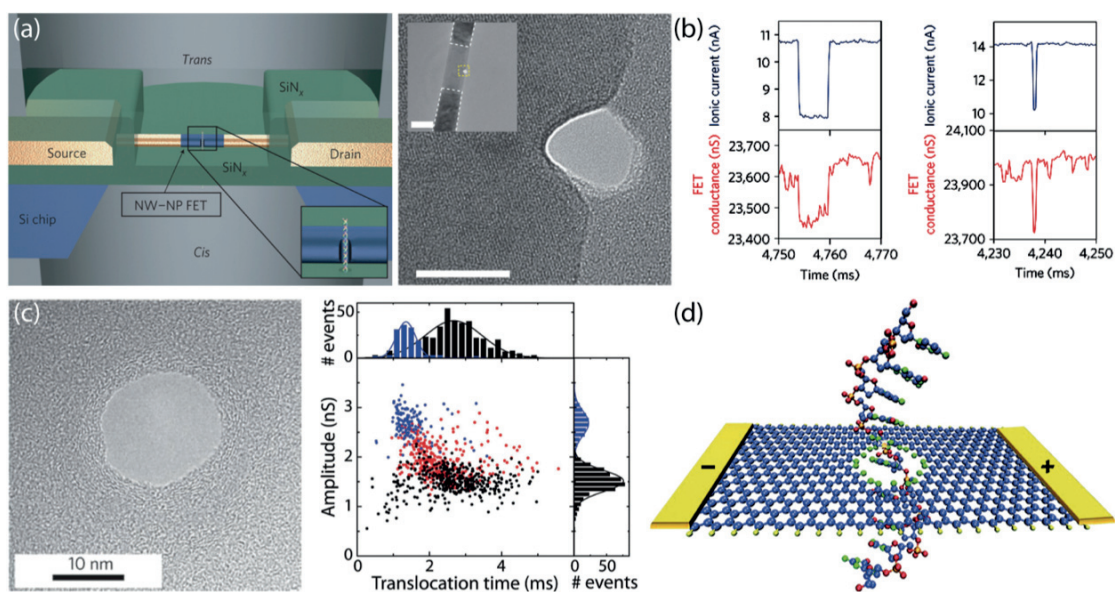


Figure 5.1. Transverse current modulation by translocating DNA molecules. (a) FET-based DNA sensors as proposed by Xie *et al.*^[205]. A solid-state nanopore is drilled through a Si₃N₄ membrane on the edge of a p-doped silicon nanowire. Localized electrical potential variations cause the nanowire conductance to change. Scale bar: 10nm (inset: 50nm). (b) Correlated ionic current and FET-conductance transient changes upon DNA translocation as published. (c) TEM picture of nanopore drilled with a focused electron beam through a graphene monolayer and corresponding DNA translocation scatter plot of the ionic current blockades amplitude versus duration. Adapted from Dekker *et al.*^[206]. (d) The use of graphene nanoribbons for transverse current modulation by DNA in two-terminal devices is a mechanism that is attracting lots of attention. Adapted from Drndić *et al.*^[208].

Finally, the use of transverse nanogap electrodes for direct tunneling current measurements is the last mechanism that is being extensively studied for single-molecule sensing. As stated earlier in chapter 1.4.1, it has been proved first theoretically^[69,72,210] and later on experimentally in a scanning tunneling microscope^[30,211,212], that the tunneling signature of individual nucleotides could be differentiated in vacuum. From these reports, the fabrication and characterization of devices exhibiting nanopores with embedded tunneling electrodes have attracted much attention. Tsutsui *et al.* first used sub-2nm gold nanoelectrodes made from mechanical break junctions to detect individual nucleotides in distilled water^[213]. With suspended nanogap electrodes in solution, they showed that electron transport

occurs by tunneling through nucleotides when freely diffusing individual bases get trapped between the tunneling tips. In such an event, characteristic current pulses were recorded and they showed that the electrical conductances of the bases were significantly different to open the way to individual bases differentiation, with current modulation due to individual bases of about 10pA. They pursued their efforts and proposed later to embed their nanogap electrodes into a planar SiO₂ layer, resulting in an in-plane nanopore formed by the nanogap itself^[214] (Figure 5.2a). In a microchannel, they could similarly detect freely diffusing mononucleotides and short DNA oligomers of up to 22 bases by tunneling measurements. However, further investigations are also needed to electrophoretically drive longer molecules and confirm their results.

There are very few experimental reports of nanopores with embedded tunneling electrodes. The main experimental challenge that we successfully overcome is indeed the high-throughput fabrication of sub-10nm nanogap electrodes combined with solid-state nanopores. Gierhart *et al.* first fabricated prototype devices that they used to detect gold nanoparticles^[215]. However, their fabrication method only yields nanogaps substantially larger than 10nm and they showed very limited evidence of tunneling detection. More recently, Ivanov and colleagues reported the fabrication of tunneling electrodes by EBID, aligned with nanopores^[201] (Figure 5.2c). Although they empirically determined the gap sizes by tunneling spectroscopy, it is unclear from their SEM pictures if whether or not the gap in the functional devices is really below 3nm. In particular, they present devices where the nanoelectrodes are not insulated, which may allow other conduction mechanisms. They also present simultaneous detections in the ionic and tunneling channels of DNA translocations. However, due to the absence of insulation and the low sampling frequency (5kHz), it is likely that they recorded non-specific DNA adsorptions on the metallic nanoelectrodes rather than actual tunneling current. More investigations are also needed in their case. The most recent experimental contribution to the field was brought by Healy and colleagues^[216] on nanogap electrodes fabricated by electron beam assisted ablation lithography in a TEM microscope. They discuss the importance of the passivation of the electrodes and the difficulty to obtain DNA translocations mostly because of device failures. They still haven't succeeded in getting evidence of tunneling current through translocation DNA molecules.

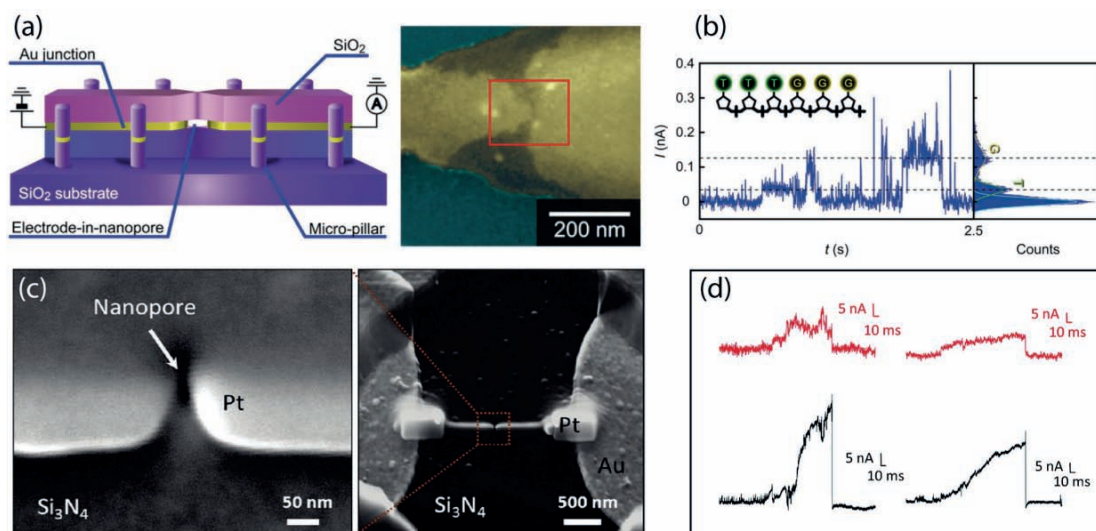


Figure 5.2. Tunneling current measurements in a nanopore. (a) In-plane nanopore-tunneling junction as reported by Tsutsui *et al.*^[214] and (b) the corresponding tunneling current recorded during the diffusion of a short T-G oligomer. (c) Tunneling junction on top of a nanopore fabricated by Ivanov and co-workers^[201]. (d) Simultaneous ionic (black) and tunneling (red) currents detection.

This chapter reports on the device characterization and DNA translocation attempts using nanopores with embedded transverse electrodes fabricated according to Chapter 4. Such a study implies the use of a very important quantity of devices. Therefore for practical reasons, most of the devices were only fabricated by EBL and were not reduced by electrochemistry to optimum tunneling sensors. As nanopore drilling is the last step of the full process, the nanogap distance can be estimated by TEM imaging prior to experimental measurements. Thus, most of the functional devices used for characterization exhibited gap sizes comprised in a range of 7 to 13nm. Microelectrodes (Ti/Pt 10/50nm) are insulated with 150nm of Al_2O_3 deposited by electron beam evaporation while the actual nanoelectrodes (Ti/Pt 3/8-20nm) are insulated with 6nm of Al_2O_3 deposited by ALD. All nanopores are drilled through 20nm Si_3N_4 membranes (20-30 μm square) on 60nm SiO_2 and Si chips.

Even though it is clear that smaller gaps are needed because of the quantum nature of direct tunneling current, the first step toward single-molecule sensing is to understand the influence of the nanogap electrodes on the nanopore behavior, notably its conductance and to understand the optimum experimental conditions for reliable DNA translocations. Only then, nanogap will have to be reduced down to the size of single-stranded DNA to achieve single-base resolution.

5.2 Influence of the nanogap electrodes on the nanopore behavior

5.2.1 Nanopore characterization

The devices characterization starts by measuring the ohmic properties of the nanopores with the nanogap electrodes disconnected (floating) from the circuit. I- V_p sweeps are therefore first performed to determine the pore ionic characteristics and conductance, where V_p is the pore voltage (Figure 2.13). To preserve the membrane integrity, sweeps are performed from 0 to up to ± 300 mV, alternating positive and negative voltages with 10sec dwell steps. Ionic current is determined with an exponential fit of the current at every plateau.

Most of the nanopores exhibit linear I-V curves within 200mV, with sometimes a non-linearity on broader sweeps. Typical results are shown in Figure 5.3. For pores around 10nm in diameter in 1M KCl, conductances from 10 to 80nS are usually measured, which is broader than the conductance model proposed by Stefan *et al.*^[54] for cylindrical to hourglass-shaped nanopores. In some cases, conductances for such pores were measured as low as 1nS. The observed discrepancy and low-conductances in nanopores are usually explained by a poor or non-reproducible wetting of the inner walls in the confined space of the nanopore or by organic residues contamination. In our case, the two sides of the membrane are coated with a thin layer of Al_2O_3 , positively charged at pH 7.4 while the nanopore walls are rather hydrophobic Si_3N_4 . Improving hydrophilicity by low-power oxygen plasma mostly resulted in aberrantly high conductances, and piranha cleaning was avoided because it is unsuitable for use with metallic electrodes. Soaking overnight nanopores in a 1:1 mixture of EtOH:diH₂O, as it was previously shown to improve pore wetting, gave satisfying results most of the time in term of linearity and stability.

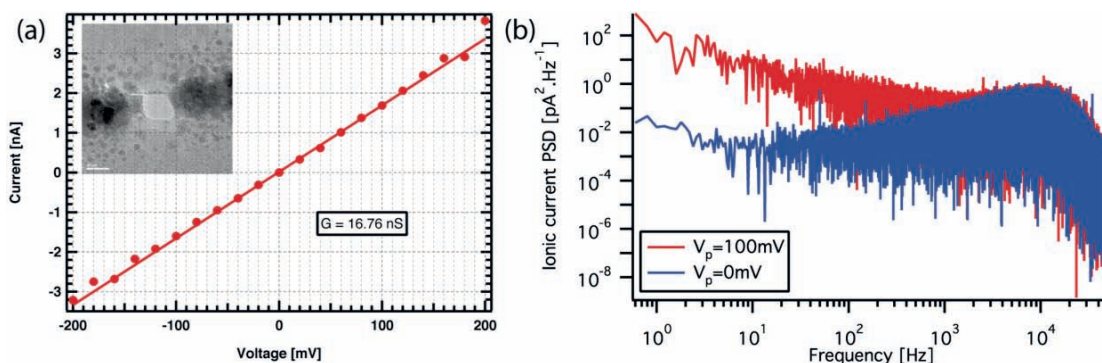


Figure 5.3. Pore behavior with nanogap electrodes disconnected from the circuit. (a) The ohmic properties of the pores are checked by I-V sweeps. Typically, conductances of few tens of nS are obtained for 10nm pores in 1M KCl. Pores with non-linear I-V curves within 200mV are discarded. (b) Power spectra density of the ionic current at pore voltage of 0 and 100mV. RMS noise of 40pA is usually achieved at $V_p=0$.

For pores with ohmic behavior and reasonable conductance, the ionic current at constant voltage was observed stable for long periods. By integration of the spectral density of the ionic current with respect to the frequency, we calculated typical RMS noise of around 40pA in 1M KCl with no transmembrane voltage. Figure 5.3b shows PSD calculated for pore voltages V_p of 0 and 100mV, giving respectively noise of 38 and 56pA. Therefore, from the analysis of the PSDs, no particular source of noise was detected when the second channel, i.e. the nanogap electrodes, is disconnected from the system. In general, the noise at low frequency in solid-state nanopores is of resistive nature and is in the form of $1/f$. In Figure 5.3, the $1/f$ noise is flat when no bias is applied and is of thermal nature. At 100mV, it has increased and corresponds to the fluctuations of the ionic flux through the pore. Hence, higher $1/f$ noise is obtained with poorly wetted or contaminated nanopores. Noise at higher frequency is associated to the membrane capacitance, and therefore, higher capacitance means higher noise, which also increases with the measurement bandwidth. Low-pass filters help to reduce noise at high frequency but necessarily induce a temporal resolution loss. The reason we choose to put an underlying SiO_2 layer between the Si_3N_4 and Si layers is therefore to lower the membrane capacitance and related noise. In addition, we also deposit another Al_2O_3 dielectric layer on the topside of the membrane for the same purpose. Finally, a last source of noise is the surface-charge fluctuations inside the pore, that can be diminished by proper functionalization^[51]. At this point, devices with non-ohmic or non-stable behaviors are discarded.

5.2.2 Nanogap characterization

In order to check the general behavior of our devices, we first checked the resistance of similar devices in which the nanogap is not present. In such devices, the design is exactly the same but the two electrodes are connected through a Ti/Pt nanowire as shown in Figure 5.4a. We measured the two terminal resistances and the robustness of the devices. For 3/5nm and 3/20nm Ti/Pt nanoelectrodes, we calculated thin-films resistance respectively in the range of 3 k Ω and 800 Ω . When performing these measurements, we observed that several devices that should have negligible resistance exhibited oppositely disconnected behaviors. After SEM investigations, it appeared that devices are very sensitive to electrostatic shocks and that extreme care has to be taken when electrically connecting the electrodes. Hence, once connected, the two electrodes are kept shorted if not connected to the system. We then determined the voltage that these devices can withstand without damage. In average, voltages of up to 100mV could safely be applied until devices would fail by electromigration.

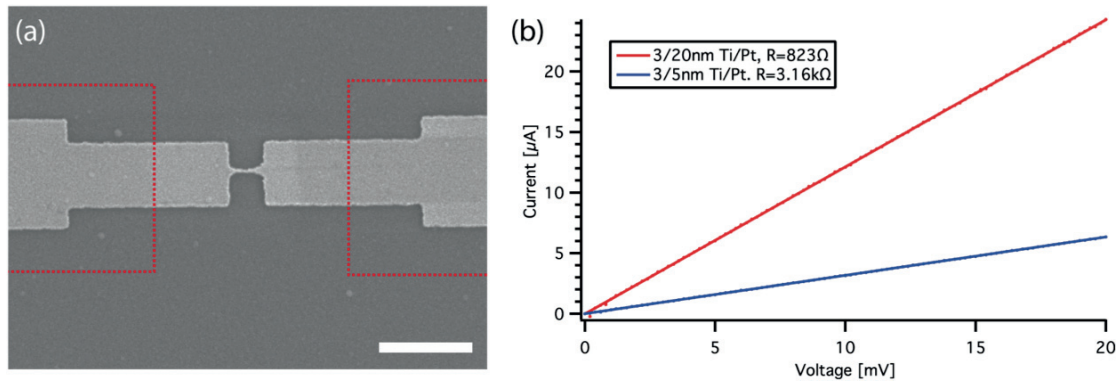


Figure 5.4. Resistance measurements on shorted nanogap electrodes. (a) The thin-films resistance was investigated with devices similar to those used for microfluidic experiments. Microelectrodes with negligible resistance (red) are contacting ultrathin films used for the fabrication of nanoelectrodes. Scale bar: 500nm. (b) 2-point resistance between few hundred ohms for 3/20nm Ti/Pt electrodes and less than 5kohms for 3/5nm Ti/Pt electrodes are typically measured.

For nanopore/nanogap devices, we move on to the characterization of the nanogap electrodes after the ohmic behavior of the pore has been checked. In the current configuration of the devices, all metallic electrodes that are in contact with the electrolyte are insulated with Al_2O_3 as explained above. For the typical experimental voltages that are applied (maximum $\pm 50\text{mV}$), the surfaces of the electrodes are therefore not electrochemically active. In the configuration where the electrodes tips have not been etched by the electron beam, no direct ionic conductance is expected. In the case where the aluminum oxide has been effectively removed, a lower resistance due to a direct current flow may be expected.

The nanogap electrodes are therefore now connected to the system. To avoid any electrostatic shock and preserve the device when connecting the second channel, the circuit is closed in presence of a variable resistor in series. From several $\text{G}\Omega$, the effective resistance is then set to 0Ω . We perform $I-V_t$ sweeps to measure the nanogap resistance with $V_p=0$. In 1M KCl with 6nm of Al_2O_3 as insulation layer, we calculate resistances comprised between few hundred of $\text{k}\Omega$ and several tens of $\text{M}\Omega$ (Figure 5.5). There is indeed a very important variability in the values measured. Besides the mechanism described above, we don't have a clear explanation for such behaviors. The nanogap resistance does not seem to correlate either with the gap distance or with the distance to the nanopore edges and the quality of the insulation remains the most probable parameter. In any case, it is important to avoid by insulation any leakage of current from metallic parts that are far from the pore and tips, as it would swamp the signal induced by translocating molecules. We check this parameter by performing $I-V_t$ sweeps at different salt concentrations (Figure 5.5) and we observe that the nanogap resistance does not scale with it. Similarly, nanogap voltage sweeps at different transmembrane potential yield similar results.

To check that there is no cross-talk between the two channels, we also record the transverse current versus the transmembrane voltage V_p and calculate what we call trans-resistance. With insulation, trans-resistance is typically higher than $50M\Omega$.

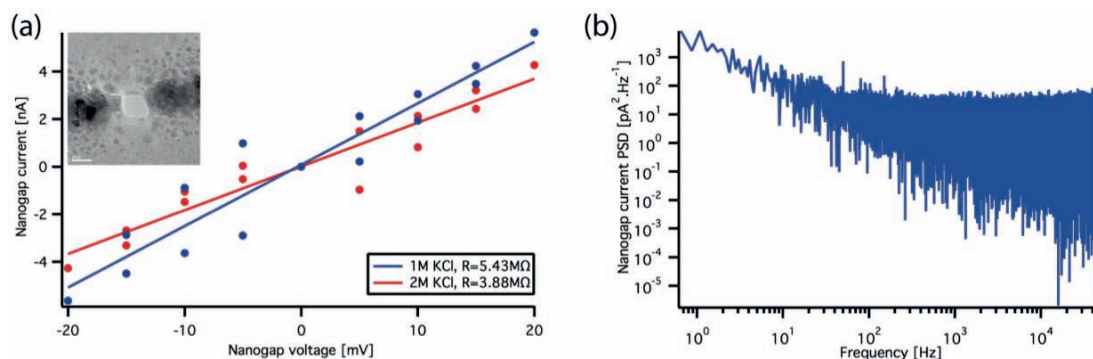


Figure 5.5. Nanogap current characterization. (a) I-V curve of the nanogap electrodes showed in the SEM picture (Scale bar: 10nm). Insulating nanogap electrodes with 6nm Al_2O_3 yields variable resistances usually in the $M\Omega$ range. (b) Power spectrum density of the nanogap current in 1M KCl. Current was recorded with a nanogap voltage of 20mV and with no ionic potential. RMS noise calculated from the PSD is 570pA.

Figure 5.5b shows a typical transverse current PSD calculated for a nanogap voltage of 20mV and an ionic voltage set to 0V. In 1M KCl, we obtain a RMS noise in the range of 600pA, which is one order of magnitude higher than the noise obtained for the ionic current.

It should also be stated that we observed some very unusual behaviors when voltages on the pore and nanogap are applied simultaneously. Specifically, we noticed on several devices an effect that could correspond to a gating of the nanogap current by the ionic voltage. Whilst the nanogap resistance is measured to $M\Omega$ with typically nA currents with no transmembrane voltage,

applying an ionic voltage may result in a drastic current increase. Normal values are recovered once the ionic current is set back to 0. Figure 5.6 shows typical current traces with the associated voltages. The transverse voltage V_t is first set to 10mV with a variation of current in the nA range. 6 seconds after the ionic voltage is set to 200mV, the transverse current increases up to more than $10\mu A$. Similarly, the transverse current returns back to its initial intensity few seconds after the pore voltage is set to 0. It is worth noting as well that the transverse voltage modifies the ionic current as discussed later in section 5.2.4.

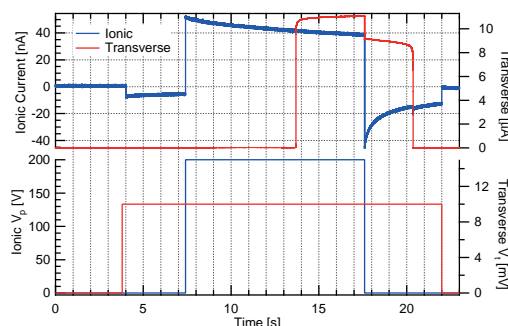


Figure 5.6. Gating of the transverse current by the transmembrane voltage.

5.2.3 Effect on noise and coupling of the two channels

In the two previous sections, we showed on one hand the PSD of the ionic current with the nanogap electrodes disconnected floating, and on the other hand the PSD of the transverse current at $V_p=0$. At the beginning of our experiments, connecting the nanogap channel resulted in the apparition of an enormous correlated noise in both channels that would have made any measurement impossible. The solution to overcome this issue was to connect the nanogap and ionic channel to the same ground, which finally allowed us to perform simultaneous recording of both current with acceptable noise.

Nevertheless, we still observe an increase of the overall ionic current noise when the second channel is connected. From the PSDs of the ionic current computed from ionic current recordings with and without the nanogap channel connected, we calculated an increase of the RMS noise that can reach hundreds of pA (Figure 5.7), 53.1pA RMS with the gap disconnected and 292pA RMS connected), which is high for ionic current. This change in the ionic noise is likely due to the increase of the membrane capacitance induced by the presence of the metallic electrodes, seen in the PSD by the increase of noise with higher frequency.

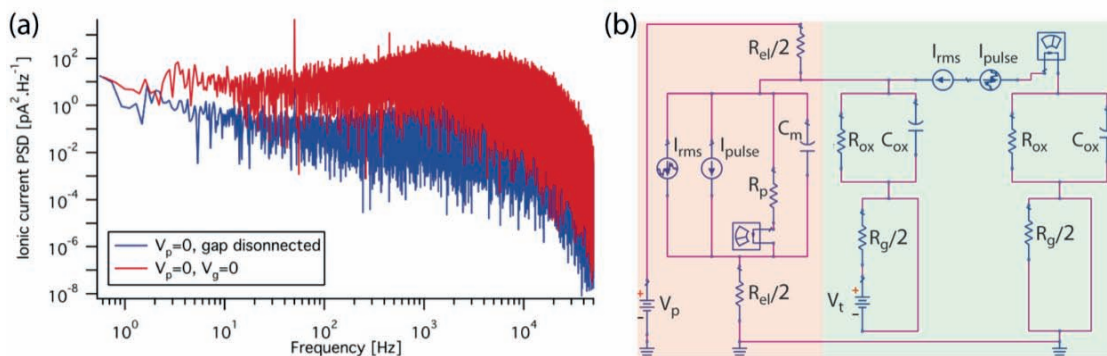


Figure 5.7. Consequence of noise of simultaneous monitoring of ionic and transverse current. (a) Comparison of the PSD of the ionic current without and with the transverse channel connected. (b) Electrical circuit model for cross-coupling analysis.

As the increase of the RMS noise of the ionic current may be a sign of a capacitive coupling between the two channels, an electrical model of the full device is being built for performing simulations and detecting any cross-coupling. The model is shown in Figure 5.7b. On the ionic channel (red), the total resistance due to the electrolyte R_{el} is split into two equal resistances for both sides of the membranes. It is dependent on the ionic strength of KCl (conductivity of 1M KCl at room temperature: $11.13 \text{ S}\cdot\text{m}^{-1}$) and can be estimated to about $5\text{M}\Omega$. The nanopore-membrane is considered as a resistor-capacitor with a resistance R_p and capacitance C_m . A conductance of 20nS corresponds to a resistance of $50\text{M}\Omega$. On the other channel (green), the two metallic electrodes are considered of equal resistances, assumed as

half of the resistance R_g measured in dry conditions for shorted electrodes ($\sim 1\text{k}\Omega$). Finally, the two electrodes are electrically connected to the electrolytic solution through the Al_2O_3 insulation layer also considered as a resistor-capacitor ($R_{\text{ox}}, C_{\text{ox}}$) and both channels share the same ground.

AC measurements on pores still need to be carried out to precisely determine the membrane capacitance as a function of the pore and transverse potential. We are still missing parameters at this point, but by simulating ionic or transverse current (I, I_{rms}) and transient current pulses in one of the two channels, it will be possible to verify that there is no correlation between the two traces or which parameters are critical to avoid any cross-talks.

5.2.4 Ionic current rectification

According to their I-V properties, nanopores can be classified in two categories. For perfectly linear I-V curves, nanopores are said ohmic and act as classical resistors. At the opposite, when non-linear I-V responses are measured, nanopores are considered as diode-like. In such cases, asymmetric I-V curves indicate a current rectification where there is a preferential direction for the ions to flow. The intensity of the rectification is often described with the rectification factor f_{rec} defined as the ratio of the ionic currents measured for pore voltages of same amplitude but opposite polarities.

We investigated the influence of the presence of the transverse electrodes on the nanopores conductance in the cases where the second channel is disconnected or connected. As shown in section 5.2.1, most of the nanopores were characterized

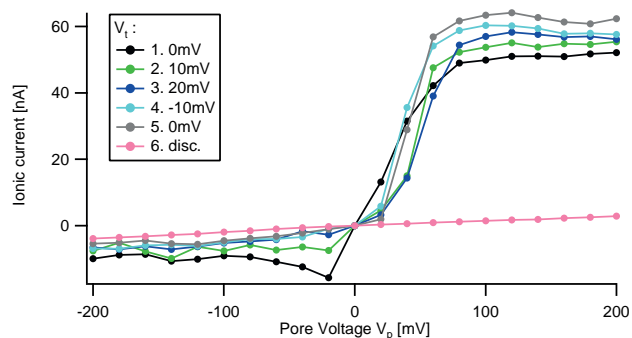


Figure 5.8. Ionic current rectification for a nanopore with connected transverse electrodes as a function of the transverse voltage. Indices indicate measurements sequence. The pink curve corresponds to disconnected electrodes.

results were sometimes substantially different when the second channel is connected where clear current rectifications could be observed. Figure 5.8 shows I-V curves of a 11nm pore measured with floating nanoelectrodes and with different transverse potential. With disconnected electrodes, the I-V response is nearly linear with a conductance calculated to 17.2nS whereas the ionic current is greatly enhanced under positive bias

when the electrodes are connected. The current rectification doesn't seem to follow a particular trend with respect to the potential V_t applied to the transverse electrodes. In the example presented here, the rectification factor is comprised between 8 and 11. For different pores, different behaviors were observed at high positive pore bias. In some cases, the current quickly reaches a plateau while it sometimes keeps increasing in the limits of the voltage sweep. In all cases however, the ionic current response at negative pore bias follows the corresponding response obtained with disconnected electrodes.

In nanofluidics systems, current rectifications mainly occurs because of asymmetric geometries or because of non-uniform surface-charges distribution^[51,217-221]. TEM-sculpted nanopores are supposed to exhibit hourglasses shapes, which are symmetric structures and we indeed didn't observe rectification in standard configuration. Therefore, connecting the electrodes must induce a modification of the surface charges that causes rectifying behaviors and in particular favors the mobility of the charge carriers at positive voltage. The mechanism is challenging to understand because the rectification behaves independently of the potential applied to the electrodes and also occurs at 0 bias. This result also differs from the conclusion drawn by Healy *et al.* who observed that the presence of nanoelectrodes does not affect the ionic current^[216].

One more time the influence of the nanoelectrodes needs to be clarified with further experiments, and it is moreover crucial to understand why rectification behaviors are observed but not all the time and if this can prevent DNA from translocating. In a first approximation, as the mobility of anions at positive voltage is enhanced, the mobility of negatively charged DNA through the channel should be favored as well.

5.3 DNA translocation detection

For DNA translocation experiments, we usually proceed first to the full characterization of the device. Similarly to the procedures described above, we establish the I-V properties of the nanopore alone and with the nanogap channel connected, as well as the characteristics of the nanogap electrodes. When linear curves are obtained and when the ionic current is steady and stable at constant pore voltage, we perform translocation measurements (see section 2.4). The DNA is flushed through the *cis* chamber in the same electrolyte conditions as used for characterization at a concentration of 50 μ g/ml. A positive potential (100-200mV) is applied to the membrane and the DNA molecules theoretically translocate from the *cis* to the *trans* side of the membrane (Figure 1.9). In the current setup configuration, the ground Ag/AgCl electrodes is therefore immersed in the *cis* side while the

working electrode in the *trans* side plays the role of current amplifier and of voltage source. The side of the device with the nanogap electrodes faces the *trans* chamber. For transverse sensing, we apply a positive potential of 20mV between the nanogap electrodes.

5.3.1 In a standard nanopore configuration

To ensure first that DNA translocations are successfully detected in a standard pore configuration, we performed measurements on solid-state nanopores drilled through identical Si₃N₄ membranes. Figure 5.9a shows translocations obtained with HindIII digested λ -DNA, which contains 8 types of DNA fragments of size ranging from 125bp to 23kb. Both chambers were filled with 1M KCl. The pore was approximately 8×10nm and a conductance of 8.95nS was measured. At $V_p=150$ mV, the current baseline was stable below 1.5nA. For translocation detections, threshold parameters were set to $5\times I_{RMS}$ for current drops and 50 μ s for dwell time. Statistical analysis was performed with a custom MATLAB code further released by C. Raillon *et al.*^[91] based on CUMSUM algorithm. Basically, automated events detection is carried out from the current-time traces, and dwell time, current drop amplitude and number of levels is extracted for every event (Figure 1.10). In Figure 5.9, the 2D scatter plot shows the distribution of the current blockades amplitude versus dwell time for 1-level events. We observe a large distribution of the dwell time, which is in agreement with the size distribution of the DNA in solution, with translocation speeds measured to 27nucleotides/ μ s at 120mV by Chen *et al.*^[59]. The analysis of the current blockade amplitudes puts in evidence two main amplitudes of 0.11nA and 0.36nA. The intensity of the current drops is associated to the excluded volume during translocation, which is itself linked the conformation of the translocating molecule (head-to-tail, one-coil, etc.). Deeper current blockades therefore correspond to molecules translocating in folded conformation. In addition, bumping events, which are collisions of molecules with the pore entry without further translocation, may also induce currents drops of very short lifetime.

Such results are in agreement with the literature for solid-state nanopores and double stranded DNA^[222] and prove that with the current design of our nanopore sensor in absence of transverse electrodes, it is possible to obtain, detect and analyze translocations of single DNA molecules.

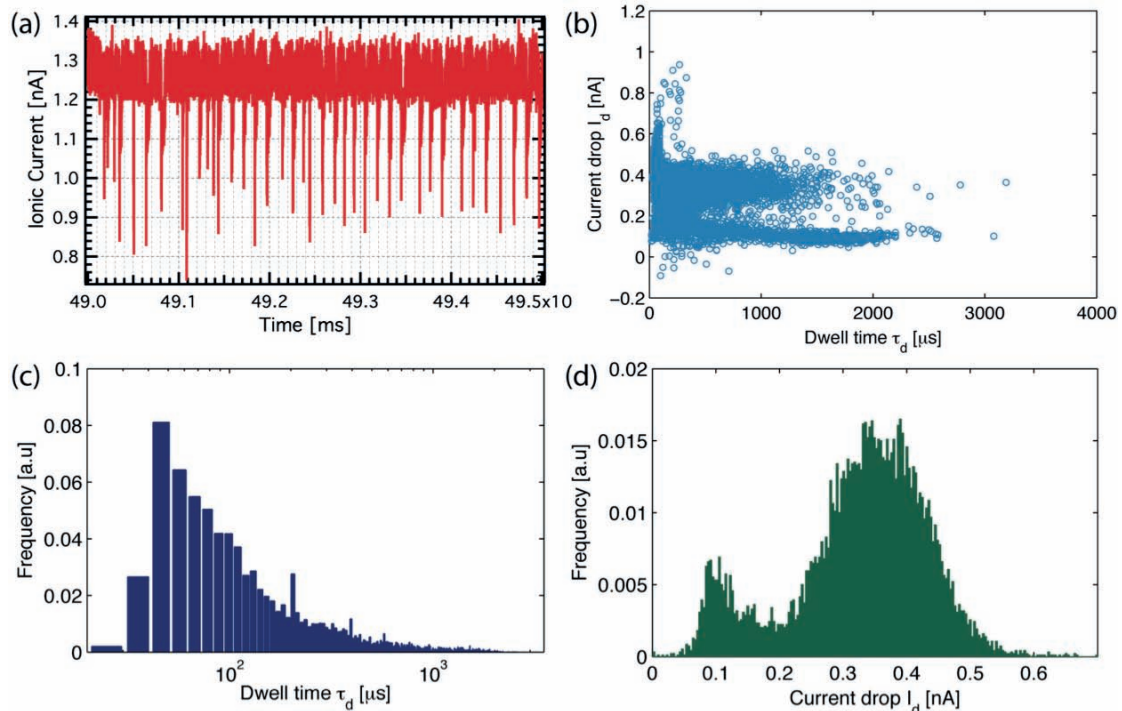


Figure 5.9. DNA translocation through a bare Si_3N_4 nanopore. (a) Ionic current-time with DNA translocations. (b) Current drop amplitude vs dwell time of ionic blockades events. (c-d) Dwell times and amplitudes distributions (see Figure 1.10).

5.3.2 By simultaneous measurements of the ionic and transverse current

The conclusion of the previous section is extremely important because the situation is dramatically different in the presence of transverse electrodes. Healy *et al.*^[216] recently claimed that DNA translocations were not affected by the presence of such nanogap electrodes in the vicinity of the pore with or without insulation but interestingly enough, they also mentioned that post-experimental TEM imaging revealed that for most of the devices, the metallic junction had ruptured and disappeared on several micrometers from the pore entry. At the opposite, we noticed for the moment an extreme difficulty of detecting DNA translocations with devices that are not damaged after experiments.

The fact that translocations don't occur can be explained by several reasons. As shown in Figure 1.9, DNA molecules freely diffuse in solution until they get within the nanopore capture radius where their motion is biased toward the nanopore entry. Then, molecules can either bump onto the aperture or translocate through the channel. The capture radius is a complex parameter to model but mostly depend on the transmembrane voltage, surface charges and salt conditions.

We tested numerous experimental conditions that could favor DNA translocation and improve the events frequency. By working at rather high DNA concentration (50 $\mu\text{g}/\text{ml}$), the diffusion-limited regime should be avoided. We also tried numerous

transmembrane voltages both positive and negative, from ± 50 to ± 300 mV that should resolve any energy or entropic barrier at the pore entry in normal situation.

At pH 7.4, Al_2O_3 is supposedly positively charged, which is favorable to negatively charged DNA molecules. However, to investigate the effect of surface charges, we tested numerous salt concentrations (10 mM–2 M) either in symmetric situation (both reservoirs with same concentration) or in a salt gradient (1 M-*cis*, 10 mM-*trans* as suggested by Xie *et al.*^[205]). We also tested functionalization of the surface with APTES to ensure a net positive surface charge^[223].

None of these conditions permitted reliable DNA translocations. To make sure that it was not a detection issue, we checked several times by PCR (polymerase chain reaction) the presence of DNA molecules in the *trans* reservoir after experiments, which all turned out as negative. Therefore, we believe that the presence of nanoelectrodes may prevent DNA from translocating but no clear explanation of a precise mechanism could be established yet. On one hand, the electric potential drop at the nanopore may be disrupted, affecting the capture radius and reducing it to such a small size that the probability for a molecule to enter it becomes negligible. On the other hand, the electrodes may induce an electrostatic barrier that the molecules can't overcome. We tested translocations with the electrodes disconnected, grounded or under numerous positive and negative potential, and none of these conditions seemed to particularly influence the occurrence of events.

Out of tens of devices on which we attempted DNA translocations, only few of them exhibited successful translocations, with a very low event frequency. The following results were extracted from a 11×9 nm pore embedded with nanogap electrodes spaced by 13 nm (Figure 5.1a), that is the only device from which we observed correlated events in the ionic and transverse currents. The pore had linear ohmic behavior within 200 mV and a conductance of 119.0 nS was calculated with in 1 M KCl (*cis/trans*) and with the transverse channel disconnected. A slight current rectification was observed with the nanoelectrodes connected at 0 potential, and with a conductance of 133.7 nS with 0 mV on the nanoelectrodes (165.7 nS with $V_t = 20$ mV). The nanoelectrodes were measured with a resistance of 13.8 M Ω . After flushing DNA in both reservoirs, the translocations were detected with an ionic potential V_p of -100 mV and a transverse voltage V_t of 20 mV. In such configuration, the *cis* chamber is the side of the membrane where the nanoelectrodes are.

The 2D scatter plot of the ionic current blockades shows results consistent with the translocation of DNA molecules, although only translocations of around 1 ms were measured. The mean current drops amplitude was calculated as 1.41 ± 0.90 nA. Strikingly, the analysis of the ionic current and transverse current traces put in

evidence that whilst numerous events were only present in the ionic channel, many events could however also be observed in both channels simultaneously. As we don't know what to expect in term of amplitude or sign for transverse current events, we analyzed the transverse current manually with respect to the ionic current events. Few typical examples of coincident events are shown in Figure 5.10h. While we expect transient positive pulses for tunneling current measurements, we observe here sudden current drops as for ionic events, whose durations are well correlated between the two channels. Such a behavior can be explained by the following mechanism. When the nanochannel is free of molecules, a direct ionic current flows between the two electrodes tips, with an intensity that depends on the state of the tip insulation and gap distance. As for standard ionic current events, the transverse current of ionic nature is partially blocked when a molecule translocates, resulting in a brief decrease and recovery to its initial value.

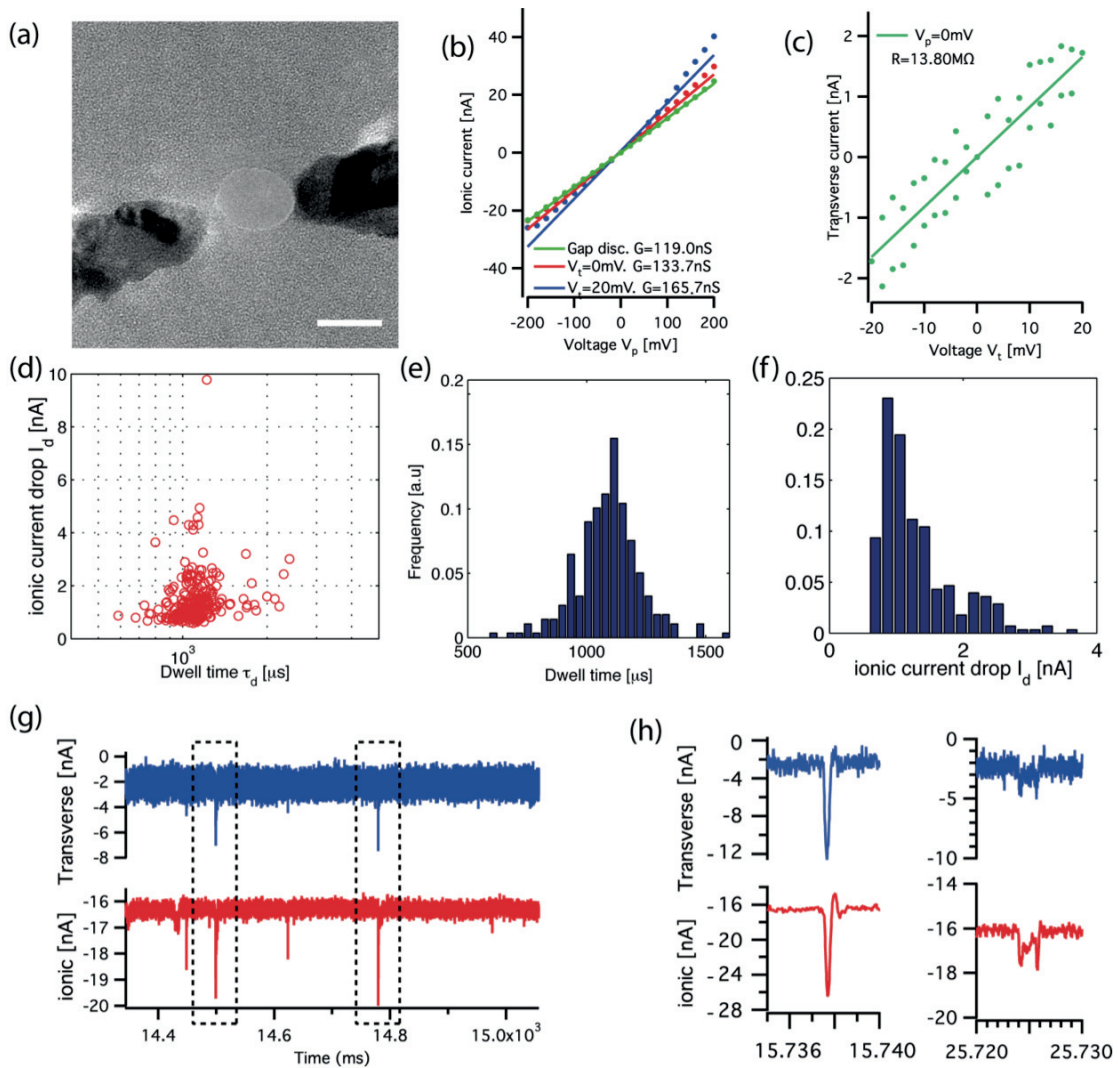


Figure 5.10 Simultaneous detection of translocation events in ionic and transverse current traces. (a) SEM image of the nanopore with the transverse metallic electrodes. Scale bar: 10nm (b-c) I-V properties of the ionic and transverse current in 1M KCl. (d) Dwell time and drop amplitude of the ionic current events as detected for HindIII digested λ -DNA (e-f) Dwell times and amplitudes

distributions analysis. (g-h) Examples of correlated events in the ionic channel (red) and transverse channel (blue) recorded during DNA translocations.

More investigations are needed to evaluate the importance of these results, but they constitute a very promising and exciting proof-of-principle experiment for sensing single molecule in a nanopore with transverse electrodes. In particular, the intensity of the transverse current drops needs to be correlated with the ionic strength of the solution, in order to assess the origin of the events. The correlation of the dwell times in the two channels also needs to be studied in deeper details and to be linked to the DNA length on solution.

5.4 Discussion

We have developed a reliable fabrication method that allowed us to start investigating and characterizing solid-state nanopores with embedded metallic electrodes and to obtain a proof-of-principle experiment showing that single-molecule analysis by transverse current measurements is very close to be achieved.

During almost a year of device assessments, we faced multiple types of failure, from device failures to the impossibility of detecting DNA translocations. The first consequence of this was the need for a tremendous number of devices, and most importantly, of a fast and reliable method of fabrication that can continuously supply new functional sensors. First, wet etching in KOH for membrane opening is a step that had required a long optimization and been a source of a non-negligible loss. Poorly controlled procedure may result in membrane cracks or in case of leakage, in lost nanogap electrodes. At the current stage of the project, roughly 80% of the devices survive all the steps until drilling. Once drilled, the chips need to be carefully loaded in the microfluidic cell and we estimate to about 20% the tested devices that have either a too high conductance (membrane leakage), no conductance (pore clogged) or unstable behaviors. In particular, low-conductance nanopores are an important source of devices loss because they exhibit usually a too-high noise level. Then, we designed our devices so that the microelectrodes contact the nanoelectrodes as close as possible to the nanogap, so that the less robust thin metal film has less chance to be damaged under normal experimental conditions. SEM investigations showed that nanoelectrodes were indeed most of the time intact after experiments but also that in some case the gap also enlarge a little (Figure 5.11b). Finally, the low occurrence of DNA translocations in most of the devices and the need to test several different experimental conditions constituted the main source of device use and has prevented us to extensively investigate DNA translocation and transverse sensing properties. Nevertheless, functional devices were shown to be incredibly robust.

When manipulated with care, devices could be used, dried, and reused again several times without mechanical or electrical rupture and with consistent and reproducible behaviors.

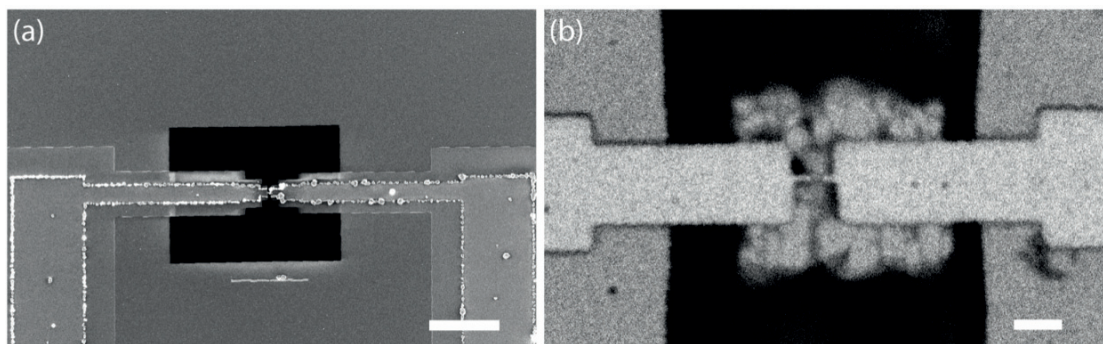


Figure 5.11. SEM images of a device after measurements. (a) Top view of the metallic electrodes and membrane. Scale bar: 20 μ m (b) Backside view (BSE) showing little enlargement of the nanoelectrodes and salt accumulation. Scale bar: 200nm.

From the recent experimental reports in the literature and our personal experience, it is very probable that the question of the feasibility of DNA sequencing with solid-state nanopores and tunneling electrodes will be answered soon. We showed that the fabrication of such single-molecule sensors could be overcome and that only experimental issues for measurements need to be resolved. First we observed that connecting the nanoelectrodes to the system results in an ionic current rectification, especially by affecting the ionic transport under positive bias and that this phenomenon doesn't occur when the electrodes are disconnected. We also observed an increase of the ionic noise when the electrodes are connected, likely due to the increase of capacitance of one side of the membrane with respect to the other or to a capacitive coupling between the two channels. Finally, we showed a relative difficulty to obtain DNA translocation in presence of transverse electrodes compared to bare solid-state nanopores. However the fact that we obtain an experiment where events seemed to be detected in both channels pushes us to continue experimental assessments. Several experimental conditions indeed are still to be tested. We used Al_2O_3 to insulate the electrodes but other dielectric should be tested to extensively study the influence of surface charges. The thickness may also have to be optimized to make sure of a proper passivation. We also didn't carry out ALD after pore drilling and tuning the inner cavity of the pore may also help translocations. Finally, we are also building a COMSOL model to simulate the electric potential profile under various experimental conditions. It is very likely that there is a combination of working voltages, ionic strength and surface charges that will make possible reproducible translocations of DNA through nanopores with embedded tunneling electrodes.

Once the optimum conditions will be worked out, we will be able to take advantage of the possibility of fabricating nanometer sized tunneling electrodes for direct tunneling measurements.

Conclusion and perspectives

The road is still long to achieve high-throughput DNA sequencing with nanopore-based devices, but although there are many experimental challenges that will have to be overcome, the possibilities and advantages that they offer is more than motivating to pursue the research. This dissertation has presented the first steps toward achieving single-molecule sensing and sequencing with nanopores and tunneling electrodes.

A particular focus has been put on solving fabrication issues that are fundamental for making devices that respect the geometrical constraints imposed by the theory. A reliable solid-state nanopore fabrication was first worked out. By EBL and etching, 20nm thick Si_3N_4 membranes of custom dimensions and with a micrometer positioning resolution could be opened. A custom TEM holder was used to accommodate the devices and proceed to nanopores formation. Circular nanopores of sub-10nm dimensions could be drilled by condensing the electron beam at any desired location, offering a real time size-control. By electron irradiation or ALD deposition in post procedures, the final diameter can be finely tuned.

As tunneling current exponentially decays with distance, it is crucial that the distance between the electrodes tips is short enough to let a single stranded DNA molecule translocate through the pore and that they are perfectly aligned along the nanopore diameter. We investigated the opportunity offered by the electronic properties and aspect ratio of SWCNTs to fabricate unique tunneling probes. A synthesis method of individual long SWCNTs with location control has been established, allowing to electrically address single SWCNTs with source and drain contacts on solid-state membranes compatible with nanopore sculpting in a TEM microscope. A specific emphasis was put on obtaining a reasonably fast and high throughput process, which is a common experimental issue for CNTs applications. For embedding carbon nanoelectrodes on the edge of a nanopore, a high-energy electron beam was used to cleave a single nanotube and drill a nanopore in a single step. Two major issues were faced: SWCNTs don't offer enough contrast during the drilling process, which most of the time resulted in misplaced nanopores. For larger diameter CNTs, a retraction of the CNT tips over several nanometers was observed, yielding dramatically large tunneling junctions.

Anticipating contact resistance and electronic properties discrepancies as well as above issues, intense efforts have also been made on a fast production procedures of metallic tunneling junctions on Si_3N_4 membranes. So far, the study of tunneling electrodes in nanopores had been limited by the poor control over the gap size in

nanoelectrodes and the slow existing fabrication methods. By optimizing and pushing the limits of EBL, we could fabricate sub-10nm metallic nanogap electrodes compatible with nanopore fabrication in TEM, and at the wafer scale. Besides the spectacular reproducibility of the method, a key advantage of the devices is their very good robustness. On one side, the electrodes geometry was optimized to resist to experimental conditions, while on the other side, the membrane showed very little occurrence of rupture. To reach tunneling capabilities, we further reduced the nanogap size by electrodeposition of platinum. With a pulsed deposition method, the final size of the gap could be controlled by monitoring the current between the two electrodes successively used as counter and working electrodes. Nanogaps as small as 3nm were reliably produced. Finally in a TEM microscope, nanopores could be drilled in between the electrodes with excellent control, offering the advantage as well to image the final gap dimensions.

Thanks to the exceptional throughput of the method, a continuous device fabrication was possible and allowed their experimental characterization for single-molecule sensing. In a microfluidic cell, we started studying the properties of these devices and the detection of DNA translocations with simultaneous ionic and transverse current. Noise issues had to be overcome but simultaneous measurements of the two channels is now possible. With the current devices design, the main conclusion that may turn out dramatic is the very low occurrence of DNA translocations in the presence of nanoelectrodes in the pore vicinity, where most of the devices didn't give rise to translocation events. Nevertheless, simultaneous detections of DNA in both ionic and transverse channels could be obtained with a device, which constitute a promising proof-of-principle experiment.

After outrageously challenging fabrication and experimental measurement issues, one may consider that everything starts now, and this would be true. Once the issue on DNA translocation will be solved, tunneling investigations will finally be possible. With junction of the appropriate size, it is a matter of time before real tunneling in a nanopore is reported. Only then, experimental conditions will have to be optimized for reaching single-nucleotide resolution, but fortunately, all researchers are heading in the same direction. Successful attempts for slowing down DNA translocation have been reported, by reducing temperature, increasing viscosity, engineering the pore walls or enzyme-driving DNA. The transverse electrodes may also be functionalized with molecular adapters to (i) orient DNA in the pore but also (ii) to slow down DNA. Metallic transverse electrodes are a here a perfect match because the surface chemistry of gold for example has been widely studied. For instance, short oligomers can be attached to the pore inner cavity and slow down translocating DNA by complementary bonding while other molecules tethered on the electrode tips would

specifically orient nucleotides in the junction. Nanopore sequencing is also exploring new fields, especially when one considers graphene nanopores, which could be combined to tunneling junctions. Graphene is a mono-atomic flat zero-gap semiconductor, which could on one hand enhance the sensitivity of ionic current measurements, but also simultaneously play the role of transverse FET sensor.

If nanopore sequencing is achieved, it will impact everyone's life and have unlimited applications. DNA molecules as long as several tens of kbp can be threaded through nanopores and measurements can be parallelized on a single chip exhibiting arrays of nanopore-based sensors. Moreover, the cost for full genome sequencing will become inexpensive, because no labeling, no amplification and milliliter reagent volumes are needed. But nanopore technologies are not only sequencing. Numerous other applications are foreseen. Sizing, sorting and counting, structural and electrical characterization of single molecules or nanoparticles is an example. Protein folding, binding assays, molecular recognition, force sensing are other possibilities.

Nanopore technologies are so promising that in the years to come there will be even more intense study and concrete application.

Bibliography

1. Feynman, R.P., *There's Plenty of Room at the bottom*. Engineering and Science, 1960. **23**:5:22.
2. Fuechsle, M., J.A. Miwa, S. Mahapatra, H. Ryu, S. Lee, O. Warschkow, L.C.L. Hollenberg, G. Klimeck and M.Y. Simmons, *A single-atom transistor*. Nat Nano, 2012. **7**(4):242.
3. Moore, G.E., *Cramming more components onto integrated circuits*. Electronics, 1965. **38**(8).
4. Wong, E.W., P.E. Sheehan and C.M. Lieber, *Nanobeam Mechanics: Elasticity, Strength, and Toughness of Nanorods and Nanotubes*. Science, 1997. **277**(5334):1971.
5. Rief, M., H. Clausen-Schaumann and H.E. Gaub, *Sequence-dependent mechanics of single DNA molecules*. Nat Struct Mol Biol, 1999. **6**(4):346.
6. Rief, M., M. Gautel, F. Oesterhelt, J.M. Fernandez and H.E. Gaub, *Reversible Unfolding of Individual Titin Immunoglobulin Domains by AFM*. Science, 1997. **276**(5315):1109.
7. Wang, M.D., H. Yin, R. Landick, J. Gelles and S.M. Block, *Stretching DNA with optical tweezers*. Biophysical Journal, 1997. **72**(3):1335.
8. Betzig, E., G.H. Patterson, R. Sougrat, O.W. Lindwasser, S. Olenych, J.S. Bonifacino, M.W. Davidson, J. Lippincott-Schwartz and H.F. Hess, *Imaging Intracellular Fluorescent Proteins at Nanometer Resolution*. Science, 2006. **313**(5793):1642.
9. Lyubchenko, Y.L., *Preparation of DNA and nucleoprotein samples for AFM imaging*. Micron, 2011. **42**(2):196.
10. Odom, T.W., J.-L. Huang, P. Kim and C.M. Lieber, *Atomic structure and electronic properties of single-walled carbon nanotubes*. Nature, 1998. **391**(6662):62.
11. Dai, H., *Carbon nanotubes: opportunities and challenges*. Surface Science, 2002. **500**(1-3):218.
12. Branton, D., D.W. Deamer, A. Marziali, H. Bayley, S.A. Benner, T. Butler, M. Di Ventra, S. Garaj, A. Hibbs, X. Huang, S.B. Jovanovich, P.S. Krstic, S. Lindsay, X.S. Ling, C.H. Mastrangelo, A. Meller, J.S. Oliver, Y.V. Pershin, J.M. Ramsey, R. Riehn, G.V. Soni, V. Tabard-Cossa, M. Wanunu, M. Wiggin and J.A. Schloss, *The potential and challenges of nanopore sequencing*. Nat Biotech, 2008. **26**(10):1146.
13. <ftp://ftp.ncbi.nih.gov/genbank/gbrel.txt>.
14. Human Genome Sequencing, C.I., *Initial sequencing and analysis of the human genome*. Nature, 2001. **409**(6822):860.
15. Human Genome Sequencing, C.I., *Finishing the euchromatic sequence of the human genome*. Nature, 2004. **431**(7011):931.
16. Watson, J.D. and F.H.C. Crick, *Molecular Structure of Nucleic Acids: A Structure for Deoxyribose Nucleic Acid*. Nature, 1953. **171**(4356):737.
17. Maxam, A.M. and W. Gilbert, *A new method for sequencing DNA*. Proceedings of the National Academy of Sciences, 1977. **74**(2):560.

18. Sanger, F., S. Nicklen and A.R. Coulson, *DNA sequencing with chain-terminating inhibitors*. Proceedings of the National Academy of Sciences, 1977. **74**(12):5463.
19. Smith, L.M., J.Z. Sanders, R.J. Kaiser, P. Hughes, C. Dodd, C.R. Connell, C. Heiner, S.B.H. Kent and L.E. Hood, *Fluorescence detection in automated DNA sequence analysis*. Nature, 1986. **321**(6071):674.
20. Pettersson, E., J. Lundeberg and A. Ahmadian, *Generations of sequencing technologies*. Genomics, 2009. **93**(2):105.
21. Staden, R., *A strategy of DNA sequencing employing computer programs*. Nucleic Acids Research, 1979. **6**(7):2601.
22. Nyrén, P.I. and A. Lundin, *Enzymatic method for continuous monitoring of inorganic pyrophosphate synthesis*. Analytical Biochemistry, 1985. **151**(2):504.
23. Rothberg, J.M. and J.H. Leamon, *The development and impact of 454 sequencing*. Nat Biotech, 2008. **26**(10):1117.
24. Metzker, M.L., *Sequencing technologies - the next generation*. Nat Rev Genet, 2010. **11**(1):31.
25. Shendure, J., G.J. Porreca, N.B. Reppas, X. Lin, J.P. McCutcheon, A.M. Rosenbaum, M.D. Wang, K. Zhang, R.D. Mitra and G.M. Church, *Accurate Multiplex Polony Sequencing of an Evolved Bacterial Genome*. Science, 2005. **309**(5741):1728.
26. Braslavsky, I., B. Hebert, E. Kartalov and S.R. Quake, *Sequence information can be obtained from single DNA molecules*. Proceedings of the National Academy of Sciences, 2003. **100**(7):3960.
27. Ansorge, W.J., *Next-generation DNA sequencing techniques*. New Biotechnology, 2009. **25**(4):195.
28. Shendure, J. and H. Ji, *Next-generation DNA sequencing*. Nat Biotech, 2008. **26**(10):1135.
29. Edwards, J.R., H. Ruparel and J. Ju, *Mass-spectrometry DNA sequencing*. Mutation Research/Fundamental and Molecular Mechanisms of Mutagenesis, 2005. **573**:3.
30. Huang, S., J. He, S. Chang, P. Zhang, F. Liang, S. Li, M. Tuchband, A. Fuhrmann, R. Ros and S. Lindsay, *Identifying single bases in a DNA oligomer with electron tunnelling*. Nature Nanotechnology, 2010. **5**(12):868.
31. Coulter, W.H., *Means for counting particles suspended in a fluid*, 1953, Coulter Wallace H.: USA.
32. Storm, A.J., C. Storm, J.H. Chen, H. Zandbergen, J.F. Joanny and C. Dekker, *Fast DNA translocation through a solid-state nanopore*. Nano Letters, 2005. **5**(7):1193.
33. Wanunu, M., J. Sutin, B. McNally, A. Chow and A. Meller, *DNA Translocation Governed by Interactions with Solid-State Nanopores*. Biophysical Journal, 2008. **95**(10):4716.
34. Lieberman, K.R., G.M. Cherf, M.J. Doody, F. Olasagasti, Y. Kolodji and M. Akeson, *Processive Replication of Single DNA Molecules in a Nanopore Catalyzed by phi29 DNA Polymerase*. J Am Chem Soc, 2010. **132**(50):17961.
35. Kasianowicz, J.J., E. Brandin, D. Branton and D.W. Deamer, *Characterization of individual polynucleotide molecules using a membrane channel*. Proceedings of the National Academy of Sciences, 1996. **93**(24):13770.
36. Akeson, M., D. Branton, J.J. Kasianowicz, E. Brandin and D.W. Deamer, *Microsecond Time-Scale Discrimination Among Polycytidylic Acid*,

- Polyadenylic Acid, and Polyuridylic Acid as Homopolymers or as Segments Within Single RNA Molecules.* Biophysical Journal, 1999. **77**(6):3227.
37. Meller, A. and D. Branton, *Single molecule measurements of DNA transport through a nanopore.* Electrophoresis, 2002. **23**(16):2583.
 38. Dekker, C., *Solid-state nanopores.* Nat Nano, 2007. **2**(4):209.
 39. Braha, O., B. Walker, S. Cheley, J.J. Kasianowicz, L. Song, J.E. Gouaux and H. Bayley, *Designed protein pores as components for biosensors.* Chemistry & biology, 1997. **4**(7):497.
 40. Kang, X.-f., L.-Q. Gu, S. Cheley and H. Bayley, *Single Protein Pores Containing Molecular Adapters at High Temperatures.* Angewandte Chemie International Edition, 2005. **44**(10):1495.
 41. Manrao, E.A., I.M. Derrington, A.H. Laszlo, K.W. Langford, M.K. Hopper, N. Gillgren, M. Pavlenok, M. Niederweis and J.H. Gundlach, *Reading DNA at single-nucleotide resolution with a mutant MspA nanopore and phi29 DNA polymerase.* Nature Biotechnology, 2012. **30**(4):349.
 42. Derrington, I.M., T.Z. Butler, M.D. Collins, E. Manrao, M. Pavlenok, M. Niederweis and J.H. Gundlach, *Nanopore DNA sequencing with MspA.* P Natl Acad Sci USA, 2010. **107**(37):16060.
 43. Butler, T.Z., M. Pavlenok, I.M. Derrington, M. Niederweis and J.H. Gundlach, *Single-molecule DNA detection with an engineered MspA protein nanopore.* P Natl Acad Sci USA, 2008. **105**(52):20647.
 44. Li, J., D. Stein, C. McMullan, D. Branton, M.J. Aziz and J.A. Golovchenko, *Ion-beam sculpting at nanometre length scales.* Nature, 2001. **412**(6843):166.
 45. Storm, A.J., J.H. Chen, X.S. Ling, H.W. Zandbergen and C. Dekker, *Fabrication of solid-state nanopores with single-nanometre precision.* Nat Mater, 2003. **2**(8):537.
 46. Storm, A.J., J.H. Chen, H.W. Zandbergen and C. Dekker, *Translocation of double-strand DNA through a silicon oxide nanopore.* Physical Review E, 2005. **71**(5).
 47. Venkatesan, B.M., B. Dorvel, S. Yemenicioglu, N. Watkins, I. Petrov and R. Bashir, *Highly Sensitive, Mechanically Stable Nanopore Sensors for DNA Analysis.* Advanced Materials, 2009. **21**(27):2771.
 48. Merchant, C.A., K. Healy, M. Wanunu, V. Ray, N. Peterman, J. Bartel, M.D. Fischbein, K. Venta, Z. Luo, A.T.C. Johnson and M. Drndic, *DNA Translocation through Graphene Nanopores.* Nano Letters, 2010. **10**(8):2915.
 49. Park, S.R., H. Peng and X.S. Ling, *Fabrication of Nanopores in Silicon Chips Using Feedback Chemical Etching.* Small, 2007. **3**(1):116.
 50. Storm, A.J., J.H. Chen, X.S. Ling, H.W. Zandbergen and C. Dekker, *Electron-beam-induced deformations of SiO₂ nanostructures.* Journal of Applied Physics, 2005. **98**(1):014307.
 51. Chen, P., T. Mitsui, D.B. Farmer, J. Golovchenko, R.G. Gordon and D. Branton, *Atomic Layer Deposition to Fine-Tune the Surface Properties and Diameters of Fabricated Nanopores.* Nano Letters, 2004. **4**(7):1333.
 52. Hall, A.R., A. Scott, D. Rotem, K.K. Mehta, H. Bayley and C. Dekker, *Hybrid pore formation by directed insertion of [alpha]-haemolysin into solid-state nanopores.* Nat Nano, 2010. **5**(12):874.
 53. Hall, J.E., *Access resistance of a small circular pore.* The Journal of General Physiology, 1975. **66**(4):531.

54. Stefan, W.K., Y.G. Alexander, R. Yitzhak and D. Cees, *Modeling the conductance and DNA blockade of solid-state nanopores*. *Nanotechnology*, 2011. **22**(31):315101.
55. Min Jun, K., M. Ben, M. Kazuyoshi and M. Amit, *Characteristics of solid-state nanometre pores fabricated using a transmission electron microscope*. *Nanotechnology*, 2007. **18**(20):205302.
56. Smeets, R.M.M., U.F. Keyser, D. Krapf, M.-Y. Wu, N.H. Dekker and C. Dekker, *Salt Dependence of Ion Transport and DNA Translocation through Solid-State Nanopores*. *Nano Letters*, 2005. **6**(1):89.
57. Ho, C., R. Qiao, J.B. Heng, A. Chatterjee, R.J. Timp, N.R. Aluru and G. Timp, *Electrolytic transport through a synthetic nanometer-diameter pore*. *P Natl Acad Sci USA*, 2005. **102**(30):10445.
58. Wanunu, M., W. Morrison, Y. Rabin, A.Y. Grosberg and A. Meller, *Electrostatic focusing of unlabelled DNA into nanoscale pores using a salt gradient*. *Nat Nano*, 2010. **5**(2):160.
59. Chen, P., J. Gu, E. Brandin, Y.-R. Kim, Q. Wang and D. Branton, *Probing Single DNA Molecule Transport Using Fabricated Nanopores*. *Nano Letters*, 2004. **4**(11):2293.
60. Heng, J.B., C. Ho, T. Kim, R. Timp, A. Aksimentiev, Y.V. Grinkova, S. Sligar, K. Schulten and G. Timp, *Sizing DNA Using a Nanometer-Diameter Pore*. *Biophysical Journal*, 2004. **87**(4):2905.
61. Fologea, D., M. Gershow, B. Ledden, D.S. McNabb, J.A. Golovchenko and J.L. Li, *Detecting single stranded DNA with a solid state nanopore*. *Nano Letters*, 2005. **5**(10):1905.
62. Meller, A., L. Nivon, E. Brandin, J. Golovchenko and D. Branton, *Rapid nanopore discrimination between single polynucleotide molecules*. *P Natl Acad Sci USA*, 2000. **97**(3):1079.
63. Mathe, J., A. Aksimentiev, D.R. Nelson, K. Schulten and A. Meller, *Orientation discrimination of single-stranded DNA inside the alpha-hemolysin membrane channel*. *P Natl Acad Sci USA*, 2005. **102**(35):12377.
64. Fologea, D., J. Uplinger, B. Thomas, D.S. McNabb and J.L. Li, *Slowing DNA translocation in a solid-state nanopore*. *Nano Letters*, 2005. **5**(9):1734.
65. Luan, B., G. Stolovitzky and G. Martyna, *Slowing and controlling the translocation of DNA in a solid-state nanopore*. *Nanoscale*, 2012. **4**(4):1068.
66. Yeh, L.-H., M. Zhang, S.W. Joo and S. Qian, *Slowing down DNA translocation through a nanopore by lowering fluid temperature*. *Electrophoresis*, 2012:n/a.
67. Kowalczyk, S.W., D.B. Wells, A. Aksimentiev and C. Dekker, *Slowing down DNA Translocation through a Nanopore in Lithium Chloride*. *Nano Letters*, 2012. **12**(2):1038.
68. Clarke, J., H.-C. Wu, L. Jayasinghe, A. Patel, S. Reid and H. Bayley, *Continuous base identification for single-molecule nanopore DNA sequencing*. *Nat Nano*, 2009. **4**(4):265.
69. Zwolak, M. and M. Di Ventra, *Electronic Signature of DNA Nucleotides via Transverse Transport*. *Nano Letters*, 2005. **5**(3):421.
70. Zikic, R., P.S. Krstić, X.G. Zhang, M. Fuentes-Cabrera, J. Wells and X. Zhao, *Characterization of the tunneling conductance across DNA bases*. *Physical Review E*, 2006. **74**(1):011919.

71. Krems, M., M. Zwolak, Y.V. Pershin and M. Di Ventra, *Effect of Noise on DNA Sequencing via Transverse Electronic Transport*. Biophysical Journal, 2009. **97**(7):1990.
72. Lagerqvist, J., M. Zwolak and M. Di Ventra, *Fast DNA sequencing via transverse electronic transport*. Nano Letters, 2006. **6**(4):779.
73. Zhang, X.G., P.S. Krstić, R. Zikić, J.C. Wells and M. Fuentes-Cabrera, *First-Principles Transversal DNA Conductance Deconstructed*. Biophysical Journal, 2006. **91**(1):L04.
74. Lagerqvist, J., M. Zwolak and M. Di Ventra, *Influence of the Environment and Probes on Rapid DNA Sequencing via Transverse Electronic Transport*. Biophysical Journal, 2007. **93**(7):2384.
75. Ohshiro, T. and Y. Umezawa, *Complementary base-pair-facilitated electron tunneling for electrically pinpointing complementary nucleobases*. P Natl Acad Sci USA, 2006. **103**(1):10.
76. Hughes, M.E., E. Brandin and J.A. Golovchenko, *Optical Absorption of DNA-Carbon Nanotube Structures*. Nano Letters, 2007. **7**(5):1191.
77. Chen, X., I. Rungger, C.D. Pemmaraju, U. Schwingenschloegl and S. Sanvito, *First-principles study of high-conductance DNA sequencing with carbon nanotube electrodes*. Physical Review B, 2012. **85**(11):5436.
78. Meunier, V. and P.S. Krstic, *Enhancement of the transverse conductance in DNA nucleotides*. The Journal of Chemical Physics, 2008. **128**(4):041103.
79. Meng, S., P. Maragakis, C. Papaloukas and E. Kaxiras, *DNA Nucleoside Interaction and Identification with Carbon Nanotubes*. Nano Letters, 2006. **7**(1):45.
80. Nojeh, A., A. Ural, R.F. Pease and H. Dai. *Electric-field-directed growth of carbon nanotubes in two dimensions*. 2004. San Diego, California (USA): AVS.
81. Yamazaki, K. and H. Namatsu, *5-nm-Order Electron-Beam Lithography for Nanodevice Fabrication*. Japanese Journal of Applied Physics. **43**:3767.
82. <http://www.gel.usherbrooke.ca/casino/What.html>.
83. Kyser, D.F., *Spatial resolution limits in electron beam nanolithography*. Journal of Vacuum Science & Technology B: Microelectronics and Nanometer Structures, 1983. **1**(4):1391.
84. Fischbein, M.D. and M. Drndic, *Nanogaps by direct lithography for high-resolution imaging and electronic characterization of nanostructures*. Applied Physics Letters, 2006. **88**(6):063116.
85. Anderson, E.H., D. Ha and J.A. Liddle, *Sub-pixel alignment for direct-write electron beam lithography*. Microelectronic Engineering, 2004. **73-4**:74.
86. Docherty, K.E., K.A. Lister, J. Romijn and J.M.R. Weaver, *High robustness of correlation-based alignment with Penrose patterns to marker damage in electron beam lithography*. Microelectronic Engineering, 2009. **86**(4–6):532.
87. <http://www.ammt.com>.
88. Michiel van den, H., R.H. Adam, W. Meng Yue, W.Z. Henny, D. Cees and H.D. Nynke, *Controlling nanopore size, shape and stability*. Nanotechnology, 2010. **21**(11):115304.
89. Anmiv, S.P., J.F. Kevin, W.F.R. Joseph, N. Zhorro, J.K. John and K. Min Jun, *SEM-induced shrinking of solid-state nanopores for single molecule detection*. Nanotechnology, 2011. **22**(42):425302.

90. Ronald, K., C. Chang, M. Guido, L. Liesbet and B. Gustaaf, *Shrinking solid-state nanopores using electron-beam-induced deposition*. *Nanotechnology*, 2009. **20**(11):115302.
91. Raillon, C., P. Granjon, M. Graf, L.J. Steinbock and A. Radenovic, *Fast and automatic processing of multi-level events in nanopore translocation experiments*. *Nanoscale*, 2012. **4**(16):4916.
92. Kroto, H.W., J.R. Heath, S.C. O'Brien, R.F. Curl and R.E. Smalley, *C60: Buckminsterfullerene*. *Nature*, 1985. **318**(6042):162.
93. Iijima, S., *Helical microtubules of graphitic carbon*. *Nature*, 1991. **354**(6348):56.
94. Monthieux, M. and V.L. Kuznetsov, *Who should be given the credit for the discovery of carbon nanotubes?* *Carbon*, 2006. **44**(9):1621.
95. Oberlin, A., M. Endo and T. Koyama, *Filamentous growth of carbon through benzene decomposition*. *Journal of crystal growth*, 1976. **32**(3):335.
96. Iijima, S. and T. Ichihashi, *Single-shell carbon nanotubes of 1-nm diameter*. *Nature*, 1993. **363**(6430):603.
97. Thess, A., L. Roland, P. Nikolaev, H. Dai, P. Petit, J. Robert, C. Xu, Y.H. Lee, K. Seong Gon, A.G. Rinzler, D.T. Colbert, G.E. Scuseria, D. Tománek, J.E. Fischer and R.E. Smalley, *Crystalline Ropes of Metallic Carbon Nanotubes*. *Science*, 1996. **273**(5274):483.
98. Avouris, P., Z. Chen and V. Perebeinos, *Carbon-based electronics*. *Nat Nano*, 2007. **2**(10):605.
99. Hamada, N., S.-i. Sawada and A. Oshiyama, *New one-dimensional conductors: Graphitic microtubules*. *Physical Review Letters*, 1992. **68**(10):1579.
100. Delaney, P., H.J. Choi, J. Ihm, S.G. Louie and M.L. Cohen, *Broken symmetry and pseudogaps in ropes of carbon nanotubes*. *Nature*, 1998. **391**(6666):466.
101. Charlier, J.C., X. Gonze and J.P. Michenaud, *First-Principles Study of Carbon Nanotube Solid-State Packings*. *EPL (Europhysics Letters)*, 1995. **29**(1):43.
102. Yao, Z., C.L. Kane and C. Dekker, *High-Field Electrical Transport in Single-Wall Carbon Nanotubes*. *Physical Review Letters*, 2000. **84**(13):2941.
103. Strano, M.S., C.A. Dyke, M.L. Usrey, P.W. Barone, M.J. Allen, H. Shan, C. Kittrell, R.H. Hauge, J.M. Tour and R.E. Smalley, *Electronic Structure Control of Single-Walled Carbon Nanotube Functionalization*. *Science*, 2003. **301**(5639):1519.
104. Peng, X. and S.S. Wong, *Functional Covalent Chemistry of Carbon Nanotube Surfaces*. *Advanced Materials*, 2009. **21**(6):625.
105. Tasis, D., N. Tagmatarchis, A. Bianco and M. Prato, *Chemistry of Carbon Nanotubes*. *Chemical Reviews*, 2006. **106**(3):1105.
106. Ando, Y. and X. Zhao, *Synthesis of carbon nanotubes by arc-discharge method*. *New Diamond and Frontier Carbon Technology*, 2006. **16**(3):123.
107. Bethune, D.S., C.H. Klang, M.S. de Vries, G. Gorman, R. Savoy, J. Vazquez and R. Beyers, *Cobalt-catalysed growth of carbon nanotubes with single-atomic-layer walls*. *Nature*, 1993. **363**(6430):605.
108. Ebbesen, T.W. and P.M. Ajayan, *Large-scale synthesis of carbon nanotubes*. *Nature*, 1992. **358**(6383):220.
109. Journet, C., W.K. Maser, P. Bernier, A. Loiseau, M.L. de la Chapelle, S. Lefrant, P. Deniard, R. Lee and J.E. Fischer, *Large-scale production of single-walled carbon nanotubes by the electric-arc technique*. *Nature*, 1997. **388**(6644):756.

110. Liu, J., A.G. Rinzler, H. Dai, J.H. Hafner, R.K. Bradley, P.J. Boul, A. Lu, T. Iverson, K. Shelimov, C.B. Huffman, F. Rodriguez-Macias, Y.-S. Shon, T.R. Lee, D.T. Colbert and R.E. Smalley, *Fullerene Pipes*. *Science*, 1998. **280**(5367):1253.
111. Ando, Y., X. Zhao, T. Sugai and M. Kumar, *Growing carbon nanotubes*. *Materials Today*, 2004. **7**(10):22.
112. Ando, Y., X. Zhao, S. Inoue and S. Iijima, *Mass production of multiwalled carbon nanotubes by hydrogen arc discharge*. *Journal of crystal growth*, 2002. **237**:1926.
113. Shi, Z., Y. Lian, X. Zhou, Z. Gu, Y. Zhang, S. Iijima, L. Zhou, K.T. Yue and S. Zhang, *Mass-production of single-wall carbon nanotubes by arc discharge method*. *Carbon*, 1999. **37**(9):1449.
114. Guo, T., P. Nikolaev, A. Rinzler, D. Tomanek, D. Colbert and R. Smalley, *Self-Assembly of Tubular Fullerenes*. *The Journal of Physical Chemistry*, 1995. **99**(27):10694.
115. Yakobson, B.I. and R.E. Smalley, *Fullerene Nanotubes: C 1,000,000 and Beyond: Some unusual new molecules, long, hollow fibers with tantalizing electronic and mechanical properties, have joined diamonds and graphite in the carbon family*. *American Scientist*, 1997. **85**(4):324.
116. Magrez, A., J.W. Seo, V.L. Kuznetsov and L. Forró, *Evidence of an Equimolar C₂H₂-CO₂ Reaction in the Synthesis of Carbon Nanotubes*. *Angewandte Chemie International Edition*, 2007. **46**(3):441.
117. Magrez, A., J.W. Seo, R. Smajda, B. Korbely, J.C. Andresen, M. Mionić, S. Casimirius and L. Forró, *Low-Temperature, Highly Efficient Growth of Carbon Nanotubes on Functional Materials by an Oxidative Dehydrogenation Reaction*. *ACS Nano*, 2010. **4**(7):3702.
118. Dai, H., *Carbon nanotubes: synthesis, integration, and properties*. *Accounts of chemical research*, 2002. **35**(12):1035.
119. Biercuk, M.J., M.C. Llaguno, M. Radosavljevic, J.K. Hyun, A.T. Johnson and J.E. Fischer, *Carbon nanotube composites for thermal management*. *Applied Physics Letters*, 2002. **80**(15):2767.
120. Qian, D., E.C. Dickey, R. Andrews and T. Rantell, *Load transfer and deformation mechanisms in carbon nanotube-polystyrene composites*. *Applied Physics Letters*, 2000. **76**(20):2868.
121. Liu, C., Y.Y. Fan, M. Liu, H.T. Cong, H.M. Cheng and M.S. Dresselhaus, *Hydrogen storage in single-walled carbon nanotubes at room temperature*. *Science*, 1999. **286**(5442):1127.
122. Dillon, A.C., K.M. Jones, T.A. Bekkedahl, C.H. Kiang, D.S. Bethune and M.J. Heben, *Storage of hydrogen in single-walled carbon nanotubes*. *Nature*, 1997. **386**(6623):377.
123. Baughman, R.H., C. Cui, A.A. Zakhidov, Z. Iqbal, J.N. Barisci, G.M. Spinks, G.G. Wallace, A. Mazzoldi, D. De Rossi, A.G. Rinzler, O. Jaschinski, S. Roth and M. Kertesz, *Carbon Nanotube Actuators*. *Science*, 1999. **284**(5418):1340.
124. Deheer, W.A., A. Chatelain and D. Ugarte, *A CARBON NANOTUBE FIELD-EMISSION ELECTRON SOURCE*. *Science*, 1995. **270**(5239):1179.
125. Choi, W.B., D.S. Chung, J.H. Kang, H.Y. Kim, Y.W. Jin, I.T. Han, Y.H. Lee, J.E. Jung, N.S. Lee, G.S. Park and J.M. Kim, *Fully sealed, high-brightness carbon-nanotube field-emission display*. *Applied Physics Letters*, 1999. **75**(20):3129.

126. Tans, S.J., A.R.M. Verschueren and C. Dekker, *Room-temperature transistor based on a single carbon nanotube*. Nature, 1998. **393**(6680):49.
127. Martel, R., T. Schmidt, H.R. Shea, T. Hertel and P. Avouris, *Single- and multi-wall carbon nanotube field-effect transistors*. Applied Physics Letters, 1998. **73**(17):2447.
128. Wong, S.S., E. Joselevich, A.T. Woolley, C.L. Cheung and C.M. Lieber, *Covalently functionalized nanotubes as nanometre-sized probes in chemistry and biology*. Nature, 1998. **394**(6688):52.
129. Hafner, J.H., C.L. Cheung, A.T. Woolley and C.M. Lieber, *Structural and functional imaging with carbon nanotube AFM probes*. Progress in Biophysics & Molecular Biology, 2001. **77**(1):73.
130. Hafner, J.H., C.L. Cheung, T.H. Oosterkamp and C.M. Lieber, *High-yield assembly of individual single-walled carbon nanotube tips for scanning probe microscopies*. Journal of Physical Chemistry B, 2001. **105**(4):743.
131. Nikolaev, P., M.J. Bronikowski, R.K. Bradley, F. Rohmund, D.T. Colbert, K.A. Smith and R.E. Smalley, *Gas-phase catalytic growth of single-walled carbon nanotubes from carbon monoxide*. Chemical Physics Letters, 1999. **313**:91.
132. Takagi, D., Y. Homma, H. Hibino, S. Suzuki and Y. Kobayashi, *Single-Walled Carbon Nanotube Growth from Highly Activated Metal Nanoparticles*. Nano Letters, 2006. **6**(12):2642.
133. Bhaviripudi, S., E. Mile, S.A. Steiner, A.T. Zare, M.S. Dresselhaus, A.M. Belcher and J. Kong, *CVD Synthesis of Single-Walled Carbon Nanotubes from Gold Nanoparticle Catalysts*. Journal of the American Chemical Society, 2007. **129**(6):1516.
134. Baker, R.T.K., *Catalytic growth of carbon filaments*. Carbon, 1989. **27**(3):315.
135. Raty, J.-Y., F.β. Gygi and G. Galli, *Growth of Carbon Nanotubes on Metal Nanoparticles: A Microscopic Mechanism from Ab Initio Molecular Dynamics Simulations*. Physical Review Letters, 2005. **95**(9):096103.
136. Baker, R.T.K. and R.J. Waite, *Formation of carbonaceous deposits from the platinum-iron catalyzed decomposition of acetylene*. Journal of Catalysis, 1975. **37**(1):101.
137. Gavillet, J., A. Loiseau, C. Journet, F. Willaime, F. Ducastelle and J.C. Charlier, *Root-Growth Mechanism for Single-Wall Carbon Nanotubes*. Physical Review Letters, 2001. **87**(27):275504.
138. Baker, R.T.K., P.S. Harris, R.B. Thomas and R.J. Waite, *Formation of filamentous carbon from iron, cobalt and chromium catalyzed decomposition of acetylene*. Journal of Catalysis, 1973. **30**(1):86.
139. Baker, R.T.K., M.A. Barber, P.S. Harris, F.S. Feates and R.J. Waite, *Nucleation and growth of carbon deposits from the nickel catalyzed decomposition of acetylene*. Journal of Catalysis, 1972. **26**(1):51.
140. Charlier, J.-C., A. De Vita, X. Blase and R. Car, *Microscopic Growth Mechanisms for Carbon Nanotubes*. Science, 1997. **275**(5300):647.
141. Hofmann, S., R. Sharma, C. Ducati, G. Du, C. Mattevi, C. Cepek, M. Cantoro, S. Pisana, A. Parvez, F. Cervantes-Sodi, A.C. Ferrari, R. Dunin-Borkowski, S. Lizzit, L. Petaccia, A. Goldoni and J. Robertson, *In situ Observations of Catalyst Dynamics during Surface-Bound Carbon Nanotube Nucleation*. Nano Letters, 2007. **7**(3):602.

142. Dai, H., A.G. Rinzler, P. Nikolaev, A. Thess, D.T. Colbert and R.E. Smalley, *Single-wall nanotubes produced by metal-catalyzed disproportionation of carbon monoxide*. Chemical Physics Letters, 1996. **260**:471.
143. Li, Y., W. Kim, Y. Zhang, M. Rolandi, D. Wang and H. Dai, *Growth of Single-Walled Carbon Nanotubes from Discrete Catalytic Nanoparticles of Various Sizes*. The Journal of Physical Chemistry B, 2001. **105**(46):11424.
144. Cheung, C.L., A. Kurtz, H. Park and C.M. Lieber, *Diameter-Controlled Synthesis of Carbon Nanotubes*. The Journal of Physical Chemistry B, 2002. **106**(10):2429.
145. Li, Y.-L., I.A. Kinloch, M.S.P. Shaffer, J. Geng, B. Johnson and A.H. Windle, *Synthesis of single-walled carbon nanotubes by a fluidized-bed method*. Chemical Physics Letters, 2004. **384**(1,Äi3):98.
146. Zhu, H., K. Suenaga, A. Hashimoto, K. Urita, K. Hata and S. Iijima, *Atomic-Resolution Imaging of the Nucleation Points of Single-Walled Carbon Nanotubes*. Small, 2005. **1**(12):1180.
147. Guan, L., K. Suenaga and S. Iijima, *Smallest Carbon Nanotube Assigned with Atomic Resolution Accuracy*. Nano Letters, 2008. **8**(2):459.
148. Kathyayini, H., N. Nagaraju, A. Fonseca and J.B. Nagy, *Catalytic activity of Fe, Co and Fe/Co supported on Ca and Mg oxides, hydroxides and carbonates in the synthesis of carbon nanotubes*. Journal of Molecular Catalysis A: Chemical, 2004. **223**(1,Äi2):129.
149. Hernadi, K., A. Fonseca, J.B. Nagy, A. Siska and I. Kiricsi, *Production of nanotubes by the catalytic decomposition of different carbon-containing compounds*. Applied Catalysis A: General, 2000. **199**(2):245.
150. Kong, J., A.M. Cassell and H. Dai, *Chemical vapor deposition of methane for single-walled carbon nanotubes*. Chemical Physics Letters, 1998. **292**(4,Äi6):567.
151. Klinke, C., J.-M. Bonard and K. Kern, *Comparative study of the catalytic growth of patterned carbon nanotube films*. Surface Science, 2001. **492**(1,Äi2):195.
152. Fonseca, A., K. Hernadi, J.B. Nagy, D. Bernaerts and A.A. Lucas, *Optimization of catalytic production and purification of buckytubes*. Journal of Molecular Catalysis A: Chemical, 1996. **107**:159.
153. Ivanov, V., J.B. Nagy, P. Lambin, A. Lucas, X.B. Zhang, X.F. Zhang, D. Bernaerts, G. Van Tendeloo, S. Amelinckx and J. Van Landuyt, *The study of carbon nanotubules produced by catalytic method*. Chemical Physics Letters, 1994. **223**(4):329.
154. Magrez, A., J.W. Seo, C. Mikó, K. Hernádi and L. Forró, *Growth of Carbon Nanotubes with Alkaline Earth Carbonate as Support*. The Journal of Physical Chemistry B, 2005. **109**(20):10087.
155. Alvarez, W.E., B. Kitiyanan, A. Borgna and D.E. Resasco, *Synergism of Co and Mo in the catalytic production of single-wall carbon nanotubes by decomposition of CO*. Carbon, 2001. **39**(4):547.
156. Li, Y., J. Liu, Y. Wang and Z.L. Wang, *Preparation of Monodispersed Fe/Mo Nanoparticles as the Catalyst for CVD Synthesis of Carbon Nanotubes*. Chemistry of Materials, 2001. **13**(3):1008.
157. Flahaut, E., A. Govindaraj, A. Peigney, C. Laurent, A. Rousset and C.N.R. Rao, *Synthesis of single-walled carbon nanotubes using binary (Fe, Co, Ni) alloy nanoparticles prepared in situ by the reduction of oxide solid solutions*. Chemical Physics Letters, 1999. **300**:236.

158. Colomer, J.F., G. Bister, I. Willems, Z. Konya, A. Fonseca, J. B. Nagy and G. Van Tendeloo, *Synthesis of single-wall carbon nanotubes by catalytic decomposition of hydrocarbons*. Chemical Communications, 1999(14):1343.
159. Herrera, J.E. and D.E. Resasco, *Loss of single-walled carbon nanotubes selectivity by disruption of the Co-Mo interaction in the catalyst*. Journal of Catalysis, 2004. **221**(2):354.
160. Tang, S., Z. Zhong, Z. Xiong, L. Sun, L. Liu, J. Lin, Z.X. Shen and K.L. Tan, *Controlled growth of single-walled carbon nanotubes by catalytic decomposition of CH₄ over Mo/Co/MgO catalysts*. Chemical Physics Letters, 2001. **350**:19.
161. Vander Wal, R.L., T.M. Ticich and V.E. Curtis, *Substrate, Åi support interactions in metal-catalyzed carbon nanofiber growth*. Carbon, 2001. **39**(15):2277.
162. Magrez, A., R. Smajda, J.W. Seo, E. HorvaÅÅth, P.R. RibicÅÜ, J.C. Andresen, D. Acquaviva, A. Olariu, G. Laurenczy and L. ForroÅÅ, *Striking Influence of the Catalyst Support and Its Acid, Åi Base Properties: New Insight into the Growth Mechanism of Carbon Nanotubes*. ACS Nano, 2011. **5**(5):3428.
163. Durrer, L., T. Helbling, C. Zenger, A. Jungen, C. Stampfer and C. Hierold, *SWNT growth by CVD on Ferritin-based iron catalyst nanoparticles towards CNT sensors*. Sensors and Actuators B: Chemical, 2008. **132**(2):485.
164. Bonard, J.-M., P. Chauvin and C. Klinke, *Monodisperse Multiwall Carbon Nanotubes Obtained with Ferritin as Catalyst*. Nano Letters, 2002. **2**(6):665.
165. Vijayaraghavan, A., S. Blatt, D. Weissenberger, M. Oron-Carl, F. Hennrich, D. Gerthsen, H. Hahn and R. Krupke, *Ultra-Large-Scale Directed Assembly of Single-Walled Carbon Nanotube Devices*. Nano Letters, 2007. **7**(6):1556.
166. Chung, J., K.-H. Lee, J. Lee and R.S. Ruoff, *Toward Large-Scale Integration of Carbon Nanotubes*. Langmuir, 2004. **20**(8):3011.
167. Teo, K.B.K., M. Chhowalla, G.A.J. Amaratunga, W.I. Milne, D.G. Hasko, G. Pirio, P. Legagneux, F. Wyczisk and D. Pribat, *Uniform patterned growth of carbon nanotubes without surface carbon*. Applied Physics Letters, 2001. **79**(10):1534.
168. Kong, J., H.T. Soh, A.M. Cassell, C.F. Quate and H. Dai, *Synthesis of individual single-walled carbon nanotubes on patterned silicon wafers*. Nature, 1998. **395**(6705):878.
169. Kind, H., J.-M. Bonard, L. Forró, K. Kern, K. Hernadi, L.-O. Nilsson and L. Schlapbach, *Printing Gel-like Catalysts for the Directed Growth of Multiwall Carbon Nanotubes*. Langmuir, 2000. **16**(17):6877.
170. Su, M., X. Liu, S.Y. Li, V.P. Dravid and C.A. Mirkin, *Moving beyond molecules: Patterning solid-state features via dip-pen nanolithography with sol-based inks*. Journal of the American Chemical Society, 2002. **124**(8):1560.
171. Huang, L., X. Cui, B. White and S.P. O'Brien, *Long and oriented single-walled carbon nanotubes grown by ethanol chemical vapor deposition*. Journal of Physical Chemistry B, 2004. **108**(42):16451.
172. Maruyama, S., R. Kojima, Y. Miyauchi, S. Chiashi and M. Kohno, *Low-temperature synthesis of high-purity single-walled carbon nanotubes from alcohol*. Chemical Physics Letters, 2002. **360**(3-4):229.
173. Huang, L., B. White, M.Y. Sfeir, M. Huang, H.X. Huang, S. Wind, J. Hone and S. O'Brien, *Cobalt Ultrathin Film Catalyzed Ethanol Chemical Vapor*

- Deposition of Single-Walled Carbon Nanotubes*. The Journal of Physical Chemistry B, 2006. **110**(23):11103.
174. Ya-Li, L., Z. Liang-Hong, Z. Xiao-Hua and H.W. Alan, *Synthesis of high purity single-walled carbon nanotubes from ethanol by catalytic gas flow CVD reactions*. Nanotechnology, 2007. **18**(22):225604.
 175. Maruyama, S., R. Kojima, Y. Miyauchi, S. Chiashi and M. Kohno, *Low-temperature synthesis of high-purity single-walled carbon nanotubes from alcohol*. Chemical Physics Letters, 2002. **360**(3–4):229.
 176. Liao, X.Z., A. Serquis, Q.X. Jia, D.E. Peterson, Y.T. Zhu and H.F. Xu, *Effect of catalyst composition on carbon nanotube growth*. Applied Physics Letters, 2003. **82**(16):2694.
 177. Dupuis, A.-C., *The catalyst in the CCVD of carbon nanotubes—a review*. Progress in Materials Science, 2005. **50**(8):929.
 178. Herrera, J.E., L. Balzano, A. Borgna, W.E. Alvarez and D.E. Resasco, *Relationship between the Structure/Composition of Co–Mo Catalysts and Their Ability to Produce Single-Walled Carbon Nanotubes by CO Disproportionation*. Journal of Catalysis, 2001. **204**(1):129.
 179. Hu, M., Y. Murakami, M. Ogura, S. Maruyama and T. Okubo, *Morphology and chemical state of Co–Mo catalysts for growth of single-walled carbon nanotubes vertically aligned on quartz substrates*. Journal of Catalysis, 2004. **225**(1):230.
 180. Engel-Herbert, R., H. Pforte and T. Hesjedal, *CVD synthesis and purification of single-walled carbon nanotubes using silica-supported metal catalyst*. Materials Letters, 2007. **61**(11–12):2589.
 181. Huang, L., S.J. Wind and S.P. O'Brien, *Controlled Growth of Single-Walled Carbon Nanotubes from an Ordered Mesoporous Silica Template*. Nano Letters, 2003. **3**(3):299.
 182. Bachilo, S.M., L. Balzano, J.E. Herrera, F. Pompeo, D.E. Resasco and R.B. Weisman, *Narrow (n,m)-Distribution of Single-Walled Carbon Nanotubes Grown Using a Solid Supported Catalyst*. Journal of the American Chemical Society, 2003. **125**(37):11186.
 183. Kitiyanan, B., W.E. Alvarez, J.H. Harwell and D.E. Resasco, *Controlled production of single-wall carbon nanotubes by catalytic decomposition of CO on bimetallic Co–Mo catalysts*. Chemical Physics Letters, 2000. **317**(3–5):497.
 184. *CRC Handbook of Chemistry and Physics 44th ed.*
 185. Hata, K., D.N. Futaba, K. Mizuno, T. Namai, M. Yumura and S. Iijima, *Water-Assisted Highly Efficient Synthesis of Impurity-Free Single-Walled Carbon Nanotubes*. Science, 2004. **306**(5700):1362.
 186. Jorio, A., R. Saito, J.H. Hafner, C.M. Lieber, M. Hunter, T. McClure, G. Dresselhaus and M.S. Dresselhaus, *Structural (n, m) Determination of Isolated Single-Wall Carbon Nanotubes by Resonant Raman Scattering*. Physical Review Letters, 2001. **86**(6):1118.
 187. Kim, W., A. Javey, R. Tu, J. Cao, Q. Wang and H. Dai, *Electrical contacts to carbon nanotubes down to 1 nm in diameter*. Applied Physics Letters, 2005. **87**(17):173101.
 188. Javey, A., J. Guo, Q. Wang, M. Lundstrom and H. Dai, *Ballistic carbon nanotube field-effect transistors*. Nature, 2003. **424**(6949):654.
 189. Mann, D., A. Javey, J. Kong, Q. Wang and H. Dai, *Ballistic Transport in Metallic Nanotubes with Reliable Pd Ohmic Contacts*. Nano Letters, 2003. **3**(11):1541.

190. Jeong, O.L., C. Park, K. Ju-Jin, K. Jinhee, P. Jong Wan and Y. Kyung-Hwa, *Formation of low-resistance ohmic contacts between carbon nanotube and metal electrodes by a rapid thermal annealing method*. Journal of Physics D: Applied Physics, 2000. **33**(16):1953.
191. Bachtold, A., M. Henny, C. Terrier, C. Strunk, C. Schonberger, J.P. Salvetat, J.M. Bonard and L. Forro, *Contacting carbon nanotubes selectively with low-ohmic contacts for four-probe electric measurements*. Applied Physics Letters, 1998. **73**(2):274.
192. Riley, F.L., *Silicon nitride and related materials*. J. Am. Ceram. Soc., 2000. **83**(2):245.
193. Smith, B.W. and D.E. Luzzi, *Electron irradiation effects in single wall carbon nanotubes*. Journal of Applied Physics, 2001. **90**(7):3509.
194. Yuzvinsky, T.D., A.M. Fennimore, W. Mickelson, C. Esquivias and A. Zettl, *Precision cutting of nanotubes with a low-energy electron beam*. Applied Physics Letters, 2005. **86**(5):053109.
195. Jiang, Z., M. Mihovilovic, J. Chan and D. Stein, *Fabrication of nanopores with embedded annular electrodes and transverse carbon nanotube electrodes*. Journal of Physics-Condensed Matter, 2010. **22**(45).
196. <http://imina.ch>.
197. Sadki, E.S., S. Garaj, D. Vlassarev, J.A. Golovchenko and D. Branton, *Embedding a carbon nanotube across the diameter of a solid state nanopore*. Journal of Vacuum Science & Technology B: Microelectronics and Nanometer Structures, 2011. **29**(5):053001.
198. Reed, M.A., C. Zhou, C.J. Muller, T.P. Burgin and J.M. Tour, *Conductance of a Molecular Junction*. Science, 1997. **278**(5336):252.
199. Strachan, D.R., D.E. Smith, D.E. Johnston, T.H. Park, M.J. Therien, D.A. Bonnell and A.T. Johnson, *Controlled fabrication of nanogaps in ambient environment for molecular electronics*. Applied Physics Letters, 2005. **86**(4):043109.
200. Kervennic, Y.V., H.S.J. Van der Zant, A.F. Morpurgo, L. Gurevich and L.P. Kouwenhoven, *Nanometer-spaced electrodes with calibrated separation*. Applied Physics Letters, 2002. **80**(2):321.
201. Ivanov, A.P., E. Instuli, C.M. McGilvery, G. Baldwin, D.W. McComb, T. Albrecht and J.B. Edel, *DNA Tunneling Detector Embedded in a Nanopore*. Nano Letters, 2010. **11**(1):279.
202. Word, M.J., I. Adesida and P.R. Berger, *Nanometer-period gratings in hydrogen silsesquioxane fabricated by electron beam lithography*. Journal of Vacuum Science & Technology B: Microelectronics and Nanometer Structures, 2003. **21**(6):L12.
203. Fischbein, M.D. and M. Drndic, *Sub-10 nm device fabrication in a transmission electron microscope*. Nano Letters, 2007. **7**(5):1329.
204. Maria, E.G., X. Anlin, A. Aleksei, S. Klaus, T. Gregory and L. Jean-Pierre, *Simulation of the electric response of DNA translocation through a semiconductor nanopore-capacitor*. Nanotechnology, 2006. **17**(3):622.
205. Xie, P., Q. Xiong, Y. Fang, Q. Qing and C.M. Lieber, *Local electrical potential detection of DNA by nanowire-nanopore sensors*. Nat Nano, 2012. **7**(2):119.
206. Schneider, G.g.F., S.W. Kowalczyk, V.E. Calado, G.g. Pandraud, H.W. Zandbergen, L.M.K. Vandersypen and C. Dekker, *DNA Translocation through Graphene Nanopores*. Nano Letters, 2010. **10**(8):3163.

-
207. Garaj, S., W. Hubbard, A. Reina, J. Kong, D. Branton and J.A. Golovchenko, *Graphene as a subnanometre trans-electrode membrane*. Nature, 2010. **467**(7312):190.
 208. Saha, K.K., M. Drndic and B.K. Nikolic, *DNA Base-Specific Modulation of Microampere Transverse Edge Currents through a Metallic Graphene Nanoribbon with a Nanopore*. Nano Letters, 2012. **12**(1):50.
 209. Nelson, T., B. Zhang and O.V. Prezhdo, *Detection of Nucleic Acids with Graphene Nanopores: Ab Initio Characterization of a Novel Sequencing Device*. Nano Letters, 2010. **10**(9):3237.
 210. Michael, Z. and V. Massimiliano Di, *Physical approaches to DNA sequencing and detection*. Reviews of Modern Physics, 2008. **80**.
 211. Huang, S., J. He, S. Chang, P. Zhang, F. Liang, S. Li, M. Tuchband, A. Fuhrmann, R. Ros and S. Lindsay, *Identifying single bases in a DNA oligomer with electron tunnelling*. Nat Nano, 2010. **5**(12):868.
 212. Tanaka, H. and T. Kawai, *Partial sequencing of a single DNA molecule with a scanning tunnelling microscope*. Nat Nano, 2009. **4**(8):518.
 213. Tsutsui, M., M. Taniguchi, K. Yokota and T. Kawai, *Identifying single nucleotides by tunnelling current*. Nature Nanotechnology, 2010. **5**(4):286.
 214. Tsutsui, M., S. Rahong, Y. Iizumi, T. Okazaki, M. Taniguchi and T. Kawai, *Single-molecule sensing electrode embedded in-plane nanopore*. Scientific Reports, 2011. **1**.
 215. Gierhart, B.C., D.G. Flowitt, S.J. Chen, Z. Zhu, D.E. Kotecki, R.L. Smith and S.D. Collins, *Nanopore with transverse nanoelectrodes for electrical characterization and sequencing of DNA*. Sensor Actuat B-Chem, 2008. **132**(2):593.
 216. Healy, K., V. Ray, L.J. Willis, N. Peterman, J. Bartel and M. Drndić, *Fabrication and characterization of nanopores with insulated transverse nanoelectrodes for DNA sensing in salt solution*. ELECTROPHORESIS, 2012. **33**(23):3488.
 217. Cervera, J., B. Schiedt and P. Ramírez, *A Poisson/Nernst-Planck model for ionic transport through synthetic conical nanopores*. EPL (Europhysics Letters), 2005. **71**(1):35.
 218. Siwy, Z., I.D. Kosińska, A. Fuliński and C.R. Martin, *Asymmetric Diffusion through Synthetic Nanopores*. Physical Review Letters, 2005. **94**(4):048102.
 219. Karnik, R., C. Duan, K. Castelino, H. Daiguji and A. Majumdar, *Rectification of Ionic Current in a Nanofluidic Diode*. Nano Letters, 2007. **7**(3):547.
 220. Ramirez, P., V. Gomez, J. Cervera, B. Schiedt and S. Mafe, *Ion transport and selectivity in nanopores with spatially inhomogeneous fixed charge distributions*. The Journal of Chemical Physics, 2007. **126**(19):194703.
 221. Kubeil, C. and A. Bund, *The Role of Nanopore Geometry for the Rectification of Ionic Currents*. The Journal of Physical Chemistry C, 2011. **115**(16):7866.
 222. Li, J., M. Gershow, D. Stein, E. Brandin and J.A. Golovchenko, *DNA molecules and configurations in a solid-state nanopore microscope*. Nat Mater, 2003. **2**(9):611.
 223. Kim, Y.-R., J. Min, I.-H. Lee, S. Kim, A.-G. Kim, K. Kim, K. Namkoong and C. Ko, *Nanopore sensor for fast label-free detection of short double-stranded DNAs*. Biosensors and Bioelectronics, 2007. **22**(12):2926.

Acknowledgments

It is, at last, time to thank all the people and friends who helped and supported me during these four years at the Nanoscale Science and Novel Electronic Materials research group and elsewhere at EPFL, without whom this work would have not been possible.

First, I would like to thank my thesis director László Forró whose trust and support allowed me to conduct this exciting research.

This thesis would not have been possible without my thesis co-director Arnaud Magrez, whose hair loss due to many hours spent correcting my thesis, while unfortunate, is very much appreciated. Of course I also appreciate his unwavering support and countless brilliant ideas, both as a mentor and a friend.

I warmly thank Aleksandra Radenovic, head of the Laboratory of Nanoscale Biology, for her advice, continuously motivating optimism and fruitful discussions, as well as Floriano Traversi, for his thoughtful assistance. It was a pleasure to work with them both.

Thanks also to Monique Bettinger, Evelyn Ludi and Anh Eyman, for the exemplary and timely assistance, the friendly atmosphere, and the much-needed laughter.

To Sylvia Jeney, who took a leap of faith to hire me for this project, I am grateful to have had this opportunity. Thank you very much.

Special thanks go to the members of the NN group, who, beyond being colleagues, became very good friends: Cristinu, colleague and roommate first and close friend later, for his help with Labview, lending me his bike every day to the point that I thought it was mine, and his daily friendship; Endre, for all his innovative ideas, fascinating stories about TiO_2 and for being a role model for all of us on how to keep a lab clean, for all the 10-ratings and fun moments; Flavio, for his help with Matlab, his clear explanations to my random questions and infectiously happy mood; Laurent, for the graphene sheets and fashion advice; Massimo Spina, for his kindness, willingness to help and inviting me to Sicily; and all the current and former members with whom I enjoyed working: Akshath, Anton, Areta, Balint, David, Dejan, Dora, Elena, Inès, Iva, Jacim, Kathrin, Lalat, Lenke, Luka, Marijana, Markus, Martial, Matthias, Maryam, Péter, Primož, Rita, Richard, Stevan, Zlatko.

My PhD could not have been accomplished without the CMI and CIME facilities at EPFL and without the quality of services offered by their staff. I can never thank Kevin Lister and Zdenek Benes enough for their precious support in electron beam lithography, for sharing their skills and knowledge to help me master the tools. This work would not have been accomplished without these two. Thanks to all the technicians, engineers and staff who are always at their best, Angélique*, Anthony, Boris, Claudia, Cyrille, Giancarlo, Guy, Jean-Baptiste*, Joffrey, Nareg, Patrick, Samuel, Valérian, A devoted thank to Didou, GAR, Phi-Phi, Yvan, for their enthusiasm, sympathy and team spirit that was always enjoyable. Thanks to Fabienne Bobard at CIME^e for her support every time I needed it and all the staff for the SEM/TEM trainings and advice.

Such intense work cannot be achieved without friends to share unforgettable moments with outside of the lab. First, my old friends Elodie, Jérémy, Marion and Romain, to whom I am particularly grateful for all the kind and supportive attention they've given me. Kevin, my sparing-partner, who made me realize that a PhD makes you lose your tennis skills but helped me get rid of my stress. To all the amazing people I have met during the last years: Pablo, for the lunches at la banana and deep conversations, Jibé, who started as a colleague but quickly became one of the best people I know: his late night assistance and hospitality, great sense of humor, and genuine kindness, along with the beach volley, paragliding and his picarde of girlfriend Stephanie are all very much appreciated. Thank you to Angélique, the manager of well being for CMI users, who aside her work proficiency, has been a pleasure to work with because of all the fun we've had together. She has been a constant moral support as well as being extremely helpful to my work.

Most importantly, my deepest and most sincere gratitude goes to my family that I love dearly: My parents Alain and Frédérique, my sister Karen and her husband Xavier. They have always been there for me, always supported me, and always made me feel that what I was doing was great and that they were proud of me.

The final lines of course go to the person I love the most, Emily. I thank you for your unconditional love, support and patience all along the stressful moments that we have had to go through together. I will always remember that this would not have been possible without you and that part of this work is also yours.

Curriculum Vitae

Axel FANGET

Rue de l'Ale, 31
1003 Lausanne, Switzerland
+41(0)794650261 - afanget@gmail.com
Single, 28 years old, French, B Permit

Education

- | | |
|------------------------------|---|
| December 2008-
April 2013 | <p><i>PhD Candidate in Biophysics</i>
Nanoscale Science and Novel Electronic Materials group
Swiss Federal Institute of Technology (EPFL)</p> <ul style="list-style-type: none"> • Led a multidisciplinary project aiming at the development and commercialization of a low-cost and high-throughput DNA sequencer involving physical chemistry, nanotechnology and molecular biology • Acquired advanced knowledge in clean room processes, particularly MEMS design and nanofabrication as well as excellent skills in characterization tools (HR-TEM & SEM, AFM) • Collaborated in a wider European program, especially regarding the device fabrication according to team requirements and project timeline |
| September 2006-
May 2008 | <p><i>Master of Science in Molecular and Biological Chemistry</i>
Swiss Federal Institute of Technology (EPFL)</p> <ul style="list-style-type: none"> • Specialization in synthesis chemistry and biological chemistry |
| September 2003-
June 2006 | <p><i>Bachelor of Science in Chemistry</i>
Swiss Federal Institute of Technology (EPFL)</p> <ul style="list-style-type: none"> • Focus on organic, inorganic, analytical and biological chemistry, cellular and molecular biology |

International Research Experience

- | | |
|-------------------------------|---|
| September 2007-
April 2008 | <p><i>Master's thesis</i>
Biomembrane Laboratory - Department of Chemical and Biomedical Engineering
University of Michigan - Ann Arbor, MI, USA</p> <ul style="list-style-type: none"> • <i>Characterization of aggregation of Aβ peptides and cytotoxicity on neuroblastoma SH-SY5Y cells</i>, a study of the toxicity on neuronal cells of potential candidates responsible for Alzheimer's disease • Successfully adapted to American research methods in a multicultural environment |
|-------------------------------|---|

Additional Experience

- | | |
|----------------------------|---|
| July 2009-
January 2012 | <p><i>Webmaster/Communications Manager</i>
Club de Vol Libre du Saleve (Paragliding Association) - France</p> <ul style="list-style-type: none"> • Responsible for the website and all communication to the community • Triple membership during this period through newsletters and events |
|----------------------------|---|

Core Competencies

- Strong multidisciplinary experience (Molecular & Cellular Biology, chemistry and Nanotechnology)
- Comfortable with challenging projects and timelines
- Problem solver, invested in finding innovative solutions
- Ability to communicate and work effectively in multicultural environments
- Teaching/mentoring experience
- Leadership skills and autonomous work ethic

Technology: Windows, MacOS, Linux, HTML and C Programming, LabView, DesignCAD, L-edit, SolidWorks. Igor, Matlab, Photoshop, Illustrator, Office Suite.

Languages: French (Mother Tongue), English (Fluent), German (Basic Vocabulary/Conversation)

Other interests: skiing, paragliding, travel, international politics, new technologies

www.linkedin.ch/in/axelfanget